Fluorogenic peptide-based probes for detection of proteases in inflammation

Maria Rodriguez-Rios

Doctorate of Philosophy

The University of Edinburgh

2023

Lay summary

Neutrophils and macrophages play a pivotal role in fighting and resolution of inflammation. These cells are very effective at fighting invading pathogens and they use digestive enzymes, so-called proteases, to destroy them. Their role is essential for an effective immune response. However, in acute and chronic inflammation, overactivation of these immune cells becomes detrimental and have been linked with a variety of disease states such as COVID-19 infection, pneumonia, lung injury or fibrosis.

Since the function of neutrophils and macrophages rely partly on their proteolytic capacity, monitoring the activity of proteolytic enzymes can give information on the activity of these cells. Thus, proteases have become excellent biomarker in inflammatory diseases, where abnormal activity can be detected. Currently, the main limitations of fluorogenic probes are their applicability *in vivo* due to their low signal-to-noise ratios, their poor solubility in water and their limited stability in complex systems.

Within my PhD, a series of fluorescence based optical probes were developed for monitoring proteolytic activity in neutrophils and macrophages. In the first two chapters of my thesis, I discuss the development a series of fluorogenic probes, with emission in the green and near infrared regions of the spectrum, which can detect the activity of human neutrophil elastase, a protease produced by neutrophils when they are activated which is a stablished disease marker in several inflammatory diseases. These probes provide excellent signal-to-noise ratios. In the third chapter, the synthesis and evaluation of a water-soluble probe for monitoring macrophage activity during bacterial infection is described. This probe targeted Cathepsin D, a lysosomal protease that mediates bacterial killing in macrophages. The probe was able to detect Cathepsin D activity in macrophages exposed to bacteria.

Abstract

Proteases can be great biomarkers of disease as these enzymes cleave amide bonds in peptides and proteins and regulate a variety of cellular process. Indeed, their dysregulation has been associated with a variety of diseases. Monitoring proteolytic activity using fluorescent probes has shown great application in disease diagnostics and for intraoperative imaging, but the current toolbox is still limited, and compounds often lack specificity for their target or provide limited signal amplification. In inflammatory diseases, overactivation of neutrophils and macrophages can lead to chronic and acute disease states in pathologies such as COVID-19 infection, pneumonia, lung injury or fibrosis. The overactivation of these immune cells is often associated with a higher proteolytic activity (to fight invading pathogens), which can be monitored using fluorogenic probes to provide information on the inflammatory response during infection and be used for diagnostic application.

In this thesis, a series of fluorogenic probes for the detection of neutrophil and macrophage proteases implicated in inflammatory processes are developed. In the first chapter a major review of proteases and fluorogenic probes is presented. In the two subsequent chapters a series of probes that provide an OFF/ON fluorescent signal for the detection of the serine protease human neutrophil elastase (hNE) is reported. Two generations of probes were developed, the first generation consists of a series of probes with fluorescence emission in the green region of the spectrum based on previous successful designs. The probes allowed detection of elastase in activated neutrophils and in so-called neutrophil extracellular traps (NETs) which have been implicated in the pathogenesis of acute and chronic inflammatory diseases. Limitations of its *in vivo* application led to the development of a second generation of probes with fluorescence emission in the NIR, where tissue penetration and fluorescence background are reduced. A novel synthetic approach was implemented to synthesise the second generation of probes with NIR emission. The NIR probes were validated *in vitro* and are currently being evaluated in cells. The optimised NIR probe could serve as an excellent tool for *in vivo* imaging. The fourth chapter focuses on the synthesis of a fluorogenic, pH stable, water-soluble FRET probe for the specific detection of CatD, an aspartic protease present in macrophages that is upregulated in macrophages when fighting bacterial infections. The probe was designed to serve as a tool to understand the mechanism of apoptosis associated bacterial killing by macrophages, where the activity of CatD was detected in macrophages exposed to bacteria.

Declaration of authorship

The research reported in this thesis was carried out by the author in the duration of her PhD study from December 2018 to November 2022 under the supervision of Professor Mark Bradley, School of Chemistry, University of Edinburgh. The work, data, and interpretation presented here are those of the author unless there was a significant collaborative contribution made, in which case it has been clearly recognised. References have been provided to all supporting literature and resources, including the published work of others. This work has not been submitted for any other degrees or professional qualifications.

Parts of the presented work in this thesis are currently published:

- M. Rodriguez-Rios, A. Megia-Fernandez, D. J. Norman, M. Bradley, *Chem. Soc. Rev.,* 2022, **51**, 2081-2120.
- M. R. Rios, G. Garoffolo, G. Rinaldi, A. Megia-Fernandez, S. Ferrari, C. T. Robb, A. G. Rossi, M. Pesce, M. Bradley, *Chem. Commun*., 2021, **57**, 97-100.

Signed:

Dated:

Contents

Acknowledgements

First and foremost, I would like to thank Professor Mark Bradley for the opportunity to do my PhD under his supervision and work on incredibly exciting projects and for the constant support from day one. I would like to also extend my gratitude to Dr Annamaria Lilienkampf, for the advice and support throughout my PhD and for being a role model for us. Thanks for believing in me and for the guidance every step of the way during these years, I could not have asked for better supervisors. Special thanks go to Alicia, my mentor when I joined the group. Thank you for your patience and constant advice, you have been an incredible mentor but also an amazing friend.

The progress in my research project would have not been possible without the help from Giulia Rinaldi, who performed most of the biological validation, thank you for being such a great colleague, it has been a pleasure to work with you in this project. Also, thanks to Gloria, Maurizio, Brian, Caitlin and Mike for their contributions on the biological and lifetime studies.

The last 4 years have been an incredible journey and I am so happy to have shared it with such an amazing group of people. Special thanks to Jess, Alessia, Dan, Assel and Antonio in the short time that we had together in the group, we had an amazing journey, and I am so happy to get the lifelong friendships that we have from that. I would like to thank all the current and past members of the group Olga, Sonia, Paige, Maulida, Max, James, Tommy, Zainab, Meltem, Richa, Yuguo, Ewan, Shufan, Nouf, Liao, Fizza and Xia, for the constant help, support and cheering, it has been a pleasure to have shared the last few years with you.

On the personal side, special thanks go to my family, thanks for the unconditional support and for believing in me and cheering me in every step. To my Scottish family, Ainhoa, Joanna, Sara, Davo, David, Ruben, Claudia, Dan and Victoria, you guys have been an incredible pillar out of the lab and helped me in so many ways to get where I am now.

Last but not least, I would like to thank Lucho, my “rock” and biggest support for the last few years. This PhD would have not been possible without you. Going “back to uni” together has been a wild and amazing ride and I am so grateful to have shared yet another journey together. Your optimism and calmness always got the best from me, and the countless adventures were the best therapy against stress. Now we both reached the finish line, and I am so proud of what we have achieved and looking forward to what comes next.

Abbreviations

Ab	Antibody
ACN	Acetonitrile
a.u	Arbitrary Units
Boc	*tert*-Butyloxycarbonyl group
CuAAC	Copper-catalysed azide-alkyne cycloaddition
Cy	Cyanine
DCC	*N,N′*-Dicyclohexylcarbodiimide
DCM	DCM
Dde-OH	2-Acetyldimedone
DIC	*N,N*-Diisopropylcarbodiimide
DIPEA	*N,N*-Diisopropylethylamine
DMAP	4-Dimethylaminopyridine
DMSO	Dimethyl sulfoxide
EG	Polyethylene glycol
ELSD	Evaporative light scattering detector
ESI	Electrospray ionization
FA	Formic acid
FACS	Fluorescence-activated cell sorting
FBS	Fetal bovine serum
Fmoc	Fluorenylmethoxycarbonyl
FRET	Forster resonance energy transfer
h	hours
HEPES	4-(2-hydroxyethyl)-1-piperazineethanesulfonic acid
HPLC	High-performance liquid chromatography
HSPyU	Dipyrrolidino(N-succinimidyloxy)carbenium hexauorophosphate
K_m	Michaelis constant

k_{cat}	Turnover number
LC-MS	Liquid chromatography mass spectrometry
MALDI-ToF	Matrix-assisted laser desorption/ionization- time of flight
min	minutes
MR	Methyl Red
m/z	Mass-to-charge ratio
NHS	N-hydroxysuccinimide
NIR	Near Infrarred Region
NMR	Nuclear magnetic resonance
Oxyma	Ethyl (hydroxyimino)cyanoacetate
PBS	Phosphate-buffered saline
PS	Polystyrene
RFU	Relative fluorescence units
RP	Reverse-phase
SPPS	Solid Phase Peptide Synthesis
TFA	Trifluoroacetic acid
THF	Tetrahydrofuran
t_R	Retention time
TLC	Thin layer chromatography
THPTA	Tris-hydroxypropyltriazolylmethylamine
TSTU	N,N,N′,N′-Tetramethyl-O-(N-succinimidyl)uronium-tetrafluoroborate
UV	Ultraviolet
V_{max}	Maximum velocity
5-FAM	5-carboxyfluorescein
δ	Chemical shift in ppm
τ	Fluorescence lifetime
λ	Wavelength
Φ	Quantum yield

Chapter 1 Introduction

Parts of this chapter are published as:

M. Rodriguez-Rios, A. Megia-Fernandez, D. J. Norman, M. Bradley*, Chem. Soc. Rev.*, 2022, **51**, 2081-2120*.*

Proteases are enzymes that hydrolyse amide bonds. They can cleave terminal amino acid residues from a peptide (so-called exopeptidases) and this can be either at the amino or carboxy termini (aminopeptidases or a carboxypeptidase); or they can cleave internal bonds (endopeptidases). Cleavage by endopeptidases happens at the so-called scissile bond[1], between two amino acid residues termed P1 and P1'.[2] Residues on the amino terminal side of the scissile bond are numbered in the C to N direction, whilst in the "prime" or C-terminal side the order is assigned from N to C (see Figure 1). The substrate specificity of most endopeptidases is determined by the sidechain of the P1 residue, however, surrounding residues also affect substrate specificity, and determining the efficiency of binding to the active site of the protease.

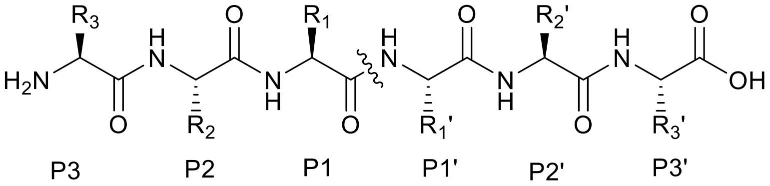

Figure 1. Example of a generic hexapeptide with the corresponding P3-P1/P1'-P3' nomenclature.

Based on their mechanism of amide bond cleavage proteases are classified into five distinct classes: aspartic, metallo, cysteine, serine, and threonine proteases.[3] Some of these classes activate a water molecule to attack the amide bond of the peptide (e.g., aspartic and metallo proteases) whereas in the remaining classes, the nucleophile is the functional group (hydroxy or thiol) on the amino acid sidechain (Cys, Ser, or Thr, respectively).

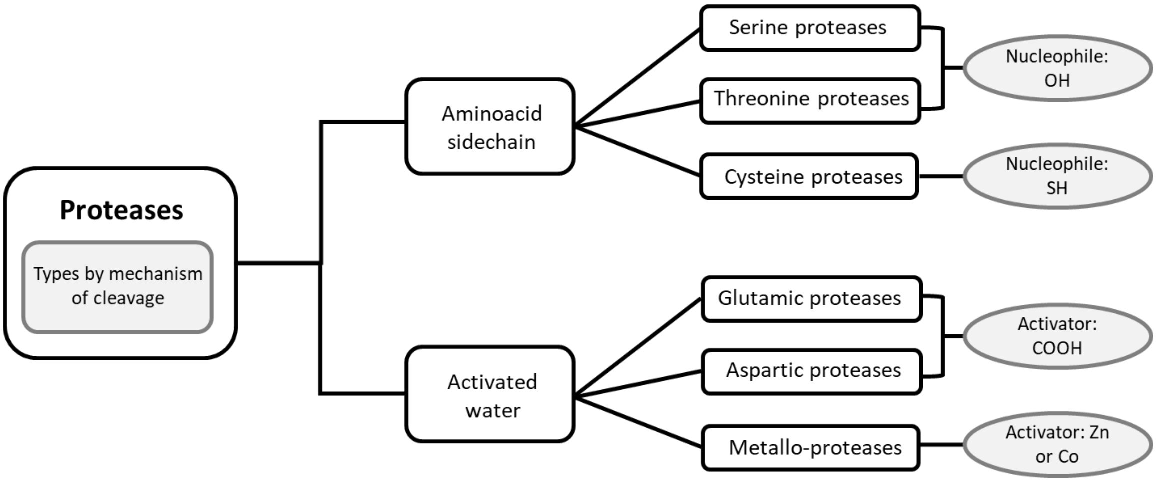

Figure 2. Classification of proteases based on their mechanism of catalytic cleavage. Based on the nucleophile used for cleavage, two main types of proteases can be distinguished, the ones that use the sidechain of amino acids in the active site, and those who can activate a molecule of water to perform the nucleophilic attack.

1.1 Proteases in disease

Proteases are essential for cell viability and can regulate fate, localization, and activity of many other biomolecules and as such, proteolysis occurs at every stage of a cell's lifecycle[4], and in every cell compartment. They activate proenzymes, destroy proteins to regulate their cellular levels and remodel the matrix to name a few examples. Proteolytic enzymes are tightly regulated and their overexpression/overactivation has been associated with many diseases, with some examples described below.[4]

Serine proteases[5] are a large family of proteolytic enzymes that play an essential role in physiological processes like blood coagulation, apoptosis and inflammation. Granzymes are serine proteases that are mostly expressed in cytotoxic lymphocytes, neutrophil elastase, cathepsin G and proteinase 3 are abundant in neutrophils and chymase and tryptase are present in mast cells. Despite their key role in inflammatory processes, serine protease dysregulation has been associated with a variety of inflammatory diseases. Examples include chronic obstructive pulmonary disease (COPD), which is associated with the presence of T cells with elevated levels of Granzyme B which may cause inflammation and lung destruction[6] or as biomarkers of kidney transplant rejection, with urinary levels of Granzyme A and Granzyme B specifically elevated in patients receiving a transplant. [7] High levels of neutrophil elastase, the most abundant serine protease in human neutrophils, have been detected in patients with cystic fibrosis.[8]

Aspartic proteases are involved in the regulation of blood pressure, with renin involved in the conversion of angiotensinogen into angiotensin I. [9] Within cells, several aspartic proteases play important roles, Cathepsin D (CatD) in the lysosomes of cells acts to activate other enzymes, pro-hormones, and growth factors. High levels of CatD have been observed in areas surrounding tumours[10] leading to the hypothesis that CatD is involved in the invasiveness of cancer cells. Cathepsin E, which is found mainly in cells of the lymphoid system and seems to have a function in the response of cells to immunological stimuli. The beta-site amyloid precursor protein cleaving enzyme (BACE) is involved in the conversion of the β-amyloid precursor protein to a form that can aggregate and cause fibrils that are found in Alzheimer's disease.[11] The viral aspartic protease in HIV[12] is essential for successful viral infection and is involved into its own N-terminal cleavage, required for maturation.

Cysteine proteases[8] are ubiquitous in most tissues. These protease's main function is to catalyse protein hydrolysis within the lysosomes, but they are also involved in MHC-II-mediated antigen presentation, bone remodelling, keratinocytes differentiation, hair follicle growth, reproduction and apoptosis. Upregulation of cathepsin activity has been demonstrated in many human tumours. High levels of Cathepsin B, one of the best understood within the cathepsin family, is associated with a variety of cancers[13, 14] and in inflammatory diseases such as rheumatoid arthritis.[15] Recent studies associate high Cathepsin B levels with increased blood pressure and aortic dilation.[16] Cysteine cathepsins could be playing a role in the infection process of SARS-CoV-2 by cleaving the spike protein on the virus' capsid that allows membrane fusion to the targeted cell.[17]

Threonine proteases are the least abundant type with only a few examples found in the MEROPS database. Their low abundance could possibly be due to the reduced nucleophilicity of the threonine sidechain to exert amide bond cleavage when compared to serine or cysteine proteases. Despite the low abundance, threonine proteases can be found in humans involved in essential homeostatic roles such as in the proteosome, which relies on a threonine catalytic residue to exert its proteolytic activity. The ubiquitin-proteosome system is a sophisticated system that is responsible for degradation of peptides and proteins inside the cell. [18] When proteins are to be removed in the cell or misfolded, they are tagged with a small protein label so-called ubiquitin. Ubiquitin labels are recognised by the proteosome, that will engulf and degrade the tagged protein. In the proteosome, the threonine residue is in the N-terminus and located close to a lysine (that has been suggested to reduce the pKa of the threonine sidechain and increase its nucleophilicity). Defective catalytic activity of the proteosome has been associated with a variety of neurodegenerative diseases such as Alzheimer's, Parkinson's, and Huntington's disease as well as heart diseases. [19, 20]

Matrix metalloproteinases (MMPs) are a family of proteolytic enzymes that perform multiple roles in the normal immune response to infection. [21] These enzymes can facilitate immune cell recruitment, cytokine or chemokine processing and matrix remodelling. However, high levels of matrix metalloproteinases activity can be the cause of immuno-pathologies, in fact, high levels of MMP-9 are detected in HIV patients[22], where MMP-9 secretion leads to increased endothelial permeability, which might be related to an increased blood–brain barrier permeability. High levels of MMP-14 may increase invasiveness in Hepatitis B infection[23], not only through a direct effect on the extracellular matrix but also by activation of other MMPs.

1.2 Protease inhibitors

Having a better understanding of the role of proteases in physiological and pathological conditions has led to the development of many inhibitors with wide ranging therapeutic uses in the treatment of a variety of diseases. To be effective, protease inhibitors must be potent and highly selective to the targeted protease, besides, good pharmacokinetic and pharmacodynamic properties that are essential for their successful application.[24]

- DPP-4 inhibitors (so-called gliptins) are used to treat type II diabetes mellitus[25], with the inhibitors blocking the activity of the serine protease DPP-4, a protease that destroys incretins. Saxaglitpin (Figure 3) is a clinically used gliptin that helps stimulate the production of insulin when it is needed and reduce the production of glucagon by the liver when it is not.

- The proteosome is a highly sophisticated protease complex evolved to carry out selective, efficient and processive hydrolysis of client proteins. There are currently several inhibitors used that target the proteosome to treat multiple myeloma. [26] Inhibition of the proteosome induces apoptosis of the cancer cells. The well-known protease inhibitor drug in this area is bortezomib (Figure 3) that contains a boronic acid and inhibits the proteosome by covalent binding to the catalytic threonines responsible for amide bond cleavage in the proteasome.

- Angiotensin converting enzyme (ACE) inhibitors have seen widespread usage in the treatment of cardiovascular and renal disease. ACE is a bivalent dipeptidyl carboxyl metallopeptidase responsible for formation of angiotensin II, which is a potent vasoconstrictor. Angiotensin-converting enzyme inhibitors were developed as therapeutic agents targeted for the treatment of hypertension, that prevent vasoconstriction in patients with hypertension improving blood flow, a common example widely used is captopril (Figure 3).[27]

- Hirudin is a naturally occurring peptide that is a potent inhibitor of thrombin, a serine protease that is key in the coagulation process, responsible for conversion of fibrinogen into fibrin. Hirudin has been used in the clinic to treat acute coronary artery disease, deep vein thrombosis and other thrombotic diseases.[28]

- Cilastatin is an inhibitor of dehydropeptidase is, an enzyme found in the kidney, which can degrade the antibiotic peptide imipenem. Co-administration of cilastatin with the antibiotic prevents degradation, prolonging its antibacterial effect.[29]

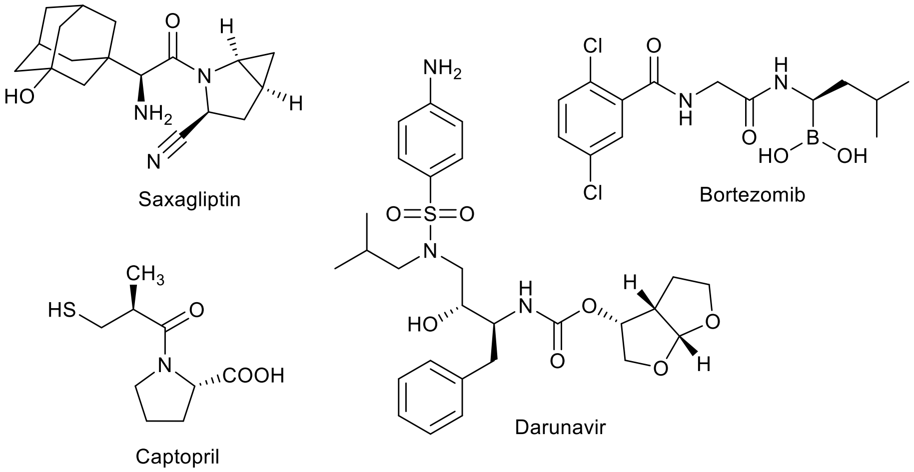

Figure 3. Examples of protease inhibitors in the clinic. Saxagliptin is one of many clinically used DPP-4 inhibitors. Bortezomib is used to inhibit the threonine protease activity of the proteosome. Darinavir targets the HIV virus protease and Captopril is used to treat hypertension, it is an inhibitor of the angiotensin converting enzyme.

Inhibitors targeting human proteases, with the objective of exploiting the overexpression in pathology, can present a challenge in terms of side effects due to physiological expression of the proteases require for proper healthy function. Hence, some medicinally used inhibitors target orthogonal proteases, i.e., proteases which are not physiologically expressed in human cells, with approved protease inhibitors targeting several viral proteases. Introduced in 1995 was saquinavir targeting the HIV retroviral aspartyl protease and this family of inhibitors have been huge success in the management of HIV infection [30], controlling the progression of HIV infection to AIDS by inhibiting its replication. Darunavir is now recommended as first line therapy choice (Figure 3). Other widely used orthogonal protease inhibitors include beta-lactams (both as inhibitors of beta-lactamase's themselves (e.g., clavulanic acid) as well as cell wall cross-linking enzymes (penicillins). Inhibitors with antifungal activity target secreted aspartic proteases (SAPs) are involved in several fungal infections, they play a role in tissue invasion, growth, and immune system evasion, among the important human fungal pathogens *Candida albicans* and *C. neoformans.* Synthetic small molecule inhibitors based on indolone derivates have been developed for secreted aspartic protease 2 (SAP2) and demonstrated high potency, with high antifungal activity against *Candida Albicans.* [31, 32]

1.3 Probes for monitoring proteolytic activity

Monitoring proteolytic activity is crucial to better understand the expression profiles and function of this proteases in physiological conditions as well as in disease, and the most widely used types of probes for detection of proteases are antibody- or peptide-based probes.

- **Antibody-based probes** are widely used for monitoring proteases in cells. These affinity probes are based on a tagged antibody that specifically binds the protease and can give quantitative information on the levels of expression and localisation of the target protein. The tag can be a fluorescent label, biotin or a radioisotope. This method of detection, however, is limited to detection in the extracellular space, because antibodies are incapable of penetrating the cell membrane so they cannot provide spatio-temporal information inside living cells, unless cells are permeabilized. In addition, antibody-based detection cannot distinguish between active proteases and the non-active zymogen and the catalytically active protease (zymogens are pro-proteases, proteins that require activation by other protease to gain catalytic activity).

- **Peptide-based probes** are based on peptide sequences that are a substrate for the protease of interest. These types of probes are excellent tools for monitoring proteolytic activity in real time, and most of these probes can access the intracellular space and serve as tools for the assessment of cell phenotype, diagnostic applications[33, 34] and the development of novel therapies. In addition, their low immunogenicities and low cell toxicities, makes them excellent tools for *in vivo* applications. There are two main types of peptide-based probes:

    - **Activity based probes** (probes that are based on inhibitors of the enzyme that bind covalently to the active site. These probes allow relative protease quantification and spatio-temporal imaging. However, signal amplification is not possible, and the enzyme activity is inhibited upon irreversible binding. In addition, since most of the activity-based probes are "always on" their signal-to-noise ratios are limited. [35-37]

    - **Substrate-based probes** offer an "OFF/ON" signal and are catalytically cleaved by the protease, with many copies of the probe activated/cleaved by the same molecule of the protease, without demonstrating inhibitory effects. [34] Substrate-based probes can be based on optical imaging by fluorescence, photoacoustic imaging or chemiluminescent detection and offer great promise for *in vivo* imaging applications. Other, more exotic detection modalities include electrochemical-based reporters and those based on MS- technologies. There is great promise for the development of point-of-care technologies for use in a number of medical scenarios.

A critical review on the current state of the art of substrate-based probes and how they compare to each other has been published and can be found here:

Chem Soc Rev

REVIEW ARTICLE

Cite this: *Chem. Soc. Rev.*, 2022, 51, 2081

Received 29th September 2021

DOI: 10.1039/d1cs00798j

rsc.li/chem-soc-rev

Peptide probes for proteases – innovations and applications for monitoring proteolytic activity

Maria Rodriguez-Rios,[a] Alicia Megia-Fernandez,[a] Daniel J. Norman[b] and Mark Bradley *[a]

Proteases are excellent biomarkers for a variety of diseases, offer multiple opportunities for diagnostic applications and are valuable targets for therapy. From a chemistry-based perspective this review discusses and critiques the most recent advances in the field of substrate-based probes for the detection and analysis of proteolytic activity both *in vitro* and *in vivo.*

Introduction

Proteases are enzymes with wide-ranging and crucial activities that mediate the hydrolysis of amide bonds. The residues within the active site of the enzyme responsible for the biological activity allow the partitioning of these enzymes into the five major classes: so-called serine, threonine, cysteine, aspartic acid or metallo-based proteases. Cleavage by proteases typically occurs on well-defined substrates to allow for discrete and precise regulation of biological functions and takes place between two amino acids (P1–P1’) (by endopeptidases) or at the N- or C-terminus of the peptide (by exopeptidases). Proteases need to recognise their substrate to allow exertion of its function, with the most crucial amino acid being that located on the P1 position of the scissile bond. The degree of substrate specificity is variable, with some proteases accepting a broad spectrum of substrates and others accepting very few.

The function of proteases is essential for an abundance of cellular processes, that includes matrix remodelling by metalloproteinases during cell growth, angiogenesis and tissue remodelling;[1] regulation of cell division by the calpain family[2] and the control of programmed cell death by caspases.[3] These physiological proteolytic functions are tightly

---

[a] *EaStCHEM School of Chemistry, University of Edinburgh, David Brewster Road, EH9 3FJ Edinburgh, UK. E-mail: Mark.Bradley@ed.ac.uk*

[b] *Technical University of Munich, Trogerstrasse, 30, 81675, Munich, Germany*

Maria Rodriguez-Rios

Maria Rodriguez-Rios received her bachelor’s degree in Biochemistry from the Universitat Autonoma de Barcelona in 2015. She obtained a MSc in Drug Design and Biomedical Sciences from Edinburgh Napier University, working on the development of optical probes for cancer imaging. Following a short period working in industry, she started her PhD studies at the University of Edinburgh under the supervision of Professor Mark Bradley working on the synthesis of fluorogenic peptide-based probes for imaging inflammation.

Alicia Megia-Fernandez

Alicia Megia-Fernandez, MRSC, obtained her MSc degree in Chemistry and PhD from the University of Granada, Spain, under the guidance of Professor Santoyo-Gonzalez, where she was awarded the Extraordinary PhD Award in Experimental Science. This was followed by the award of Fundación Ramón Areces and Marie Curie IEF Fellowships to work as a postdoctoral researcher at the University of Edinburgh with Professor Bradley. In 2022 she was appointed to a Maria Zambrano Senior Fellowship at the University of Granada. Her current research interests are in Chemical Biology and include chemical methodology and molecular imaging probes for diagnosis and treatment of different diseases.

regulated and dysfunction of proteases can be highly detrimental and has been linked to a variety of diseases with examples including cancer,[4] diabetes,[5] inflammation,[6] vascular diseases[7] and Alzheimer's.[8] Indeed, Alzheimer's disease, which is characterised by a cognitive decline, is associated with an accumulation of amyloid-b (Ab) plaques produced by a sequence of proteolytic events of the amyloid precursor protein by a-, b- and g-secretases that result in aggregation and generation of Ab.[8] The disease-causing proteolytic network of Alzheimer's disease exemplifies the need for specific and versatile protease probes in order to distinguish and elucidate the biochemical processes responsible, such as chemical probes that enable the specific identification of the aspartyl protease g-secretase.[9] Proteases have emerged as excellent disease biomarkers. For instance, thrombin is widely used as a biomarker in the diagnosis of blood disorders and prostate cancer. Proteases are also attractive drug targets, with a variety of inhibitors developed used to treat diseases such as the HIV-1 protease inhibitors to treat AIDS,[10] and captopril to treat hypertension.[11]

Understanding the role of proteases in disease and the evaluation of treatment efficacy are crucial for the success of the drug development process, but current gold-standard methods typically rely on *in vitro* detection by genetic expression measurements or immunostaining. However, these methods base their detection on indirect measurement of protease concentration instead of proteolytic activity and they cannot distinguish between active and inactive (pro-forms) of the protease. Peptide-based probes have emerged as an alternative to these methods to allow the evaluation of the activity of a variety of proteases.[12,13] A key advantage is that these probes rely solely on ''real'' proteolytic activity and allow both *in vitro* and *in vivo* evaluation in real time. These probes typically contain a peptide-targeting moiety (that is recognised by the protease) and a reporter (*e.g.* a fluorophore, a contrast agent, an electrochemical tag or a mass tag). Peptides are ideal as the recognition element as they mimic the endogenous substrate and offer high natural specificity, while providing a scaffold for the attachment of labels or signal transducers.

In vivo imaging of proteolytic activity is becoming extremely useful in the area of diagnostics or for optical-image-guided surgery.[14] Fluorescent peptide-based probes are widely used in optical imaging, with many efforts pushing into the near infrared imaging window of the spectrum,[15] where biological tissues are silent and penetration of light is enhanced. In recent years, other approaches have made an appearance as promising alternatives to fluorescence-based technologies. These include chemiluminescent probes, that do not need an external light source and provide virtually no background signal, and photoacoustic imaging that offers great promise for deep-tissue imaging, with the main advantage of being able to image tissue at depths of more than 1 cm.

Bench-top or *in vitro* technologies for laboratory analysis of proteolytic activity have seen advances in the area of colorimetric detection; with applications for *in vitro*, low cost and easy-to read analysis, electrochemical probes, with redox-based detection of proteases offering an alternative to other methods where complex media samples might affect other detection methods such as fluorescence. The area of MS and proteomics has seen proteolytic profiling appearing with applications in disease diagnostics and comparative analysis of proteolytic activity in health and disease. In this review, we discuss recent advances in the area of probes for the detection of proteases and new strategies in the area of FRET, pro-fluorophores, bioorthogonal reactions, aggregation-induced emission and chemiluminescence based optical probes as well as methods based on photoacoustic contrast agents, electrochemical detection, mass spectrometry and colorimetric reporters.

Comprehensive reviews have been published in the field of protease activity and we would like to highlight those of Ong,[16] Oliveira-Silva[17] and Zhang.[14]

Daniel J. Norman

Dr Daniel Norman obtained his BSc (Hons) at the University of Dundee in Medicinal Chemistry and then worked on the development of peptide-based hydrogels at Biogelx. He obtained his PhD in Chemistry at the University of Edinburgh under the guidance of Prof. Mark Bradley with a research focus on novel prodrug activation methods for cancer treatment. Following a post-doctorate with Professor Bradley developing diagnostics for tuberculosis, he began a post-doc position at the Technical University of Munich with Dr Hannelore Meyer in drug discovery of novel antibiotics and b-*lactamase inhibitors for resistant infections.*

Mark Bradley

Professor Mark Bradley has led research groups in the UK for over 30 years with funding from across the research councils and a variety of commercial and translational concerns. He has published over 440 papers and book chapters, has an H-factor of 62, filed 425 patents and spun-out five (still active) companies. The main focus of the Bradley group is in the area of life-sciences, specifically the application of the tools of chemistry to allow the manipulation, control and understanding of specific biological processes and functions and to address specific biological questions, problems in the areas of fluorescent reporters, smart materials/polymers and in vivo chemistry (see www.combichem.co.uk).

1. Optical imaging

1.1 Fluorescence

1.1.1 FRET. FRET based probes for proteases are based on the F¨orster Resonance Energy Transfer (FRET), process where a fluorophore (donor) in its excited state non-radiatively transfers its energy to another chromophore in its ground state through long range dipole–dipole interactions[18] (or perhaps viewed more simply *via* orbital overlap). When the acceptor molecule is a non-emissive quencher such as a simple dye it undergoes relaxation to its ground state by non-emissive processes. The energy transfer efficiency is determined by the orientation/rotation of the fluorophores and the extent of overlap between the emission spectrum of the donor fluorophore and the absorption spectrum of the acceptor as well as distance, with a separation of 4 to 6 nm considered optimal for the energy transfer to be efficient,[19,20] although molecules are non-static, and small peptides undergo large conformational changes.

Cleavage stops the energy transfer (the quenching) of the fluorophore, ‘‘turning on’’ the fluorescence (Scheme 1). It is vital that peptide cleavable ‘‘spacers’’ display high specificity towards the target protease, while the signal to noise ratio of the cleaved and non-cleaved FRET pair is high. Many routes to discover optimal substrates/spacers for FRET protease assays exist. These include a variety of combinatorial approaches (both solid[21,22] and solution based,[23] MS substrate profiling methods,[24,25] phage libraries[26] or substrate modification of known substrates, including direct screening on complex tumour tissues.[27] Many FRET peptide probes have been developed[28–30] and there are reviews covering this area so here we highlight some key and novel examples[14,19] with FRET based probes developed for legumain,[31] thrombin,[30] SARS-CoV protease,[32] Granzyme B[33] and Cathepsins,[34] among others.

Key successes in this area include improvement of the signal to noise ratio of conventional linear FRET-probes, shifting the emission into the NIR range[35] or by addition of chains of positively and negatively charged amino acids on opposite sides of the cleavage site that result in an ‘‘electrostatic zipper’’ whereby folding of the peptide brings the fluorophore and quencher into closer proximity *via* a hairpin-type structure to facilitate activity-dependent imaging.[28,36] In these probes, not only does the hairpin enhance the quenching but the polycationic species promotes cellular entry upon cleavage. A useful review covering this field was published by Tsien,[37] and clearly the concept could be extended to include oppositely charged fluorophores, that by themselves promote hairpin formation.

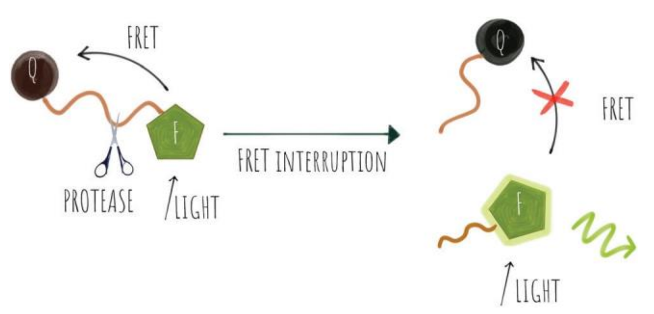

Scheme 1 FRET probes where the light emitted by the fluorophore (F) is transferred to the quencher (Q) until the FRET is disrupted by the action of a protease causing the release of the fluorophore and restoring its emission.

Some FRET probes have shown excellent applicability *in vivo*. Thus, a broad spectrum probe for detection of cathepsins using sulfo-Cy5 and QSY21 as a FRET pair was developed[38] and later optimized incorporating the FDA-approved dye ICG, as the NIR-emitting dye and was successfully used for fluorescence-guided-surgery in mouse and *ex vivo* in keratinocyte carcinoma.[39] One probe[40] (**1**), was recently validated for intraoperative assessment of cancer margins during surgery. It uses the same FRET pair and was designed for the detection of activated cathepsins K, L, S and B (Fig. 1a).[41–43] A series of fluorescent FRET based probes (**2**) (ProSense), based on self-quenching of multiple copies of the same fluorophore (Cy5.5) within a repeating graft copolymer[44] have successfully been developed for *in vivo* imaging in animal models for the detection of MMPs, cathepsins, renin and neutrophil elastase (Fig. 1b). Recently, a tribranched FRET based probe for sensing MMP activity[45] in patients with fibroproliferative lung disease allowed *in situ* imaging of MMP activity and allowed the assessment of pharmacological action in human disease using optical molecular imaging. A ‘‘tumour painting probe’’ (**3**)[46] (Fig. 1c) has also been developed that contained a green FRET pair (FAM/Methyl Red) on opposite sides of an MMP 2/9 cleavable sequence, that produced a signal upon protease cleavage. The construct also contained a NIR fluorophore that served as an ‘‘always on’’ reference (sulfoCy5). Thus, activation of the probe by MMPs resulted in two signals, the reference NIR dye and the liberated carboxyfluorescein. Interestingly, once the construct was cleaved, the reference NIR dye fragment, ‘‘painted’’ the tumour tissue allowing tumour margin visualization on *ex vivo* tissue (Fig. 3a).

Two-photo excitation (TPE) fluorescence has attracted much attention in the area of optical imaging as it allows for deeper and more accurate localisation of the probe (the focal volume for TPE is small) but the method also needs higher power laser sources compared to one-photon technology (although at far longer wavelengths). Probes based on TPE technology have been designed for the detection of caspase 3 using the generic substrate (DEVD)[47] with the naphthalene–pyrazoline two-photon absorber coupled to a dabcyl quencher *via* a caspase 3 cleavable peptide. The construct also allowed for tuneable targetability with modification of the pyrazoline substituent accommodating a cRGD motif to target cancer cell uptake. Yan[48] developed a two-photon fluorogenic reporter for caspase-3 using two-photon absorbing nanomicelles, with the b-cyclodextrin based micelles contained the two-photon absorbing dye *trans*-4-[*p*-(*N*,*N*-diethylamino)styryl]-*N*-methylpyridinium iodide. The micelles were modified with caspase 3 cleavable peptides labelled with the Black Hole Quencher (BHQ-2) that quenched the emission from the micelles until cleaved by the protease.

Multi-branched scaffolds[37,49–52] have been used to reduce probe background signals and enhance signal amplification *via*

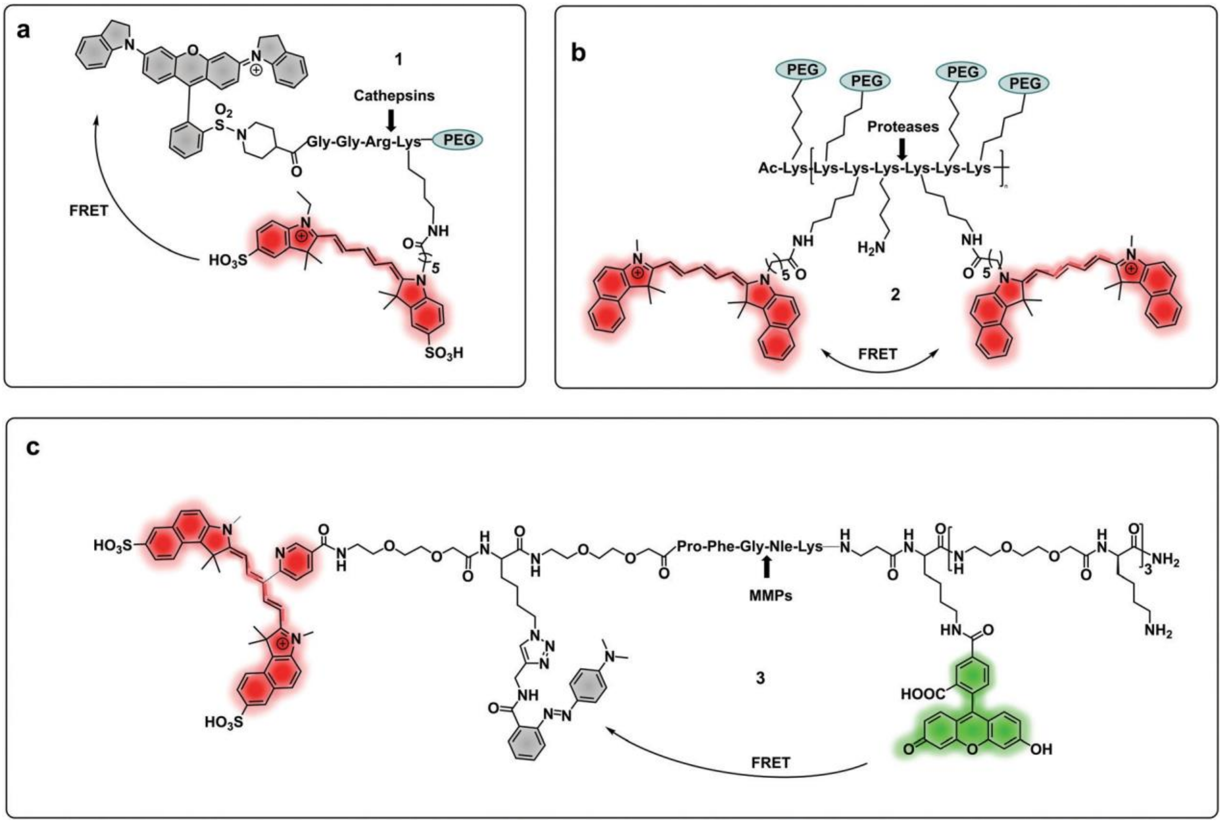

Fig. 1 (a) A cathepsin reporter using the ICG/QSY21 FRET pair probe in clinical studies.[40] (b) Structure of the generic ''ProSense'' probe using Cy5.5 homo-labelling.[44] (c) MMP dual probe for painting tumours,[46] with cleavage generating a Cy5.5 fragment that sticks to the tumor tissue. Also note that this probe is terminated with a D-Lys residue to provide proteolytic stability.

the generation of multiples copies of the same fluorophore. This strategy initially used ''self-quenching'' between identical fluorophores of homo-labelled probes, where each chromophore had a dual role of being a donor as well as an acceptor.[53,54] A self-quenching green emitting tri-branched dendrimer probe for human neutrophil elastase (HNE) was reported,[50] with the multivalent scaffold consisting of three-peptide branches specifically cleaved by HNE, each capped with a 5-carboxyfluorescein group.[55] In 2018, the concept was modified to include a quencher on each of the peptide sequences to allow the synthesis of a broad-spectrum serprocidin probe, yielding a so-called ''super-silent probe'' with negligible background fluorescence and much higher signal amplification.[49] More recently, optimisation of the system allowed the synthesis of a highly specific HNE probe (**4**, Fig. 2a), with excellent signal amplification and negligible background fluorescencethat allowed visualisation of Neutrophil Extracellular Traps[55] without the need of antibodies[56] (Fig. 3b). Multivalent or dendrimeric FRET reporters have been reported where scaffolds are modified with FRET-peptide reporters and targeting moieties on a central core. Nagai used anionic carboxy-terminal polyamidoamine (PAMAM) based-dendrimers (**5**), known to accumulate in the lymph nodes, as a core for the incorporation of a FRET substrate peptide allowing the detection of MMP-2[57] (Fig. 2b). Brennecke used a tetravalent DOTAM scaffold to prepare probe (**6**) for the detection of Cathepsin S, each scaffold being modified to accommodate two copies of a cRGD tumour-directing peptide on two of the four carboxylic acids, a Cy3 on a third functionality and finally a Cathepsin S cleavable sequence containing a BHQ-2 quencher (Fig. 2c),[58] on the fourth arm. The incorporation of FRET-reporters onto/into nanoparticles as carriers, offers opportunities for novel diagnostic applications. A recent example is the development of a non-invasive nanoprobe capable of detecting granzyme B dependent transplant rejection *via* analysis of urine samples. Exposure to iron oxide nanoparticles functionalised with FRET-labelled peptides, releases the fluorescent reporter into the urine and allows identification of the onset of rejection with high sensitivity and specificity.[59,60] Detection of multiple target proteases offers the possibility of establishing molecular signatures of diseases and therapy monitoring.[61] Polydopamine nanoparticles (PDANPs) have been used as broad-spectrum quenchers and carriers of multiple fluorophore-labelled peptides.[62] Thus, a 4-colour nano-reporter (7) was developed by assembly of four differently labelled fluorescent peptide substrates (urokinase-type plasminogen activator (uPA), MMP-2, cathepsin B, and MMP-7) labelled with AF405, FITC, Cy3 and Cy5 respectively, onto the PDANPs *via* p–p interactions with aromatic amino acid residues in the peptides/dyes (Fig. 2d). Negatively charged fluorescent PDANPs have been

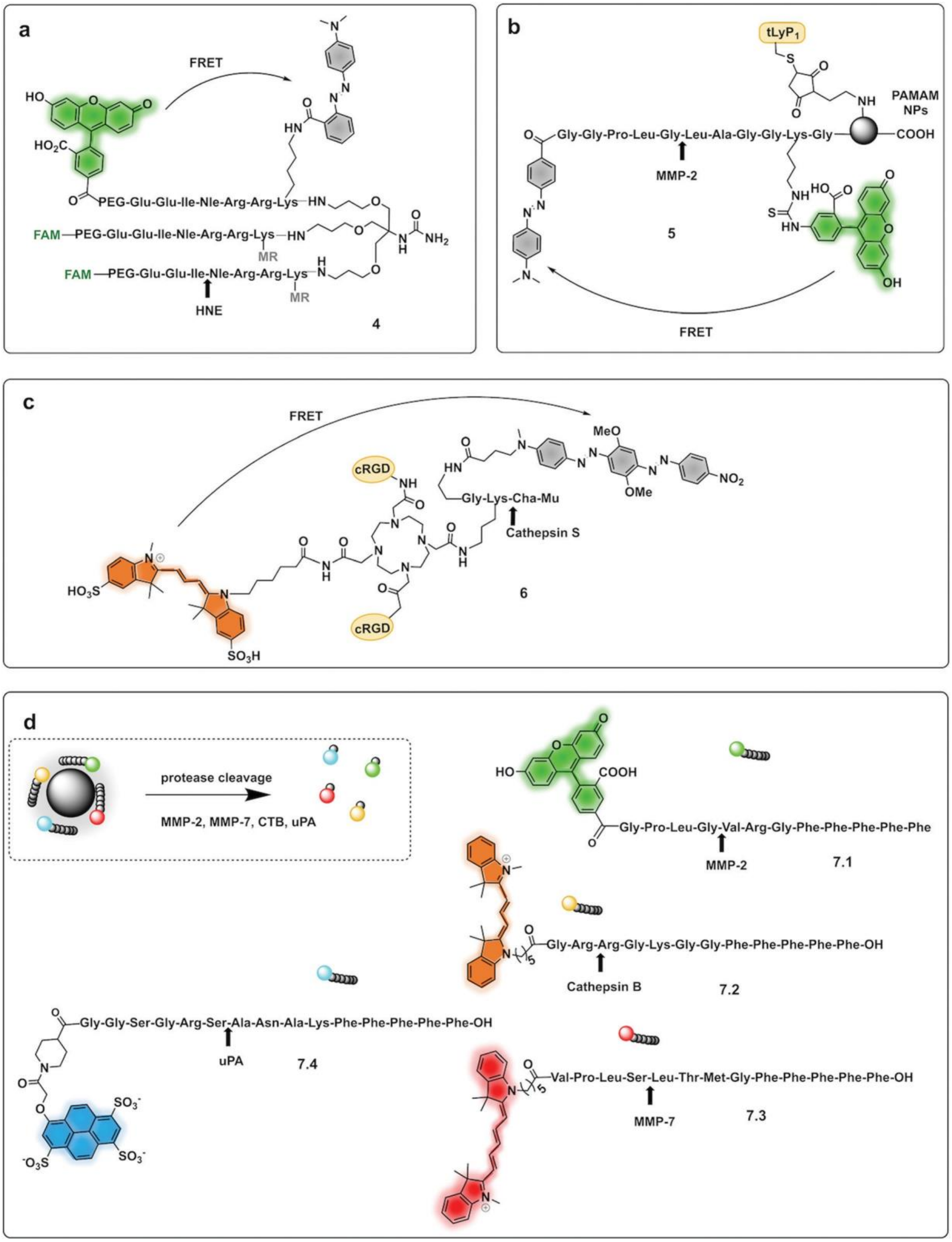

Fig. 2 Dendrimer, multibranched and nanoparticle based FRET probes. (a) Tribranched probe for detection of human neutrophil elastase.[56] (b) PAMAM-based fluorogenic dendrimers for detection of MMPs. tLyP-1: tumor homing peptide.[57] (c) Tetravalent DOTAM-based probe for detection of cathepsin S.[58] Mu: morpholine carboxamide; Cha: cyclohexylalanine. (d) 4-Colour nano-reporter for detection of uPA, MMP-2, cathepsin B and MMP-7.[63]

used to build a system with protamine to form an aggregation-based quenching system (*via* a static quenching mechanism).[63] The fluorescence quenching mechanism relying here on electrostatic interactions between the positively charged protamine and the negatively charged PADNPs with Trypsin cleavage de-quenching the system.

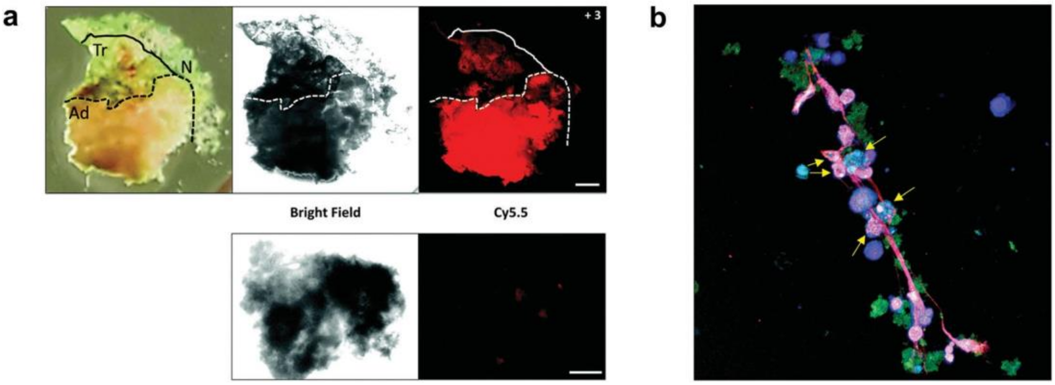

Fig. 3 (a) Fluorescence images delineating tumour margins using the MMP FRET probe 3.[46] Upper row: Bright field microscopy image and fluorescence image of freshly excised lung slice, with pathologically identified adenocarcinoma (Ad), transition zone (Tr) and normal (N) tissue, following incubation with the probe. Lower row: Control tissue from the same patient sample without the addition of compound 3 was used as a measure of tissue autofluorescence within this spectral window. Reproduced from ref. 46 with permission from the Royal Society of Chemistry, copyright 2020. (b) Fluorescence microscopy image of a Neutrophil Extracellular Trap stained with HNE FRET probe 4[56] (green), DAPI (blue) and SYTOX orange (red). Arrows indicate chromatin studded with activated probe, indicative of chromatin release by activated cells. Reproduced from ref. 56 with permission from the Royal Society of Chemistry, copyright 2021.

A probe (**8**) that allowed multiple molecular targets to be simultaneously analysed was demonstrated with a dual-enzyme probe[64] for thrombin and MMPs, allowing detection of two distinct classes of proteolytic extracellular proteins that play important roles in early carcinogenesis. The probe construct was assembled by copper mediated ''click'' conjugation of two FRET-labelled substrates with orthogonal excitation–emission wavelengths (Fig. 4a). Widen recently reported an AND-gate (**9**) that relies on activation by two proteases for a fluorogenic response,[65] in this system, a central fluorophore was flanked by two quencher-labelled peptides targeting different proteases, cleavage of both substrates and release of the two quenchers was required to restore the fluorescence of the central fluorophore (Fig. 4b).

Some protease-FRET probes initially used for diagnostics have been combined with therapeutic moieties to generate theragnostic entities allowing both diagnosis and therapy. Following this principle, Li[66] developed a FRET-based (carboxyfluorescein–dabcyl) caspase 3 cleavable probe (**10**) conjugated to doxorubicin (DOX) and a targeting peptide (Fig. 4c). Enhanced delivery to the tumour tissue was enabled by the directing peptide, where the acidic pH in the cancer microenvironment (and during uptake in the endosome) triggered the release of DOX from the construct while caspase-3 cleaved the peptide resulting in a fluorescent signal. Transcription-dependent fluorogenic probes have been used for specific protease dependent activation or amplification of signal,[67,68] while analysis kits for plasma and peripheral blood testing have been developed using polymer immobilization of FRET-based protease substrates.[69]

1.1.2 **Ratiometric**. Ratiometric fluorescence is a method where the emission intensities at two or more wavelengths are measured. Ratiometric fluorescence detection for proteases offers benefits over quenched-FRET as it provides a reference signal allowing traceability on the distribution of the probe with the main strategy employed for protease ratiometric detection using two target-responsive signal changes which allows concentrations to be measured. FRET between two fluorophores has been widely used to develop ratiometric probes with a donor–acceptor pair on opposite sides of a cleavable peptide.[70] In the absence of the target protease, the energy is transferred from the donor into the acceptor and only the acceptor signal is detected if the acceptor is a fluorophore (Scheme 2). Upon exposure to the target protease, cleavage results in ''switch-on'' of the fluorescent signal from the donor. Following cleavage, the acceptor emission will become independent of the donor.[70] Modification of conventional substrates includes the addition of directing moieties, for example, a human neutrophil elastase ratiometric FRET probe (**15**) has been reported,[71] with an additional DNA minor groove binder moiety allowing successful visualization of activated neutrophils and Neutrophil Extracellular Traps (Fig. 5). A ratiometric hairpin-type probe for *in vivo* imaging has been developed that used Cy5 and Cy7 as a FRET pair and a

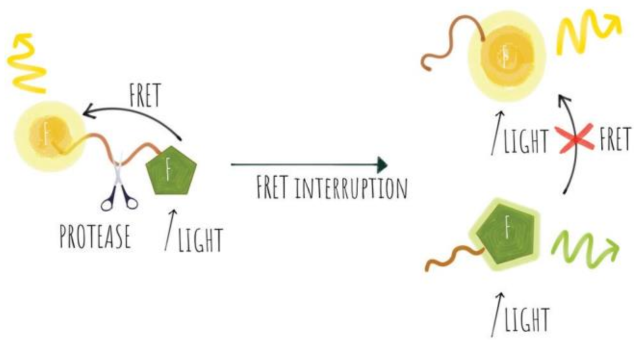

Scheme 2 Concept of a probe that can be used for ratiometric FRET with energy transfer between two different fluorophores that is removed upon cleavage by proteases.

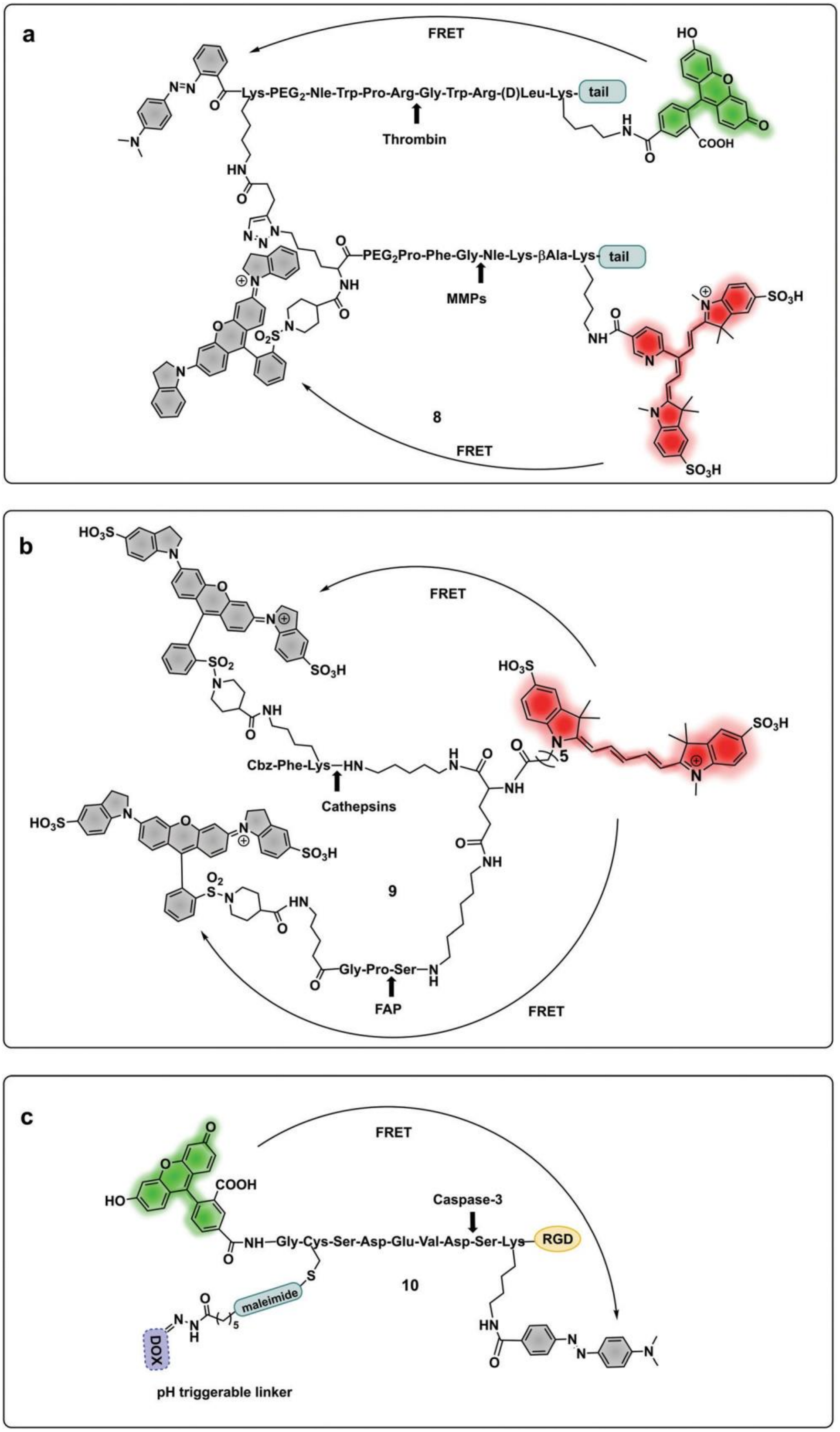

Fig. 4 Multimodal probes. (a) Dual targeting probe for detection of thrombin and MMP.[64] (b) AND-gate system based on dual quenching of one fluorophore activated following cleavage by cathepsins and FAP.[65] (c) Theragnostic probe for detection of caspase-3.[66] DOX: doxorubicin.

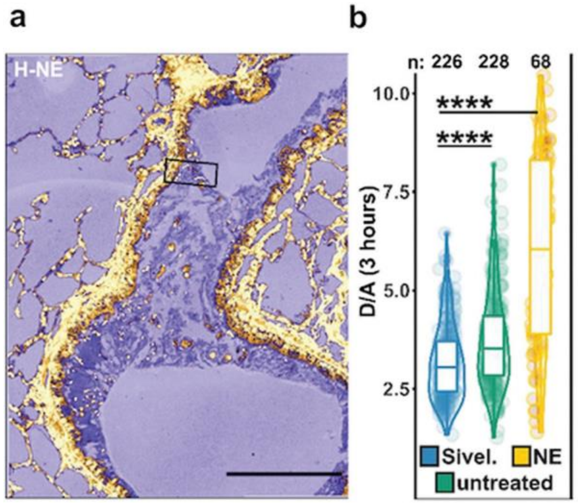

Fig. 5 *Ex vivo* mouse lung slices stained with ratiometric elastase probe **15.** (a) Confocal images of 5 μm thick lung slices from Scnn1b-Tg mice stained with compound **15** [2 μM] for 3 h. Scale bar: 200 mm. (b) Quantification of NE activity using the probe donor/acceptor (D/A) fluorescence on lung slices either untreated, pre-treated with Sivelestat or with elastase for 30 min before adding the probe. Reproduced from ref. 71 with permission from American Chemical Society, copyright 2020.

solubilizing PEG moiety[72] and was activated by thrombin. Using a similar approach, a MMP probe was developed (**11**) (Fig. 6) that is currently in Phase 2 studies.[73] The main drawback of this design being the background ''off-target'' fluorescence signal of the probe.

A ratiometric protease probe (**12**) was designed[74] and applied for *ex vivo* imaging of b-Secretase (BACE1) in an Alzheimer's disease mouse brain model. The reporter used the two-photon absorbing merocyanine (mCyd) as a donor conjugated to the acceptor fluorophore Alexa Fluor 633 (a sulfonated rhodamine derivative) as the acceptor *via* a b-Secretase peptide sequence (Fig. 7a).

A sophisticated assay for MMP sensing in the extracellular matrix *in vitro* (**13**) has been reported[75] with collagen-immobilized FRET reporters allowing the visualisation of time-dependent secreted protease activity using an extracellular matrix (ECM) collagen anchor, conjugated to enhanced green fluorescent protein (EGFP). In this case TAMRA was attached, by intein-mediated splicing to form a collagen-adherent MMP-2 probe with a FRET pair TAMRA/GFP (Fig. 7a), linked by an MMP cleavable peptide. This strategy allowed the probe to bind to collagen in the ECM where it could interact with the secreted protease of interest, interrupting the FRET pair. The probe was validated in a 3D cell spheroid model to analyse secreted MMP-2 activity. Similarly, but by fusing the cyan fluorescent protein (CFP) and the yellow fluorescent protein (YFP) through a NE-specific cleavable linker, a neutrophil elastase fluorescent ratiometric reporter was assembled.[76]

The combination of three dyes in a dual FRET system yielded a dual-target probe (**14**) for detection of trypsin and chymotrypsin. Using a peptide-like structure (Fig. 7b) a cascade FRET system was generated using 7-diethylaminocoumarin-3-carboxylic acid, fluorescein and rhodamine B.[77] This allowed for multiplexed assaying of protease activity.

Other strategies for ratiometric probes include a single fluorophore with tunable emission following activation by a protease, which uses the pro-fluorophore principle, where decaging of the fluorophore leads to changes in emission profile.[78–80] A *y*-glutamyltranspeptidase-triggered theragnostic probe was designed for cancer detection using a caged NIR photosensitiser.[81] The construct when caged emits fluorescence in the NIR region of the spectrum and cannot produce ROS. Upon decaging by *y*-glutamyltranspeptidase there is a shift in fluorescence emission into the yellow region which allows photodynamic therapy (PDT) due to the activity of the photosensitizer with the production of ROS at the site of activation. This field has been extensively reviewed by Huang.[82] Du reported a ratiometric fluorescent probe[83] for the detection of leucine aminopeptidase (LAP) based on a quinoline derived fluorophore for imaging LAP on liver tumour cells. The probe contained a galactose moiety for targeting active tumours and a caged quinolone. The probe was internalised in cancer cells, where it was decaged by LAP, producing a red shift in emission of the construct (425 nm to 510 nm). Using a cell penetrating peptide and a substrate for caspase-3 to cage cresyl violet, a probe was generated that gave a red-shift in fluorescence emission upon caspase-3 cleavage. Recently, Cao developed the first non-peptide

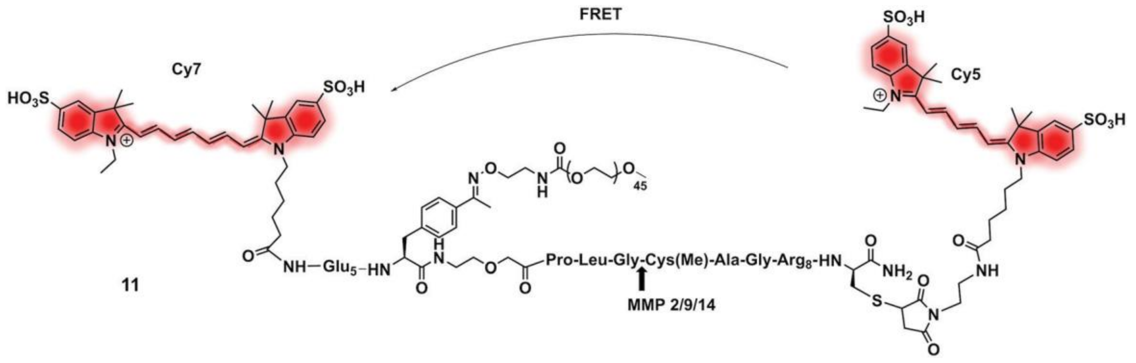

Fig. 6 Structure of the clinically validated ratiometric probe AVB-620 for detection of MMPs based on the FRET pair Cy5/Cy7.[73]

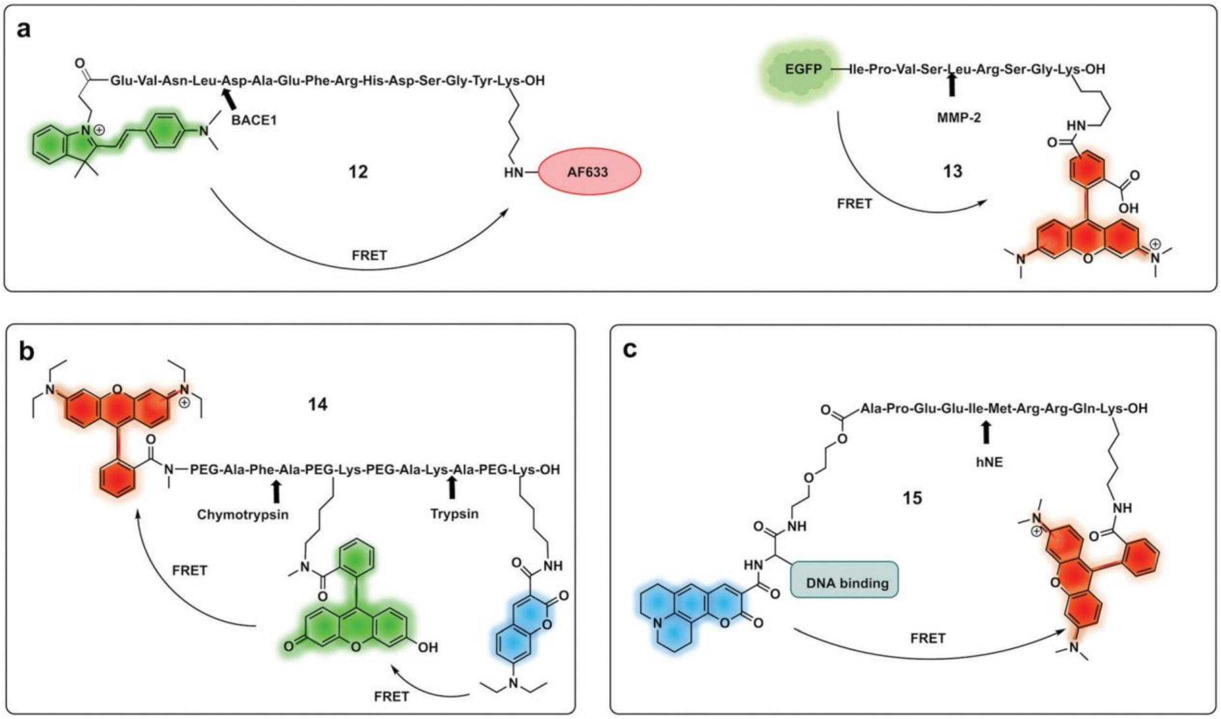

Fig. 7 Ratiometric fluorescence detection of proteases. (a) Ratiometric FRET based probes for BACE1 (**12**)[74] and MMP-2 (**13**).[75] (b) dual activation-3-dye-FRET sensor providing three orthogonal fluorescence signals upon full activation of the probe.[77] (c) DNA targeting ratiometric probe for human neutrophil elastase.[71]

based ratiometric pro-fluorophore probe for hNE[84] using a pentafluoropropanoic acid caging group.

The use of biocompatible nanocrystals has been widely explored to build protease probes, acting as scaffolds and carriers with many offering the ability to act as spectrally broad light quenchers. Fe_3O_4 nanocrystals and quantum dots (QDs) have been widely used as FRET quenchers and carriers for the synthesis of several protease probes. Mingyuan developed a series of probes combining pH sensing with protease detection for tumour optical imaging.[85,86] The probes (**16, 17**) simultaneously mapping MMP-9 activity and the extracellular pH of tumours were able to target tumour cells *via* conjugation to an antibody. These were based on a modified naphthalimide as a ratiometric pH sensitive fluorophore and Fe_3O_4 nanoparticles as a quencher by covalent attachment through an MMP-9 cleavable peptide. Upon cleavage of the peptide, naphthalimide fluorescence was switched on with the ratio of the two pH-dependent emission maxima used to quantitatively determine pH (Fig. 8a). In a second-generation reporter that was used for *in vivo* imaging, folic acid was incorporated as a targeting moiety, and an ‘‘always on’’ Cy5.5 dye with an orthogonal fluorescence signal serving as an MMP-9 reporter.[85,86]

Quantum dots (QDs) have been used as FRET donors for ratiometric sensing of proteases with fluorophore-labelled cleavable peptides immobilised as acceptors.[87] Concentric Fo¨rster Resonance Energy Transfer (cFRET) imaging is a novel application of semiconductor QDs where a central emissive QD is conjugated with multiple copies of two different biomolecular probes. Each of these probes is labelled with one or two, similar or different, fluorophores that engage in energy transfer with the QD and, in many cases, with one another. These configurations are referred to as ‘‘concentric’’ because the dyes on the surface form a sphere that shares the same centre as the quantum dot. A recently reported cFRET QD system[88] comprised green-emitting QDs and peptides labelled with Alexa Fluor 555 (a bis-sulfonated carboxy-rhodamine) (**18**) and Alexa Fluor 647 (a bis-sulfonated Cy5). The two peptide sequences were selected as substrates for trypsin and chymotrypsin, whose cleavage modulate signal output by decreasing the number of dyes per QD. A bi-modal QD-type probe (**19**), combining charge transfer (CT) and a FRET quenching system was recently developed,[89] using QDs with a hydrophilic coating assembled with multiple copies of a number of peptides. Some were labelled with ruthenium(II) phenanthroline (Ru-phen), which quenched the QD *via* a CT mechanism, others had a distal fluorescent label, which are well-known to quench QD emission *via* FRET (Fig. 8b). Acceptor dye-labelled peptide-DNA conjugates were assembled onto the QD donors as an input gate. The addition of trypsin or chymotrypsin cleaved the peptide and altered the efficiency of FRET with the QD, and liberated a DNA output (**20.1**) which then interacted with a tetrahedral output gate (**20.2**). Downstream output gate rearrangement resulted in FRET sensitization of a new acceptor dye[90] (Fig. 8c).

1.1.3 **Pro-fluorophore approach**. Many widely used fluorogenic probes are based on the synthesis of ‘‘pro-fluorophores’’,

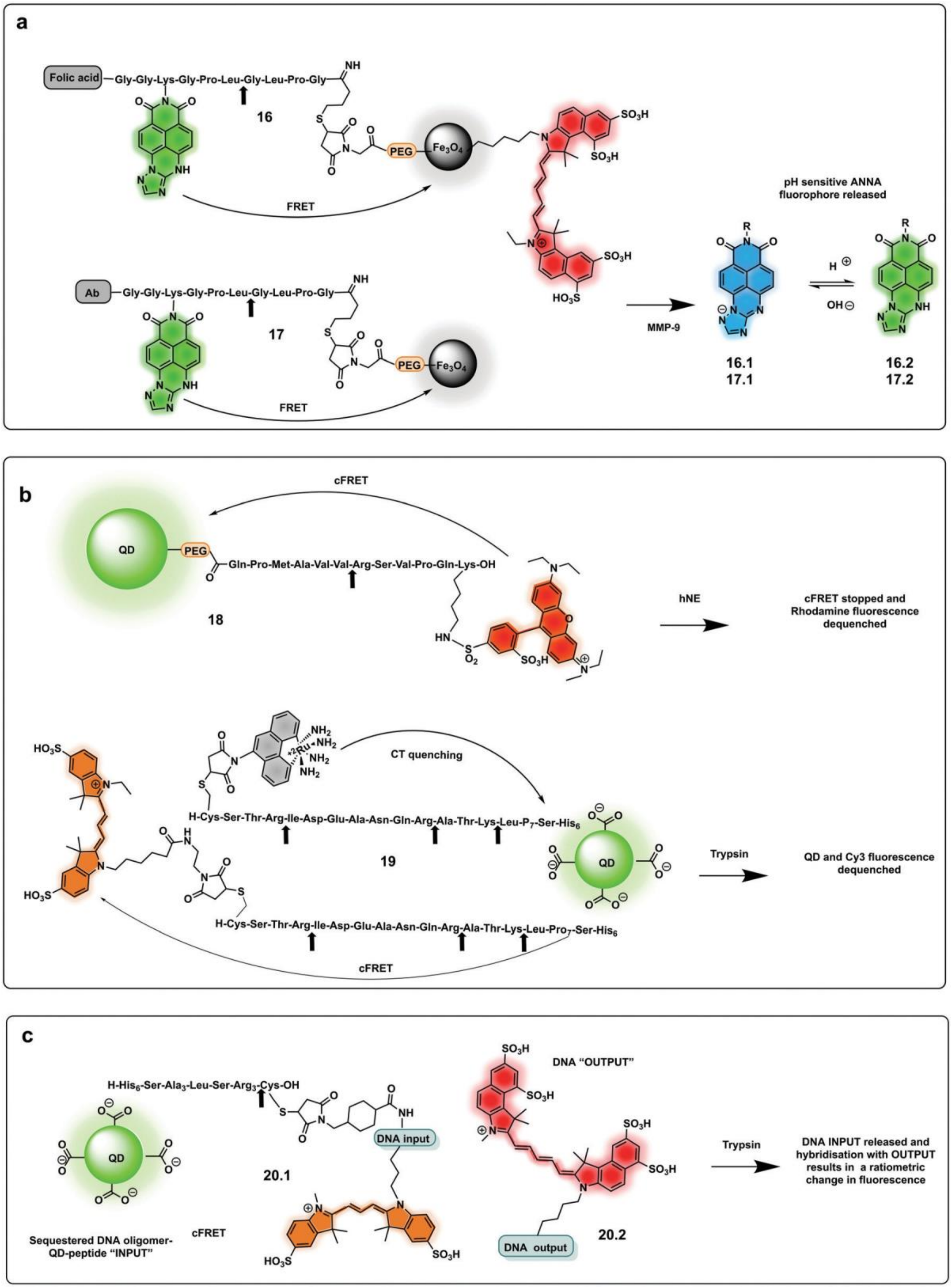

Fig. 8 Nanoparticle and QDs based ratiometric probes. (a) Fe_3O_4 nanocrystals FRET based probes systems based on quantum dots (QDs) with tumour targeting capacity using folic acid or antibody targeting and generating a pH ratiometric sensor upon cleavage by MMP-9.[85,86] (b) QD based FRET system with a rhodamine fluorophore donor (**18**)[88] and a QD conjugated system allowing multiplexed sensing combining FRET quenching (using Cy3 as the acceptor and QD as a donor) and charge transfer quenching (using a ruthenium dye as a donor with the QD as an acceptor (**19**).[89] (c) DNA-QD-conjugated approach relying on DNA hybridisation of complementary strands, with dyes inserted into the DNA *via* double phosphoramidite modifications.[90]

substrate-based probes that become fluorescent upon decaging. The most widely studied and used fluorophores in this area are 7-amino-coumarins, whose emission is significantly reduced when conjugated to a peptide chain *via* an amide bond.[91,92] The approach generally uses a protease cleavable moiety linked directly, or *via* a safety-catch (or self-immolative linker)[93,94] with probe cleavage releasing the fluorophore (Scheme 3).

Several fluorogenic probes have been designed for the detection of N-terminal exopeptidases such as dipeptidyl peptidase (DPP-IV),[95–97] leucine aminopeptidase (LAP), pyroglutamate aminopeptidase (PGP1)[98] or aminopeptidase N (APN)[99,100] with attachment of the appropriate amino acid residues to a fluorophore that affects its internal charge transfer (ICT) and yields probes that switch-on upon peptidase exposure.

Dipeptidyl peptidase-IV cleaves X-Pro or X-Ala dipeptides from the amino-terminus of peptides and is known to be overexpressed in diabetes[101] and cancer.[102,103] Probes for detection of this protease[95] were constructed by the incorporation of a DPP-IV substrate (an amino acid[104] or dipeptide[96]) onto a fluorophore, with quenching of its fluorescence. Urano reported a series of probes for DPP-IV detection using hydroxymethyl rhodamine green (HMRG) as a green fluorophore scaffold in combination with a series of X-Pro dipeptides,[105] with one of the compounds (**21.1**, Fig. 10a) used successfully for imaging of head and neck squamous cell carcinoma[106] and esophagic adenocarcinoma[107] (Fig. 9). Another example includes a probe that uses the NIR fluorophore SiR600,[97] conjugated to the dipeptide Glu-Pro, with the quenching mechanism relying on PeT (**22.1**).[97] Leucine aminopeptidase (LAP) has attracted significant attention, as it is known to be overexpressed in ovarian and breast cancer and several probes have been developed to detect its activity. Such probes are generally based on modification of the amino group of a fluorophore through an amide bond to a leucine residue (Fig. 10b). NIR hemicyanines[99] (**23.1**), crysol violet[108] (**24.1**), dicyanoisophorone derivatives (**25.1**)[109] or rhodamine (**26.1**)[110] have all been modified to generate fluorogenic probes to detect this peptidase, with new approaches adding targeting capacity.[111]

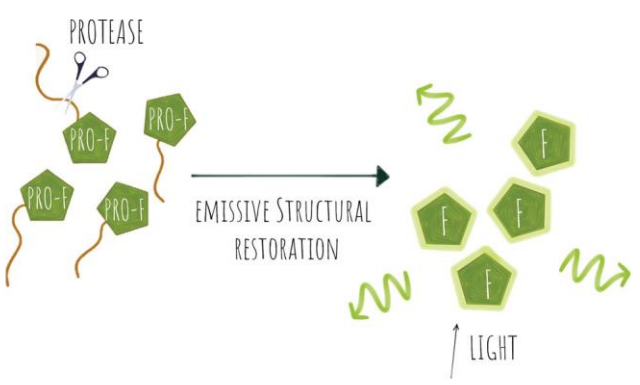

Scheme 3 Concept of pro-fluorophore (PRO-F) activation by a protease to generate emissive molecules (F).

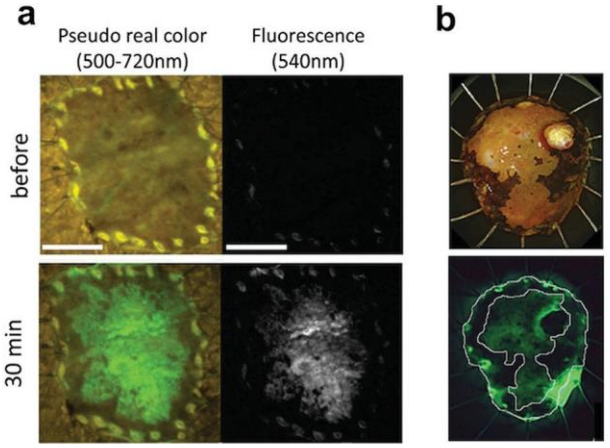

Fig. 9 *Ex vivo* fluorescent imaging of tumor tissue following spraying of DPPIV profluorophore **21.1** (a) esophagic carcinoma: a rapid fluorescent increase was observed in the tumor lesion after 30 min. Scale bar, 10 mm (b) head and neck squamous cell carcinoma tissue, upper: resected specimen observed with iodine staining shows normal mucosa (darker, periferic) *vs.* tumor mucosa (central area), lower: fluorescent imaging after spraying **21.1**. Reproduced from ref. 105 with permission from Nature, copyright 2016 and ref. 106 with permission from Head Neck, copyright 2018.

A small-molecule probe targeting hNE (**28.1**),[112,113] a serine protease expressed in activated neutrophils in inflammatory processes, was designed where the amino group of the NIR hemicyanine dye was conjugated to a pentafluoropropanoic acid caging group, and was optically silent until de-caged by the protease (Fig. 10d).

The same concept has been extended to include so-called safety catch or self-immolative linkers, with *p*-hydroxy or *p*-amino-benzyl alcohol the most widely used. Here enzymatic cleavage releases the conjugated fluorophores and restores fluorescence.[114] Shasha[94] developed a Granzyme B probe based on this approach for detecting T cell activation. The probe (**29.1**) consisted of a short peptide conjugated to a PEGylated NIR hemicyanine dye *via* a self-immolative linker. Using the same principle, a probe (**30.1**) for cathepsin B was developed,[115] bearing a morpholine targeting moiety and a specific peptide connected to aminoluciferin. Based on the same self-immolative linker strategy, Chen synthesised a BODIPY-derived fluorogenic probe (**27.1**) with phenyl acetamide as a triggerable motif for penicillin G amidase detection.[93]

Urano also reported g–glutamyl–transferase (GGT) fluorogenic probes based on spirocyclic caging of g-glutamyl hydroxymethyl rhodamine green,[116] with activation occurring by a rapid one-step cleavage of glutamate to release hydroxymethyl rhodamine green in its ring-open, fluorescent form. A modification of this strategy[117] added a fluoromethyl group at the 4-position of the xanthene ring (**31.1**). Cleavage by the protease liberates the fluoride anion to produce an azaquinone methide intermediate (**31.2**) that can be attacked by intracellular nucleophiles (*e.g.* a group on a protein) to restore the hydroxymethyl

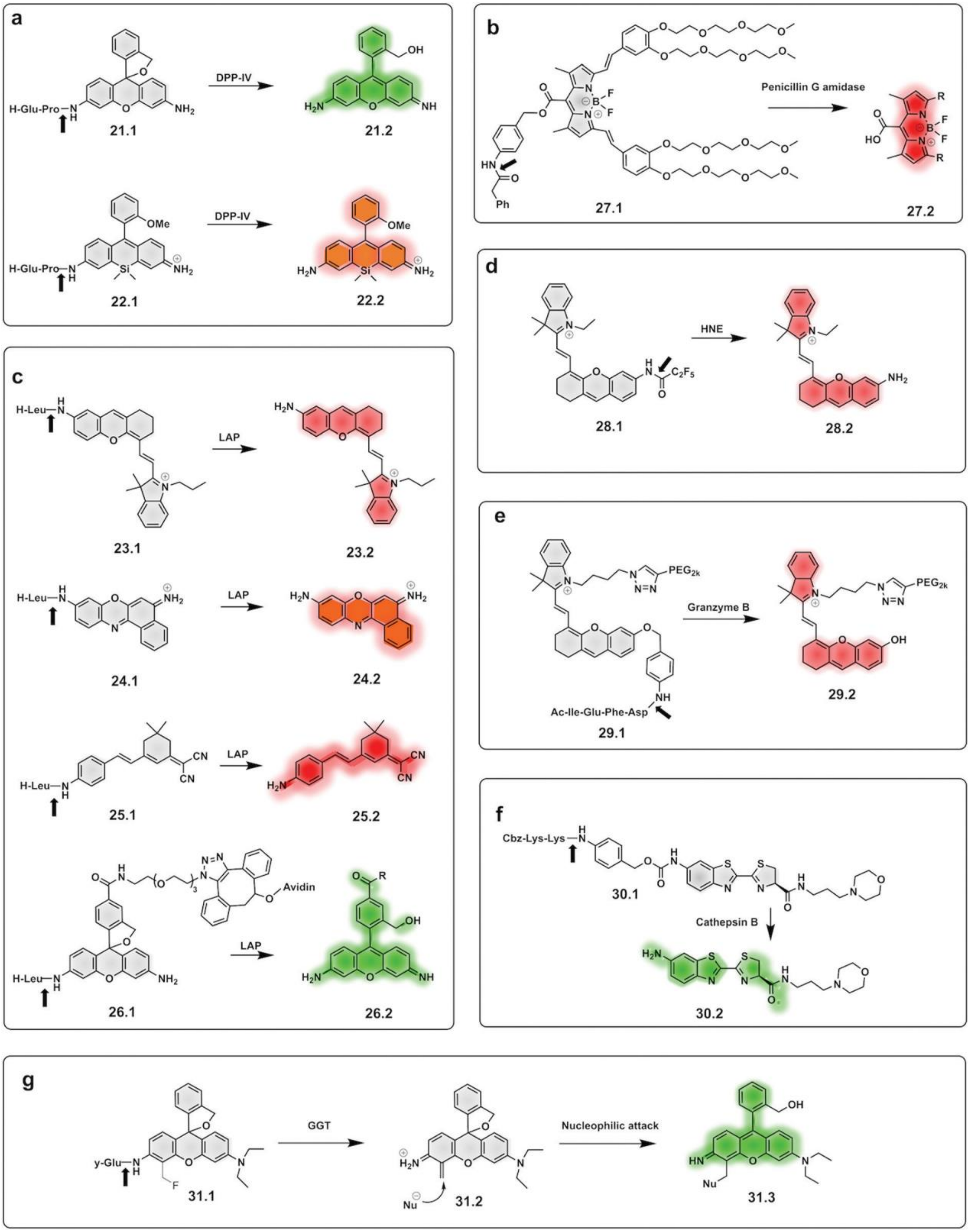

Fig. 10 Examples of fluorogenic probes for proteases based on pro-fluorophores for detection of (a) dipeptidyl peptidase-IV (DPP-IV) using Glu-Pro[97,105] (**21.1** and **22.1**) dipeptide substrates (b) penicilin G amidase[93] (**27.1**) (c) leucine aminopeptidase (LAP) based on NIR hemicyanines (23.1),[76] crysol violet[87] (**24.1**), dicyanoisophorone derivatives (**25.1**)[89] and rhodamine[88] (**26.1**) (d) human neutrophil elastase (**28.1**)[112,113] (e) granzyme B[94] (**29.1**) (f) cathepsin B[115] (**30.1**) and (g) g-glutamyl-transferase (GGT)[117] (**31.1**).

diethylrhodamine (**31.3**) fluorescence and also trap the compound within the intracellular space, *via* conjugation to an intracellular protein.

1.1.4 AIEgen probes.

Aggregation-induced emission (AIE) is a fluorescence phenomenon proposed by Tang in 2001.[118] Most conventional organic dyes exhibit aggregation-caused quenching (ACQ) due to strong intermolecular p–p stacking when at high concentrations and internal FRET. However, AIE fluorogens (AIEgens) display weak or no emission as dilute solutions, but exhibit strong fluorescence turn-on when aggregated (Scheme 4).[119] Restriction of intramolecular motions is recognized as the general mechanism behind AIE and as such, many AIE luminogens have structures that consist of one or more ''rotors'' attached to a so-called ''stator''. In solution, the rotors are twisted out of conjugation because of steric congestion, but upon aggregation the rotors are prevented from undergoing free rotation and the molecule enjoys maximal conjugation, which results in the irradiative emission.[120] Currently, most AIEgens are derivatives of silole, tri- and tetraphenylethenes (TPE), distyrylanthracenes (DSA) and tetraphenyl-1,4-butadienes (TPBD).[121] New strategies exploiting AIEgens have been applied to protease detection, with probes that self-aggregate upon cleavage and exhibit high fluorescence emission. Classic AIEgen protease probes consist of a peptide substrate for the protease of interest with an AIEgen fluorophore that will only become fluorescent upon aggregation of several fluorophore units by hydrophobic interactions. An example of an AIEgen protease probe using tetraphenylethene (TPE) was reported by Haibin,[122] where the fluorophore TPE was conjugated to a caspase 3/7 cleavable peptide, that prevented the dye from aggregating until cleaved by the protease (**32**). Some of these constructs also contained a targeting moiety *e.g.* an RGD motif for cancer cell targeting or morpholine for lysosomal localization.[123–128]

A novel probe for real-time *in vivo* detection of MMP-13 activity in osteoarthritis was synthesized using a NIR emissive AIEgen (**33**) based on a cyanine–pyrene unit, which introduced a donor–acceptor system where a dimethylaminophenyl group act as an electron-donor, while nitrile and pyridinium containing units functioned as electron acceptors.[129]

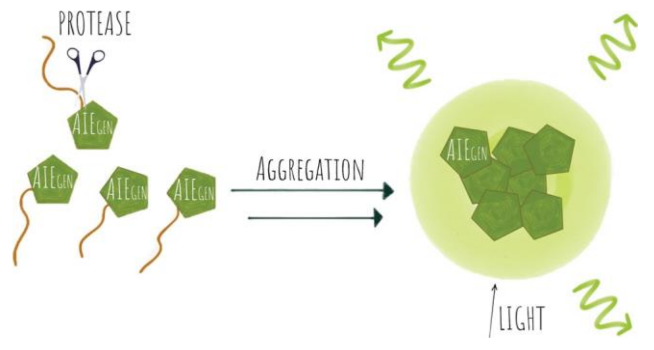

Scheme 4 Fluorescent activation by proteases *via* aggregation-induced emission.

Yuan, developed a probe for apoptosis (**34**) based on the sequential detection of caspases 8 and 3.[130] The probe consisted of a central peptide containing the two substrates functionalised with two AIEgens with distinctive green (caspase 8) and red (caspase 3) emissions (Fig. 11b). The green and red fluorescence were sequentially turned on when the peptide substrate was cleaved by the action of caspase-8, cleaving the TPS containing fragment, followed by caspase-3, cleaving the TPETH containing fragment, with fluorophore aggregation in early apoptotic cells (Fig. 12). In the same area, a theragnostic compound (**36**) targeting cathepsin B/caspase-3[131] was synthesised, which consisted of three components: an RGD targeting moiety, a cathepsin B-activatable gemcitabine prodrug, and a caspase-3 specific reporter based on tetraphenylene (TPE) to give AIE.

Yuan developed a FRET-AIEgen probe (**35**) where a caspase-3 peptide substrate was modified with a FRET pair,[132] with the donor being a green emitting coumarin capping the amino terminus. The acceptor, tetraphenylethenethiophene (TPETP), was attached onto the carboxy terminus of the caspase-3 peptide. The probe was silent as the acceptor fluorophore (TPETP) absorbs the energy from the coumarin, however, when caspase-3 cleaves the peptide both fluorophores are released and recover the emission of fluorescence at two different wavelengths simultaneously. The same group developed theragnostic probe combining a therapeutic moiety and an AIEgen linked though the caspase-3 cleavable peptide using a photosensitiser[123,133] or a platinum(IV) prodrug.[134] Caspase-mediated apoptosis, induced by the concurrently released therapeutic agents, could then be measured based on the fluorescence of the released AIEgen and aggregation.

Cheng published an MMP2 activatable reporter (**37**) for cancer theragnostics,[135] based on a doxorubicin hydrophilic cell penetrating peptide conjugate linked through an MMP2-cleavable peptide conjugated to a PyTPE fluorophore (Fig. 11e). Upon cleavage by MMP2 the hydrophilic fragment containing DOX enters cells, while the hydrophobic part self-aggregates giving a strong yellow fluorescence emission.

An *in vitro* assay for protease activity[136] has been reported (**38**) that uses heparin to drive aggregation of the TPE fluorophore (Fig. 11f). Heparin, a highly sulfonated (hence negatively charged) aminoglycan induces the aggregation of the positively charged AIEgen fluorophores by electrostatic interactions, to give fluorescent enhancement. Histones have a high affinity to heparin, and can displace the fluorophores, reducing the fluorescence signal. If trypsin is added, the histones are hydrolysed and the heparin-TPE retains the fluorescence signal. Kaur developed a trypsin AIEgen probe[137] based on electrostatic interaction driven aggregation induced emission combining a negatively charged TPE dye and the positively charged protein protamine. The tetra-anionic dye, a sulphonyl-derivative of tetraphenyl ethylene (Su-TPE) is almost non-fluorescent when free in aqueous solution but protamine sulphate (PrS), an overall cationic protein, induces aggregation of Su-TPE by electrostatic interactions and leads to a highly emissive Su-TPE/PrS supramolecular complex with AIE characteristics. In the presence of trypsin, the cationic protein is

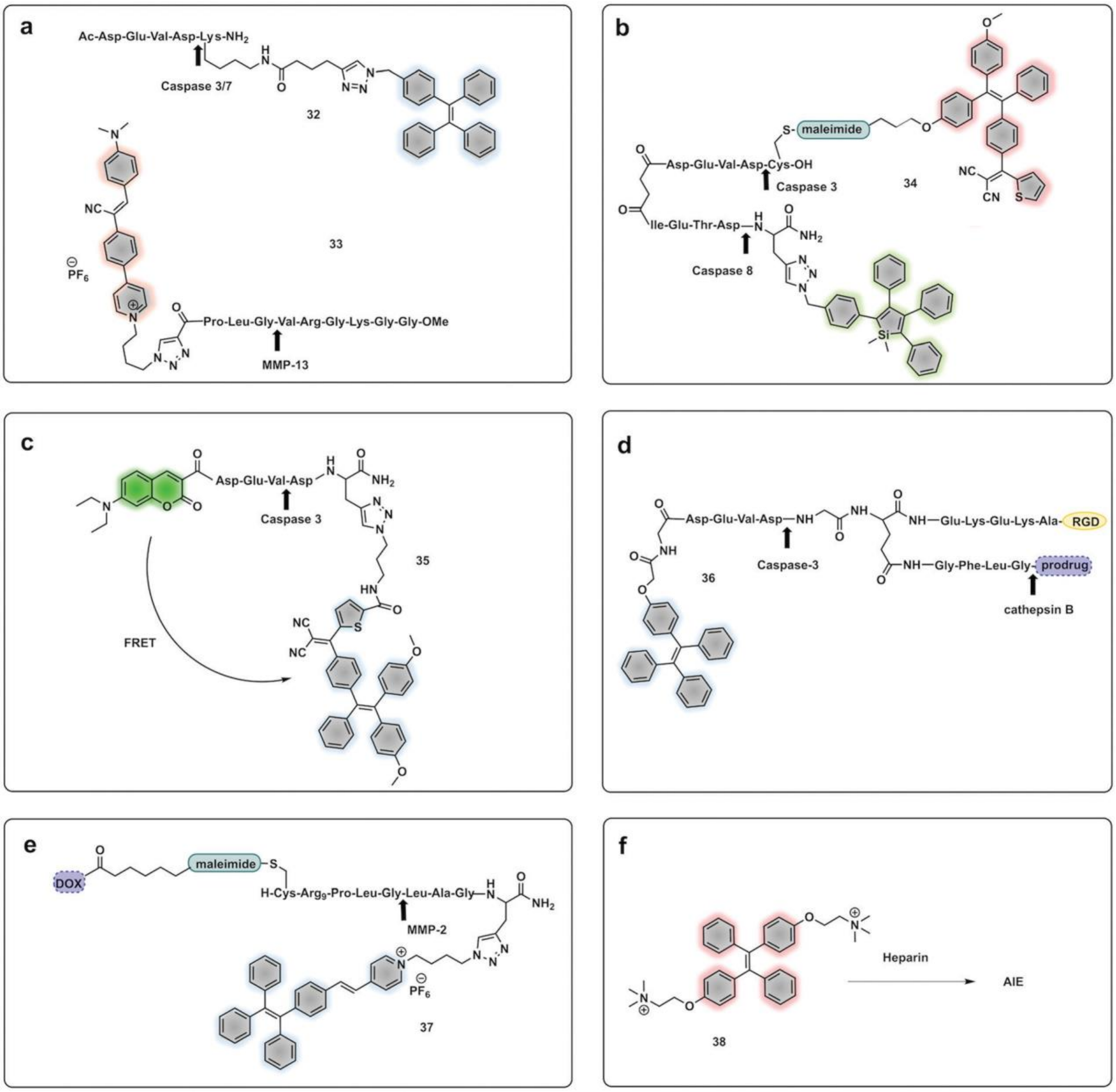

Fig. 11 Example of fluorogenic probes where protease cleavage activates AIE fluorescence. Arrows indicate cleavage site. (a) Probes for detection of Caspase 3/7 based on TPE (**32**)[122] or MMP-13 based on cyanine-derivates (**33**)[129] AIEgens. (b) Cascade activatable probe with sequential fluorescence signal in the green and red.[130] (c) FRET-AIEgen using a coumarin green emitting dye coupled to a TPETP AIEgen providing a dual signal upon cleavage (35).[132] (d) Theragnostic AIEgen protease probe with a tumour targeting moiety, and different proteases mediating signal and therapeutic agent release.[131] (e) Theragnostic probe that releases the drug doxorubicin (DOX) and a TPE derivative that generates an AIEgen upon cleavage by MMP-2.[135] (f) An AIEgen detection system based on negatively charge heparin and the positively charged TPE fluorophore that allows aggregation induced emission.[136]

digested and the supramolecular complex disassembles, reducing the fluorescent emission.

A bimodal reporter using Gadolinium as a contrast agent for MRI combined with an AIEgen fluorophore for optical imaging was developed.[138] The probe used a DOTA-Gd(III) chelate that provides MRI signal enhancement, and TPE as the AIEgen linked to a caspase 3/7 cleavable peptide. In response to the protease, the Gd-AIEgen conjugate is released and aggregates leading to increased fluorescence and MRI signals.

1.1.5 **Bioorthogonal.** The field of chemical biology has been revolutionised by the advent of bioorthogonal reactions – chemical transformations that can be performed in living systems without interference of biomolecules.[139,140] This approach has been used to develop fluorogenic compounds that amplify a fluorescent signal upon bioorthogonal reactions,[141] with protease activity used as a trigger to allow *in situ* synthesis of fluorophores (Scheme 5).

Romieu developed a reporter (**39.1**) whose mechanism of activation was based on pyronin assembly triggered by a protease.[142,143] Following peptidase cleavage and decaging of an amino group, the mechanism involves *in situ* generation of an unsymmetrical pyronin *via* cyclisation/aromatization

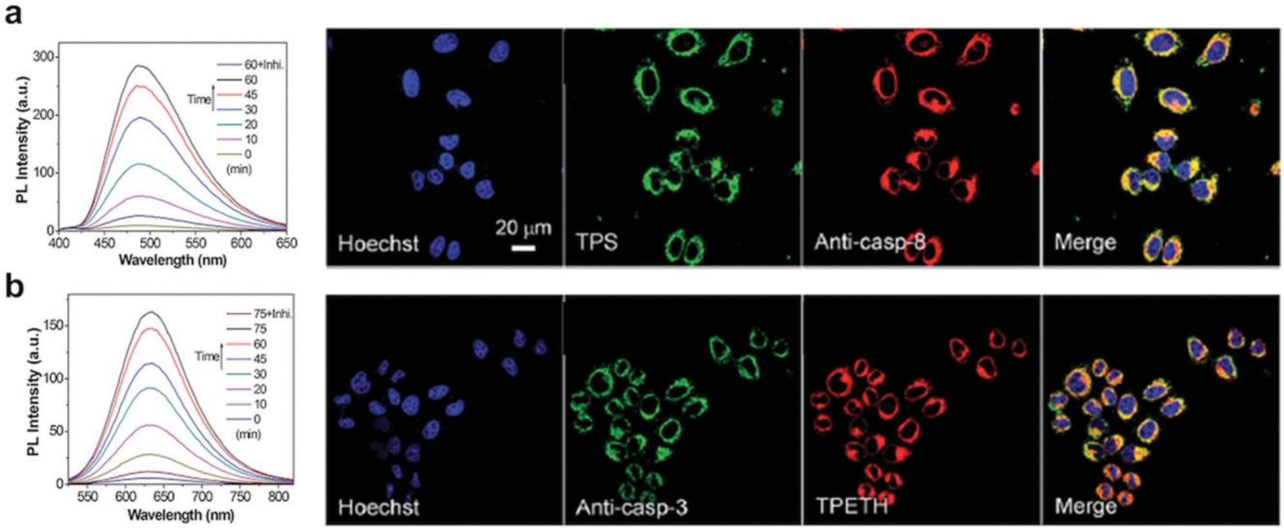

Fig. 12 Detection of apoptotic cells using the AIEgen probe (**34**).[130] (a) Left: Fluorescence spectra of probe **34** incubated with caspase-8 with or without inhibitor. Right: Confocal images of HeLa cells pretreated with probe **34** and further treated with H_2O_2 and stained with Hoechst (blue channel, for nuclear DNA), Texas red/anti-casp-8 antibodies (red channel). The probe's fluorescence is detected in the green channel (by TPS AIEgen). (b) Left: Fluorescence spectra of probe **34** incubated with caspase-3 with or without inhibitor. Right: Confocal images of HeLa cells pretreated with probe **34** and further treated with H_2O_2 and stained with Hoechst (blue channel, for nuclear DNA), Texas red/anti-casp-3 antibodies (artificially labeled with green color). The probe's fluorescence is detected in the green channel (by TPETH AIEgen). Reproduced from ref. 130 with permission from Royal Society of Chemistry, copyright 2017.

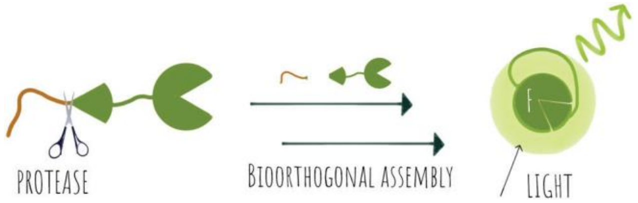

Scheme 5 The concept of protease activation followed by a subsequent bioorthogonal fluorogenic labelling reaction.

cascade (**39.3**). This strategy offers advantages over some pro-fluorophore strategies as the fluorophore is not pre-formed (so no background signal), but one potential disadvantage is that the kinetics of the reaction might impact on the time the system takes to assemble the dye. The design principle was successfully applied to leucine aminopeptidase (LAP) and penicillin amidase (PGA). Huo developed a g-glutamyl transpeptidase (GGT) activating two-photon fluorescent probe (**40.1**)[144] using a similar strategy. The probe could selectively detect GGT, upon cleavage, with intramolecular cyclisation resulting in a two-photon absorbing green emitting fluorophore.

Wu reported an approach using a ''labelling after recognition'' mechanism with phosphorescence lifetime analysis.[145] The approach was based on a caspase 3 specific substrate modified with two independent bioorthogonal reactive sites that allowed FRET-labelling (**41.1**). The strategy takes advantage of labelling the cleaved fragments and the uncleaved full peptide in the presence or absence of the protease. The novelty of this approach is that the FRET labels are added by bioorthogonal reactions following cleavage by the protease, with the rationale that conventional FRET-labelled peptides used for protease detection are pre-labelled and the bulky fluorophores may hinder recognition and cleavage. Here, the FRET pair used was an iridium(III) complex as a donor (**41.2**) (attached by strain promoted alkyne–azide cycloaddition (SPAAC) and RhoB as an acceptor (**41.3**) (attached *via* an iEDDAC tetrazine–norbornene click reaction). In the absence of the protease, the intact peptide with the bioorthogonally reactive moieties undergoes bis-labelling of the uncleaved peptide and leads to a change in lifetime *via* FRET, with the Ir(III) complex emission quenched due to the energy transfer to rhodamine B. However, the phosphorescence lifetime of the Ir complex was not quenched when labelling occurred after cleavage.[145] Potential limitations of this approach could come from incomplete labelling of the full or fragmented peptide or by differing labelling kinetics in/during the bioorthogonal labelling, an issue especially on more complex samples.

Demonstration of molecules that undergo aggregation upon activation and bioorthogonal cyclization were applied in molecular imaging (Fig. 13c) using caspase-3/7-controlled self-assembly of molecules into ''nanoparticles''[146] as a measure of the response of cancer tissue to chemotherapy. The intramolecular cyclization was possible by reaction between a free Cys residue and a 2-cyano-4-hydroxy-quinoline (**42.1**) that proceeded under physiological conditions to form a thiazoline linkage. This biocompatible reaction was possible due to the reductive environment that generates the free thiol and enzyme cleavage releasing a free amino group, which then mediate the cyclisation reaction. The cyclic molecule (**42.2**) then aggregates forming *in situ* fluorescent NPs. This aggregation enhances retention inside the cell, increasing the *in vivo* half-life, while

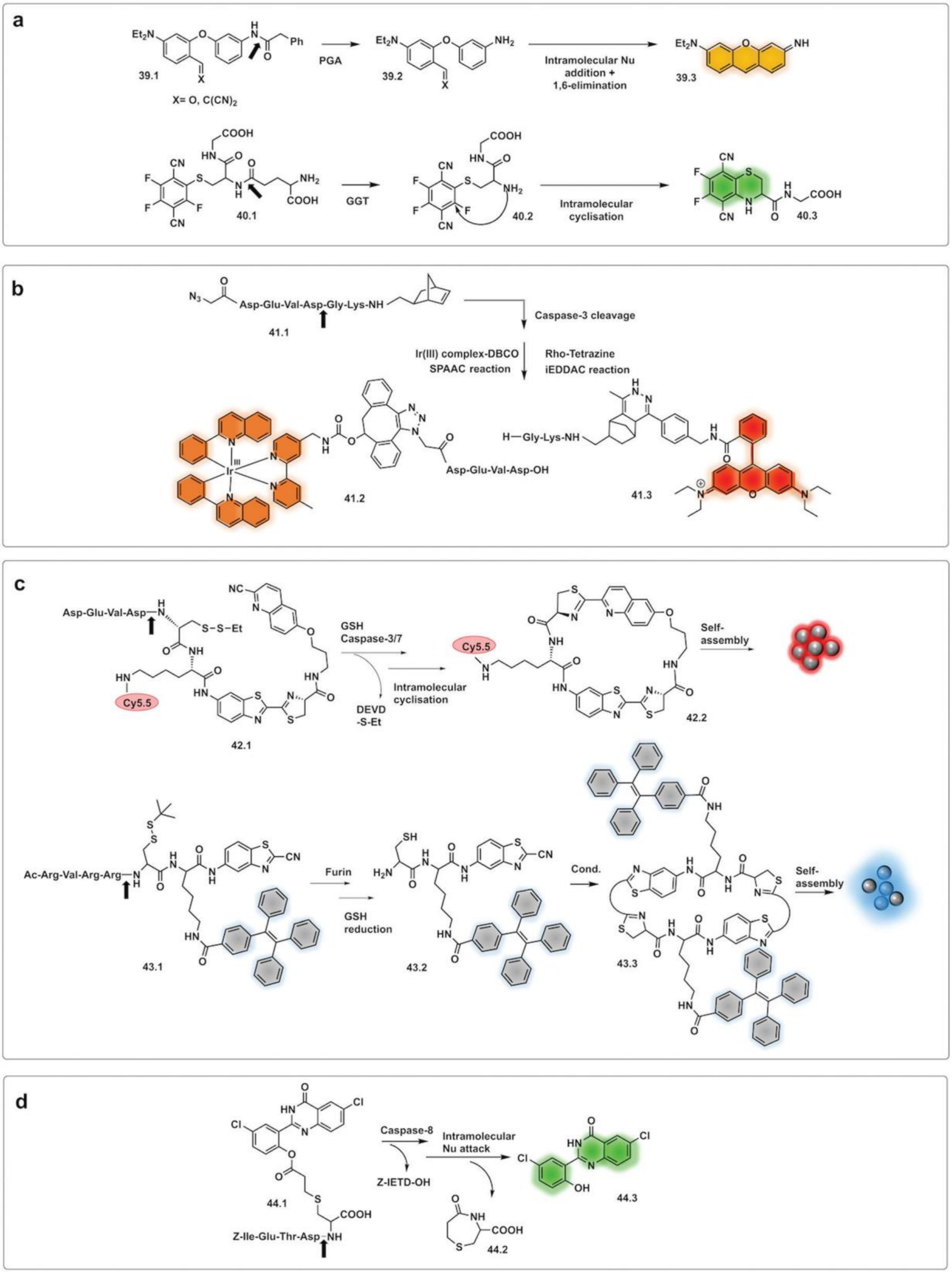

Fig. 13 Examples of bioorthogonal strategies for protease detection. (a) After cleavage by the protease, caged precursor (**39.1** and **40.1**) undergo bioorthogonal addition/elimination to yield the fluorophore pyronin (39.3)[142,143] or the two-photon-absorbing fluorophore (**40.3**).[144] (b) FRET labelling after cleavage by caspase-3.[145] (c) Assembling strategies based on thiazoline linkage formation in response to GSH and Caspase 3/7[146] or Furin.[127] (d) Excited-state intramolecular photon transfer based strategy, with cyclative cleavage following caspase-8 activation liberates the phenolic ester (**44.3**).[148]

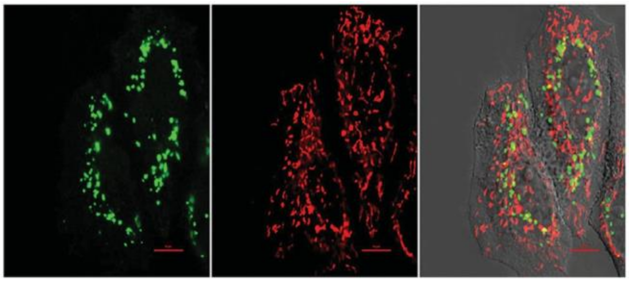

Fig. 14 Fluorescence images of HeLa cells treated with the bioorthogonal Caspase-8 probe **44.1**,[148] followed by treatment with the apoptotic inducer Mitomycin C for 120 min. Left to right: Green channel (probe **44.1** (see Fig. 13d), red channel (Mitotracker) and merged channel. Reproduced from ref. 148 with permission from American Chemical Society, copyright 2016.

the precursor units, in the absence of the protease undergo rapid clearance. The probe accumulated extensively in the cytosol allowing visualisation of apoptotic bodies in cells and tumour tissue using three-dimensional structured illumination microscopy (3D-SIM). A combination of AIE and bioorthogonal strategies were used in a probe designed for fluorescence sensing of furin activity *in vitro*.[127] The probe (**43.1**) was cleaved by furin exposing a free 1,2-aminothiol unit (**43.2**) that reacts with the cyano group on a cyanobenzothiazole motif yielding the more hydrophobic dimer (**43.3**) which self-assembles into fluorescent NPs.

A fluorescent activatable caspase-8 probe, consisting of an ESIPT (excited-state intramolecular photon transfer[147]) fluorophore attached to a Cys-residue has been reported.[148] These ESIPT fluorophores produce insoluble fluorescent aggregates with fluorophores localized in close proximity to the enzyme with enhancement of fluorescent emission – a process that is similar, but different to AIE. The protease probe was synthesized by a thiol-1,4 addition reaction[149] of a Cys containing peptide (caging group) with an acryloylated fluorophore (**44.1**). Upon internalisation of the probe in cells, cleavage of the peptide by activated caspase-8 results in intramolecular bioorthogonal cyclisation, liberating the amino group which reacts with an ester to release a 1,4-thiazepine seven-membered ring (44.2).[150] Decaging the fluorophore (**44.3**) switches on bright green fluorescence by excited-state intramolecular photon transfer, allowing high-sensitivity and high-resolution imaging (Fig. 14).

1.2 Chemiluminescence

Chemiluminescence (CL) is a powerful imaging technology that requires no external light source, does not suffer from photobleaching and has negligible background luminescence, but each molecule will only produce one photon. The phenomena of chemiluminescence can be defined as the emission of light resulting from a chemical reaction (Scheme 6) and differs from fluorescence in that the generation of the excited state arises thanks to the energy of a chemical reaction and does not depend on light irradiation.[151] The field of chemiluminescence for imaging applications has grown rapidly with the discovery of several natural and new synthetic luminogens.[152,153]

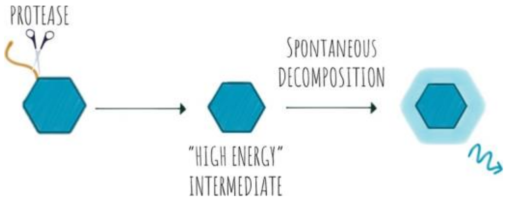

Scheme 6 The concept of protease activatable chemiluminescence.

Synthetic chemiluminescent systems take inspiration from natural bioluminescent systems that generate light following two sequential reactions, firstly oxidation of a substrate by an oxidizing agent or an enzyme into a ‘‘high energy intermediate’’ and secondly, the rapid decomposition of this intermediate in a process that produces light, with the Luciferin/Luciferase/O_2 system being the most studied.[154]

In the last decade, the field of chemiluminescence for imaging *in vivo* has expanded with synthetic modification of the natural luminogens to move beyond the limitations of natural luciferin.[155,156] This includes tuning the emission properties of the natural luciferin substrate to improve its quantum yield and give NIR emission by increasing the conjugation of natural D-luciferin[157–160] or by exploiting FRET with red shifted fluorophores.[161] Caging of luciferin by the addition of a triggerable protecting group to the 6^0-OH/NH_2 group generates a non-recognisable substrate for luciferase (**45.1**) allowing for turn-on of signal upon protecting group removal by the given trigger (*e.g.* enzyme or analyte). This strategy has been adopted to develop luminogenic probes for proteases such as cathepsin B (**46**),[162] chymotrypsin (**47**),[163] carboxypeptidases A and B (**48**),[164] Caspase-1 (**49**)[165] and furin (**50 and 51**)[166] (Fig. 15a). A novel strategy was devised with the *in situ* bioorthogonal assembly of firefly luciferin,[167] the design consisting of two complementary caged precursors of luciferin, a peptide-based probe (**52.1**) that released D-Cys in the presence of Caspase-8 and a boronic acid probe (**52.3**) that released 6-hydroxy-2-cyanobenzothiazole upon reaction with H_2O_2 (Fig. 15b). Once decaged, the two precursors undergo a bioorthogonal condensation reaction to form D-luciferin (**52.5**), with cyclisation between the carbonitrile and the thiol group of D-cysteine, thus reporting simultaneously oxidative stress (H_2O_2) and inflammation (caspase-8). Another approach focused on the *in situ* assembly of the enzyme luciferase (instead of the luciferin substrate) was engineered by Talley.[168] A modified luciferase specifically activated by Caspase-1 was generated by inserting a known target sequence into a ‘‘circular luciferase’’. Cleavage by Caspase-1 allowed the generation of a functional luciferase thus, generating a biolu- minescent system.

Natural bioluminescent organisms can modulate the colour of light emitted by the same principles as FRET by coupling luciferase to fluorescent proteins with overlapping spectral properties.[169] Bioluminescence resonance energy transfer

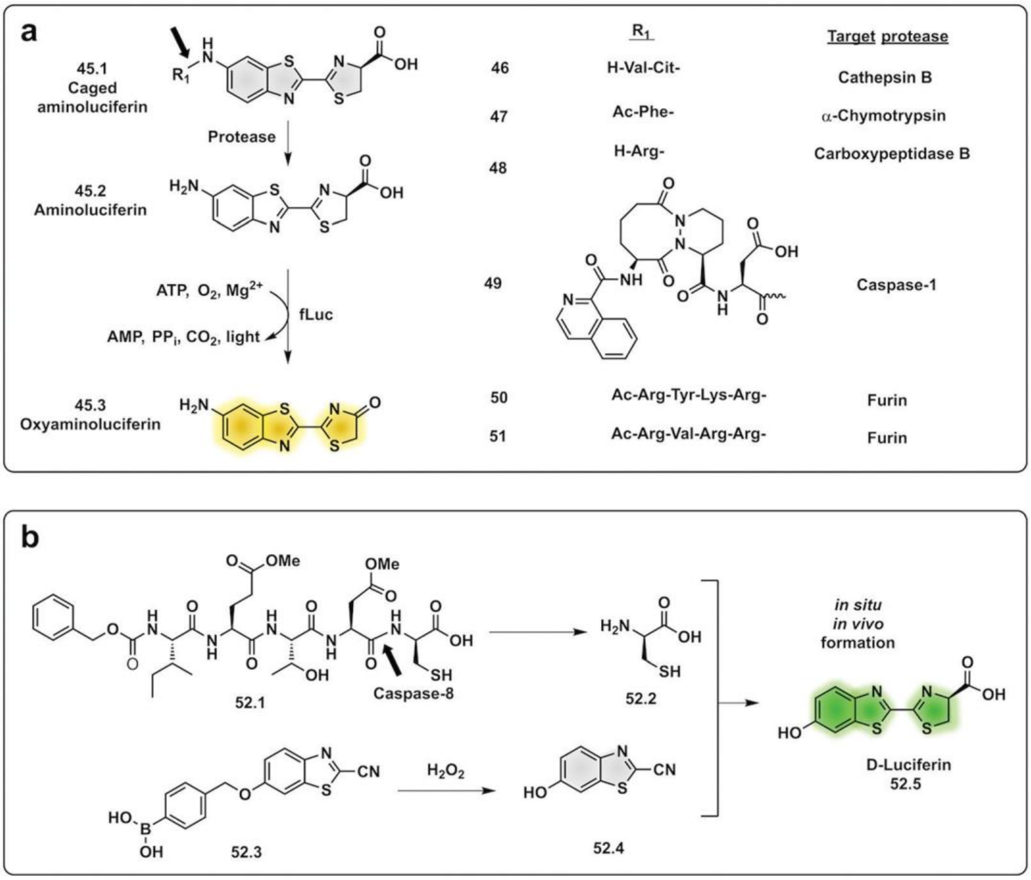

Fig. 15 Examples of protease probes based on chemiluminescence. (a) Probes based on decaging of aminoluciferin, a substrate for fLuciferase that produces luminescent oxyaminoluciferin (b) bioorthogonal assembly of D-luciferin *in situ* requiring dual activation by Caspase-8 and hydrogen peroxide.[167] fLuc: firefly luciferase.

(BRET) systems for protease sensing take advantage of the luciferin–luciferase system as an energy/light donor for fluorescent acceptors (generally GFP) and commonly use an optimised luciferase-substrate system coupled to a fluorescent protein through a protease cleavable linker. Upon cleavage and energy transfer, emission from the fluorescent molecule stops and the emission corresponds solely to the bioluminescent luciferase.[170–173] The original systems used a blue emitting luciferase and GFP, but in 2020 the first red-shifted BRET probe for detection of plasmin was reported.[174]

In an effort to simplify the system and remove the need of the enzyme luciferase for oxidation of D-luciferin, Shabat developed a series of caged 1,2-dioxetane phenols (**53.1 and 53.2**), highly stable compounds that rely solely on decaging of the dioxetane phenol-protecting group to produce luminescence.[175,176] Upon interaction with the decaging target trigger, an unstable phenolate–dioxetane intermediate (**53.3**) is released producing the excited ester (**53.4**) that relaxes with photon emission (Fig. 16a). Caging of 1,2-dioxetane intermediates have been widely used for protease sensing and generally use a protease sensitive peptide conjugated to the 1,2-dioxetane *via* a safety catch or self-immolative linker (**54 and 55**).[177,178] The emission properties of the 1,2-dioxetane can be tuned by increasing the conjugation of the phenolate, adding a conjugated p system and an electron withdrawing group (EWG) at the *ortho*-position.[179] Using this strategy, chemiluminescent Cathepsin B probes were designed (**56–58**), that showed high sensitivity[180] with enhanced tumour penetration by linking to a tumour targeting peptide.[181] Recently, the speed of chemiexcitation was also improved, allowing for greater light emission efficiency and better signal/noise ratios, by modifying the *ortho*-phenol EWG functionality to an a,b-unsaturated carboxylic acid functionality. Using this system, a Granzyme B probe (**59**), that could detect natural killer cell activity in live mouse models tumours,[182] was developed (Fig. 17). Using a similar strategy, Bogyo developed a system for detection of M. Tuberculosis,[183] that uses a chemiluminogenic FLASH probe bearing the substrate of Hip1, a protease of Mtb (Ac-Igl-(4-Cl-Phe)-Lys-Leu), where Igl is a the non-natural amino acid H-(2-indanyl)Gly-OH. This probe (**60**) allows detection and quantification of Mtb in human sputum samples *in vitro* and, importantly, the system can differentiate between live and dead bacteria. As such it shows real potential as a point-of-care sensing platform, as do the PSA probes (**61**) developed by Shabat that allows on-site measurements using a small portable luminometer.[184,185]

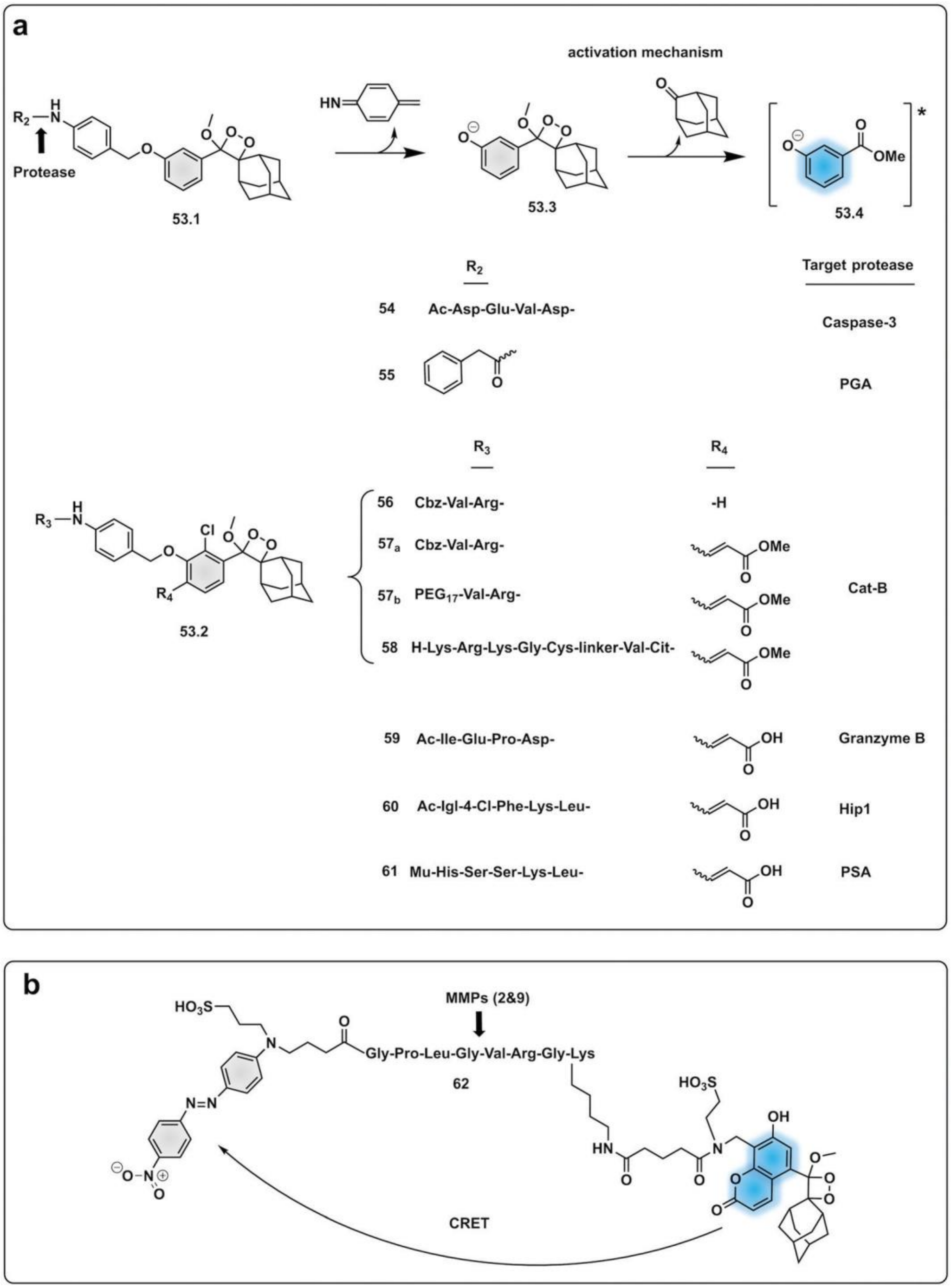

Fig. 16 Examples of protease probes based on chemiluminescence. (a) 1,2-Dioxetane phenols relying on decaging of the dioxetane phenol-protecting group to produce luminescence from initial probes for Caspase 3 and PGA.[177,178] Optimisation of light emission efficiency by increasing the conjugation of the phenolate in probes for cathepsin B,[180,181] Granzyme B[182] or PSA.[184,185] Ac: acetyl group; Mu: morpholine carboxamide moiety. (b) Chemiluminescence Resonance Energy Transfer (CRET) strategy for detection of MMP activity utilising a phenoxy-dioxetane luminophore and a nitro-dabsyl quencher.[187]

Modifications of the emission capabilities of 1,2-dioxetane probes by the addition of a fluorophore substituent at the *meta*-position of the benzoate unit allowed significant amplification of the signal thanks to transfer of light from the emission of the chemiluminogen to the fluorophore by Chemiluminescence Resonance Energy Transfer (CRET) (Fig. 16b). A model galactosidase triggerable probe[186] has been reported with great potential for applications in protease sensing by replacing the galactosidase moiety by a cleavable peptide.[187] Using CRET, a phenoxy-dioxetane luminophore attached to a 7-hydroxycoumarin scaffold was developed and linked to a quencher-peptide construct. The coumarin-dioxane luminogen

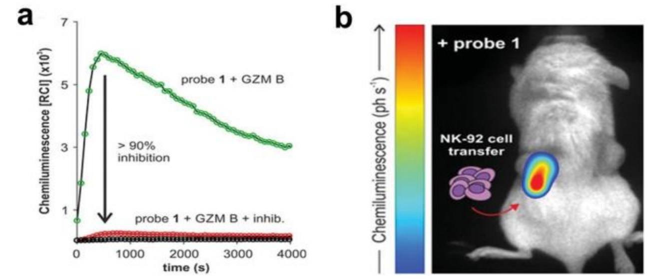

Fig. 17 (a) Chemiluminescence spectra of granzyme B chemiluminogenic probe 59[182] following incubation with granzyme B (green line) or without enzyme (black line) or with a granzyme B inhibitor (red line). (b) *In vivo* representative chemiluminescence image of a NSG mouse containing MDA-MB-231-xenograft tumours where NK-92 cells were adoptively transferred. Only the right tumour (red arrow) was injected with NK-92 cells with the left tumour being NK cell-free. After 8 h of the NK cell injection, probe was injected into both tumours. Reproduced from ref. 182 with permission John Wiley and Sons, copyright 2021.

exhibits intense and persistent chemiluminescence (62). Following the same principles as FRET conjugation of a non-emissive quencher acceptor molecule to the luminogen quenches any chemiluminescence emission until the peptide is cleaved by the protease.

1.3 Optoacoustics

Photoacoustic imaging (PAI) is an imaging strategy that bridges the traditional limited penetration depth and the resolution limits of diffuse optical imaging. Some reviews have been recently published[188–190] and thus here we will only report on very recent papers, applications and novel concepts.

In photoacoustic imaging, a laser pulse is used to ''illuminate'' specific structures in the body by virtue of them containing molecules that absorb photons. This causes local heating that generates pressure waves (the thermoelastic effect due to vibrational and translational relaxation). These pressure waves are in the ultrasound frequency range and as such can be measured by traditional ultrasonic transducers to generate an image. Photoacoustic imaging has rapidly been adopted in preclinical *in vivo* imaging in small animals for a range of disease indications, where it has provided in a non-invasive manner, images that in essence show where optical energy has been absorbed by detection of the acoustic waves generated. A key attribute is that it can do this at depths of several centimetres while offering a resolution of B100 mm.

PAI can exploit the absorption capacity of naturally occurring molecules, such as haemoglobin[191] and melanin,[192] however, probe-based contrast agents are now being used to allow directed ''molecular photoacoustic imaging'' at greater depths (Fig. 18). Typical molecules used in PAI have included indocyanine green (ICG) and methylene blue (MB) and some take advantage of both the photoacoustic and the fluorescence signals. The combination of optical and photoacoustic imaging has become a widely implemented strategy (Table 1).[193–195]

Traditional non-fluorescent dyes of various types are actually more efficient in terms of conversion of light absorption into heat and acoustic signals[196,197] (simplistically it is better that light is converted to heat and not emitted as a photon). Thus, dyes offer greater thermoelastic expansion than fluorochromes, making quenchers *e.g.* dabsyl and the so-called black-hole quenchers (BHQ) good candidates for photoacoustic contrast agents but any dye with a high extinction coefficient and good conversion of light to heat should work well as contrast agents

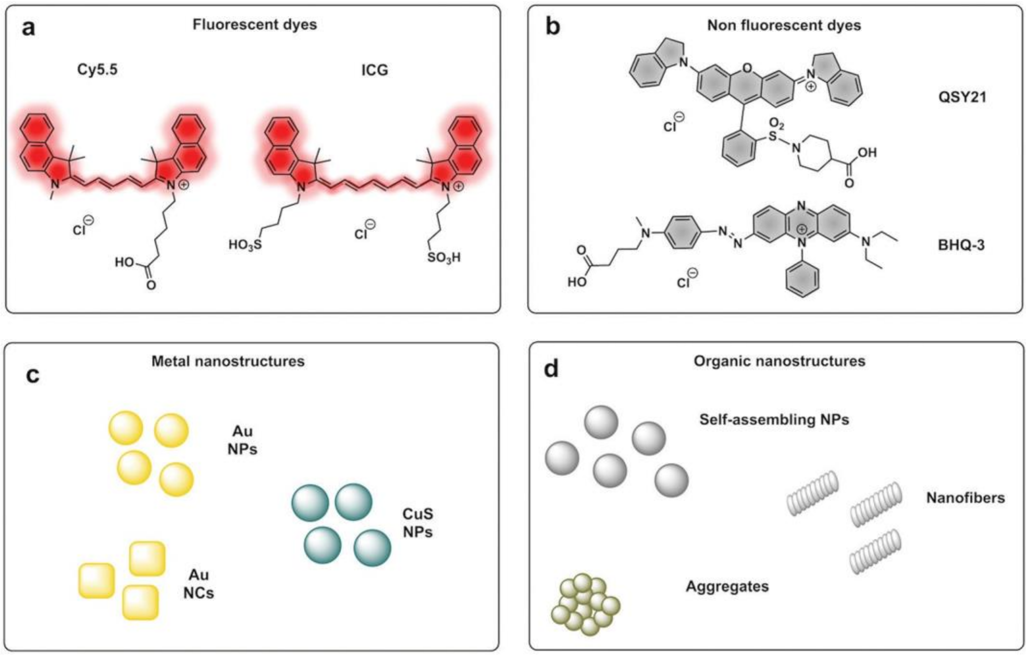

Fig. 18 Examples of some contrast agents and strategies for photoacoustic imaging.

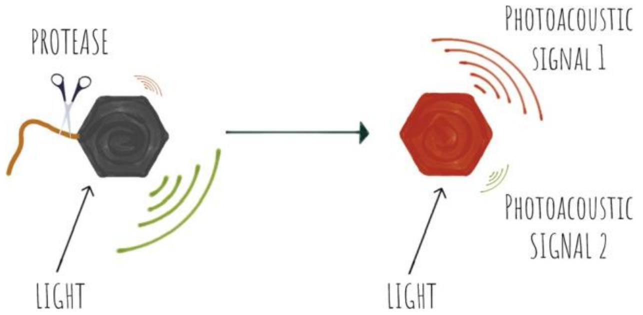

Scheme 7 The concept of photoacoustic probes activated by proteases.

for PAI. One PA contrast agent reported recently used BHQ-1 conjugated to a cRGD targeting moiety.[198]

Recently, activatable photoacoustic imaging contrast agents have appeared. Design of these probes utilize similar approaches to those discussed for fluorescence base probes (FRET, self-assembly/bioorthogonal, pro-PAI, AIEgens), generating a specific switchable signal upon alteration of their structure, with proteases allowing disease-specific targeting/activation (Scheme 7).

NIR fluorescent dyes can act also as photoacoustic agents. MMP-Prosense 680,[199] the NIR probe previously described, was evaluated for photoacoustic imaging, achieving high-resolution mapping of MMP activity deep in vulnerable plaques of intact human carotid specimens. Multispectral optoacoustic tomography allowed three-dimensional reconstruction of targeted structures *in vivo*[200] with morphologies similar to heterogeneous MMP activity but with better than 200 μm resolution throughout intact plaque tissues and allowing volumetric images of activatable molecular probe distribution deep within optically diffuse tissues.

Levi[201] developed a FRET-based protease activatable PAI probe using an AF750/BHQ-3 labelled MMP-2 cleavable peptide that under physiological conditions generates two photoacoustic signals. Cleavage/activation generates a BHQ-3 labelled cell penetrating peptide that results in accumulation of the PA contrast agent into cancer cells and a NIR dye labelled fragment that produces orthogonal photoacoustic signals.

Using a similar approach to that covered in the pro-fluorophores section, a urokinase-type plasminogen activator (uPa) activatable probe was designed[202] that provides a turn-on in fluorescence and photoacoustic signals and optimal renal clearance due to the hydrophilicity dextran backbone. The probe consists of a ‘‘caged’’ dextran functionalised-Cyanine dye, connected to a cleavable uPA peptide sequence *via* a self-immolative linker. Upon cleavage by the protease, the dye is decaged and its fluorescent and photoacoustic properties restored. Using the same strategy, a probe for dual imaging of acute kidney injury, cleavable by g-glutamyl transferase (GGT), was developed by Chen (**63**, Fig. 19a),[194] allowing real-time imaging of kidney function at a molecular level (Fig. 20).

CuS nanoparticles, exhibit strong (broad spectrum) absorbance, and have been used as photothermal agents for tumour ablation. As might be anticipated from their ‘‘black colour’’ they absorb broadly and show strong photoacoustic signals at 930 nm. A probe based on a BHQ-3 labelled MMP-cleavable-peptide conjugated to CuS nanoparticles was developed,[203] that provided a combination of two PA signals in absence of the MMP. Upon cleavage by the protease, only the PA signal from the nanoparticles remained. The probe successfully sensed MMP-activity in mice in a promising alternative to optical imaging techniques with improved detection depth. Due to their strong and tunable optical absorptions gold-based nanoprobes have been widely used as PAI agents. Probes have been developed that produce a change in the emitted PA signal and produce combined fluorescence signals in response to proteases. Using a nanocage, a probe for MMP-2 was developed,[204] which produces a strong acoustic signal at 800 nm. In the intact construct fluorescence emission by the Alexa Fluor 680-conjugated peptide was quenched by the gold nanocage and producing a PA signal by illumination at 680 nm indirectly. Upon MMP cleavage, the NIR dye is released and cleared from the tumour tissue which results in changes in the photoacoustic spectral signature, going from a signal contributed by both reporters to one generated by the gold nanocage alone.

An optoacoustic activatable probe[205] with capacity for simultaneous photoacoustic and NIR optical imaging based on a self-assembly strategy activated by protease cleavage, driven by

Table 1 Photoacoustic probes

Modality	Contrast agents	Strategy	Protease	Sequence	Ref.
Optoacoustics	Cy5.5 dimer	FRET	MMPs	Ac-K(PEG)-[K(PEG)-K(Cy5.5)) K/K(Cy5.5)-K(PEG)]$_n$-	199
	Alexa750/BHQ-3	FRET	MMPs	Not reported	201
	Hemicyanine	De-caging	GGT	GGR	194
			uPa	g-Glu	202
	Cy5.5/QSY21	Self-assembly	MMPs	KCPLGVRGY	205
Photoacoustics	CuS nanoparticles/BHQ-3	FRET	MMPs	GLPGVRGKGG	203
	Gold nanocages/Dye 680	FRET	MMPs	GKGPLGVRGC	204
	Purpurin 18	Self-assembly	Gelatinase	PLGVRG	206
	ATTO740	Bioorthogonal	Furin	RVRRC	207
	ICG	Bioorthogonal	Caspase-3	DEDV	208
	Gas Vesicle Protein (GvpC)	Buckling of the GvpC	TEV	ENLYFQG	209
PA/PTT/PDT	Gold nanostars/IR – 780	FRET	MMPs	GPLGIAGQ	210

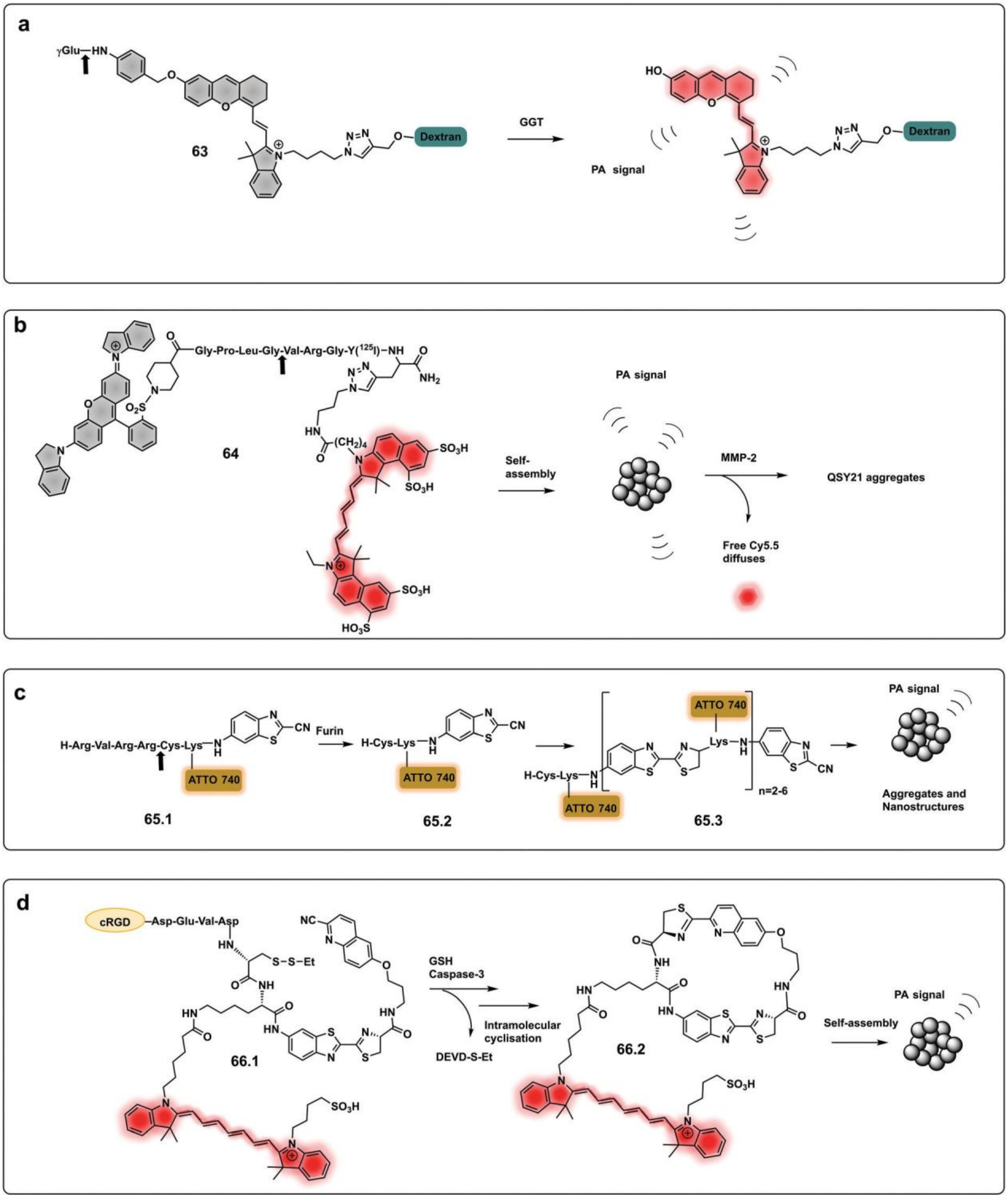

Fig. 19 Dual and aggregation based optoacoustic activatable probes. (a) Dual imaging, fluorescence/photoacoustic probe for detection GGT, cleavage by the protease decages a cyanine dye with fluorescence and photoacoustic properties.[194] (b) Amphiphilic construct using QSY21 as a photoacoustic agent and sulfonated Cy5.5 as a fluorophore. Amphiphilicity of the construct drives nanoparticle formation, while cleavage by MMP-2 disassembles the nanoparticles and results in a change in photoacoustic signal.[205] (c) Bioorthogonal photoacoustic emissive oligomer forming probe for furin.[207] (d) Dual activation dependent probe for sensing of GSH and caspase-3 that results in photoacoustic emissive nanoparticle assembly.[208]

hydrophobic interactions has been reported. The probe was constructed with a near-infrared dye (Cy5.5) and a quencher (QSY21) linked through a peptide substrate of MMP-2. The construct is amphiphilic as QSY21 is highly hydrophobic while sulfonated Cy5.5 is hydrophilic, which drives self-assembly into nanoparticles. When cleaved by the protease enhanced NIR

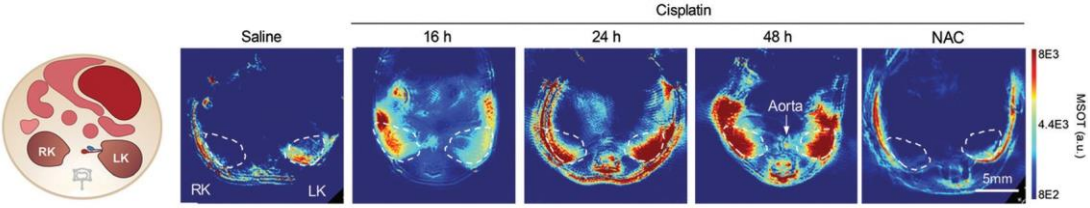

Fig. 20 PA imaging of cisplatin-induced Acute Kidney Injury using a g-glutamyl transferase optoacoustic probe (63).[194] Mice transverse section after i.v. injection of the probe in different treatment groups (detection at 700 nm). The white circles indicate the two kidneys. RK, right kidney; LK, left kidney, NAC: *N*-acetyl-l-cysteine protected. Reproduced from ref. 194 with permission John Wiley and Sons, copyright 2021.

fluorescence is generated, simultaneously with photoacoustic signal ratiometric changes as the nanoparticle-assemblies disaggregate. Photoacoustic emissions from the intact construct were detectable with high intensity at 680 nm and at 730 nm. Upon cleavage, a reduction in the 680 nm photoacoustic signal was observed in an MMP concentration dependent manner with the corresponding increase in fluorescent emission by the de-quenching of Cy5.5 (the photoacoustic signal at 730 nm remained constant (MMP independent) and served as a reference signal (**64**, Fig. 19b). Following the same mechanistic principle (but in reverse), a self-assembling gelatinase probe used Purpurin 18 as the functional photoacoustic stimulator[206] with self-assembly upon protease cleavage leading to the formation of photoacoustic emitting nanofibers. Another PAI self-assembling probe (**65.1**) for detection of furin has been developed where cleavage leads to the formation of photoacoustic emissive oligomers *via* a bioorthogonal reaction.[207] The activation of the probe *via* furin cleavage of the peptide substrate released (ATTO740)-1,2-aminothiol that undergoes self-condensation to form oligomers (**65.3**) containing ATTO740 (Fig. 19c). These nanostructures enhance the quenching effect of the fluorophores thus minimizing radiative emission, which increases the photoacoustic signal. The same bioorthogonal reaction was used to design a caspase-3 probe.[208] In this case dual activation was dependent on caspase-3 and glutathione (GSH). The construct (**66.1**) contained a cyano-6-hydroxyquinoline (CHQ), a D-Cys residue, a caspase-3-cleavable peptide substrate (DEVD), ICG and contained a cRGD targeting peptide (Fig. 19d). Owing to aggregation-caused quenching (ACQ) the nonradiative relaxation process was favoured, which increased the PA signal and decreased the fluorescence of ICG.

Anupama recently developed photoacoustic probes for the detection of proteases[209] consisting of engineered gas vesicle based biosensors, air-filled protein nanostructures that change their ultrasound contrast in response to the activity of different biomolecules. In this case, they used tobacco etch virus protease (TEV). In presence of the protease, the gas vesicle shell becomes less stiff, thereby allowing it to undergo buckling and produce enhanced nonlinear ultrasound signals that can be easily distinguished from the intact, non-digested ‘‘gas vesicles’’.

A theranostic approach based on gold nanostars was developed[210] with multiple and simultaneous imaging modalities. The probe consisted of a gold nanostars core (photoacoustic and photothermal effector), conjugated to the MMP-2 peptide (Ac-GPLGIAGQ) *via* BSA loaded with a NIR dye IR-780, for optical imaging and photodynamic therapy.

2 Bench-top or *in vitro* applications

2.1 Colorimetric

Colorimetric sensing determines the presence or absence of target analytes by measuring optical density (Beer–Lambert law) and depends on the generation of coloured species. Due to the advantages of simple operation with no need for complicated instrumentation, colorimetric sensing offers a good strategy for point-of-care diagnosis with test results that can be interpreted with the naked eye (classic examples are Gram staining of bacteria). This is useful in terms of speed of analysis, and the reduction in the cost of testing in resource-limited settings where sophisticated technologies and time delays would limit application. In the field of protease sensing, there are two main types of colorimetric probes used: colorimetric probes based on enzyme-catalyzed organic chromogenic substrates that form coloured products[211] and biosensors based on modification of the surface plasmon resonance (SPR) of noble metal nanoconstructs.[212] Indeed gold nanoparticle (AuNPs) colorimetric assays are the most widely used with many publications over the past 30 years taking advantage of the AuNPs excellent tunable properties as simple chromophores[213] with the optical properties of AuNPs depending on the SPR of the nanoparticles.[214] Modifications of the surface of the AuNPs can induce or prevent aggregation, which correlates with changes in the SPR that leads to a colour dependence (Scheme 8). The surface of the AuNPs are usually modified using thiol-gold chemistry to simultaneously add specific molecular recognition moieties and to tune the stability of the particle suspension. Surface modification of the construct by targeted biomarkers can trigger changes in the aggregation behaviour of the AuNPs that can be visible by the naked eye as a colorimetric response. Generally the aggregated particles give rise to a distinct purple colour, while the dispersed AuNPs look red. A simple protease colorimetric probe can thus use peptides conjugated to AuNPs[215] *e.g. via* thiol chemistry or by electrostatic interactions, with cleavage of the peptide resulting in either induction or prevention of

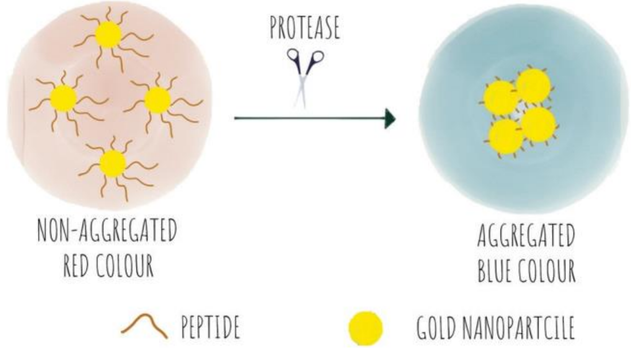

Scheme 8 The concept of colorimetric sensing based on gold nanoparticle aggregation in response to the presence of proteases.

aggregation that results in a change in colour. The systems based on AuNPs aggregation can use a ''mix and detect'' system where standard unmodified gold nanoparticles (generally stabilised with citrate) are mixed with a peptide. Alternatively, gold nanoparticles may be pre-modified, where the protease substrate peptide is immobilised on the surface of the nanoparticles which can then generate a visual response based on the exposure to (or lack of) the protease.

A probe for MMP-7[216] was synthesised (**67**) using pre-modified gold nanoparticles using a C terminal Cys peptide substrate for the protease. The negatively charged peptide sequence prevented aggregation of the AuNP until cleavage by the protease, that removed the negatively charged residues causing a reduction of the net charge and decrease in nanoparticle size, leading to a loss in stability of the nanoparticles that would aggregate and shift from red to purple; a colour shift detectable by the naked eye. A mix and detect system (**68**) used unmodified free gold nanoparticles (citrate stabilised, negatively charged) and a caspase-3 cleavable peptide.[217] The peptide contained two adjacent Cys at the C terminus, three negatively charged residues and one positively charged arginine. When the peptide was pre-incubated with the protease, the three negatively charged residues were cleaved off, leaving a net positively charged thiol fragment that would be immobilised on the gold nanoparticle *via* the cysteine side-chains and induce aggregation (due to interaction between the positively charged arginine and remaining negatively charged areas of the AuNPs). When the free AuNPs were incubated with the mixture of peptide and protease, a blue colour would be observed due to aggregation whilst the incubation with the intact peptide and no protease prevented aggregation retaining the initial red colour.[217] Chen[218] reported a probe for MMP-2 (**69**) following a similar strategy with the negatively-charged fragment on the N terminus (as a Glu$_4$ moiety) and the positively charged residue being Lys on the thiol containing fragment.

Conjugation by electrostatic interactions has used peptides containing high levels of positively charged residues that coordinate with the free negatively charged AuNPs (citrate stabilised) in suspension. Using this approach, a colorimetric assay for trypsin was reported (**72**)[219] that used a hexa-Arg peptide as both a substrate for trypsin and to allow conjugation to the nanoparticles. When the free (negatively charged) nanoparticles are exposed to the positively charged peptide, the peptide intercalates between gold nanoparticles and induces cross-linking and aggregation of Au-NPs leading to the red-shift. If, however, the peptide is pre-incubated with enzyme prior to exposure to the nanoparticles, the peptide is digested, and the nanoparticles remain dispersed. Another probe using electrostatic conjugation was reported[220] which used negatively charged carboxyl-functionalised AuNPs (using a carboxy-PEG$_{12}$-thiol) in combination with a MMP substrate with hexa-His tags at both ends (metal ions drive metal-affinity coordination between the carboxyl groups and the His-tags). The intact peptide therefore drives aggregation whilst the cleaved peptide promotes the dispersion of the nanoparticles.

Ding[221] used a ''mix and detect'' trypsin (**70**) assay with a peptide bearing a Cys residue at the C-terminus and a positively charged Lys at the P1 position. Since the oligopeptide contains both Cys and a positively charged Lys residue, it causes aggregation of the citrate-stabilised, negatively charged, AuNPs. However, since trypsin cleaves the peptide, separating the Cys and Lys residues, the cleaved oligopeptide no longer causes aggregation of the AuNPs.

Meng-Qi reported a novel strategy[222] allowing the properties of the SPR to be tunable *via* the modification of gold nanorods (AuNRs) (Fig. 21c). This protease detector (**71.1, 71.2, 71.3**) was based on a protease specific peptide with two central Cys residues at the cleavage site. Cleavage by the protease thus releases two fragments exposing the monothiol groups from the Cys, that are otherwise non-accessible, and react with the AuNRs causing morphological changes, with ''new spikes'' formed by addition of the peptides fragments to the surface, resulting in unique SPR peak shifts that were also seen by the naked eye (red-to-blue). Using this strategy, the group developed a probe for the detection of trypsin activity in a label and instrument-free manner and with ultrahigh sensitivity, with a LoD of 60 fM.

A colorimetric method for prostate-specific antigen (PSA) detection was developed by Liu[223] using the formation or inhibition of formation of AuNPs as a colorimetric indicator. The method was based on ascorbic acid induced formation of AuNPs, a process that can be inhibited by the presence of Cu^{2+}. HAuCl$_4$ (**74.1**) can be reduced to form AuNPs (**74.2**) by ascorbic acid (**73.1**), however, in the presence of Cu^{2+}, ascorbic acid is oxidised (**73.2**), and can no longer reduce the HAuCl$_4$. The designed construct was based on peptide coated gold magnetic microbeads containing a Cu^{2+} binding triad (Asp-Ala-His) followed by a PSA cleavable sequence (Fig. 22a). When the protease is present, the peptide is cleaved and the Cu^{2+} binding triad released. Consequently, the copper ions are not trapped, resulting in oxidation of ascorbic acid and no AuNP formation. Alternatively, the Cu^{2+} binding triad can be localized internally so that it remains masked (Fig. 22b), but can be demasked by proteolytic hydrolysis (b-secretase) exposing the Cu^{2+} chelating ligand. In this design, formation of AuNPs only happens in the presence of the protease.[224]

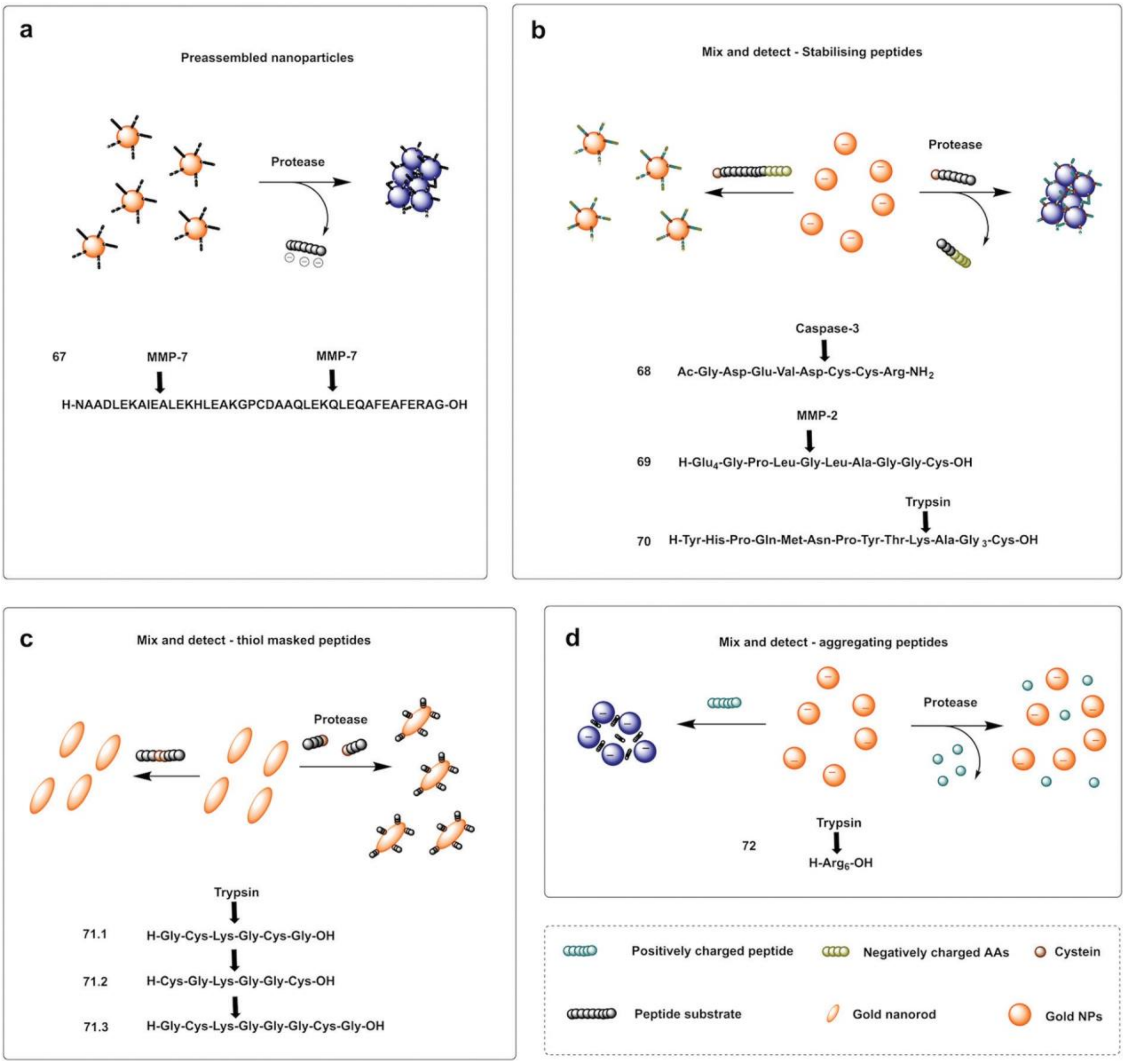

Fig. 21 Examples of protease colorimetric assays based on gold nanoparticles. (a) Premodified gold nanoparticles conjugated to a cysteine terminal cleavable peptide for MMP-7.[216] (b) Mix and detect strategies based on gold nanoparticles and stabilising peptides (with destabilising effect if protease is present) for detection of caspase-3,[217] MMP-2[218] or trypsin.[221] (c) Mix and detect method based on tunable SPR of gold nanorods (AuNRs)[222] using a protease specific peptide with two central Cys residues at the cleavage site. Cleavage by the protease causes morphological changes, with ''new spikes'' formed by addition of the peptides fragments to the surface *via* newly exposed thiol groups. (d) Colorimetric assay for trypsin[219] that uses a hexa-Arg peptide as both a substrate for trypsin and to allow aggregation of the nanoparticles. When nanoparticles are exposed to the positively charged peptide, the peptide intercalates between Gold nanoparticles and induces aggregation of Au-NPs leading to the red-shift, which is prevented when the peptide is digested by trypsin.

Bhatia reported on the design and synthesis of protease probes for pre-clinical use developing a series of colorimetric assays/platforms as diagnostics tools for detection of disease related proteases. They used a variety of peptide-modified platforms that can be administered intravenously, activated at the site of the disease and detected in the urine. The urinary, colorimetric, *in vivo* assay[225] conjugates gold nanoclusters (AuNC) to a carrier protein (neutravidin) tethered to a protease cleavable peptide with a Cys residue for binding to the AuNC (**76–79**). Exposure to the protease (thrombin or MMP) at the disease site, following IV administration, resulted in the release of the AuNC from the construct enabling passage into the urine to produce a direct colorimetric readout of the disease state. The strategy exploited the peroxidase capacity of the ultra-small AuNC, with a size <2 nm that also showed efficient filtration capacity through the kidneys into the urine. These AuNCs had an intrinsic catalytic peroxidase activity, catalysing the oxidation of 3,3^0,5,5^0-tetramethylbenzidine (TMB) (**75.1**), that could be monitored by absorbance at 652 nm (Fig. 23a).

Zourob designed a series of low-cost, easy-to-handle, highly sensitive and portable colorimetric biosensors (Fig. 24) capable

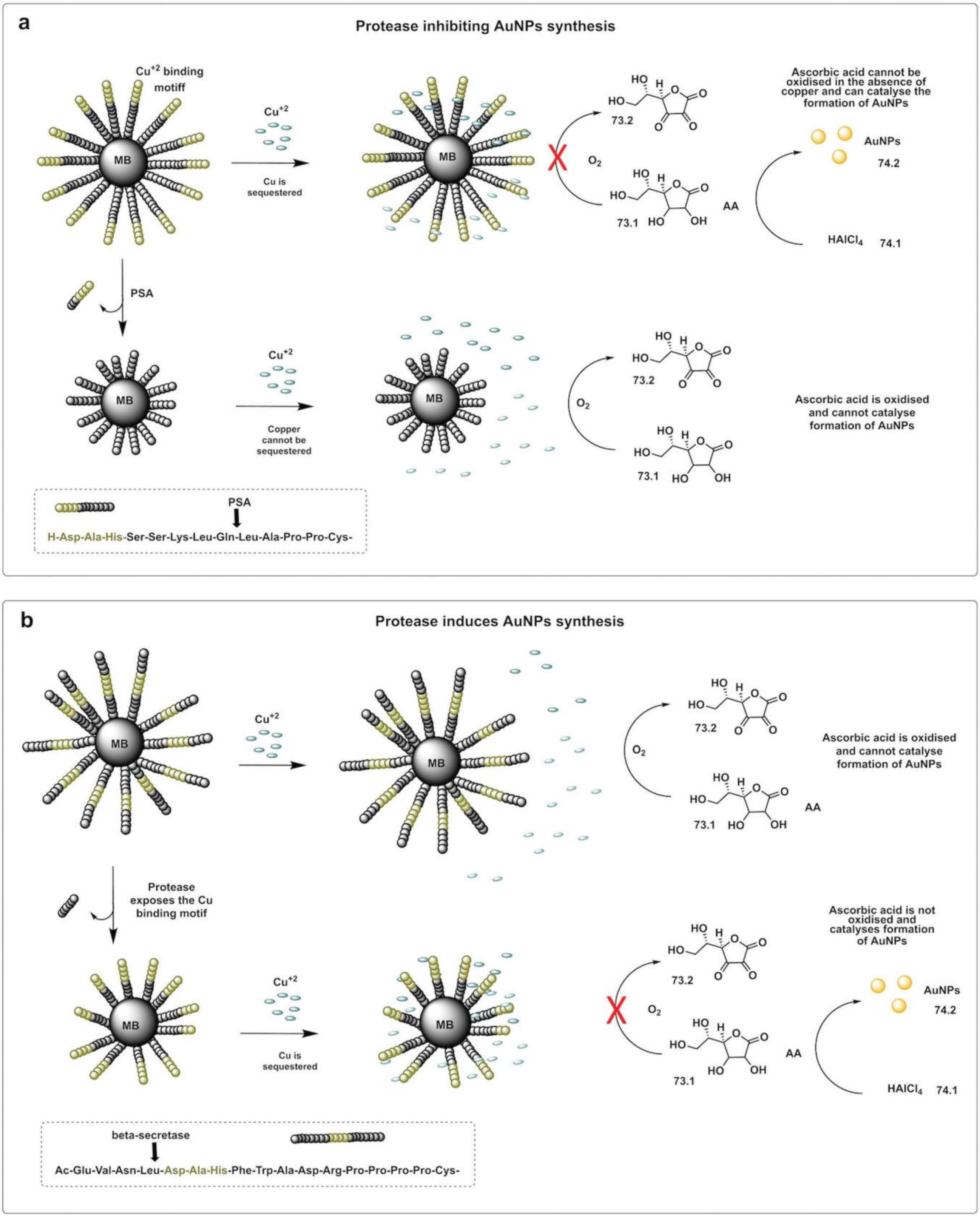

Fig. 22 *In situ* formation of catalytic AuNPs. (a) Colorimetric assay for detection of PSA based on *in situ* synthesis of gold nanoparticles from the precursor $HAuCl_4$ catalysed by ascorbic acid in absence of Cu(II).[223] The design used peptide-modified magnetic nanoparticles containing a Cu^{2+} binding triad. The peptide was cleaved by PSA and the Cu^{2+} binding triad released. Consequently, the copper ions are not trapped, resulting in oxidation of ascorbic acid and no AuNP formation. (b) System with the Cu^{2+} binding triad is localized internally and demasked by proteolytic hydrolysis (b-secretase) exposing the Cu^{2+} chelating ligand. In this design, formation of AuNPs only happens in the presence of the protease.[224] MB: magnetic beads. AA: Ascorbic Acid.

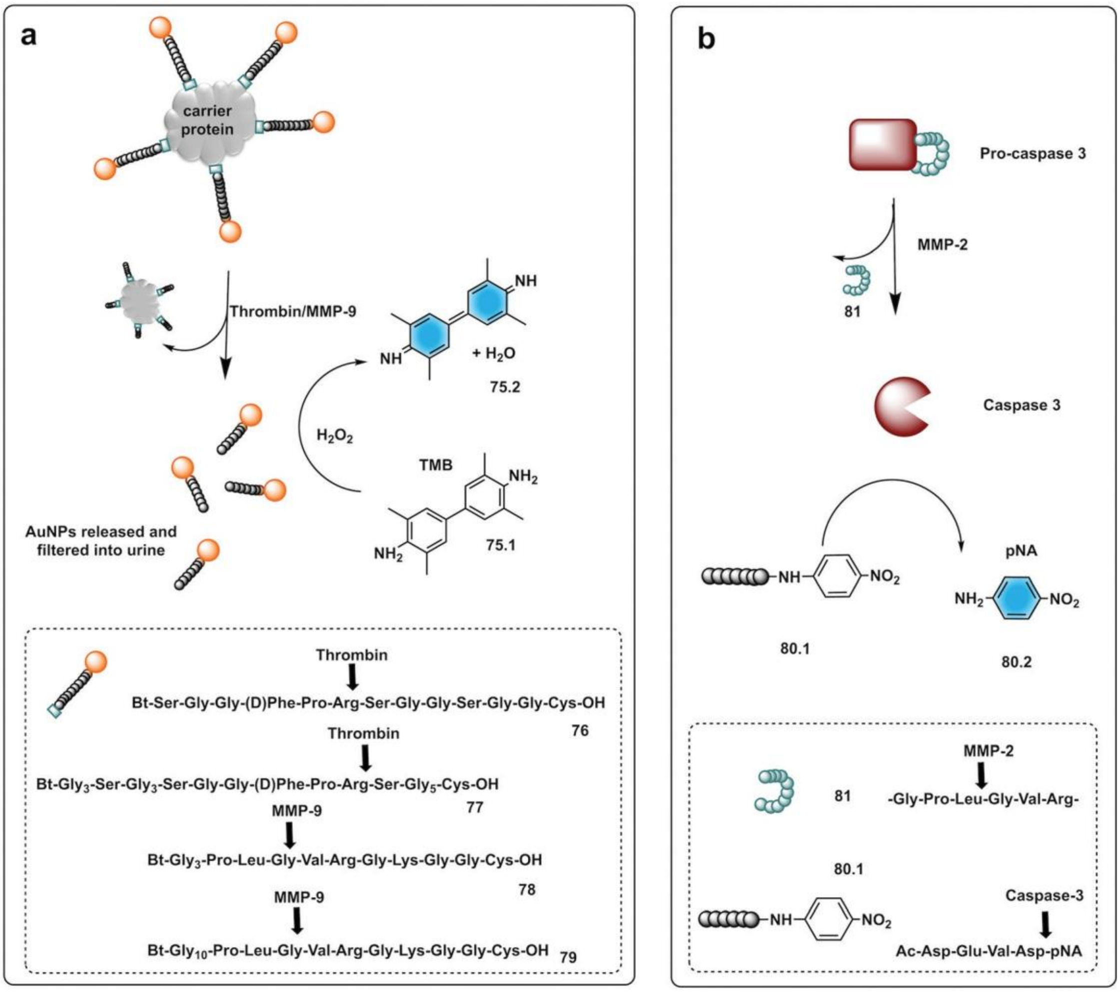

Fig. 23 Small molecule based systems for colorimetric sensing of proteases. (a) Urinary colorimetric *in vivo* assay[225] using gold nanoclusters (AuNC) attached to a carrier protein *via* a protease cleavable linker. Exposure to thrombin or MMP-9 releases AuNCs to produce a direct colorimetric readout exploiting the intrinsic catalytic peroxidase activity of AuNCs to oxidise TMB. (b) Engineered procaspase-3 is auto-inhibited in the absence of the target protease (MMP-2) by a weak reversible inhibitor attached to the enzyme by a peptide linker. Upon activation by MMP-2 active caspase-3 is generated that cleaves the substrate Ac-DEVD-pNA generating a chromogenic response.[231]

of detecting different disease-related proteases (**82**, Fig. 24). The method used a probe that consisted of a specific peptide substrate covalently attached to magnetic beads through its N-terminus and linked to a gold probe surface at the C-terminus *via* a Cys residue. This construct resulted in a layer of magnetic beads adsorbed on the probe surface masking its golden colour in the absence of the protease. Upon protease cleavage the peptide linkage between the magnetic beads and the gold probe surface is lost and the released magnetic beads were magnetically collected and analysed. This idea was applied to develop portable probes for PSA,[226] HNE and Cathepsin G,[227] Listeria monocytogenes protease[228] and *P. aeruginosa* proteases.[229]

Small molecules have found successful applicability in this area with *p*-nitroaniline (pNA), a well-known reporter. Thus, chromogenic peptides, conjugated to pNA (**80.2**) have been used for colorimetric-based testing, which when conjugated are colourless, but upon cleavage result in a colorimetric response.[230] An interesting strategy was developed by Dokyung, where an engineered procaspase-3 was modified to be auto-inhibited in absence of the target protease (MMP-2) by adding a weak reversible inhibitor linked to the enzyme by a peptide linker (**81**) that was cleaved by the protease of interest (Fig. 23b). This cascade system also used a chromogenic caspase-3 substrate (Ac-DEVD-pNA, **80.1**) to generate a chromogenic response with its hydrolysis rate reporting on MMP-2 activity.[231] Using pNA-peptides, immobilised on cellulose, a paper-based chromogenic probe to detect inflammation was developed.[232]

2.2 MS based detection

MS has been used as a method for a variety of proteomic analysis studies including as a diagnostic tool to differentiate disease from healthy profiles as well as staging and disease monitoring. Proteome profiling for diagnostic purposes is a thriving area in proteomics, however, the complexity of the

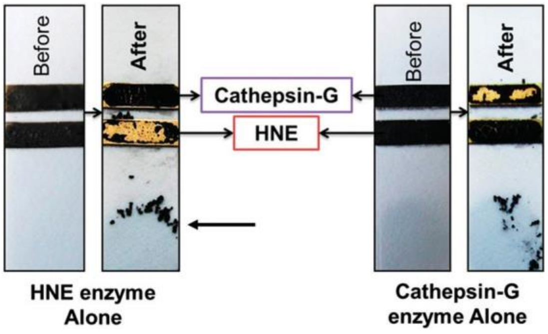

Fig. 24 Colorimetric sensing platform for HNE and Cat G.[227] These probes consist of specific protease substrates covalently bound to a magnetic bead at one end and to a gold surface by the other. Cleavage by the protease results in dissociation of the magnetic bead complex. A magnet placed on the back of the strip (see arrow) attracts the cleaved beads that are displaced exposing the gold color. HNE sequence: -GSGSGGGAAPVAAKGGGSGSC- (**82.1**) and cathepsin-G sequence: -GPQGIWGQR- (**82.2**). Reproduces with permission of the American Chemical Society, copyright 2015.

samples and the inter-individual (not disease-related) heterogeneity poses challenges.[24] Analysis of proteases *via* activity profiling has attracted significant attention, but the complexity of samples still poses a problem. Certain proteolytic fragments, from high abundant serum proteins, are potential markers of tumour-specific proteolytic activity that can be analysed in blood/serum specimen, but they present a significant analytical challenge. This problem can be circumvented using exogenous synthetic substrates. Thus, ''spiking'' exogenous reporter peptides into biological samples for the characterization of protease activity offers substantial advantages over profiling of 'native' proteomic serum. These reporter peptides allow accumulation of signal to levels that are readily detectable with MS and eliminate the background signal provided by high-abundance 'native' proteins or peptides in the sample (Scheme 9).[24] When reporter peptides are added to the specimen, the proteolysis of these exogenous reporters produces a unique MS spectrum that will be different in the absence or presence of the protease (excess reporter peptides are necessary not only to ensure substrate saturation, but also to displace competing natural substrates from any tumour-associated proteases).[233]

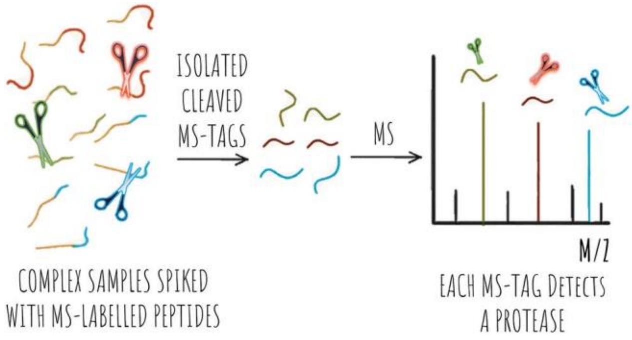

Scheme 9 MS proteolytic profiling, where protease peptide substrates are modified with MS tags (shown here in blue, red or green) and used as reporters. Complex samples can be spiked with these mixtures of reporters and the targeted proteases cleave the peptides releasing the MS tags. Each tag has a unique MS spectrum and each reports on the activity of a different protease.

The use of isotopic MS tags has greatly simplified analysis of complex samples with tagging of freshly generated peptide fragments prior to separation and analysis allowing quantitative MS/MS analysis of digested peptides. The first isotope-based MS tags for peptides incorporated stable heavy isotopes such as ^{13}C, ^{15}N,^{18}O and ^{2}H with initial tags consisting of a duplex system with ''heavy/light'' isotope tags,[234] allowing comparison of two different conditions (Table 2).

ICAT (Isotope-Coded Affinity Tags)[235] is an isotopic, duplex system of MS tags that contain a biotin moiety that allows isolation by affinity chromatography, allowing co-elution of isotopically labelled peptides for further analysis.[236] However, screening of larger number of variable conditions was not possible.[237] In 2002, isobaric tags were introduced, ITRAQ (Isobaric Tags for Relative and Absolute Quantitation)[238] and tandem mass tags (TMT)[239,240] as powerful tools for multiplexed MS proteomic analysis. These tags contain multiple isotopic variants that are chemically identical, and co-migrate in liquid chromatography separations but offer different MS signatures.

Optimisation of MS reporter peptides led to the design of a generation of reporters that used isobaric and non-isobaric isotope mass tagging for targeting proteases overexpressed in disease. The reporters generally contained a specific peptide-based substrate covalently linked to a MS tag. The tag-containing peptides co-eluted in chromatographic separations, while the combination of reporter peptides could be analysed by MS/MS. Findeisen developed a series of synthetic MS tagged reporter peptides[25,241,242] to help address a key challenge of protease profiling in complex biological samples, namely the risk of cleavage by non-specific peptidases, that are generally very abundant in complex samples. This was achieved by incorporating a flanking aminohexanoic acid groups in the peptide substrate that successfully reduced degradation by native exopeptidases.[242]

Ouyang developed non-isotopic labels to screen for caspase-3 cleavable peptides,[243] using MALDI-MS as the analytical method with peptides labelled by virtue of a terminal maleimide handle. This demonstrated sensitive detection of caspase-3 activity and offers a platform that would be applicable to other proteases.

Bhatia[244] developed a variety of synthetic biomarkers for disease-related proteases based on photocaged tandem isobaric peptides allowing up to 10-plexed protease analysis in a single run for possible disease stratification (Fig. 25). The probes/reporters consisted of nanocluster carriers, conjugated to cleavable peptide mass reporters for proteases overexpressed in a variety of diseases. The reporters contained substrate peptides with isobaric MS tags conjugated through a photolabile linker[245] with an additional peptide that enhances renal clearance. The nanocluster constructs were cleaved by disease related proteases and since the released fragments were connected to isobaric MS tags (*via* a photocleavable linker), this allowed comparative relative abundance quantification of all 10

Table 2 MS-based methods for protease profiling

Strategy	Reporter peptide	Type of tag	Tag	Systems/ conditions	Protease	Ref.
Unlabelled peptide	Exogenous peptide from bacteria	Non-isotopic	Tryptic digest of the N-terminal adenomatous polyposis coli protein	2	Non-specific	Findeisen 2008[233]
MS encoded peptide	Synthetic protease substrate with protease resistant label	Non-isotopic	AhxAhx-HHHHHH	2	Cysteine-endopeptidase cancer procoagulant	Peccerella 2010[241] Yepes 2011[242]
			Ahx-ateevlkl	2	Cysteine-endopeptidase cancer procoagulant	Yepes 2012[25]
			Dual maleimide (DuMal)	2	Caspase-3	Ouyuong 2019[243]
	Isobaric tagged peptides (iCore)	Isobaric	One letter code D-Amino acids lowercase Note: Charges in the structures below refer to isotope mass additions not formal charges $\mathrm{e^{+3}G^{+6}VndneeGFfsAr}$ $\mathrm{e^{+2}G^{+6}Vndnee^{+1}GFfsAr}$ $\mathrm{e^{+1}G^{+6}Vndnee^{+2}GFfsAr}$ $\mathrm{eG^{+6}Vndnee^{+2}GFfs^{+1}Ar}$ $\mathrm{eG^{+5}VndneeGFfs^{+4}Ar}$ $\mathrm{e^{+3}G^{+1}Vndnee^{+1}GFfs^{+4}Ar}$ $\mathrm{e^{+3}GVndneeG^{+6}FfsAr}$ $\mathrm{e^{+2}GVndneeG^{+6}Ffs^{+1}Ar}$ $\mathrm{e^{+1}GVndnee^{+2}G^{+6}FfsAr}$ $\mathrm{eGVndnee^{+3}G^{+6}FfsAr}$	10	Thrombin Tissue factor FXa Cathepsin B MMP2 MMP7 MMP8 MMP9 MMP14	Bathia 2020[244]

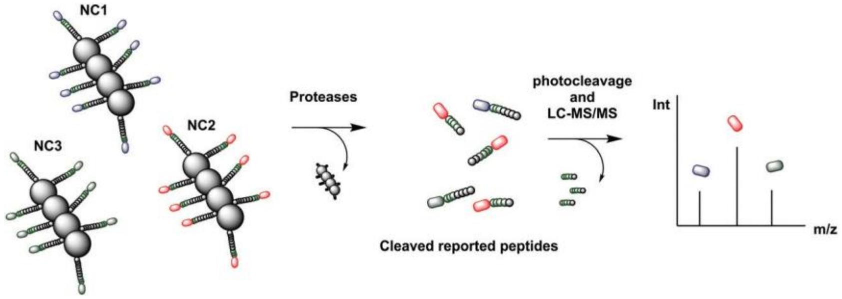

Fig. 25 Mass tagged nanocluster carriers, conjugated to cleavable peptide mass reporters for profiling of MMP protease activity overexpressed in a variety of diseases.[244] The nanoclusters (each containing a different peptide sequence) are delivered to the disease site where overexpressed proteases release the isobaric MS reporter tags that are filtered into the urine. The reporters in the urine are treated with light to release the MS isobaric tags that are analysed by MS/MS. NC: nanocluster

conditions/tags. One biomarker approach was developed for detection of fibrosis using so-called iron oxide nanoworms as carriers for the reporters,[245] with each nanoworm containing multiple copies of the same isobaric peptide, with 10 different isobaric nanoworm complexes co-administered. Cleavage of the constructs led to reporters in urine, and an indication of active protease present. Following the same approach, probes were developed for the detection the protease activity in prostate[246] and lung cancer.[244]

2.3 Electrochemical

Electrochemical probes are a class of chemical probes in which an electrode is used as a transducer element in the presence of an analyte that allows generation of an electrochemical signal change. Electrochemical biosensors have been used for the last 60 years[247] and were first reported was by Clark and Lyons[248] to allow measurement of glucose levels. Based on their mode of operation and the type of electrode, electrochemical biosensors can be classified as potentiometric, amperometric or impedimetric but all have in common the conversion of chemical information into a measurable electrochemical signal.

Electrochemical protease biosensors offer some advantages over those based on fluorescence as they can offer higher specificity and sensitivity even in turbid or intrinsically fluorescent solutions. Many of these are also compatible with miniaturisation and mass-manufacture for point-of-care devices (Fig. 27).[249] Comprehensive reviews covering this area include those by Vanova,[250] Ming[249] and Ong.[16] Typically, protease analysis probes are composed of a redox-tagged recognition peptide for the enzyme of interest, which is then attached to an electrode surface (Scheme 10). The flexibility of the peptide allows for the redox tag to come into contact with the electrode surface to elicit an electrochemical signal. Upon cleavage of the peptide by the enzyme of interest, the redox tag is released into the bulk solution and a quantifiable signal decrease can be used to determine enzyme activity. This was demonstrated by a probe (**83**) developed by Liu with ferrocene-labelled MMP-7-cleavable peptides immobilised onto a gold electrode.[251] In the absence of MMP-7, maximal voltammetric signal was achieved as the redox labels were close to the surface allowing redox cycling with the electrode surface. Observable decreases in the signal corresponded to various levels of MMP-7 in solution with a limit of detection of 0.1 ng mL^{-1}. *p*-Aminodiphenylamine (pADA) and methylene blue have been used as redox reporters in probes for thrombin (**84**)[252] and MMP-9 (**85**),[253] and similar approaches have been employed for a range of other proteases including the cathepsin family,[254] neutrophil elastase (**87**, Fig. 26)[255] and HIV-1 protease (**88**).[256]

Gold electrodes have been always the classical choice when designing electrochemical protease probes, however, in recent years, several novel electrode platforms have been used showing excellent performance on protease sensing. Indium Tin Oxide electrodes[257] and carbon based electrodes are examples of alternatives to gold electrodes used in the field. Embedded vertical carbon nanofiber electrodes, separated from each other forming a bush-like platform, were used for the detection of Cathepsin B (**86**).[258] These approaches reduce steric hindrance and improve temporal resolution. Novel Pt based microelectrodes for detection of trypsin were pioneered by Ucar,[259] whose results demonstrate similar specificity when compared to Au electrodes and enhanced reproducibility and stability. However, all these strategies rely on a 'signal-off' output, which may be undesirable.

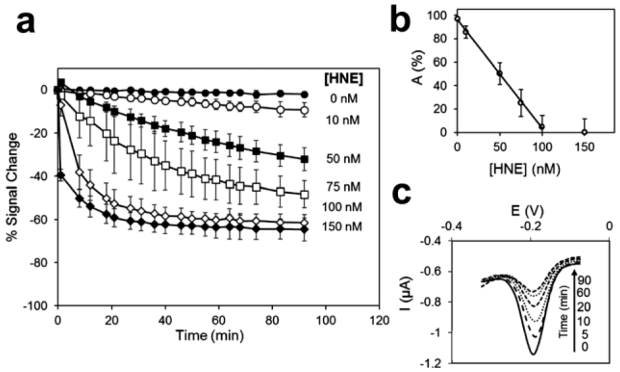

Fig. 26 Electrochemical detection of HNE (**87**).[255] (a) % signal change-time course for substrate-modified electrodes immersed in varying HNE concentrations (0, 10, 50, 75, 100 and 150 nM) in HEPES buffer. (b) Adjusted signal, A (%), after 90 min plotted against the concentration of HNE. (c) Electrical signal registered at different incubation times (0, 5, 10, 20, 60 and 90 min) for 100 nM HNE in HEPES buffer. Reproduced from ref. 255 with permission Elsevier, copyright 2018.

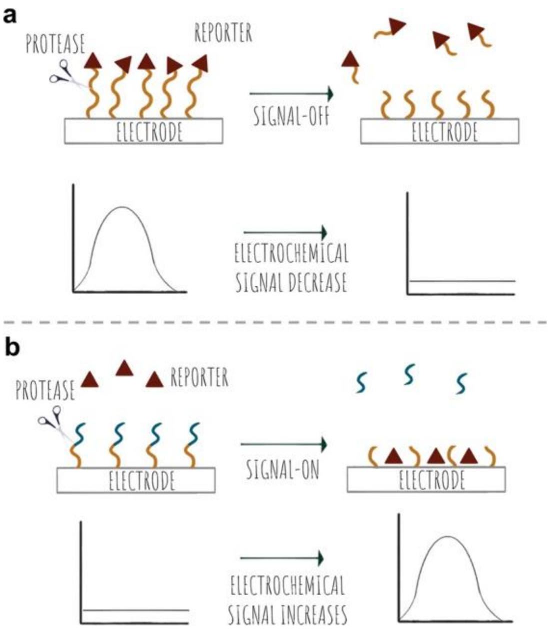

Scheme 10 Electrochemical sensing strategies for proteases. (a) Signal-off detection. Cleavage by the protease, releases the reporter from the electrode resulting in a decrease of signal. (b) Signal-on detection. Cleavage by the peptide demasks a high-affinity sequence that promotes electrochemical reporter binding, resulting in an increase in the electrochemical signal.

A label-free strategy can be employed to overcome these drawbacks, wherein a peptide sequence is used to preclude or promote the approach of a redox mediator to the electrode surface; either by steric or electrostatic repulsion. An advantage of this strategy is that peptide substrates can be used without the need of a label, allowing for more sensitive assays. Cao has demonstrated a general method using electrostatic repulsion in a system where a peptide with a cationic region is immobilised on the electrode. The peptide formed a layer that prevents the penetration of the cationic $[Ru(NH_3)_6]Cl_2]^+$ redox reporter due to electrostatic repulsion, and no electrical signal was transferred. Upon the cleavage of the peptide, the positively charged region was released and the reporter can approach the electrode surface to produce a ''signal-on'' (**89**).[260] However, this signal requires the addition of an electrochemical reporter to the assay. Deng designed a 'signal off' probe, using $[Fe(CN)_6]^{3-/4-}$ as a redox reporter and a peptide immobilised to a gold surface. A positively charged Lys in a peptide induced binding of the negatively charged redox reporter resulting in an electrical signal output. Upon the addition of the serine protease PSA, the Lys residue was cleaved and the reporter no longer binds the peptide, resulting in a decrease in the electrical signal.[261] However, high background-to-signal ratios limit the sensitivity of this method compared to redox labelled-peptide strategies.

Li,[262] using a gold electrode with immobilised peptides (*via* 11-mercaptoundecanoic acid) developed a system that contained a ''seed peptide'' that accelerates/catalyses amyloid b misfolding on the electrode surface. The incorporation of a cleavable sequence between the anchoring fragment and the seed sequence allowed protease mediated release of the seed motif (and prevention of amyloid formation) allowing the electrode surface to be available for interactions with the free redox reporter.

Another example that falls in between a redox-labelled and label-free design is the 'signal on' system designed by Ko,[263] based on the triggerable interaction of a redox reporter with the electrode. The system was used to report on the presence of thrombin using ferrocene as the redox reporter and a fibrinogen coated electrode. The electrode, coated with Fc-fibrinogen, was susceptible to thrombin mediated hydrolysis of the coating fibrinogen, that ''demasked'' the surface of the support.

Other strategies that depend on a complex formation or secondary triggered reactions have also been developed. Thus, proteolytic activity has been measured electrochemically by use of the cleaved peptide acting as a ligand for an electrocatalyst: for example, an electrocatalyic reaction can be triggered by caspase-3.[264] Cleavage of the substrate peptide (**90**) released a Cu(II)/Ni(II) peptide binding motif (Ser-Lys-His) that resulted in the *in situ* synthesis of the reporter, a copper electrocatalyst for water oxidation at the electrode surface. The use of water as a substrate negates the need for addition of other reagents and provides a straightforward and simple operating procedure with low background current for caspase-3, and a LoD of 0.2 pg mL^{-1}. This sensing platform was shown to be robust

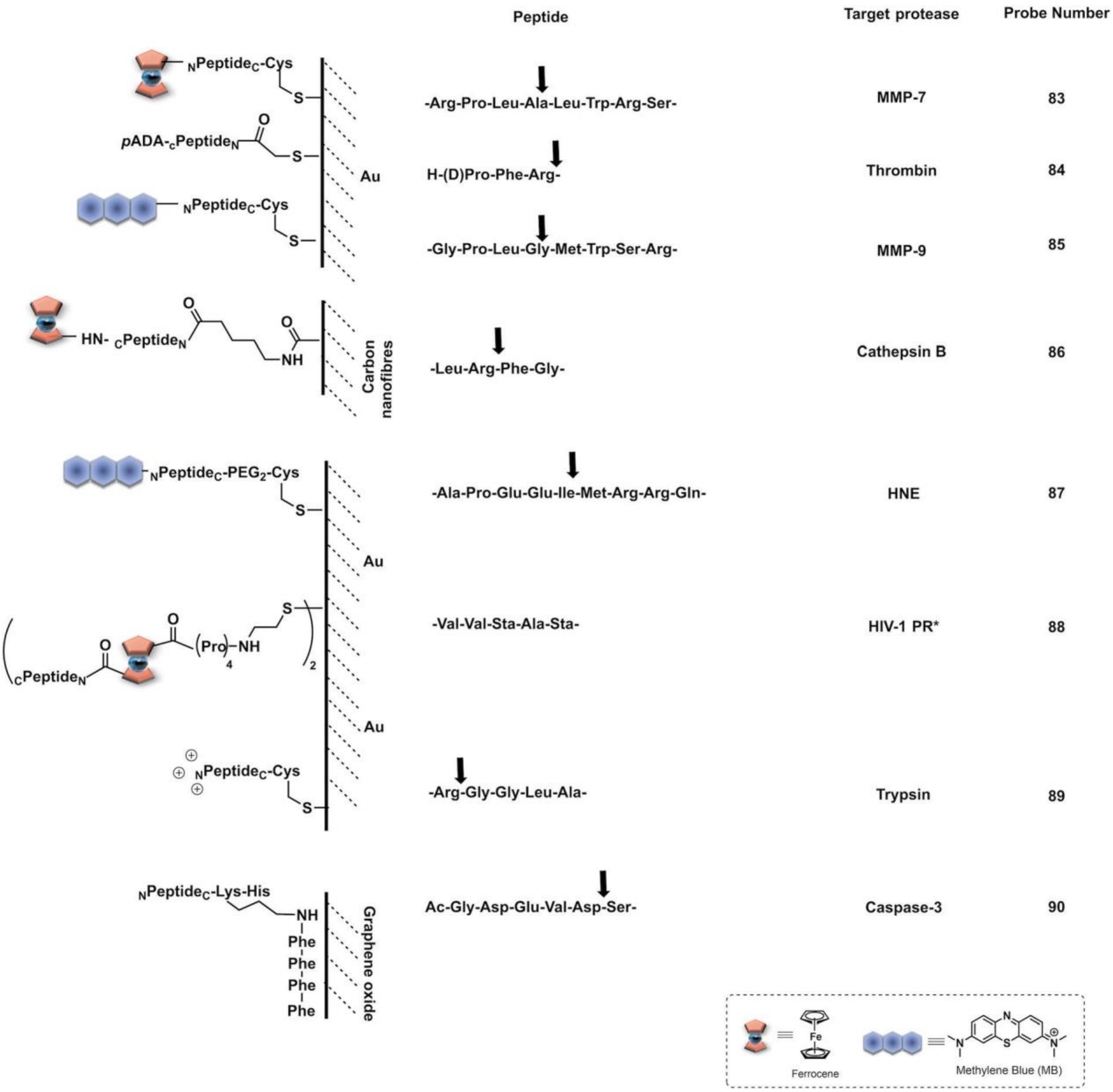

Fig. 27 Electrochemical probes for proteases where the signal deceases upon protease activation. Abbreviations: pADA: *p*-aminodiphenylamine; Sta: statin (4-amino-3-hydroxy-6-methylheptanoic acid); Bt: biotin; arrows indicate cleavage site. While peptide sequences are always written N — C terminal by convention (NPeptideC), we have utilised some C - N (cPeptideN) to allow ease of presentation. *Binding based assay. Abbreviations: pADA: *p*-aminodiphenylamine; Sta: statin (4-amino-3-hydroxy-6-methylheptanoic acid); Bt: biotin; arrows indicate cleavage sites.

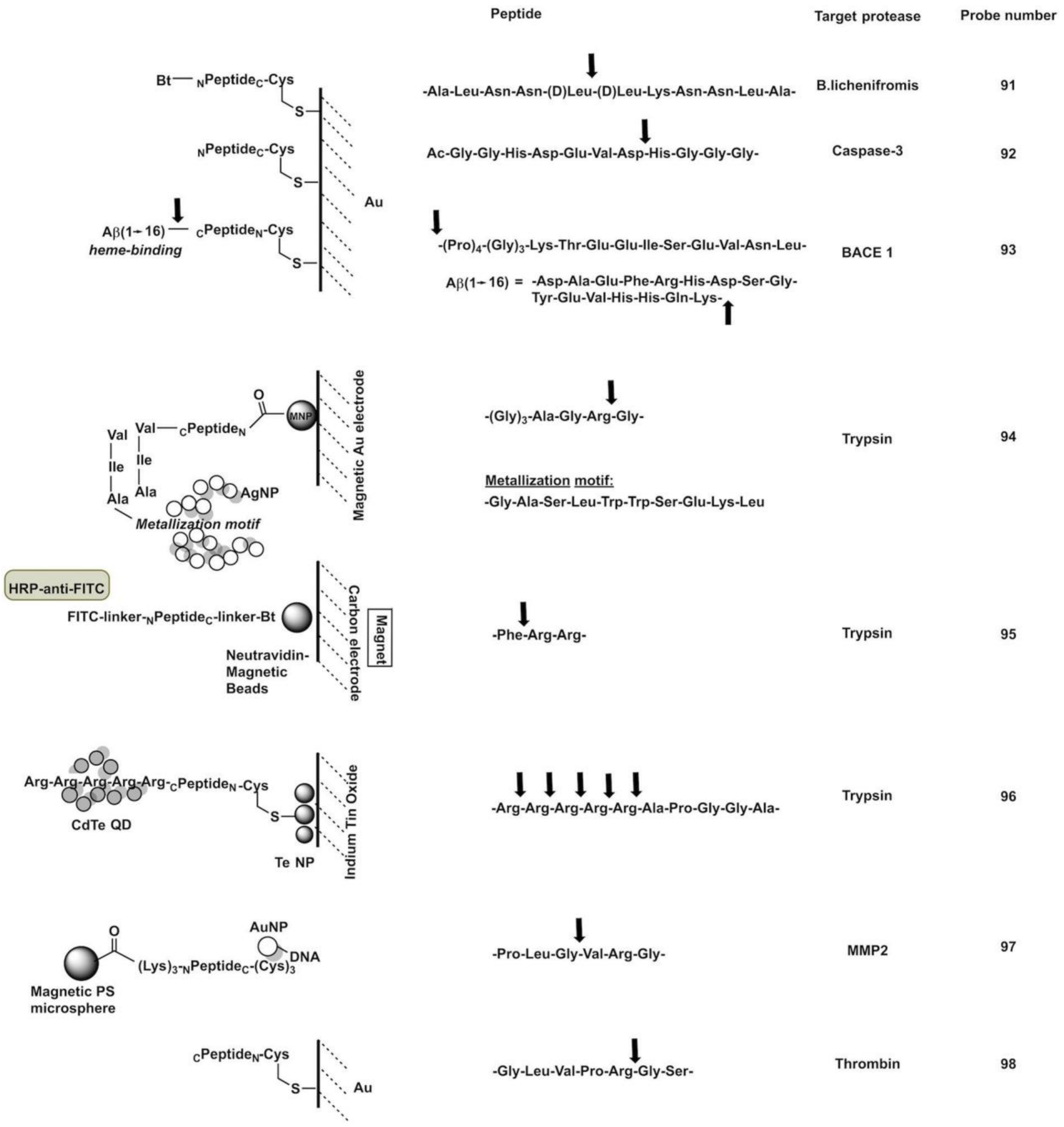

Fig. 27 (*cont.*)

in complex media, such as cell lysate. Following a similar principle, Wu[265] developed a two-enzyme system (**91**) where the catalyst in this case was alkaline phosphatase (ALP) and the activating protease *B lichenifromis*. ALP catalyses the formation of electrochemically active phenol. The system incorporated streptavidin-alkaline phosphatase (Sav-ALP) on the electrodes through a biotin-labelled peptide substrate. In absence of the protease, streptavidin-alkaline phosphatase catalyses the formation of a redox reporter, while in its presence the biotin moiety was removed from the electrodes reducing the electrochemical signal.

Chen[266] reported a system with a LoD for caspase-3 of 0.06 pg mL^{-1} (~3 fM). The system used the triggerable binding of methylene blue to the electrode by immobilisation of a peptide substrate. Thus, an acetylated caspase-3 peptide substrate was anchored into an electrode *via* a C-terminal Cys residue (**94**). Cleavage exposed a free terminal amine group on the remaining anchored fragment, which was able to covalently bind graphene oxide. Electroactive methylene blue then bound through p–p stacking and resulted in an increase of electrochemical signal. Meng[267] used graphene oxide for the *in situ* generation of silver nanoparticles on a peptide functionalised gold electrode. In the absence of PSA, the graphene oxide was immobilised on the peptide and silver nanoparticles were generated *in situ*, resulting in an electrochemical signal.

Xia used an immobilised peptide–heme catalyst complex[268] to increase electrochemical signals in response to the b-amyloid precursor protein enzyme 1 (BACE1). The construct (**93**) consisted of a heme-binding segment (Ab1 — 16), the heme being capable of the electrocatalytic reduction of O_2. This sequence was bound to the BACE1 substrate whose cleavage by BACE1 released the heme binding region of the peptide, such that reduction of O_2 was no longer possible.

Attempts have been made to incorporate amplification within these systems to further increase their sensitivity. Magnetic beads or nanoparticles[269] functionalised with peptide-reporter systems (**94**), have been used to assay activity in complex media (*e.g.* blood or urine) and can then be extracted and deposited onto magnetic electrodes, to allow analysis in less complex media (*e.g.* aqueous buffers). Neutravidin coated magnetic beads **(95)** were used for detection of trypsin[270] with enhanced sensitivity and robustness in cell lysate and clinical samples (probe consisting of neutravidin magnetic nanoparticles functionalised with substrate peptides *via* a biotin moiety, labelled with a FITC antigen tag detectable by a labelled antibody). In the absence of trypsin, the peptide probe was intact and a high number of redox tags providing a large amperometric response (using the hydroquinone (HQ)/HRP/H_2O_2 system). While the presence of trypsin decreased the amperometric signals. Fluorescence from cadmium telluride quantum dots (CdTe-QDs) was converted into measurable photocurrent by Liu,[271] using electrodes functionalised with a peptide that contained a positively charged region to attract the QDs (**96**). Upon trypsin cleavage, the QDs were released from the surface and the signal decreased.

A related strategy was designed by Yuan to translate the peptide cleavage event to a nucleic acid-based detection platform.[272] Peptide-functionalised magnetic polystyrene microspheres were coupled to DNA–AuNPs (**97**). The proteolytic action of the enzyme of interest (MMP-2) decouples the DNA–AuNPs from the peptide-microspheres with the DNA released by proteolytic activity hybridising to a redox-labelled complementary strand of DNA. Next, an exonuclease III assisted cycling signal amplification step was applied, whereby the duplex DNA was selectively digested to release the redox label (methylene blue), as well as the DNA-AuNP. The electrode surface, functionalised with a macrocyclic cavity (cucurbituril) binds the redox label and provides an electrical signal. The release of the DNA–AuNPs allows for another hybridisation event to occur with cyclical amplification system allowing a single DNA-AuNP to allow multiple redox labels to approach the electrode surface. The host–guest interactions at the electrode surface provided a LoD of 0.15 pg mL^{-1}. This 'signal-on' sensing platform allows for robust analysis, with multiple steps preventing false positive results and could be applied to a range of proteases in human serum.

Another method for amplification has been developed by Hu[273] that combined the use of substrate peptides as a recognition element and RAFT polymerization for signal amplification. Thrombin substrate peptides were immobilised onto a gold electrode *via* an N-terminal cysteine residue (98). Following cleavage by thrombin, the electrode was immersed into a solution containing a Zr(IV) source and a carboxylate-containing RAFT initiator. Only at the site of the cleaved peptide (free carboxylic acid), did the Zr complex form a bridge between the carboxylate of the RAFT initiator and the peptide. The addition of acrylate-ferrocene allowed polymerisation and recruitment of multiple redox reporters at the site of cleavage, allowing for very sensitive detection.

3 Summary and perspectives

In this review, we have discussed the recent advances, and highlighted the most relevant and novel substrate-based reporters and strategies, for the detection of proteolytic activity.

The design of substrate-based reporters for the detection of proteolytic activity needs to overcome a number of challenges, namely the level of sensitivity can be a challenge when trying to target relevant proteases where expression levels can be low; while specificity is another key issue. This means that the generation of highly specific probes to target a single protease within a relatively broad family (*e.g.* caspases or MMPs), becomes a difficult task due to overlap in substrate recognition, while by-stander cleavage by generic/non-specific proteases is a common problem. Most of the reporters described in this review, target model proteases that are well understood and have been extensively used in a variety of applications, but the targeting of novel, low abundance, protease biomarkers remains a challenge.

A key challenge in the area of optical probes remains their *in vivo* application, due to poor tissue penetration of light enabled by current imaging technologies and high background signals from complex biological environments. However, several reporters for proteolytic activity have entered clinical studies *e.g.* for margin detection during surgery, in the last decade. New strategies are driving improvements in tissue penetration and background signal reduction with the shifting of the emission of fluorescent probes into the near-infrared region and beyond.

Photoacoustic imaging allows for enhanced tissue penetration and can be used in combination with fluorescence, reaping the benefits of both worlds. Chemiluminogens show great promise as alternatives to fluorescence, with virtually no background signal, with efforts focused on improvement of probe stability and shifting of emission wavelength by tuning natural substrates. Quantitative analysis is not easily achieved with optical substrate-based probes and only a few examples exist that allows quantitative analysis in association with signal amplification. Activity-based probes, that covalently bind to the protease following activation, can overcome this problem, however, they render the protease inactive and provide no signal amplification. There has been much work in the area of theragnostics, with multimodal probes combining optical imaging-based diagnosis and therapeutic intent, using photodynamic, photothermal strategies and activatable prodrugs.

On the *in vitro*-based application side, the novel applications of colorimetric sensing and electrochemical sensors offer great promise as low-cost and highly sensitive chemistries for point-of-care testing, but the immobilisation of the substrate probe can still present challenges. Electrochemical probes offer great promise as a point-of-care technology with the possibility of miniaturisation with relatively simple designs, however most rely on a signal-off response. MS based protease detection is a powerful tool for protease activity profiling, but a key challenge is the complexity of biological samples, that can affect the sensitivity/specificity of the assay and the resulting read-out.

The field of protease-based chemical probes is rapidly evolving to allow further detailed analysis of proteolytic events. In this review, we have described a few from the many examples of each type of probe applied in a variety of situations. The breadth of technologies developed enable access to protease detection in almost any situation, be it *in vivo* real-time fluorescent imaging by applying the concept of aggregation-induced emission or low-cost easily applied, colorimetric platforms for use in resource-limited settings. The future of protease chemical probes will continue to be bright, diverse and innovative.

Conflicts of interest

There are no conflicts to declare.

Acknowledgements

We would like to thank the Engineering and Physical Sciences. Research Council (EPSRC, UK) for Interdisciplinary Research Collaboration grant EP/R005257/1.

Notes and references

1 R. Visse and H. Nagase, *Circ. Res.*, 2003, 92, 827–839.
2 S. Gottesman and M. R. Maurizi, *Microbiol. Rev.*, 1992, 56, 592–621.
3 N. A. Thornberry and Y. Lazebnik, *Science*, 1998, 281, 1312–1316.
4 J. E. Koblinskia, M. Ahrama and B. F. Sloane, *Clin. Chim. Acta*, 2000, 291, 113–135.
5 P. V. Ravindra and T. K. Girish, in *Proteases in Physiology and Pathology*, ed. S. Chakraborti and N. S. Dhalla, Springer Singapore, Singapore, 2017, DOI: 10.1007/978-981-10-2513-6-13, pp. 289–296.
6 C. E. Reed and H. Kita, *J. Allergy Clin. Immunol.*, 2004, 114, 997–1008.
7 M. A. Slack and S. M. Gordon, *Arterioscler., Thromb., Vasc. Biol.*, 2019, 39, e210–e218.
8 D. J. Selkoe and J. Hardy, *EMBO Mol. Med.*, 2016, 8, 595–608.
9 M. S. Wolfe, M. Citron, T. S. Diehl, W. Xia, I. O. Donkor and D. J. Selkoe, *J. Med. Chem.*, 1998, 41, 6–9.
10 Z. Lv, Y. Chu and Y. Wang, *HIV AIDS*, 2015, 7, 95–104.
11 C. G. Smith and J. R. Vane, *FASEB J.*, 2003, 788–789.
12 M. Staderini, A. Megia-Fernandez, K. Dhaliwal and M. Bradley, *Bioorg. Med. Chem.*, 2018, 26, 2816–2826.
13 L. E. Edgington, M. Verdoes and M. Bogyo, *Chem. Biol.*, 2011, 15, 798–805.
14 J. Zhang, X. Chai, X. P. He, H. J. Kim, J. Yoon and H. Tian, *Chem. Soc. Rev.*, 2019, 48, 683–722.
15 J. Chin and H. J. Kim, *Coord. Chem. Rev.*, 2018, 354, 169–181.
16 I. L. H. Ong and K. L. Yang, *Analyst*, 2017, 142, 1867–1881.
17 R. Oliveira-Silva, M. Sousa-Jeronimo, D. Botequim, N. J. O. Silva, P. M. R. Paulo and D. M. F. Prazeres, *Trends Biochem. Sci.*, 2020, 45, 604–618.
18 T. Fo¨rster, *Ann. Phys.*, 1948, 437, 55–75.
19 B. Wallace and P. J. Atzberger, *PLoS One*, 2017, 12, e0177122.
20 T. W. Liu, J. Chen and G. Zheng, *Amino Acids*, 2011, 41, 1123–1134.
21 J. J. Diaz-Mochon, L. Bialy, L. Keinicke and M. Bradley, *Chem. Commun.*, 2005, 1384–1386, DOI: 10.1039/b415847d.
22 P. M. S. Hilaire, M. Willert, M. A. Juliano, L. Juliano and M. Meldal, *J. Comb. Chem.*, 1999, 1, 509–523.
23 C. Pinilla, J. Appel, S. Blondelle, C. Dooley, B. Dorner, J. Eichler, J. Ostresh and R. A. Houghte, *Biopolymers*, 1995, 37, 221–240.
24 P. Findeisen and M. Neumaier, *Proteomics Clin. Appl.*, 2012, 6, 60–78.
25 D. Yepes, A. Jacob, M. Dauber, V. Costina, R. Hofheinz, M. Neumaier and P. Findeisen, *Int. J. Oncol.*, 2011, 39, 145–154.
26 D. J. M. a. J. A. Wells, *Sci. Transl. Med.*, 1993, 260, 1113–1117.
27 M. Tholen, J. J. Yim, K. Groborz, E. Yoo, B. A. Martin, N. S. van den Berg, M. Drag and M. Bogyo, *Angew. Chem., Int. Ed.*, 2020, 59, 19143–19152.
28 M. Wartenberg, A. Saidi, M. Galibert, A. Joulin-Giet, J. Burlaud-Gaillard, F. Lecaille, C. J. Scott, V. Aucagne, A. F. Delmas and G. Lalmanach, *Biochimie*, 2019, 166, 84–93.
29 P. Kasperkiewicz, M. Poreba, S. J. Snipas, S. J. Lin, D. Kirchhofer, G. S. Salvesen and M. Drag, *PLoS One*, 2015, 10, e0132818.
30 A. Megia-Fernandez, B. Mills, C. Michels, S. V. Chankeshwara, K. Dhaliwal and M. Bradley, *Org. Biomol. Chem.*, 2017, 15, 4344–4350.
31 S. Mathur, A. Turnbull, I. Akaev, C. Stevens, N. Agrawal, M. Chopra and D. Mincher, *Int. J. Pept. Res. Ther.*, 2019, 26, 1965–1980.
32 H. A. Alhadrami, A. M. Hassan, R. Chinnappan, H. Al-Hadrami, W. H. Abdulaal, E. I. Azhar and M. Zourob, *Mikrochim. Acta*, 2021, 188, 137.
33 T. Janiszewski, S. Kołt, D. Kaiserman, S. J. Snipas, S. Li, J. Kulbacka, J. Saczko, N. Bovenschen, G. Salvesen,

M. Dr ag, P. I. Bird and P. Kasperkiewicz, *J. Biol. Chem.*, 2020, 295, 9567–9582.

34 J. J. Yim, S. Harmsen, K. Flisikowski, T. Flisikowska, H. Namkoong, M. Garland, N. S. van den Berg, J. G. Vilches-Moure, A. Schnieke, D. Saur, S. Glasl, D. Gorpas, A. Habtezion, V. Ntziachristos, C. H. Contag, S. S. Gambhir, M. Bogyo and S. Rogalla, *Proc. Natl. Acad. Sci. U. S. A.*, 2021, 118, e2008072118.

35 J. I. Scott, Q. Deng and M. Vendrell, *ACS Chem. Biol.*, 2021, 16, 1304–1317.

36 T. Jiang, E. S. Olson, Q. T. Nguyen, M. Roy, P. A. Jennings and R. Y. Tsien, *Proc. Natl. Acad. Sci. U. S. A.*, 2004, 101, 17867–17872.

37 Y. Cheng, L. Zhao, Y. Li and T. Xu, *Chem. Soc. Rev.*, 2011, 40, 2673–2703.

38 L. O. Ofori, N. P. Withana, T. R. Prestwood, M. Verdoes, J. J. Brady, M. M. Winslow, J. Sorger and M. Bogyo, *ACS Chem. Biol.*, 2015, 10, 1977–1988.

39 E. Walker, Y. Liu, I. Kim, M. Biro, S. R. Iyer, H. Ezaldein, J. Scott, M. Merati, R. Mistur, B. Zhou, B. Straight, J. J. Yim, M. Bogyo, M. Mann, D. L. Wilson, J. P. Basilion and D. L. Popkin, *Cancer Res.*, 2020, 80, 2045–2055.

40 M. J. Whitley, D. M. Cardona, A. L. Lazarides, I. Spasojevic, J. M. Ferrer, J. Cahill, C.-L. Lee, M. Snuderl, D. G. Blazer, E. S. Hwang, R. A. Greenup, P. J. Mosca, J. K. Mito, K. C. Cuneo, N. A. Larrier, E. K. O'Reilly, R. F. Riedel, W. C. Eward, D. B. Strasfeld, D. Fukumura, R. K. Jain, W. D. Lee, L. G. Griffith, M. G. Bawendi, D. G. Kirsch and B. E. Brigman, *Sci. Trans. Med.*, 2016, 8, 320ra324.

41 B. L. Smith, C. R. Lanahan, M. C. Specht, B. N. Kelly, C. Brown, D. B. Strasfeld, J. M. Ferrer, U. Rai, R. Tang, T. Rice-Stitt, A. Biernacka, E. F. Brachtel and M. A. Gadd, *Ann. Surg. Oncol.*, 2020, 27, 1854–1861.

42 B. L. Smith, M. A. Gadd, C. R. Lanahan, U. Rai, R. Tang, T. Rice-Stitt, A. L. Merrill, D. B. Strasfeld, J. M. Ferrer, E. F. Brachtel and M. C. Specht, *Breast Cancer Res. Treat.*, 2018, 171, 413–420.

43 C. R. Lanahan, B. N. Kelly, M. A. Gadd, M. C. Specht, C. L. Brown, K. S. Hughes, R. Tang, U. Rai, E. F. Brachtel, T. Rice-Stitt and B. L. Smith, *Breast Cancer Res. Treat.*, 2021, 187, 145–153.

44 R. Weissleder, C.-H. Tung, U. Mahmood and A. B. Jr, *Nat. Biotechnol.*, 1999, 17, 375–378.

45 A. Megia-Fernandez, A. Marshall, A. R. Akram, B. Mills, S. V. Chankeshwara, E. Scholefield, A. Miele, B. C. McGorum, C. Michaels, N. Knighton, T. Vercauteren, F. Lacombe, V. Dentan, A. M. Bruce, J. Mair, R. Hitchcock, N. Hirani, C. Haslett, M. Bradley and K. Dhaliwal, *BME Front.*, 2021, 2021, 1–11.

46 B. Mills, D. Norberg, K. Dhaliwal, A. R. Akram, M. Bradley and A. Megia-Fernandez, *Chem. Commun.*, 2020, 56, 9962–9965.

47 M. Zhou, J. Hu, M. Zheng, Q. Song, J. Li and Y. Zhang, *Chem. Commun.*, 2016, 52, 2342–2345.

48 H. Yan, L. He, W. Zhao, J. Li, Y. Xiao, R. Yang and W. Tan, *Anal. Chem.*, 2014, 86, 11440–11450.

49 T. H. Craven, N. Avlonitis, N. McDonald, T. Walton, E. Scholefield, A. R. Akram, T. S. Walsh, C. Haslett, M. Bradley and K. Dhaliwal, *Sci. Rep.*, 2018, 8, 13490.

50 N. Avlonitis, M. Debunne, T. Aslam, N. McDonald, C. Haslett, K. Dhaliwal and M. Bradley, *Org. Biomol. Chem.*, 2013, 11, 4414–4418.

51 S. Lebreton, S. E. How, M. Buchholz, B. E. Yingyongnarongkul and M. Bradley, *Tetrahedron*, 2003, 59, 3945–3953.

52 Y. Zhang, M. Ucuncu, A. Gambardella, A. Baibek, J. Geng, S. Zhang, J. Clavadetscher, I. Litzen, M. Bradley and A. Lilienkampf, *J. Am. Chem. Soc.*, 2020, 142(52), 21615–21621.

53 A. K. Galande, S. A. Hilderbrand, R. Weissleder and C.-H. Tung, *J. Med. Chem.*, 2006, 49, 4715–4720.

54 J. M. Ellard, T. Zollitsch, W. J. Cummins, A. L. Hamilton and M. Bradley, *Angew. Chem., Int. Ed.*, 2002, 41, 3233–3236.

55 V. Brinkmann, C. Goosmann, B. Fauler, Y. Uhelmann, D. S. Weiss, Y. Weinrauch and A. Zichlinsky, *Science*, 2004, 303, 1532–1535.

56 M. R. Rios, G. Garoffolo, G. Rinaldi, A. Megia-Fernandez, S. Ferrari, C. T. Robb, A. G. Rossi, M. Pesce and M. Bradley, *Chem. Commun.*, 2020, 57, 97–100.

57 K. Nagai, T. Sato and C. Kojima, *Bioorg. Med. Chem. Lett.*, 2021, 33, 127726.

58 B. Brennecke, Q. Wang, W. Haap, U. Grether, H. Y. Hu and M. Nazare, *Bioconjugate Chem.*, 2021, 32, 702–712.

59 Q. D. Mac, D. V. Mathews, J. A. Kahla, C. M. Stoffers, O. M. Delmas, B. A. Holt, A. B. Adams and G. A. Kwong, *Nat. Biomed. Eng.*, 2019, 3, 281–291.

60 E. J. Kwon, J. S. Dudani and S. N. Bhatia, *Nat. Biomed. Eng.*, 2017, 1, 1–10.

61 S. Y. Li, L. H. Liu, H. Cheng, B. Li, W. X. Qiu and X. Z. Zhang, *Chem. Commun.*, 2015, 51, 14520–14523.

62 J. Xu, L. Fang, M. Shi, Y. Huang, L. Yao, S. Zhao, L. Zhang and H. Liang, *Chem. Commun.*, 2019, 55, 1651–1654.

63 F. Li, Y. Chen, R. Lin, C. Miao, J. Ye, Q. Cai, Z. Huang, Y. Zheng, X. Lin, Z. Zheng and S. Weng, *Anal. Chim. Acta*, 2021, 1148, 338201.

64 A. Megia-Fernandez, B. Mills, C. Michels, S. V. Chankeshwara, N. Krstajic, C. Haslett, K. Dhaliwal and M. Bradley, *Org. Biomol. Chem.*, 2018, 16, 8056–8063.

65 J. C. Widen, M. Tholen, J. J. Yim, A. Antaris, K. M. Casey, S. Rogalla, A. Klaassen, J. Sorger and M. Bogyo, *Nat. Biomed. Eng.*, 2021, 5, 264–277.

66 S.-Y. Li, L.-H. Liu, L. Rong, W.-X. Qiu, H.-Z. Jia, B. Li, F. Li and X.-Z. Zhang, *Adv. Funct. Mater.*, 2015, 25, 7317–7326.

67 F. Liu, M. Yang, W. Song, X. Luo, R. Tang, Z. Duan, W. Kang, S. Xie, Q. Liu, C. Lei, Y. Huang, Z. Nie and S. Yao, *Chem. Sci.*, 2020, 11, 2993–2998.

68 R. R. Jetson and C. J. Krusemark, *Angew. Chem., Int. Ed.*, 2016, 55, 9562–9566.

69 R. Lee, S.-J. Choi, K. C. Moon, J. W. Park, K. Kim, S.-Y. Yoon and I. Youn, *ACS Biomater. Sci. Eng.*, 2019, 5, 3039–3048.

70 S. Gehrig, M. A. Mall and C. Schultz, *Angew. Chem., Int. Ed.*, 2012, 51, 6258–6261.

71 M. Guerra, V. S. Halls, J. Schatterny, M. Hagner, M. A. Mall and C. Schultz, *J. Am. Chem. Soc.*, 2020, 142, 20299–20305.

72 M. Whitney, E. N. Savariar, B. Friedman, R. A. Levin, J. L. Crisp, H. L. Glasgow, R. Lefkowitz, S. R. Adams, P. Steinbach, N. Nashi, Q. T. Nguyen and R. Y. Tsien, *Angew. Chem., Int. Ed.*, 2013, 52, 325–330.

73 M. Miampamba, J. Liu, A. Harootunian, A. J. Gale, S. Baird, S. L. Chen, Q. T. Nguyen, R. Y. Tsien and J. E. Gonzalez, *Theranostics*, 2017, 7, 3369–3386.

74 L. Ge, Z. Liu and Y. Tian, *Chem. Sci.*, 2020, 11, 2215–2224.

75 H. Lee, S. J. Kim, H. Shin and Y. P. Kim, *ACS Sens.*, 2020, 5, 655–664.

76 C. Schulenburg, G. Faccio, D. Jankowska, K. Maniura-Weber and M. Richter, *Analyst*, 2016, 141, 1645–1648.

77 Y. Okorochenkova, M. Porubsky, S. Benicka and J. Hlavac, *Chem. Commun.*, 2018, 54, 7589–7592.

78 L. Chen, W. Sun, W. Li, J. Li, L. Du, W. Xu, H. Fang and M. Li, *Anal. Methods*, 2012, 4, 2661–2663.

79 L. W. Zou, P. Wang, X. K. Qian, L. Feng, Y. Yu, D. D. Wang, Q. Jin, J. Hou, Z. H. Liu, G. B. Ge and L. Yang, *Biosens. Bioelectron.*, 2017, 90, 283–289.

80 X. He, Y. Xu, W. Shi and H. Ma, *Anal. Chem.*, 2017, 89, 3217–3221.

81 Z. Yang, W. Xu, J. Wang, L. Liu, Y. Chu, Y. Wang, Y. Hu, T. Yi and J. Hua, *J. Mater. Chem. C*, 2020, 8, 8183–8190.

82 X. Huang, J. Song, B. C. Yung, X. Huang, Y. Xiong and X. Chen, *Chem. Soc. Rev.*, 2018, 47, 2873–2920.

83 K. Du, L. Sheng, X. Luo, G. Fan, D. Shen, C. Wu and R. Shen, *Spectrochim. Acta, Part A*, 2021, 249, 119328.

84 T. Cao, Z. Teng, L. Zheng, J. Qian, H. Ma, J. Wang, W. Qin and H. Guo, *Anal. Chim. Acta*, 2020, 1127, 295–302.

85 T. Ma, Y. Hou, J. Zeng, C. Liu, P. Zhang, L. Jing, D. Shangguan and M. Gao, *J. Am. Chem. Soc.*, 2018, 140, 211–218.

86 Y. Hou, J. Zhou, Z. Gao, X. Sun, C. Liu, D. Shangguan, W. Yang and M. Gao, *ACS Nano*, 2015, 9, 3199–3205.

87 S. Y. Liu, A. M. Yan, W. Y. Guo, Y. Y. Fang, Q. J. Dong, R. R. Li, S. N. Ni, Y. Sun, W. C. Yang and G. F. Yang, *ACS Nano*, 2020, 14, 4244–4254.

88 M. Wu and W. R. Algar, *Anal. Chem.*, 2015, 87, 8078–8083.

89 W. R. Algar, A. Khachatrian, J. S. Melinger, A. L. Huston, M. H. Stewart, K. Susumu, J. B. Blanco-Canosa, E. Oh, P. E. Dawson and I. L. Medintz, *J. Am. Chem. Soc.*, 2017, 139, 363–372.

90 H. Bui, C. W. Brown, 3rd, S. Buckhout-White, S. A. Diaz, M. H. Stewart, K. Susumu, E. Oh, M. G. Ancona, E. R. Goldman and I. L. Medintz, *Small*, 2019, 15, 1805384.

91 J. Breidenbach, U. Bartz and M. Gutschow, *Biochim. Biophys. Acta, Proteins Proteomics*, 2020, 1868, 140445.

92 M. Zimmerman, B. Ashe, E. C. Yurewicz and G. Patel, *Anal. Biochem.*, 1977, 78, 47–51.

93 H. Chen, X. He, M. Su, W. Zhai, H. Zhang and C. Li, *J. Am. Chem. Soc.*, 2017, 139, 10157–10163.

94 S. He, J. Li, Y. Lyu, J. Huang and K. Pu, *J. Am. Chem. Soc.*, 2020, 142, 7075–7082.

95 Q. Gong, W. Shi, L. Li, X. Wu and H. Ma, *Anal. Chem.*, 2016, 88, 8309–8314.

96 X. Guo, S. Mu, J. Li, Y. Zhang, X. Liu, H. Zhang and H. Gao, *J. Mater. Chem. B*, 2020, 8, 767–775.

97 A. Ogasawara, M. Kamiya, K. Sakamoto, Y. Kuriki, K. Fujita, T. Komatsu, T. Ueno, K. Hanaoka, H. Onoyama, H. Abe, Y. Tsuji, M. Fujishiro, K. Koike, M. Fukayama, Y. Seto and Y. Urano, *Bioconjugate Chem.*, 2019, 30, 1055–1060.

98 Q. Gong, L. Li, X. Wu and H. Ma, *Chem. Sci.*, 2016, 7, 4694–4697.

99 X. He, L. Li, Y. Fang, W. Shi, X. Li and H. Ma, *Chem. Sci.*, 2017, 8, 3479–3483.

100 X. He, Y. Hu, W. Shi, X. Li and H. Ma, *Chem. Commun.*, 2017, 53, 9438–9441.

101 E. E. Mulvihill and D. J. Drucker, *Endocr. Rev.*, 2014, 35, 992–1019.

102 A. P. Femia, L. Raimondi, G. Maglieri, M. Lodovici, E. Mannucci and G. Caderni, *Int. J. Cancer*, 2013, 133, 2498–2503.

103 A. Beckenkamp, J. B. Willig, D. B. Santana, J. Nascimento, J. D. Paccez, L. F. Zerbini, A. N. Bruno, D. A. Pilger, M. R. Wink and A. Buffon, *PLoS One*, 2015, 10, 1–17.

104 T. Liu, J. Ning, B. Wang, B. Dong, S. Li, X. Tian, Z. Yu, Y. Peng, C. Wang, X. Zhao, X. Huo, C. Sun, J. Cui, L. Feng and X. Ma, *Anal. Chem.*, 2018, 90, 3965–3973.

105 H. Onoyama, M. Kamiya, Y. Kuriki, T. Komatsu, H. Abe, Y. Tsuji, K. Yagi, Y. Yamagata, S. Aikou, M. Nishida, K. Mori, H. Yamashita, M. Fujishiro, S. Nomura, N. Shimizu, M. Fukayama, K. Koike, Y. Urano and Y. Seto, *Sci. Rep.*, 2016, 6, 26399.

106 T. Mizushima, S. Ohnishi, Y. Shimizu, Y. Hatanaka, K. C. Hatanaka, Y. Kuriki, M. Kamiya, A. Homma, K. Yamamoto, S. Ono, Y. Urano and N. Sakamoto, *Head Neck*, 2018, 40, 1466–1475.

107 K. Yamamoto, S. Ohnishi, T. Mizushima, J. Kodaira, M. Ono, Y. Hatanaka, K. C. Hatanaka, Y. Kuriki, M. Kamiya, N. Ehira, K. Shinada, H. Takahashi, Y. Shimizu, Y. Urano and N. Sakamoto, *BMC Cancer*, 2020, 20, 64.

108 Q. Gong, W. Shi, L. Li and H. Ma, *Chem. Sci.*, 2016, 7, 788–792.

109 W. Zhang, F. Liu, C. Zhang, J. G. Luo, J. Luo, W. Yu and L. Kong, *Anal. Chem.*, 2017, 89, 12319–12326.

110 M. Sakabe, D. Asanuma, M. Kamiya, R. J. Iwatate, K. Hanaoka, T. Terai, T. Nagano and Y. Urano, *J. Am. Chem. Soc.*, 2013, 135, 409–414.

111 K. Yamamoto, M. Kamiya and Y. Urano, *Bioorg. Med. Chem. Lett.*, 2019, 29, 126663.

112 S. Y. Liu, H. Xiong, R. R. Li, W. C. Yang and G. F. Yang, *Anal. Chem.*, 2019, 91, 3877–3884.

113 Q. Sun, J. Li, W. N. Liu, Q. J. Dong, W. C. Yang and G. F. Yang, *Anal. Chem.*, 2013, 85, 11304–11311.

114 S. Wang, B. G. Vigliarolo, M. A. Chowdhury, J. N. K. Nyarko, D. D. Mousseau and C. P. Phenix, *Bioorg. Chem.*, 2019, 92, 103194.

115 Y. Wang, J. Li, L. Feng, J. Yu, Y. Zhang, D. Ye and H. Y. Chen, *Anal. Chem.*, 2016, 88, 12403–12410.

116 Y. Urano, M. Sakabe, N. Kosaka, M. Ogawa, M. Mitsunaga, D. Asanuma, M. Kamiya, M. R. Young, T. Nagano, P. L. Choyke and H. Kobayashi, *Sci. Transl. Med.*, 2011, 3, 110ra119.

117 R. Obara, M. Kamiya, Y. Tanaka, A. Abe, R. Kojima, T. Kawaguchi, M. Sugawara, A. Takahashi, T. Noda and Y. Urano, *Angew. Chem., Int. Ed.*, 2021, 60, 2125–2129.

118 J. Luo, Z. Xie, J. W. Lam, L. Cheng, H. Chen, C. Qiu, H. S. Kwok, X. Zhan, Y. Liu, D. Zhu and B. Z. Tang, *Chem. Commun.*, 2001, 1740–1741, DOI: 10.1039/b105159h.

119 Y. Chen, J. W. Y. Lam, R. T. K. Kwok, B. Liu and B. Z. Tang, *Mater. Horiz.*, 2019, 6, 428–433.

120 Y. Hong, *Methods Appl. Fluoresc.*, 2016, 4, 022003.

121 M. Chen, L. Li, H. Nie, J. Tong, L. Yan, B. Xu, J. Z. Sun, W. Tian, Z. Zhao, A. Qin and B. Z. Tang, *Chem. Sci.*, 2015, 6, 1932–1937.

122 H. Shi, R. T. Kwok, J. Liu, B. Xing, B. Z. Tang and B. Liu, *J. Am. Chem. Soc.*, 2012, 134, 17972–17981.

123 Y. Yuan, C. J. Zhang, M. Gao, R. Zhang, B. Z. Tang and B. Liu, *Angew. Chem., Int. Ed.*, 2015, 54, 1780–1786.

124 D. Ding, J. Liang, H. Shi, R. T. K. Kwok, M. Gao, G. Feng, Y. Yuan, B. Z. Tang and B. Liu, *J. Mater. Chem. B*, 2014, 2, 231–238.

125 Y. Wang, X. Wu, Y. Cheng and X. Zhao, *Chem. Commun.*, 2016, 52, 3478–3481.

126 S. Huang, Y. Wu, F. Zeng, J. Chen and S. Wu, *Anal. Chim. Acta*, 2018, 1031, 169–177.

127 X. Liu and G. Liang, *Chem. Commun.*, 2017, 53, 1037–1040.

128 T. I. Kim, H. Jin, J. Bae and Y. Kim, *Anal. Chem.*, 2017, 89, 10565–10569.

129 J. Li, W. Y. Lee, T. Wu, C. W. Leung, J. Xu, D. S. Wong, R. Li, G. Li, B. Z. Tang and L. Bian, *Adv. Biosyst.*, 2018, 2, 1800010.

130 Y. Yuan, C. J. Zhang, R. T. K. Kwok, D. Mao, B. Z. Tang and B. Liu, *Chem. Sci.*, 2017, 8, 2723–2728.

131 H. Han, W. Teng, T. Chen, J. Zhao, Q. Jin, Z. Qin and J. Ji, *Chem. Commun.*, 2017, 53, 9214–9217.

132 Y. Yuan, R. Zhang, X. Cheng, S. Xu and B. Liu, *Chem. Sci.*, 2016, 7, 4245–4250.

133 Y. Yuan, C.-J. Zhang, R. T. K. Kwok, S. Xu, R. Zhang, J. Wu, B. Z. Tang and B. Liu, *Adv. Funct. Mater.*, 2015, 25, 6586–6595.

134 Y. Yuan, R. T. Kwok, B. Z. Tang and B. Liu, *J. Am. Chem. Soc.*, 2014, 136, 2546–2554.

135 Y. Cheng, F. Huang, X. Min, P. Gao, T. Zhang, X. Li, B. Liu, Y. Hong, X. Lou and F. Xia, *Anal. Chem.*, 2016, 88, 8913–8919.

136 Y. Zhang, Y. Li, N. Yang, X. Yu, C. He, N. Niu, C. Zhang, H. Zhou, C. Yu and S. Jiang, *Sens. Actuators, B*, 2018, 257, 1143–1149.

137 J. Kaur, J. N. Malegaonkar, S. V. Bhosale and P. K. Singh, *J. Mol. Liq.*, 2021, 333, 115980.

138 H. Li, G. Parigi, C. Luchinat and T. J. Meade, *J. Am. Chem. Soc.*, 2019, 141, 6224–6233.

139 E. M. Sletten and C. R. Bertozzi, *Acc. Chem. Res.*, 2011, 44, 666–676.

140 J. A. Prescher, D. H. Dube and C. R. Bertozzi, *Nature*, 2004, 430, 873–877.

141 P. Shieh and C. R. Bertozzi, *Org. Biomol. Chem.*, 2014, 12, 9307–9320.

142 S. Debieu and A. Romieu, *Org. Biomol. Chem.*, 2017, 15, 2575–2584.

143 S. Debieu and A. Romieu, *Tetrahedron Lett.*, 2018, 59, 1940–1944.

144 R. Huo, X. Zheng, W. Liu, L. Zhang, J. Wu, F. Li, W. Zhang, C. S. Lee and P. Wang, *Chem. Commun.*, 2020, 56, 10902–10905.

145 Q. Wu, K. Y. Zhang, P. Dai, H. Zhu, Y. Wang, L. Song, L. Wang, S. Liu, Q. Zhao and W. Huang, *J. Am. Chem. Soc.*, 2020, 142, 1057–1064.

146 D. Ye, A. J. Shuhendler, L. Cui, L. Tong, S. S. Tee, G. Tikhomirov, D. W. Felsher and J. Rao, *Nat. Chem.*, 2014, 6, 519–526.

147 V. S. Padalkar and S. Seki, *Chem. Soc. Rev.*, 2016, 45, 169–202.

148 W. Liu, S. J. Liu, Y. Q. Kuang, F. Y. Luo and J. H. Jiang, *Anal. Chem.*, 2016, 88, 7867–7872.

149 D. P. Nair, M. Podgo´rski, S. Chatani, T. Gong, W. Xi, C. R. Fenoli and C. N. Bowman, *Chem. Mater.*, 2013, 26, 724–744.

150 X. Yang, Y. Guo and R. M. Strongin, *Angew. Chem., Int. Ed.*, 2011, 50, 10690–10693.

151 G. Zomer, *Chemiluminescence and Bioluminescence*, 2010, DOI: 10.1039/9781849732024-00051, pp. 51–90.

152 A. Roda, M. Guardigli, P. Pasini, M. Mirasoli, E. Michelini and M. Musiani, *Anal. Chim. Acta*, 2005, 541, 25–35.

153 Y. Yan, P. Shi, W. Song and S. Bi, *Theranostics*, 2019, 9, 4047–4065.

154 N. Thorne, J. Inglese and D. S. Auld, *Chem. Biol.*, 2010, 17, 646–657.

155 A. Fleiss and K. S. Sarkisyan, *Curr. Genet.*, 2019, 65, 877–882.

156 N. Hananya and D. Shabat, *Angew. Chem., Int. Ed.*, 2017, 56, 16454–16463.

157 A. P. Jathoul, H. Grounds, J. C. Anderson and M. A. Pule, *Angew. Chem., Int. Ed.*, 2014, 53, 13059–13063.

158 S. Iwano, R. Obata, C. Miura, M. Kiyama, K. Hama, M. Nakamura, Y. Amano, S. Kojima, T. Hirano, S. Maki and H. Niwa, *Tetrahedron*, 2013, 69, 3847–3856.

159 M. S. Evans, J. P. Chaurette, S. T. Adams, Jr., G. R. Reddy, M. A. Paley, N. Aronin, J. A. Prescher and S. C. Miller, *Nat. Methods*, 2014, 11, 393–395.

160 T. Kuchimaru, S. Iwano, M. Kiyama, S. Mitsumata, T. Kadonosono, H. Niwa, S. Maki and S. Kizaka-Kondoh, *Nat. Commun.*, 2016, 7, 11856.

161 R. Kojima, H. Takakura, T. Ozawa, Y. Tada, T. Nagano and Y. Urano, *Angew. Chem., Int. Ed.*, 2013, 52, 1175–1179.

162 Y. Ni, Z. Hai, T. Zhang, Y. Wang, Y. Yang, S. Zhang and G. Liang, *Anal. Chem.*, 2019, 91, 14834–14837.

163 T. Monsees, W. Miska and R. Geiger, *Anal. Biochem.*, 1994, 221, 329–334.

164 W. Miska and R. Geiger, *J. Clin. Chem. Clin. Biochem.*, 1987, 25, 23–30.

165 M. Kindermann, H. Roschitzki-Voser, D. Caglic, U. Repnik, C. Miniejew, P. R. Mittl, G. Kosec, M. G. Grutter, B. Turk and K. U. Wendt, *Chem. Biol.*, 2010, 17, 999–1007.

166 A. Dragulescu-Andrasi, G. Liang and J. Rao, *Bioconjugate Chem.*, 2009, 20, 1660–1666.

167 G. C. Van de Bittner, C. R. Bertozzi and C. J. Chang, *J. Am. Chem. Soc.*, 2013, 135, 1783–1795.

168 S. Talley, O. Kalinina, M. Winek, W. Paik, A. R. Cannon, F. Alonzo, 3rd, M. A. Choudhry, K. L. Knight and E. M. Campbell, *J. Immunol.*, 2019, 203, 2497–2507.

169 J. G. Morin and J. W. Hastings, *J. Cell. Physiol.*, 1970, 77, 313–318.

170 H. Dacres, M. Michie and S. C. Trowell, *Anal. Biochem.*, 2012, 424, 206–210.

171 F. Weihs, M. Gel, J. Wang, A. Anderson, S. Trowell and H. Dacres, *Biosens. Bioelectron.*, 2020, 158, 112162.

172 A. den Hamer, P. Dierickx, R. Arts, J. de Vries, L. Brunsveld and M. Merkx, *ACS Sens.*, 2017, 2, 729–734.

173 H. Dacres, J. Wangb, A. Andersonb and S. C. Trowellb, *Sens. Actuators, B*, 2019, 301, 127141.

174 F. Weihs, A. Peh and H. Dacres, *Anal. Chim. Acta*, 2020, 1102, 99–108.

175 A. P. Schaap, R. S. Handley and B. P. Gin, *Tetrahedron Lett.*, 1987, 28, 935–938.

176 N. Hananya and D. Shabat, *ACS Cent. Sci.*, 2019, 5, 949–959.

177 J. A. Richard, L. Jean, C. Schenkels, M. Massonneau, A. Romieu and P. Y. Renard, *Org. Biomol. Chem.*, 2009, 7, 2941–2957.

178 J.-A. Richard, L. Jean, A. Romieu, M. Massonneau, P. Noack-Fraissignes and P.-Y. Renard, *Org. Lett.*, 2007, 9, 4853–4855.

179 O. Green, T. Eilon, N. Hananya, S. Gutkin, C. R. Bauer and D. Shabat, *ACS Cent. Sci.*, 2017, 3, 349–358.

180 M. E. Roth-Konforti, C. R. Bauer and D. Shabat, *Angew. Chem., Int. Ed.*, 2017, 56, 15633–15638.

181 L. S. Ryan and A. R. Lippert, *Angew. Chem., Int. Ed.*, 2018, 57, 622–624.

182 J. I. Scott, S. Gutkin, O. Green, E. J. Thompson, T. Kitamura, D. Shabat and M. Vendrell, *Angew. Chem., Int. Ed.*, 2021, 60, 5699–5703.

183 B. M. Babin, G. Fernandez-Cuervo, J. Sheng, O. Green, A. A. Ordonez, M. L. Turner, L. J. Keller, S. K. Jain, D. Shabat and M. Bogyo, *ACS Cent. Sci.*, 2021, 7, 803–814.

184 N. Hananya, J. P. Reid, O. Green, M. S. Sigman and D. Shabat, *Chem. Sci.*, 2019, 10, 1380–1385.

185 S. Gutkin, O. Green, G. Raviv, D. Shabat and O. Portnoy, *Bioconjugate Chem.*, 2020, 31, 2488–2493.

186 N. Hananya, A. Eldar Boock, C. R. Bauer, R. Satchi-Fainaro and D. Shabat, *J. Am. Chem. Soc.*, 2016, 138, 13438–13446.

187 N. Hananya, O. Press, A. Das, A. Scomparin, R. Satchi-Fainaro, I. Sagi and D. Shabat, *Chemistry*, 2019, 25, 14679–14687.

188 Q. Miao and K. Pu, *Bioconjugate Chem.*, 2016, 27, 2808–2823.

189 Y. Zhang, H. Hong and W. Cai, *Cold Spring Harb. Protoc.*, 2011, DOI: 10.1101/pdb.top065508.

190 J. Weber, P. C. Beard and S. E. Bohndiek, *Nat. Methods*, 2016, 13, 639–650.

191 Y. P. a. G. K. Xueding Wang, *Opt. Lett.*, 2003, 28, 1739–1741.

192 J. T. Oh, M. L. Li, H. F. Zhang, K. Maslov, G. Stoica and L. V. Wang, *J. Biomed. Opt.*, 2006, 11, 34032.

193 H. Wang, K. Xue, Z. Duan, Y. Yang, Z. He, C. Wu, W. Zhang, W. Zhang, P. Li and B. Tang, *Sens. Actuators, B*, 2019, 286, 243–249.

194 P. Cheng, W. Chen, S. Li, S. He, Q. Miao and K. Pu, *Adv. Mater.*, 2020, 32, e1908530.

195 L. Yin, H. Sun, M. Zhao, A. Wang, S. Qiu, Y. Gao, J. Ding, S. J. Ji, H. Shi and M. Gao, *J. Org. Chem.*, 2019, 84, 6126–6133.

196 C. Lee, M. Jeon and C. Kim, *Applications of Nanoscience in Photomedicine*, 2015, DOI: 10.1533/9781908818782.31, pp. 31–47.

197 J. Weber, P. C. Beard and S. E. Bohndiek, *Nat. Methods*, 2016, 13, 639–650.

198 K. Haedicke, C. Brand, M. Omar, V. Ntziachristos, T. Reiner and J. Grimm, *Photoacoustics*, 2017, 6, 1–8.

199 B. M. Wallis de Vries, J. L. Hillebrands, G. M. van Dam, R. A. Tio, J. S. de Jong, R. H. Slart and C. J. Zeebregts, *Circulation*, 2009, 119, e534–e536.

200 D. Razansky, N. J. Harlaar, J. L. Hillebrands, A. Taruttis, E. Herzog, C. J. Zeebregts, G. M. van Dam and V. Ntziachristos, *Mol. Imaging Biol.*, 2012, 14, 277–285.

201 J. Levi, S. R. Kothapalli, T.-J. Ma, K. Hartman, B. T. Khuri-Yakub and S. S. Gambhir, *J. Am. Chem. Soc.*, 2010, 132, 11264–11269.

202 Q. Li, S. Li, S. He, W. Chen, P. Cheng, Y. Zhang, Q. Miao and K. Pu, *Angew. Chem., Int. Ed.*, 2020, 59, 7018–7023.

203 K. Yang, L. Zhu, L. Nie, X. Sun, L. Cheng, C. Wu, G. Niu, X. Chen and Z. Liu, *Theranostics*, 2014, 4, 134–141.

204 C. Liu, S. Li, Y. Gu, H. Xiong, W. T. Wong and L. Sun, *Mol. Imaging Biol.*, 2018, 20, 919–929.

205 L. Yin, H. Sun, H. Zhang, L. He, L. Qiu, J. Lin, H. Xia, Y. Zhang, S. Ji, H. Shi and M. Gao, *J. Am. Chem. Soc.*, 2019, 141, 3265–3273.

206 D. Zhang, G. B. Qi, Y. X. Zhao, S. L. Qiao, C. Yang and H. Wang, *Adv. Mater.*, 2015, 27, 6125–6130.

207 A. Dragulescu-Andrasi, S. R. Kothapalli, G. A. Tikhomirov, J. Rao and S. S. Gambhir, *J. Am. Chem. Soc.*, 2013, 135, 11015–11022.

208 Y. Wang, X. Hu, J. Weng, J. Li, Q. Fan, Y. Zhang and D. Ye, *Angew. Chem., Int. Ed.*, 2019, 58, 4886–4890.

209 A. Lakshmanan, Z. Jin, S. P. Nety, D. P. Sawyer, A. Lee-Gosselin, D. Malounda, M. B. Swift, D. Maresca and M. G. Shapiro, *Nat. Chem. Biol.*, 2020, 16, 988–996.

210 F. Xia, J. Niu, Y. Hong, C. Li, W. Cao, L. Wang, W. Hou, Y. Liu and D. Cui, *Acta Biomater.*, 2019, 89, 289–299.

211 S. Nakamura, T. Morita, S. Iwanaga, M. Miwa and K. Takahashi, *J. Biochem.*, 1977, 81, 1567–1569.

212 X. Zhu and T. Gao, *Nano-Inspired Biosensors for Protein Assay with Clinical Applications*, 2019, DOI: 10.1016/b978-0-12-815053-5.00010-6, pp. 237–264.

213 H. Aldewachi, T. Chalati, M. N. Woodroofe, N. Bricklebank, B. Sharrack and P. Gardiner, *Nanoscale*, 2017, 10, 18–33.

214 E. Petryayeva and U. J. Krull, *Anal. Chim. Acta*, 2011, 706, 8–24.

215 Q. Zhang, Y. Lu, S. Li, J. Wu and Q. Liu, *Peptide Applications in Biomedicine, Biotechnology and Bioengineering*, 2018, DOI: 10.1016/b978-0-08-100736-5.00024-7, pp. 565–601.

216 P. Chen, R. Selegard, D. Aili and B. Liedberg, *Nanoscale*, 2013, 5, 8973–8976.

217 Y. Pan, M. Guo, Z. Nie, Y. Huang, Y. Peng, A. Liu, M. Qing and S. Yao, *Chem. Commun.*, 2012, 48, 997–999.

218 G. Chen, Y. Xie, H. Zhang, P. Wang, H.-Y. Cheung, M. Yang and H. Sun, *RSC Adv.*, 2014, 4, 6560–6563.

219 W. Xue, G. Zhang and D. Zhang, *Analyst*, 2011, 136, 3136–3141.

220 G. B. Kim, K. H. Kim, Y. H. Park, S. Ko and Y. P. Kim, *Biosens. Bioelectron.*, 2013, 41, 833–839.

221 X. Ding, D. Ge and K.-L. Yang, *Sens. Actuators, B*, 2014, 201, 234–239.

222 M. Q. He, S. Chen, K. Yao, J. Meng, K. Wang, Y. L. Yu and J. H. Wang, *Anal. Chem.*, 2020, 92, 1395–1401.

223 N. Xia, D. Deng, Y. Wang, C. Fang and S. J. Li, *Int. J. Nanomed.*, 2018, 13, 2521–2530.

224 L. Liu, D. Deng, Y. Wang, K. Song, Z. Shang, Q. Wang, N. Xia and B. Zhang, *Sens. Actuators, B*, 2018, 266, 246–254.

225 C. N. Loynachan, A. P. Soleimany, J. S. Dudani, Y. Lin, A. Najer, A. Bekdemir, Q. Chen, S. N. Bhatia and M. M. Stevens, *Nat. Nanotechnol.*, 2019, 14, 883–890.

226 G. A. Suaifan, C. Esseghaier, A. Ng and M. Zourob, *Analyst*, 2013, 138, 3735–3739.

227 S. Wignarajah, G. A. Suaifan, S. Bizzarro, F. J. Bikker, W. E. Kaman and M. Zourob, *Anal. Chem.*, 2015, 87, 12161–12168.

228 S. Alhogail, G. Suaifan and M. Zourob, *Biosens. Bioelectron.*, 2016, 86, 1061–1066.

229 S. Alhogail, G. Suaifan, F. J. Bikker, W. E. Kaman, K. Weber, D. Cialla-May, J. Popp and M. M. Zourob, *ACS Omega*, 2019, 4, 21684–21688.

230 R. I. Roth and J. Levin, *J. Biochem. Biophys. Methods*, 1989, 19, 129–142.

231 D. Yang, H. J. Park and T. H. Yoo, *Anal. Methods*, 2016, 8, 6270–6276.

232 Z. Ling, F. Xu, J. V. Edwards, N. T. Prevost, S. Nam, B. D. Condon and A. D. French, *Carbohydr. Polym.*, 2019, 216, 360–368.

233 P. Findeisen, T. Peccerella, S. Post, F. Wenz and M. Neumaier, *Rapid Commun. Mass Spectrom.*, 2008, 22, 1223–1229.

234 J.-L. Hsu, S.-Y. Huang, N.-H. Chow and S.-H. Chen, *Anal. Chem.*, 2003, 75, 6843–6852.

235 S. P. Gygi, B. Rist, S. A. Gerber, F. Turecek, M. H. Gelb and R. Aebersold, *Nat. Biotechnol.*, 1999, 17, 994–999.

236 T. J. Griffin, D. K. M. Han, S. P. Gygi, B. Rist, H. Lee and R. Aebersold, *J. Am. Soc. Mass Spectrom.*, 2001, 12, 1238–1246.

237 R. Bachor, M. Waliczek, P. Stefanowicz and Z. Szewczuk, *Molecules*, 2019, 24, 701.

238 K. Jia, X. Zhao and X. Dang, *Oncol. Lett.*, 2020, 19, 4106–4114.

239 N. Rauniyar and J. R. Yates, 3rd, *J. Proteome Res.*, 2014, 13, 5293–5309.

240 A. Thompson, J. Schafer, K. Kuhn, S. Kienle, J. Schwarz, G. Schmidt, T. Neumann and C. Hamon, *Anal. Chem.*, 2002, 75, 1895–1904.

241 T. Peccerella, N. Lukan, R. Hofheinz, D. Schadendorf, M. Kostrezewa, M. Neumaier and P. Findeisen, *Clin. Chem.*, 2010, 56, 272–280.

242 P. Findeisen, V. Costina, D. Yepes, R. Hofheinz and M. Neumaier, *J. Exp. Clin. Cancer Res.*, 2012, 31, 56.

243 F. Ouyang, T. Yu, C. Gu, G. Wang, R. Shi, R. Lv, E. Wu, C. Ma, R. Guo, J. Li, A. Zaczek and J. Liu, *Analyst*, 2019, 144, 6751–6759.

244 J. D. Kirkpatrick, A. D. Warren, A. P. Soleimany, P. M. K. Westcott, J. C. Voog, C. Martin-Alonso, H. E. Fleming, T. Tammela, T. Jacks and S. N. Bhatia, *Sci. Trans. Med.*, 2020, 12, eaaw0262.

245 B. B. Brown, D. S. Wagner and H. M. Geysen, *Mol. Diversity*, 1995, 1, 4–12.

246 J. S. Dudani, M. Ibrahim, J. Kirkpatrick, A. D. Warren and S. N. Bhatia, *Proc. Natl. Acad. Sci. U. S. A.*, 2018, 115, 8954–8959.

247 M. Pohanka and P. Skl´adal, *J. Appl. Biomed.*, 2008, 6, 57–64.

248 L. C. Clark, Jr. and C. Lyons, *Ann. N. Y. Acad. Sci.*, 1962, 102, 29–45.

249 X.-Y. Z. Ming La, Q.-L. Peng, C.-D. Chen and G.-Q. Zhao, *Int. J. Electrochem. Sci.*, 2015, 10, 3329–3339.

250 V. Vanova, K. Mitrevska, V. Milosavljevic, D. Hynek, L. Richtera and V. Adam, *Biosens. Bioelectron.*, 2021, 180, 113087.

251 G. Liu, J. Wang, D. S. Wunschel and Y. Lin, *J. Am. Chem. Soc.*, 2006, 128, 12382–12383.

252 J. Ji, J. Gan, J. Kong, P. Yang, B. Liu and C. Ji, *Electrochem. Commun.*, 2012, 16, 53–56.

253 D. S. Shin, Y. Liu, Y. Gao, T. Kwa, Z. Matharu and A. Revzin, *Anal. Chem.*, 2013, 85, 220–227.

254 L. Z. Swisher, A. M. Prior, S. Shishido, T. A. Nguyen, D. H. Hua and J. Li, *Biosens. Bioelectron.*, 2014, 56, 129–136.

255 E. Gonz´alez-Fern´andez, M. Staderini, A. Yussof, E. Scholefield, A. F. Murray, A. R. Mount and M. Bradley, *Biosens. Bioelectron.*, 2018, 119, 209–214.

256 K. Kerman, K. A. Mahmoud and H.-B. Kraatz, *Chem. Commun.*, 2007, 3829–3831.

257 J. Liu, H. Cheng, D. He, X. He, K. Wang, Q. Liu, S. Zhao and X. Yang, *Anal. Chem.*, 2017, 89, 9062–9068.

258 Y. Song, H. Fan, M. J. Anderson, J. G. Wright, D. H. Hua, J. Koehne, M. Meyyappan and J. Li, *Anal. Chem.*, 2019, 91, 3971–3979.

259 A. Ucar, E. Gonzalez-Fernandez, M. Staderini, N. Avlonitis, A. F. Murray, M. Bradley and A. R. Mount, *Analyst*, 2020, 145, 975–982.

260 Y. Cao, J. Yu, B. Bo, Y. Shu and G. Li, *Biosens. Bioelectron.*, 2013, 45, 1–5.

261 Y. S. Dehua Deng, H. Feng, Q. Chen, D. Li and L. Liu, *Int. J. Electrochem. Sci.*, 2013, 8, 6933–6940.
262 H. Li, Y. Huang, B. Zhang, D. Yang, X. Zhu and G. Li, *Theranostics*, 2014, 4, 701–707.
263 H. Ko, S. Park and K. Kim, *J. Electroanal. Chem.*, 2015, 742, 70–73.
264 D. Deng, Y. Hao, S. Yang, Q. Han, L. Liu, Y. Xiang, F. Tu and N. Xia, *Sens. Actuators, B*, 2019, 286, 415–420.
265 H. Wu, S. Liu, J. Jiang, G. Shen and R. Yu, *Analyst*, 2012, 137, 4829–4833.
266 H. Chen, J. Zhang, Y. Gao, S. Liu, K. Koh, X. Zhu and Y. Yin, *Biosens. Bioelectron.*, 2015, 68, 777–782.
267 F. Meng, H. Sun, Y. Huang, Y. Tang, Q. Chen and P. Miao, *Anal. Chim. Acta*, 2019, 1047, 45–51.
268 N. Xia, Y. Zhang, P. Guan, Y. Hao and L. Liu, *Sens. Actuators, B*, 2015, 213, 111–115.
269 X. Miao, H. Yu, Z. Gu, L. Yang, J. Teng, Y. Cao and J. Zhao, *Anal. Bioanal. Chem.*, 2017, 409, 6723–6730.
270 C. Muñoz-San Martin, M. Pedrero, M. Gamella, A. Montero-Calle, R. Barderas, S. Campuzano and J. M. Pingarron, *Anal. Bioanal. Chem.*, 2020, 412, 6177–6188.
271 Y.-F. Liu, J.-X. Chen, M.-Q. Xu and G.-C. Zhao, *Int. J. Electrochem. Sci.*, 2014, 9, 4014–4023.
272 D. Wang, Y. Yuan, Y. Zheng, Y. Chai and R. Yuan, *Chem. Commun.*, 2016, 52, 5943–5945.
273 Q. Hu, Y. Bao, S. Gan, Y. Zhang, D. Han and L. Niu, *Anal. Chem.*, 2020, 92, 3470–3476.

1.4 Conclusions

Proteases are essential enzymes for proper cellular function and dysregulation of protease activity has been associated with a variety of diseases. Detection and monitoring of proteolytic activity is crucial to better understand the function of these enzymes and their connection to certain pathologies, and many methods have been explored to monitor and better understand their activity. Progress has been made in the areas of optical imaging detection, point-of care diagnostics and bench-top detection that serve not only to provide diagnostic tools but also as essential assets for the development and evaluation of efficient inhibitors for therapeutic applications.

There are, however, still challenges in the field of proteolytic activity detection. The need for high sensitivity and specificity are two of the most important ones. Interference from other proteases in complex samples still poses a problem when trying to detect activity specifically among other closely related proteases. Understanding the substrate specificity of proteases is key to allow the development of successful detection methods, currently, only a limited number of proteases can be monitored or detected, with the substrate specificity of most proteases remaining unknown. Hence, there is a need for better protease substrate screening methods to select the best substrates to be used in method development. Sensitivity of current technologies is technique-dependent, with methods like electrochemistry or mass spectrometry showing very low limits of detection, however they are costly, and their applicability is limited, while others that might be most cost-effective such as colorimetric or antibody labelling might allow the study of more complex samples, but they require higher concentrations. Finally sample preparation time and reproducibility of the method are also key factors to implement methodologies in the market or the clinic.

Chapter 2 Aims of the thesis

Monitoring the proteolytic activity of neutrophils and macrophages can provide information on inflammation-related diseases and help tailor the disease treatment and management. Indeed, the response to infection by these immune cells provides unique signatures in acute and chronic diseases. This thesis aimed to develop a series fluorogenic peptide-based probes for the detection of proteolytic activity in neutrophils and macrophages allowing the monitoring of an immune cell's response during inflammation and offering a diagnostic tool for acute and chronic inflammatory diseases.

The first family of probes I synthesised monitored the proteolytic activity of neutrophils. The probes designed targeted human neutrophil elastase, a protease produced by neutrophils upon activation and whose abnormal activity has been linked to several inflammatory diseases. These probes, with fluorescence emission in the green, were successful used to monitor human neutrophil elastase (hNE) in activated neutrophils in induced inflammatory conditions. The second family consisted of a series of optical probes with emission in the near infrared region of the spectrum. These probes with emission in the near infrared were validated for hNE detection *in vitro* and are currently being validated in cells.

Finally, a probe for monitoring macrophage activity was developed that targets Cathepsin D, a lysosomal protease involved in the bacterial fighting mechanisms of macrophages and were used to detect the activity of Cathepsin D in a *S. pneumoniae* infection model.

Chapter 3 Green fluorogenic probes for detection of human neutrophil elastase

Parts of this chapter are published as:

> M. R. Rios, G. Garoffolo, G. Rinaldi, A. Megia-Fernandez, S. Ferrari, C. T. Robb, A. G. Rossi, M. Pesce, M. Bradley, *Chem. Commun*., 2021, **57**, 97-100.

The probes were synthesised and validated *in vitro* by M. Rodriguez-Rios. Microscopy images and flow cytometry assays HL-60 and primary human neutrophils were performed by Gloria Garoffolo and Giulia Rinaldi, respectively.

3.1 Neutrophils

Neutrophils are granulated polynuclear cells, with cytoplasmic granules containing high levels of the serine proteases (serprodicins) human neutrophil elastase (HNE), proteinase 3, and cathepsin G. [38] They are phagocytic leukocytes and are the most abundant immune cells circulating in human blood and are amongst the first cells to be recruited to inflammatory sites, providing a first line of immune defence against pathogens. [39] These cells are very short-lived, thus if there is no immunological stimulus after 24 h following their production and migration from the bone marrow, they undergo caspase-dependent apoptosis. [39]

Neutrophils can destroy microbes by phagocytosis, degranulation and release of proteases, and by producing neutrophil extracellular traps (Figure 4).[40] In phagocytosis, the pathogen is firstly taken up into a vacuole within the cell (typically by receptor-mediated phagocytosis). The vacuole containing the pathogen produces highly toxic reactive oxygen species and is fused with granules, which contain various antimicrobial mediators and activated serprocidins, resulting in the destruction of the foreign material.

During degranulation, azurophilic granules are released into the extracellular space, allowing active proteases to be localised with, and kill, extracellular pathogens. In 2004, it was discovered that neutrophils can also "trap" and kill microbes by producing so-called neutrophil extracellular traps (NETs). [41] During what has been called "NETosis", neutrophils die and extrude chromatin studded with antimicrobial proteins in the extracellular environment to entrap and kill invading pathogens, such as bacteria,[41] viruses [42] and fungi. [43] Elastase activity is essential for the migration of neutrophils, cleaving several connective tissue substrates, which is part of its role in allowing neutrophils to reach sites of infection.

Overactivation of neutrophils and production of NETs has been associated with inflammatory diseases,[44-46] and has become a good biomarker and therapeutic target for inflammation. [47, 48]

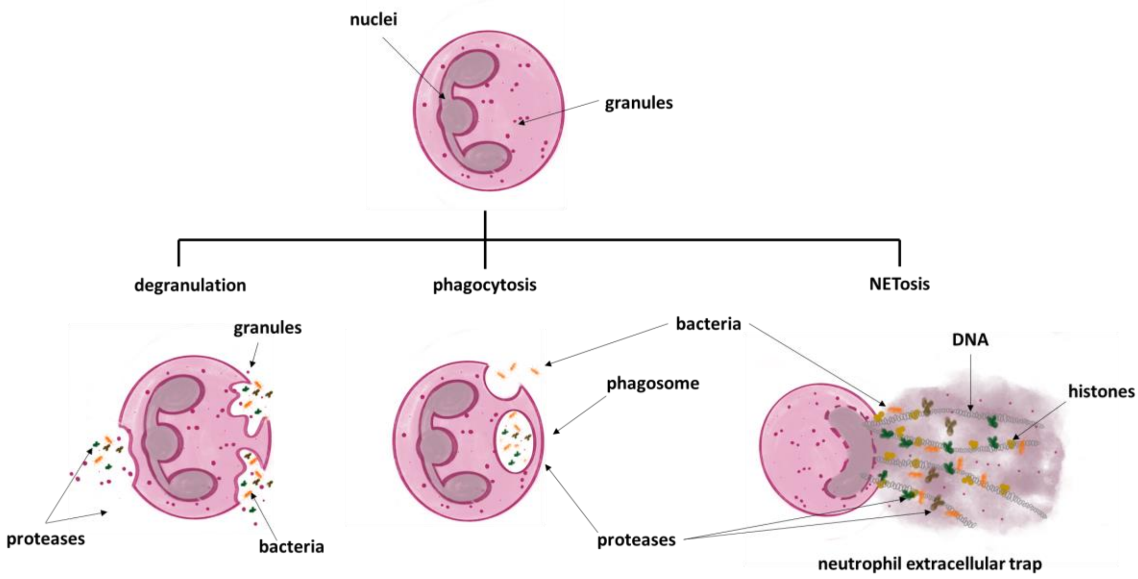

Figure 4 Neutrophil-mediated mechanisms to fight infection. Degranulation, phagocytosis and NETosis.

3.1.1 Neutrophil Extracellular Traps in Disease

NETs are known to play pivotal roles in host defence, but aberrant NET formation has been linked to acute respiratory distress syndrome (ARDS), [49] acute lung injury (ALI), [46] and more recently, COVID-19 infection. [47, 50] Indeed, neutrophils isolated from COVID-19 patients are more susceptible to form NETs; a response that correlates with severity and mortality of the disease.[46] NETs forming in arteries and veins are thought to be important in initiating thrombosis in the vasculature, again of relevance during the immunopathology in COVID-19 patients. 51 Several inhibitors for hNE have been developed and some of them used clinically including the inhibitor sivelestat[52, 53], which has been used to treat COVID-19 patients.[53]

Detection and visualisation of NETs has therefore become a potential tool for diagnosis of NET-associated pathologies. To date, detection has largely been based on immuno-staining of different NET markers, including DNA, histones and granule proteases such as human neutrophil elastase (Figure 5), however, antibody-based imaging techniques have a number of limitations, with limited intracellular accessibility due to their large size and, when targeting enzymes such as proteases, they cannot give information on their activity.

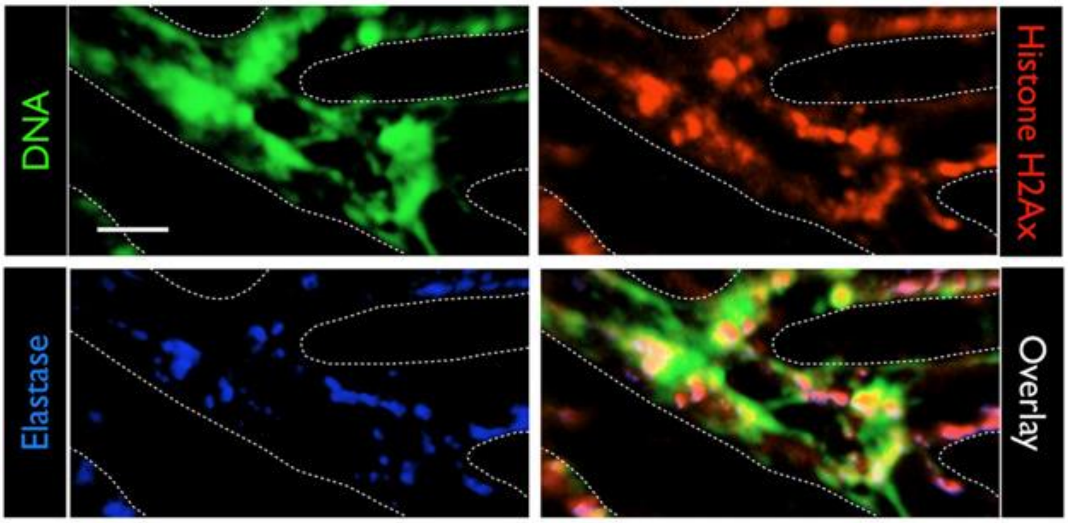

Figure 5 Neutrophil extracellular traps imaging. Multichannel intravital microscopy was used to visualise the liver of mice with systemic inflammation 4 h after the administration of 1 mg/kg LPS. NETs were stained with fluorescent antibodies or dyes, injected i.v. 15 min prior to imaging. Extracellular DNA was labelled with a Sytox Green DNA dye (5 µM), histone H2Ax was labelled with the antibody AF555-anti-H2Ax Ab (5 µg), and neutrophil elastase (NE) was labelled with AF647-anti-neutrophil elastase Ab (0.6 µg). Representative images of *in vivo* induced NETs induced *in vivo* using intravital imaging of the liver revealed intravascular NETs consisting of DNA (green), histones (H2Ax, red), and neutrophil elastase (blue). The scale bar represents 10 mm. Reproduced from reference 54 with permission from the Elsevier Inc©. [54]

3.1.2 Human neutrophil elastase (hNE)

Activated serine proteases are present in activated neutrophils[55] and NETs.[56] Human neutrophil elastase (hNE) is one of the four key active neutrophil serine proteases and is the most abundant serine protease, being the main component of neutrophils and stored in the granules at millimolar concentrations.[39] Based on their primary cleavage specificities, serine proteases can generally be subdivided into chymases, elastases, tryptases, aspases, and metases.

- **Chymases** are chymotrypsin like proteases and cleave substrates after aromatic amino acids.
- **Elastases** cleave after aliphatic amino acids.
- **Tryptases** after basic amino acids, arginine and lysine.
- **Aspases** recognise aspartic acid at the P1 position.
- **Metases** cleave after methionine, leucine or norleucine residues.

The powerful proteolytic activity of hNE relies on the serine residue in the His57-Asp102-Ser195 triad (chymotrypsin numbering system) of hNE[55] (Figure 6) with preference for Val, Ala, or Ile, in the P1 position[57] (cleavage site nomenclature, P2-P1-P1'-P2'). Elastase activity is essential for the migration of neutrophils through connective tissue and the destruction of microbes. It cleaves a number of connective tissue substrates, which is part of its role in paving the way for the neutrophil to reach sites of infection.[39]

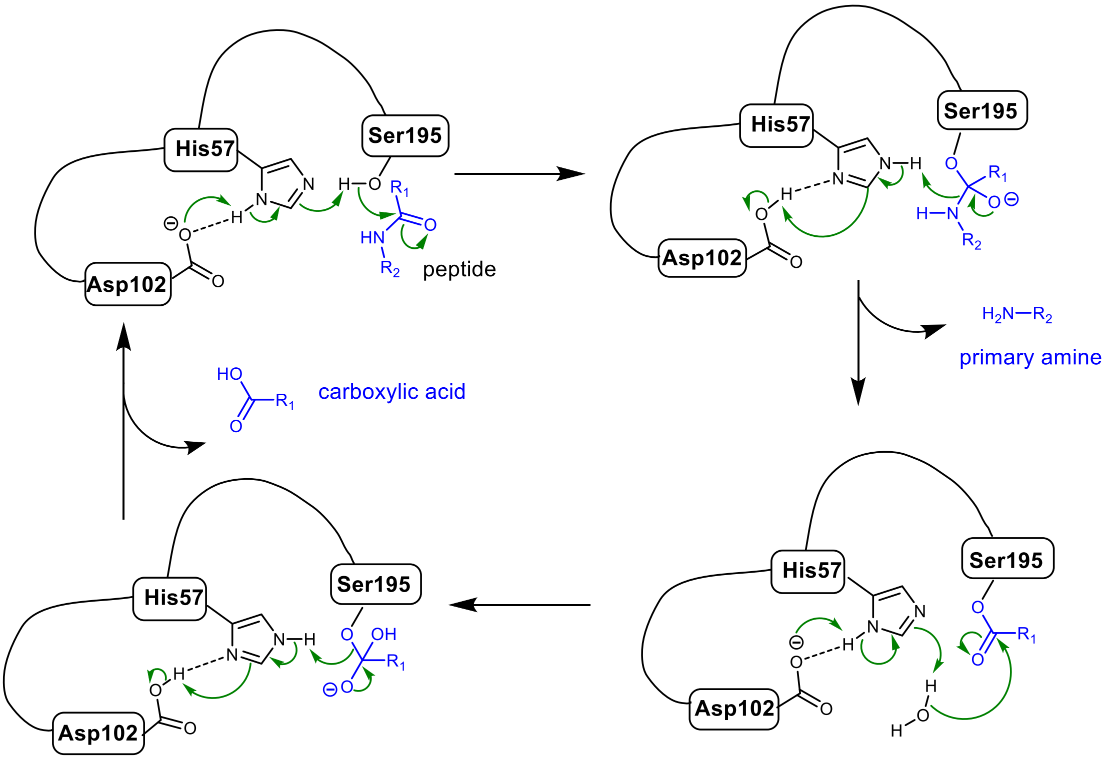

Figure 6 Mechanism of peptide hydrolysis by human neutrophil elastase. Catalytic triad composed of His57-Asp102-Ser195.

Under usual physiological conditions, expression of hNE is tightly regulated and it is only released upon exposure to an immune stimulus. [58] hNE activity is also regulated in plasma by protease inhibitors, such as antitrypsin and α2-macroglobulin, which form complexes with the protease. [58] In the absence of inhibitors, or an overexpression of elastase, severe tissue damage can occur and hNE activity has been related to pulmonary emphysema, [59] acute lung injury, [45] chronic obstructive pulmonary disease, [48] glomerulonephritis, [60] rheumatoid arthritis. [61] As such, hNE has become a validated biomarker for inflammatory disorders and disease progression[45] and is a therapeutic target for drug discovery. [48, 62]

When it comes to protease detection, most substrates rely on chromogenic reporters or fluorescent labels, including antibody labelling and peptide-based probes. For hNE, most known substrates are based on the peptide sequence Ala-Ala-Pro-Val (P4-P1), which this is also cleavable by the closely related serine protease Proteinase 3. [37] Only a limited number of specific probes have been developed that have preference for hNE over

Proteinase 3. hNE specific activity-based probes consisting of a short P4-P1 substrate bearing a covalent warhead were developed from combinatorial libraries, [63, 64] however these are "always on" so their signal amplification is limited and result in inhibition of the protease. hNE specific cleavable substrates include the self-quenching NE680 probe for murine elastase[65] (see page 103, Figure 46) and the FRET substrates developed by Korkmaz, based on the sequence Ala-Pro-Glu-Glu-Ile↑Met-Arg-Arg-Gln, that is not cleaved by PR3, however the latter are limited by their emission in the blue region of the spectrum, and the presence of methionine (susceptible to oxidation), that limit their applicability *in vivo*. [66, 67] Thus, there is a need for tools that show high specificity, sensitivity, and signal-to-noise ratios for the analysis of hNE.

3.1.3 Tribranched fluorogenic probes for the detection of neutrophil elastase

Detection and visualisation of hNE in activated neutrophils and NETs is key to understand and develop therapies for neutrophil and NET associated pathologies and fluorescent small molecule probes for hNE detection are excellent alternatives to antibody-based imaging as they specifically detect the proteolytic activity of the targeted protease.

Fluorogenic peptide based "dendritic" or multi-branched probes can provide significantly higher signal amplification and lower background noise[68-70] when compared to their linear counterparts. Using this approach, a series of multi-branched fluorogenic probes to detect neutrophil serine proteases activity in the lung were developed, that provide information in either intra or extracellular environments. [71, 72]

The first generation of tribranched substrate-based probes used an internal self-quenching approach, where multiple copies of the same fluorophore were incorporated in the structure leading to self-quenching of fluorescence between the fluorophores and making the probes "relatively silent" until activated by the protease[73] (see Figure 7), that cleaved the peptide sequences and released the fluorophores from the construct, allowing for an amplification of the fluorescence signal. Using this approach, an elastase probe, a so-called Neutrophil Activation Probe (**1**, Figure 8), was developed. [74] However, the amplification of the signal here was limited, and the background fluorescence was very high.

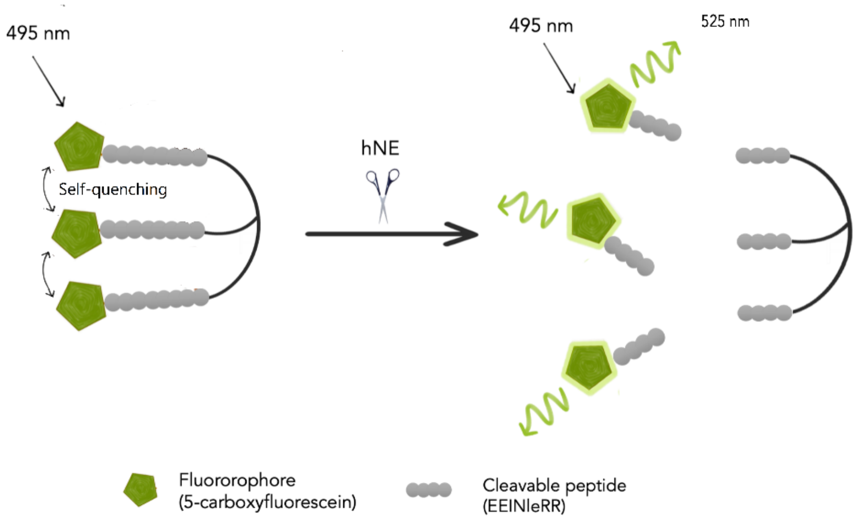

Figure 7. Neutrophil Activation Probe (**NAP**, **1**) relies on self-quenching of the fluorescein molecules between themselves in the tribranched construct. Upon cleavage by hNE, the three molecules of fluorescein are released, and the fluorescence signal is amplified.

In this case the peptide sequence, a substrate for hNE (Glu-Glu-Ile↑Met-Arg-Arg), was adapted from the previously reported peptide substrate by Korkmaz[75] with the amino acid in the P1’ residue replaced by norleucine (Nle) (this providing *in vivo* stability against methionine oxidation). [76] In order to increase its water solubility and to provide space between the fluorophore and the cleavage site, an ethylene glycol (EG) spacer was also added (see Figure 8). This probe proved to be highly specific for hNE over other serprocidins present in neutrophils during inflammation[57, 62] (Proteinase 3, Cathepsin G) and showed an ability to access the intracellular compartments in neutrophils despite their high molecular weight.

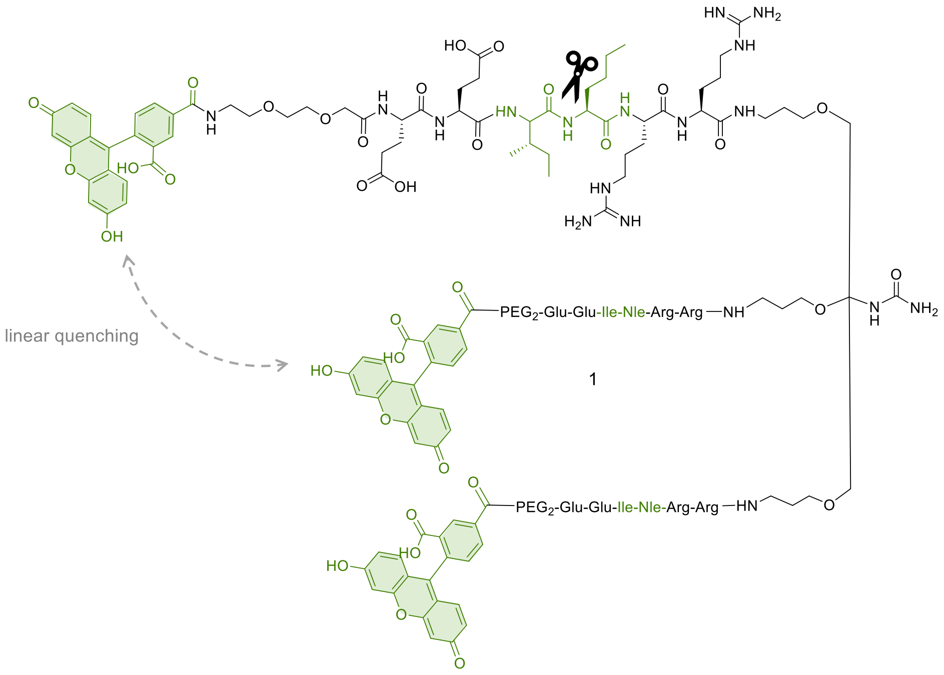

Figure 8. Structure of the so-called Neutrophil Activation Probe (**NAP**, **1**). The cleavage site and is highlighted in green (between the Ile↑Nle residues). 5-carboxyfluorescein is the fluorophore.

It is important to point out that **NAP** (**1**) is a fluorogenic probe, but unfortunately it has a high background fluorescence due to low quenching efficiency and showed only a (limited) 3-fold increase in fluorescence upon cleavage by hNE. Thanks to the use of fluorescein, it can provide information on pH, being capable of tracking a variety of processes associated with neutrophil activity without the need for cleavage. **NAP** was evaluated *in vitro* and *ex vivo* before being used in a limited clinical study (NCT02804854), where imaging of neutrophil activity was attempted in real-time but the probe's high fluorescence background levels and tissue autofluorescence resulted in limited/no amplification/detection of the signal.

An updated version of the neutrophil activation probe (**NAP**), the so-called Neutrophil Elastase Sensor (**NES**, **2**)[77] was reported, and successfully incorporated two strategies into a single compound both a "self-quenching" scaffold and FRET labelling.

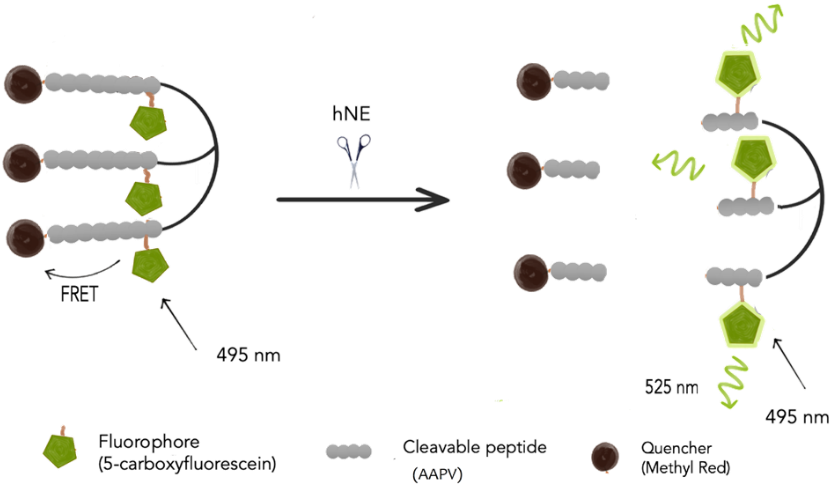

Figure 9. Neutrophil Elastase Sensor (**2**) relies on FRET quenching of the fluorescein (green pentagon) by Methyl Red (black bead). A generic serprocidin substrate (grey beads) is capped with Methyl Red on at the N-terminus and with the construct contains containing three molecules of fluorescein and three of Methyl Red. Upon cleavage by hNE, the quenchers are released, and the fluorescence of the fluorescein restored.

This construct contained three quenchers (3 × Methyl Red) enhancing the quenching of 5-carboxyfluorescein by FRET, making this probe "super-silent" until activated by serine protease activity (Figure 9 and Figure 10). Importantly this sensor provided an OFF/ON fluorescent signal upon cleavage by hNE, however, **NES** was not specific for hNE as it used a generic peptidic substrate (AAPV↑) which is cleavable by many other serine proteases including Cathepsin G and Proteinase 3.

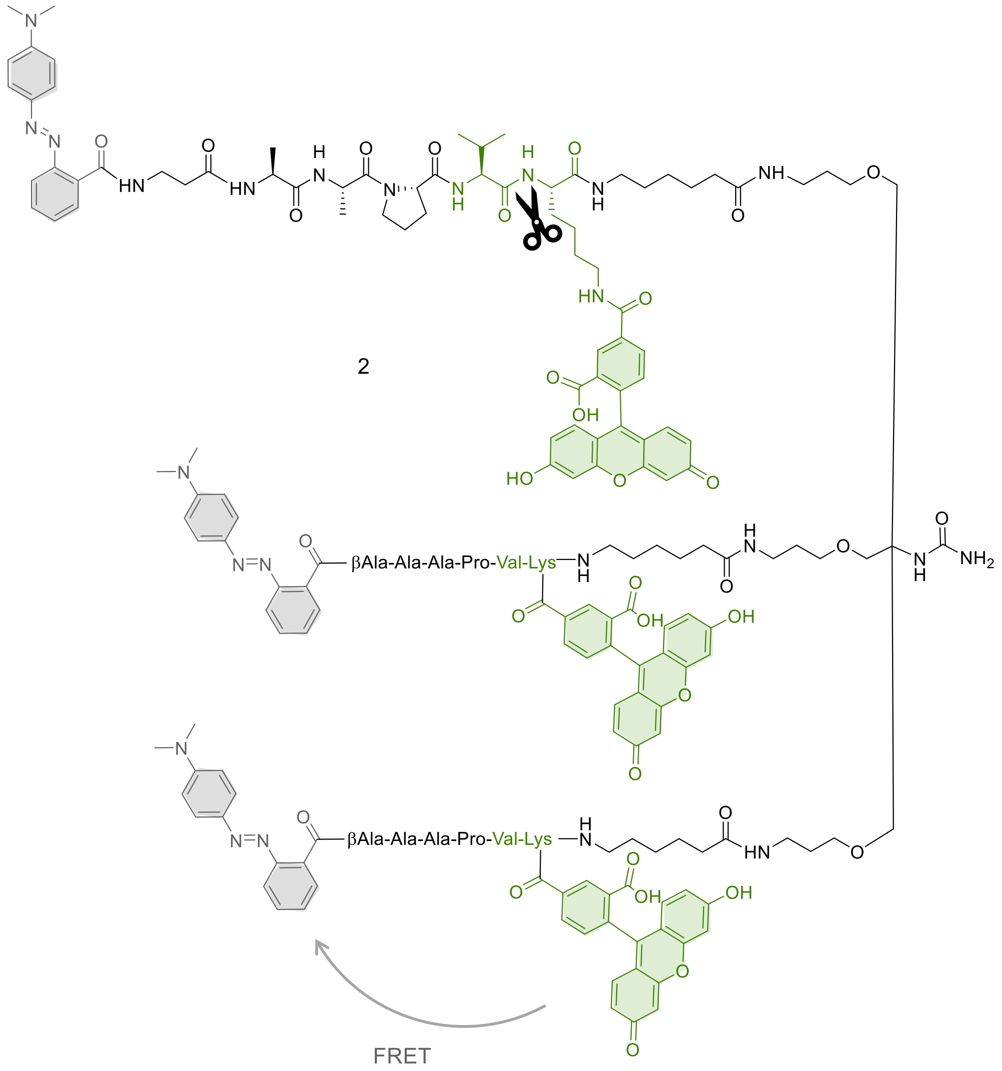
2

Figure 10 Structure of compound **2** (Neutrophil Elastase Sensor, **NES**). The cleavage site is highlighted in green, between the Val↑Lys residues. 5-carboxyfluorescein is the fluorophore (FRET donor) at the amino terminus and the quencher (Methyl Red) is located at the C-terminal end of the peptide (FRET acceptor).

NES (**2**) provided an improvement in amplification of signal capacity when compared to **NAP** (**1**) thanks to the presence of the Methyl Red quenchers, but amplification was still limited. This limited amplification can be explained by the effect of self-quenching following cleavage (during activation, Methyl Red containing fragments are released, but three molecules of fluorescein remain attached to the tribranched "core" with their close proximity leading to self-quenching, limiting fluorescence emission). It was also non-specifically cleaved.

3.2 Synthesis of fluorogenic probes for elastase detection

3.2.1 Synthesis of tribranched scaffold

The first step in the synthesis of the tri-branched probes was the synthesis of the trimeric scaffold **7,**[78] that can be immobilized into a solid support to build the peptide sequences (Figure 10). Thus, tris-nitrile **3** was prepared by the 1,4-addition of acrylonitrile to tris(hydroxymethyl)aminomethane. [79] The free amino group in **3** was then Boc protected using Boc_2O. The three terminal nitriles in **4** were reduced to the corresponding primary amines with borane–THF complex to **5.** The free amino groups of **5** were protected with **8** (2-acetyl-dimedone) to yield **6**. At this point, cleavage of the Boc group exposes the free amine, which was transformed to the isocyanate **7** following the procedure reported by Knölker. [80] Purification steps reported following the synthesis of compounds **3** and **4** were removed, with crudes taken forward. Thus, only one silica gel column purification was required following the protection of **5** with 2-acetyl-dimedone, to give the pure scaffold **6**, that can be converted into the corresponding isocyanate **7** *in situ*.

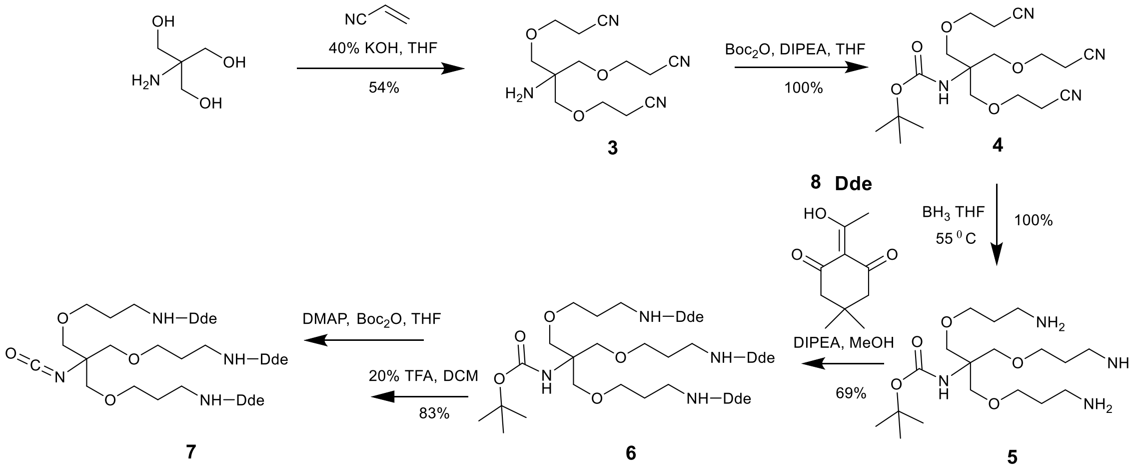

Figure 11. Synthesis of the tri-branched scaffold **7.** The overall yield was 8.4 %.

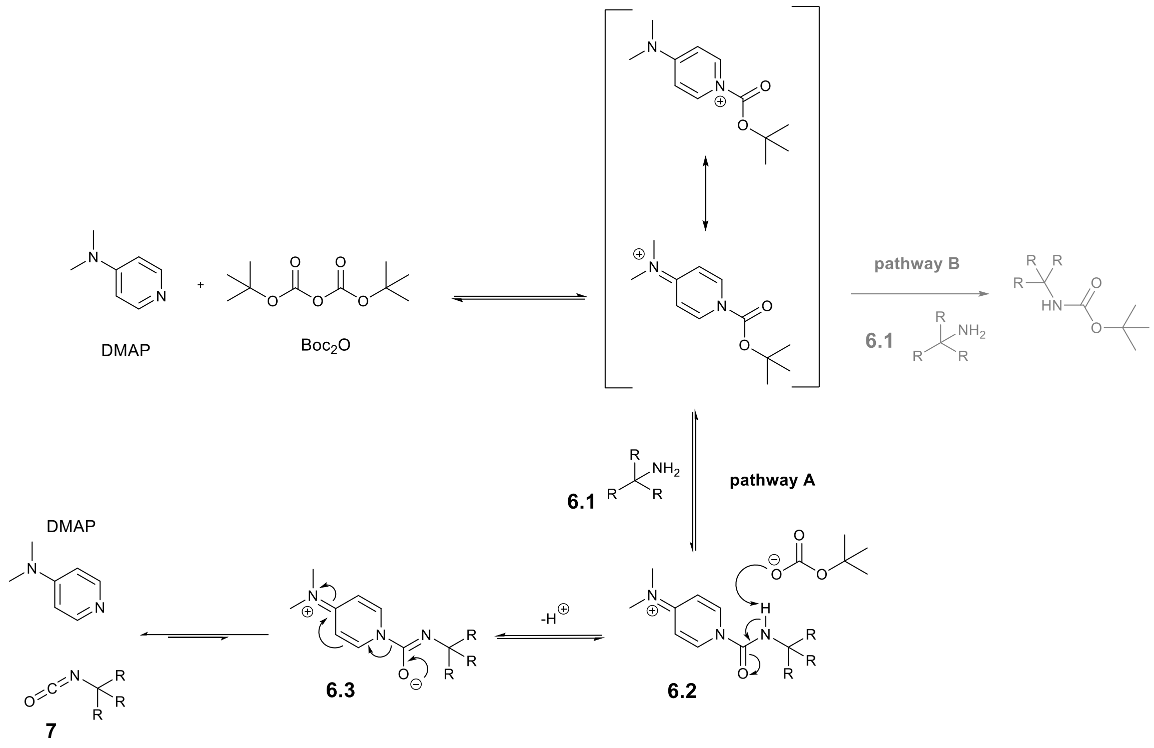

Figure 12. Mechanism of formation of isocyanate **7** from the hindered amine **6.1.**

The isocyanate formation reported by Knolker[80] is based on the conversion of highly hindered amines into isocyanates in the presence of Boc$_2$O and stoichiometric amounts of DMAP leading to the synthesis of the corresponding isocyanate (instead of the Boc protected amine). DMAP first reacts with Boc$_2$O to give Boc pyridinium in a stoichiometric ratio to form the Boc protected DMAP. Nucleophilic attack of the amine at the tert-butoxycarbonyl group on the pyridinium leads to loss of tert-butanol and formation of **6.2**. Finally, loss of the pyridinium leaving group results in formation of the isocyanate **7** and re-generation of DMAP. The reaction is predominantly occurring via pathway A, whilst pathway B (conventional Boc protection using catalytic amount of DMAP) would lead to the formation of the Boc-protected amine.

3.2.2 Neutrophil Elastase Sensor (NES)

For the synthesis of **NES** (**2**), the tribranched isocyanate scaffold (**7**) was inmobilised into an aminomethyl ChemMatrix (0.7-1 mmol/g, 100-200 mesh) resin via an Fmoc-Rink amide linker using DIPEA and DMAP. Once the tribranched compound was immobilized into the solid support, the Dde protecting groups were removed using 2% hydrazine in DMF and the resulting free amines served as the starting point to build the peptide sequences by standard Fmoc SPPS with DIC/Oxyma as the coupling combination (Figure 13).

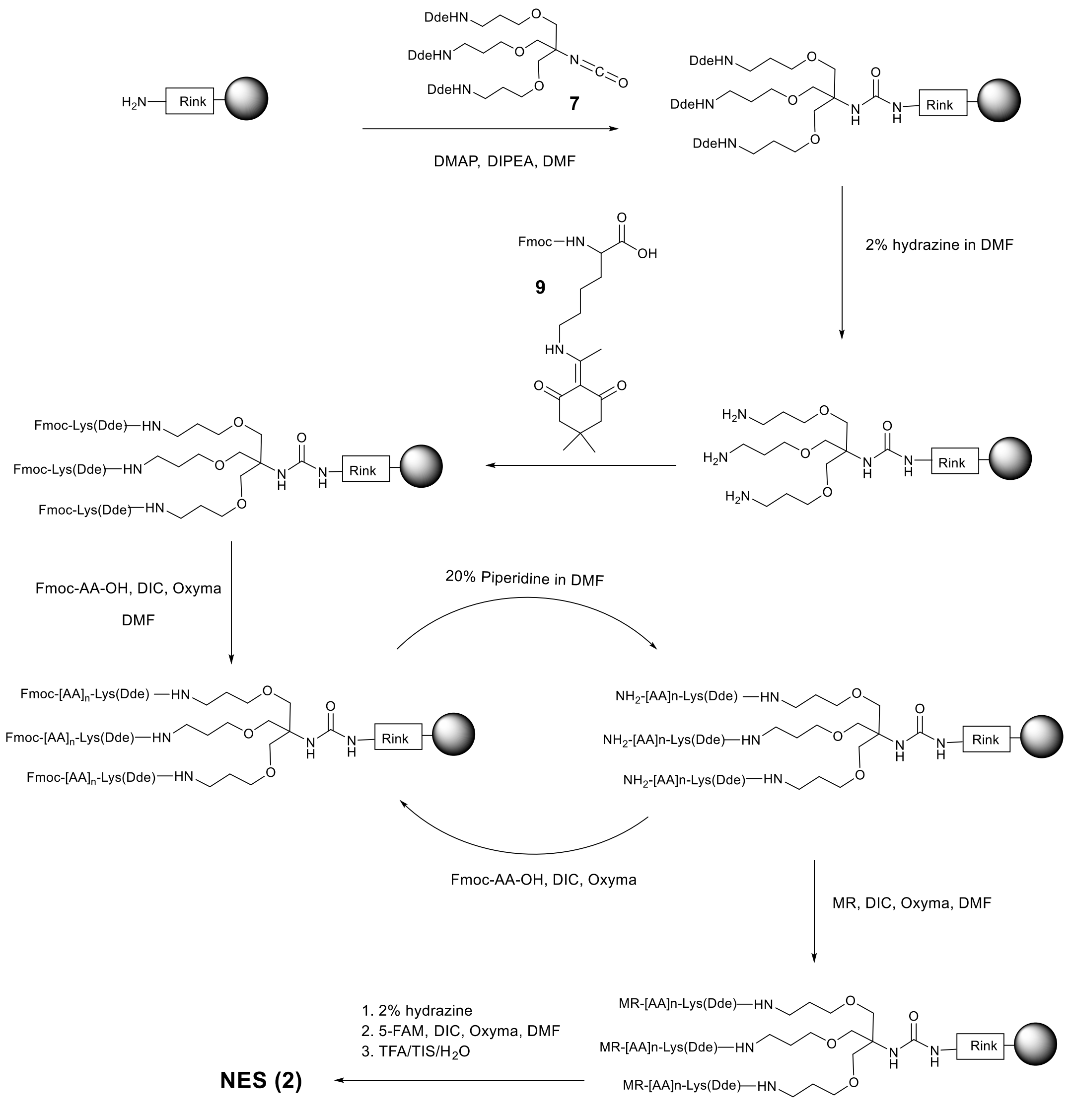

Figure 13. Procedure for the synthesis of the tri-branched probe **2** (**NES**) on the solid phase. The tribranched scaffold (**7**) was immobilised on an aminomethyl resin. This was followed by standard Fmoc solid-phase peptide synthesis to build the FRET labelled peptides. The last steps involved orthogonal deprotection of the lysine and incorporation of the 5-carboxyfluorescein fluorophore.

Fmoc-Lys(Dde)-OH (**9**) was synthesised from Fmoc-Lys-OH·HCl[81] by protecting the amino side chain using 2-acetyldimedone (**8**), which was synthesised from dimedone in presence of acetic acid, DMAP and EDC·HCl (Figure 14).

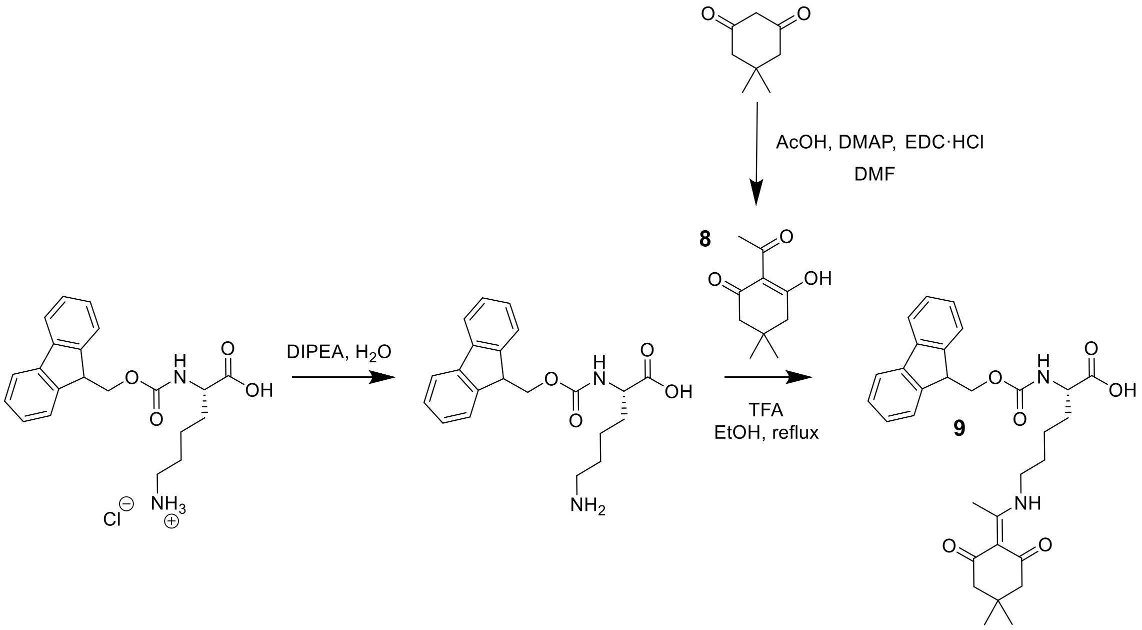

Figure 14. Synthesis of compound **9**. The Dde protected lysine was synthesized from Fmoc-Lys-OH·HCl and allowed orthogonal deprotection of the lysine side-chain amino group during SPPS synthesis. Yield 66%.

Fmoc-Lys(Dde)-OH (**9**) was coupled onto the three free terminal amino groups on the immobilised tribranched scaffold, followed by the consecutive Fmoc-amino acids. Fmoc-Lys(Dde)-OH (**9**) allows orthogonal deprotection to incorporate the fluorophore 5-carboxyfluorescein in the last step before final cleavage from the resin (Figure 13). Each deprotection and coupling step was verified by ninhydrin tests and cleavage tests were performed following certain couplings to allow the intermediate peptides to be analysed by HPLC and MALDI-MS and ascertain problematic couplings.

NES (**2**) was isolated *via* semi-preparative RP-HPLC purification (90% purity), but in an overall yield of only 2%, (attributed to the complexity of the tri-branched compound with many impurities with similar retention times. The absorbance spectrum was consistent with the FRET pair choice, with a maximum absorption observed at 500 nm due to the presence of the dyes (5-carboxyfluorescein and Methyl Red) with MS data consistent with the structure of the desired probe.

- **Biological evaluation of NES**

The probe when exposed to hNE gave full activation within seconds (Figure 15b), providing a maximal 8-fold increase in fluorescence after 10 min. Since **NES** was designed to target the three serprocidins that are present in neutrophils following an immune challenge, Proteinase 3 and and Cathepsin G were also observed to cleave the probe (Figure 15c).

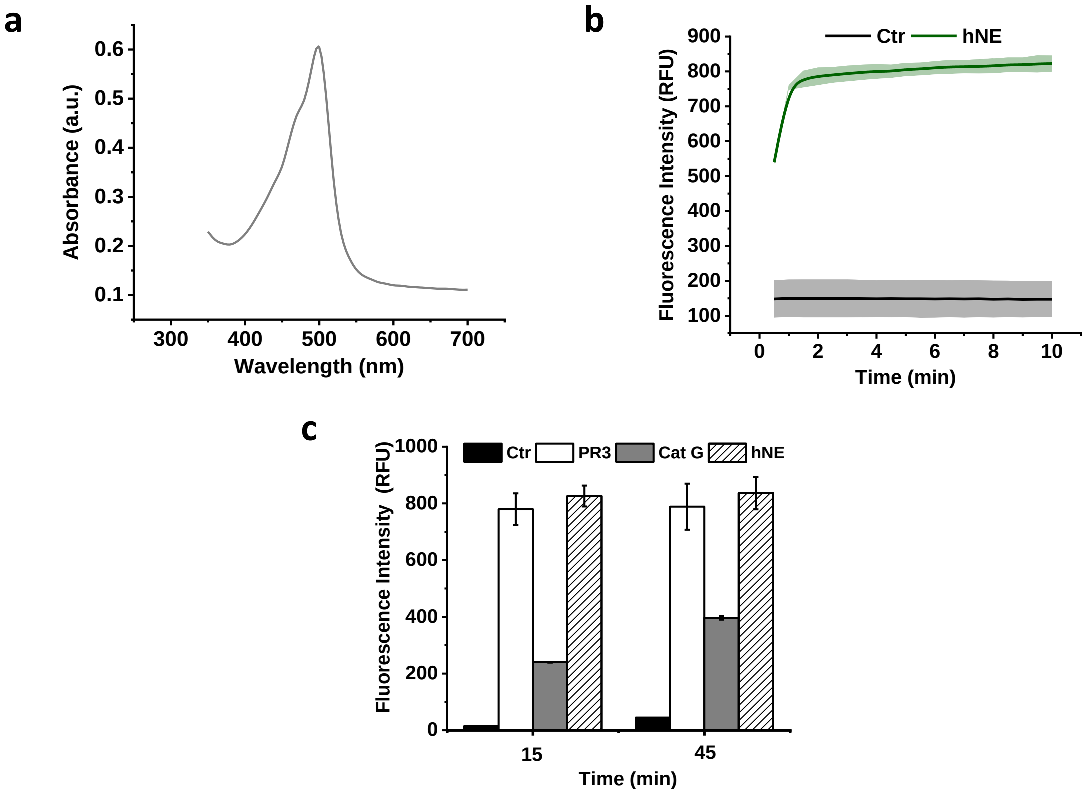

Figure 15. a) Absorption spectrum of the **NES** probe (5 µM) measured in the range from 350 to 700 nm; **b)** The time-dependent activation of fluorescence emission (de-quenching) of **NES** (**2**, 5 µM) following incubation with or without hNE (100 nM, n = 2). **c)** Specificity assessment of the **NES** (5 µM) incubated in HEPES buffer pH 7.4 or in the presence of 100 nM of hNE, Proteinase 3 (PR3) or Cathepsin G (CG) (37°C, n = 2). Ctr: Control, no hNE.

To evaluate the probe's capacity to detect hNE in cells, primary human neutrophils were isolated from healthy patients and activated in presence of calcium ionophore activator (A23187) [82], which binds calcium ion triggering an influx of Ca^{2+} across the plasma membrane into the intracellular space in neutrophils. [83] High levels of intracellular Ca^{2+} result in activation of neutrophils and lead to granule proteases activation and ROS production via activation of the NADPH-oxidase, effective mechanisms to kill bacterial pathogens by digesting them or damage their DNA, proteins, and cell membranes. [83]

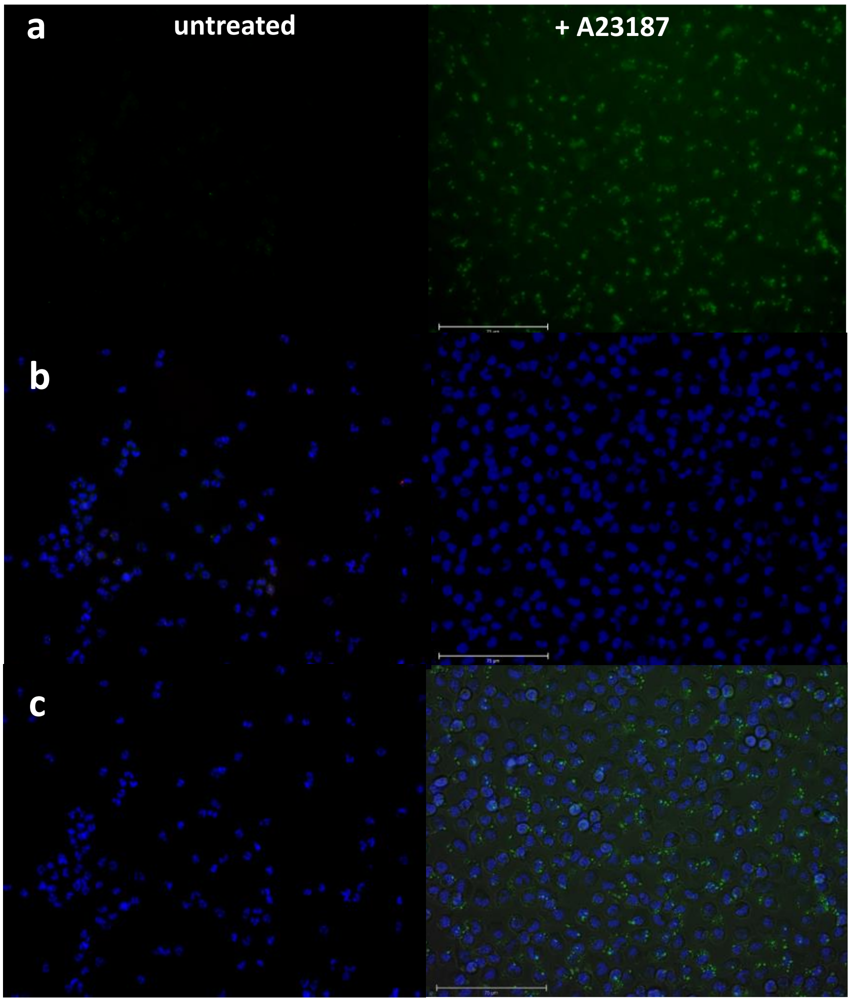

Figure 16. Calcium ionophore A23187 (10 µM) activated neutrophils in the presence of **NES (2)** show a moderate increase in fluorescence signal from the probe. Calcium ionophore A23187 (10 µM) and **NES** (5 µM) were incubated with the neutrophils for 30 min at 37°C. The nuclei were stained with Hoescht (5 µM) for 30 min before acquiring the images. **a)** Green channel (**NES**) (λ_{ex}: 447-494 nm λ_{em}: 500-554 nm) **b)** Blue channel (Hoescht) λ_{ex}: 340-395 nm λ_{em}: 430-505 nm **c)** Merged. Scale bar = 75 µm. Imaged with EVOS FL AUTO2 Cell Imaging System. Images from G. Rinaldi.

Upon activation of neutrophils, an increase in fluorescence was detected in neutrophils that were exposed to the calcium ionophore activator (A23187) and **NES** (Figure 16) and no fluorescence was observed in the neutrophils that were not exposed to the activator (but in the presence of **NES**). However, no significant differences were observed between NETotic and non-NETotic neutrophils (not shown).

3.2.3 Optimisation of the probe - HNE-FQ (11)

In an attempt to tackle the key limitation of signal amplification that both **NAP**(**1**) and **NES** (**2**) suffered from, the design was optimised incorporating the best features of both probes; the high specificity for human neutrophil elastase of **NAP** and the "super-silent" character of **NES** while using the tribranched approach for signal amplification.

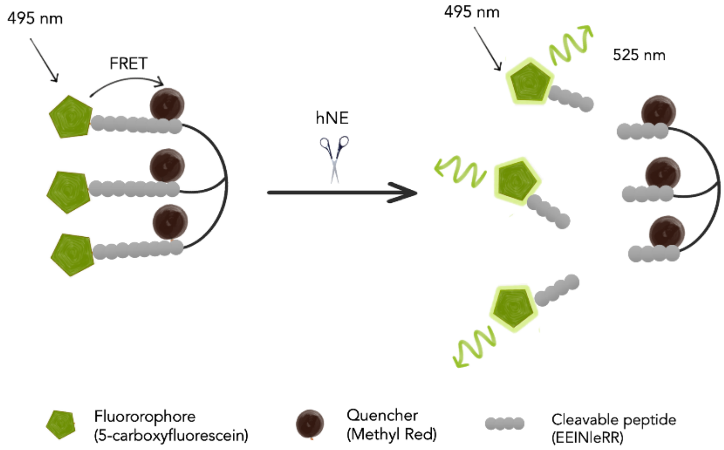

Figure 17. HNE-FQ uses the highly selective substrate used in **NAP** and FRET quenching with the FRET pair FAM and MR. Upon cleavage by hNE, the fluorophores are released far from the three quenchers (that remain as part of the core).

- **Probe design and synthesis**

The design used the same trivalent scaffold combined with three FRET-labelled peptides using the highly specific sequence for hNE used in **NAP** (**1**) and the same FRET pair as used in **NES** (**2**), 5-carboxyfluorescein and Methyl Red. [84] In order to improve the signal amplification capacity of the probe, a reorientation of the FRET pair was investigated, with 5-carboxyfluorescein located at the amino terminus of the peptide, with Methyl Red located at the C-terminus of each peptide chain. This design allowed the release of the three peptide fragments, each containing a 5-carboxyfluorescein moiety, allowing signal amplification, and preventing the linear quenching that **NES** (**2**) suffered from, allowing full activation/amplification upon cleavage by the protease.

In order to simplify the synthesis of the probe and to avoid the need for orthogonal deprotection[85] on the lysine (which can complicate the synthesis of these branched peptides due to incomplete deprotection on one or more branches), the quencher Methyl Red was incorporated as the building block Fmoc-Lys(MR)-OH (**10**) and was synthesised by coupling Fmoc-Lys-OH with the activated NHS ester of Methyl Red (Figure 18).

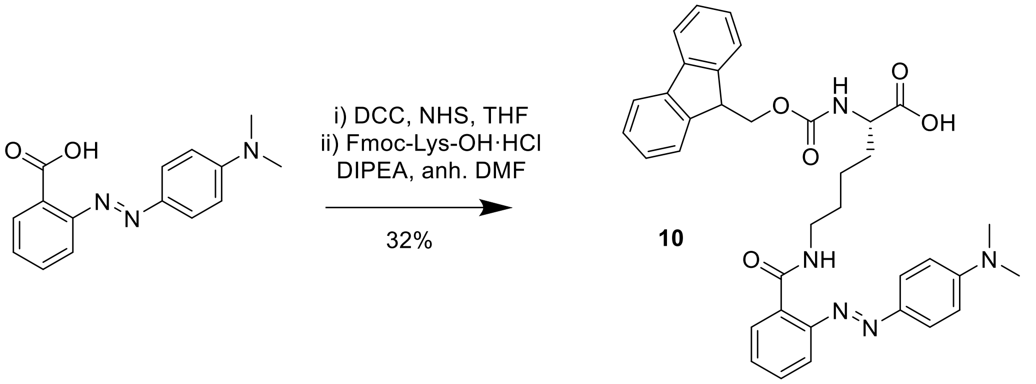

Figure 18. Synthesis of compound **10**. The quencher containing amino acid was synthesized from Fmoc-Lys-OH by coupling of the Methyl Red quencher on the Ɛ-amino to simplify the synthesis of the tribranched compound by avoiding the need for orthogonal deprotection during the SPPS.

HNE-FQ (**11**, Figure 19) was synthesised using a similar approach to that described for **NES** (**2**), with isocyanate **7** immobilised onto an aminomethyl ChemMatrix resin (Figure 13) and the quencher containing lysine residue (**10**) incorporated as the first amino acid (using DIC/Oxyma). Attachment of the fluorophore (5-carboxyfluorescein) was carried out as the final step.

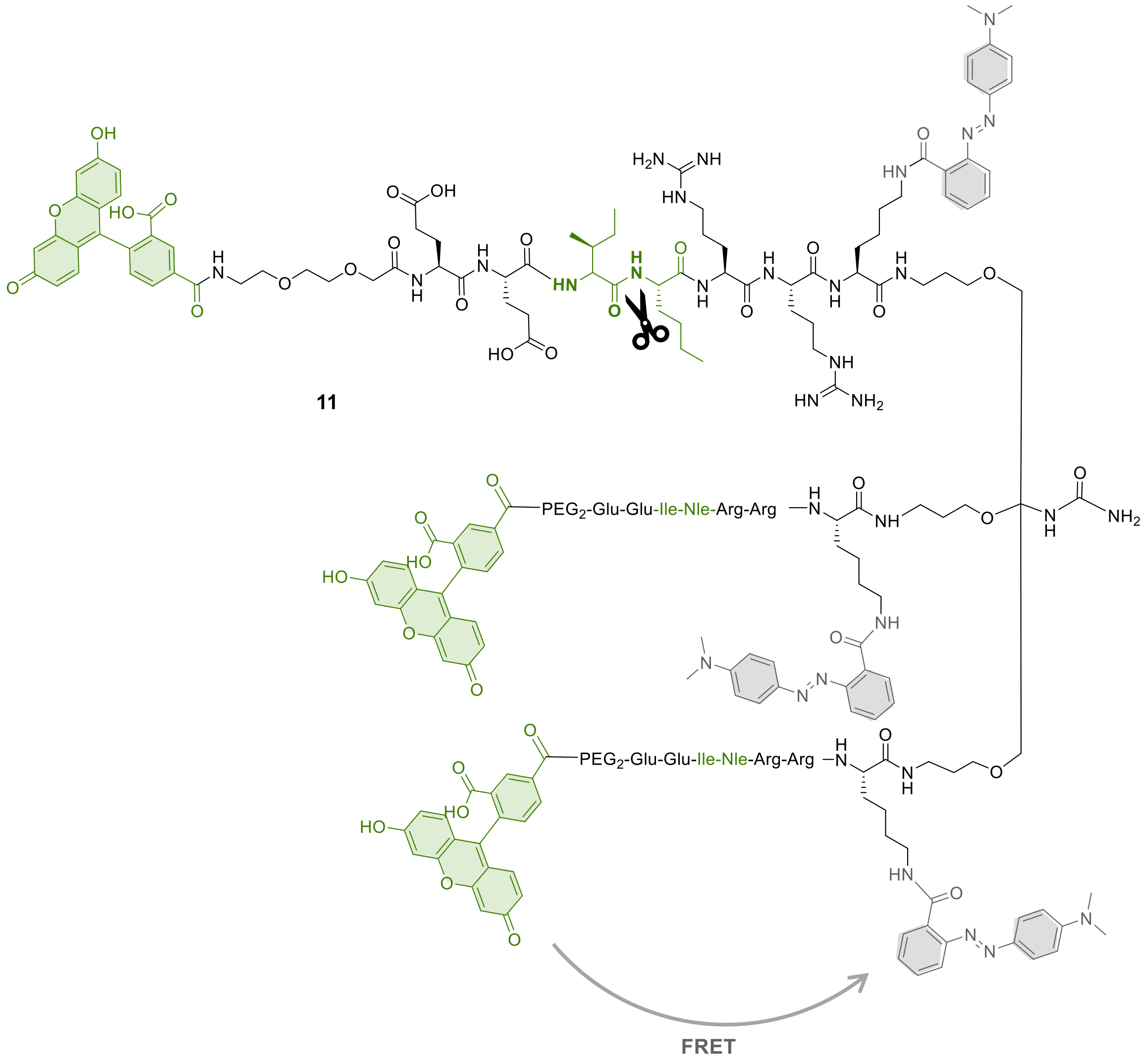

11

Figure 19. Structure of **HNE-FQ**. 5-carboxyfluorescein is the fluorophore (FRET donor) at the amino terminus and the quencher (Methyl Red) is located at the C-terminal end of the peptide (FRET acceptor). The cleavage site is highlighted in green, between the Ile↑Nle residues and a bis-ethylene glycol spacer was incorporated between the last amino acid and the fluorophore, to increase hydrophilicity and promote aqueous solubility.

Initially, attachment of carboxyfluorescein was done using the coupling combination of DIC/Oxyma. Semipreparative HPLC purification gave the trace shown in Figure 20, with the desired compound isolated in very low yield. On an attempt to improve the purity of the product (due to the issue with the fluorophore coupling step), a new set of coupling conditions were explored, using the NHS ester of 5-carboxyfluorescein diacetate. The use of the NHS ester led to a much higher purity of the crude product dramatically increasing the yield and ease of purification.

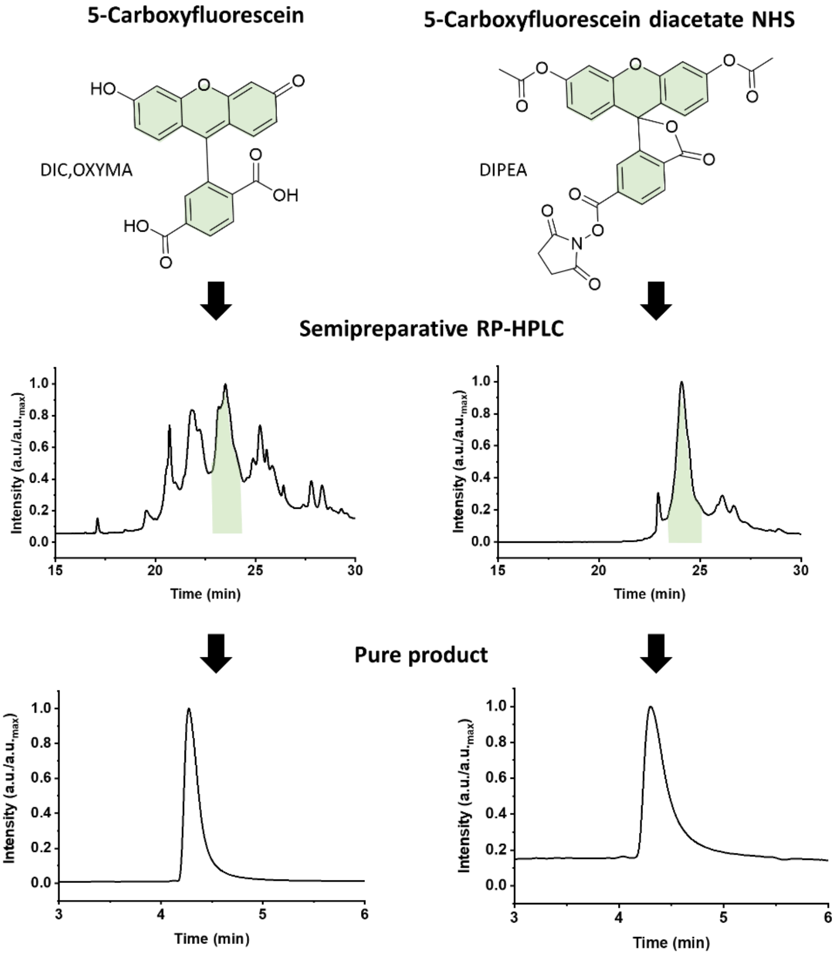

Figure 20. Reverse phase semipreparative HPLC chromatograms (detection 495 nm) showing the differences in the purity of the crude peptide following the final coupling using two different coupling combinations: 5-Carboxyfluorescein/DIC/Oxyma (left) or the NHS ester of 5-Carboxyfluorescein diacetate (right), and the corresponding pure traces after purification (bottom traces). The flow rate was 2.5 mL/min and eluting with 0.1% FA in H_2O and 0.1% FA in ACN, with a gradient of 5 to 95% B over 35 min and an initial isocratic period of 2 min.

- ***In vitro* validation**

The absorption and emission spectrum of **HNE-FQ** (**11**) were consistent with the absorption of 5-carboxyfluorescein (Figure 21a) and the probe was optically silent. However, the addition of hNE (100 nM) rapidly de-quenched the probe (5 µM) (within minutes) with a 20-fold increase in fluorescence, while pre-incubation with hNE inhibitor sivelestat (100 µM) (Figure 21b) resulted in no increase of fluorescence (Figure 21b). The closely related neutrophil serine proteases Cathepsin G and Proteinase 3, showed negligible cleavage demonstrating that the probe was specific to hNE (Figure 21d).

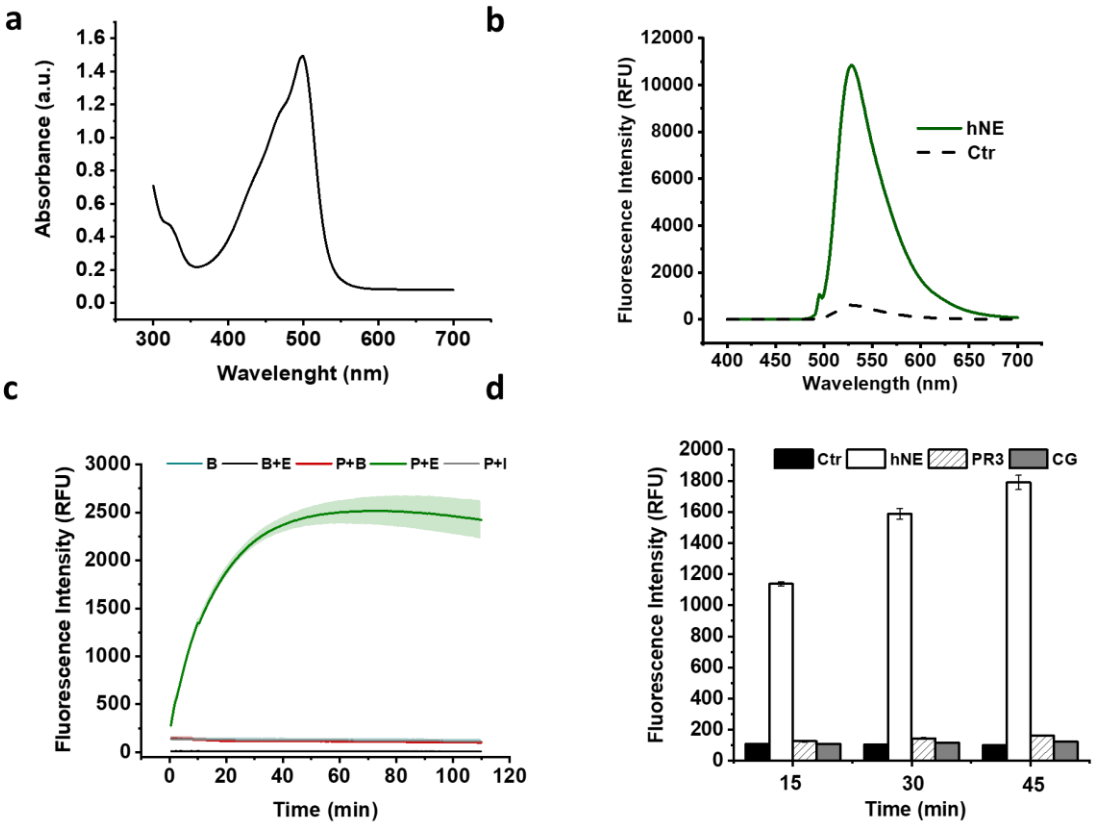

Figure 21. a) Absorption spectrum of probe **HNE-FQ** (**11**, 5 µM) ; **b)** Fluorescence emission spectrum of the **HNE-FQ** (**11**, 5 µM) before (black) and after (green) 40 min incubation with hNE (100 nM), n = 2, (ex/em = 495/528 nm); **c)** The time-course de-quenching of the probe (5 µM) following incubation with hNE (100 nM), in the presence or absence of the inhibitor sivelestat (SIV, 100 µM) n = 3. B = buffer; E = enzyme; P = probe; I = inhibitor. **d)** Specificity assessment of the probe (5 µM) incubated in the presence of hNE (100 nM) and related serprocidins Proteinase 3 (PR3, 100 nM) and Cathepsin G (CG, 300 nM) with time at 37°C, n = 3. Ctr: Control, no hNE

Specific hydrolytic cleavage in **HNE-FQ**, between Ile↑Nle, was confirmed following probe incubation with hNE by analysis of the reaction mixture by MALDI-TOF MS and LC-MS and confirmation of the appearance of peaks with the expected masses (Table 1).

Table 1. Cleavage site confirmation of probe **HNE-FQ** (**11**) using mass spectrometry.

Fragment	**Chemical formula**	**Method**	**Expected *m/z***	**Found *m/z***
Full probe	$C_{260}H_{351}N_{59}O_{67}^{+}$	MALDI-TOF MS	5375.10	5371.00
N terminal	$C_{43}H_{48}N_{4}O_{17}^{+}$	LC-MS	893.3	893.2
C terminal (1-branched)	$C_{174}H_{259}N_{51}O_{35}^{+}$	MALDI-TOF MS	3625.01	3625.09
C terminal (fully cleaved)	$C_{131}H_{213}N_{47}O_{19}^{+}$	MALDI-TOF MS	2750.72	2750.63

In order to determine the catalytic parameters of the probe, hNE was incubated with the probe at concentrations ranging from 0.04 μM to 100 μM (in triplicate). At higher concentrations of the probe (50 to 100 µM), saturation of signal was observed. The relative fluorescence was plotted against time (min) to allow initial (linear) velocity values (Vo) (during the first 10 min of reaction) to be determined (Table 2 and Figure 22).

Table 2. Initial velocities at increasing concentrations of probe **HNE-FQ** * Excluded data due to saturation of signal. Velocity units were converted to M/s using the conversion factor [P]/RFU_{max}**,** where [P] is the concentration of the probe and RFU_{max} the maximum fluorescence emission provided by the probe once fully activated at that given concentration). The conversion factor was calculated from the activation profile of **HNE-FQ** at 5 μM, whose maximum fluorescence emission (RFU_{max}) observed was 2071 units (conversion factor is 0.000005/2071).

[Probe] (μM)	**E_T (nM)**	**V_o** (RFU/min)	**V_{o*} (M/s)**	**1/[Probe]**	**1/V_o**
50*	100	143.7*	$5.8 \times 10^{-9*}$	$2.0 \times 10^{4*}$	$1.8 \times 10^{8*}$
25		173.7	7.0×10^{-9}	4.0×10^{4}	1.4×10^{8}
12.5		169.8	6.8×10^{-9}	8.0×10^{4}	1.5×10^{8}
5		88.4	3.6×10^{-9}	2.0×10^{5}	2.8×10^{8}
1		25.0	1.0×10^{-9}	1.0×10^{6}	9.9×10^{8}
0.2		6.3	2.5×10^{-10}	5.0×10^{6}	3.9×10^{9}
0.04		1.4	5.8×10^{-11}	2.5×10^{7}	1.7×10^{10}

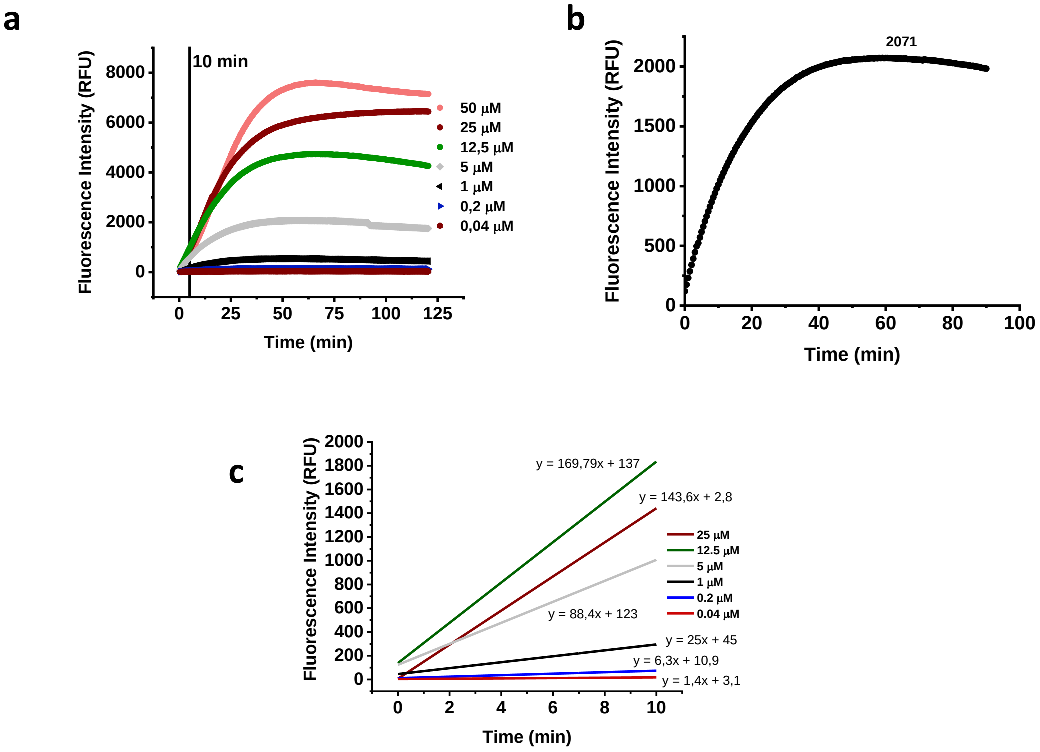

Figure 22. a) The time-course de-quenching of probe at increasing concentrations following incubation with a constant concentration of hNE (100 nM). Reference lines indicates the cutoff time (10 min) for calculation of initial velocity. **b)** Conversion factor [P]/RFU$_{max}$**,** where [P] is 5 μM, concentration of **HNE-FQ**, and the maximum fluorescence emission (RFU$_{max}$) observed following full activation was 2071 units. n = 3 **c)** Initial velocity plots were calculated based on the linear section of the curve, over the first 10 minutes of activation and used to plot Michaelis Menten and Linewaver-Burk plots , plots display average of n = 3.

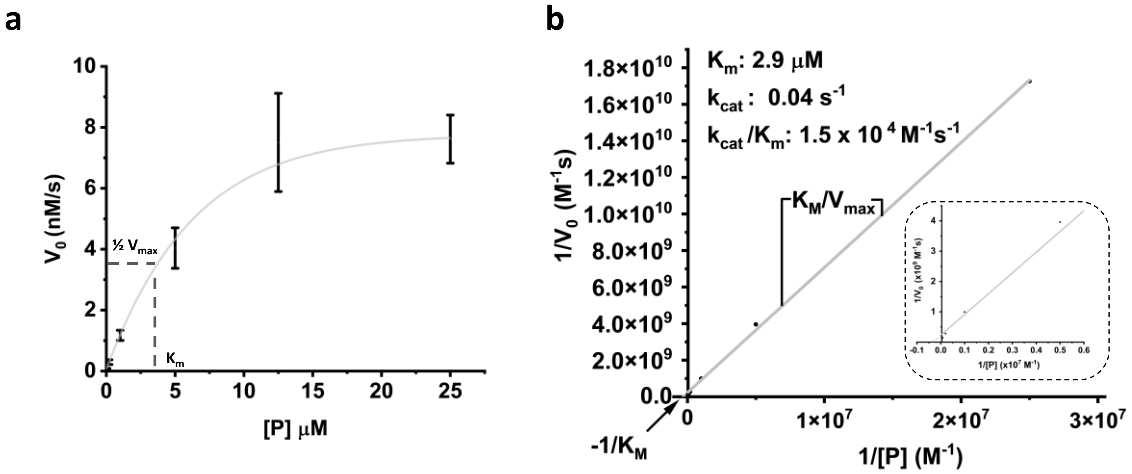

Figure 23 a) Michaelis Menten curve generated from the initial velocities calculated in the range of 0.04 to 25 μM. Linearisation of the data allows generation of **c)** Lineweaver Burk plot (1/V vs 1/[P]) or **d)** Eadie Hofstee plot (V vs V/S). All datapoints are n=3.

The values of 1/V were plotted against concentration of probe 1/[S] to give a Lineweaver-Burk Plot allowing kinetic values to be determined, K_m was 2.9 µM, V_{max} 4.3 nM/s and k_{cat} 0.04 s^{-1}. The catalytic efficiency (K_{cat}/k_m) was 1.5 × 10^4 $M^{-1}s^{-1}$.

The probe should be able to provide information on the activity of elastase at physiological pH, therefore it was important to evaluate the effect of pH in the probe, since the fluorescence emission of fluorescein shows pH dependency[86-88], with the fluorescence emission and absorption significantly reduced below neutral pH (Figure 24).

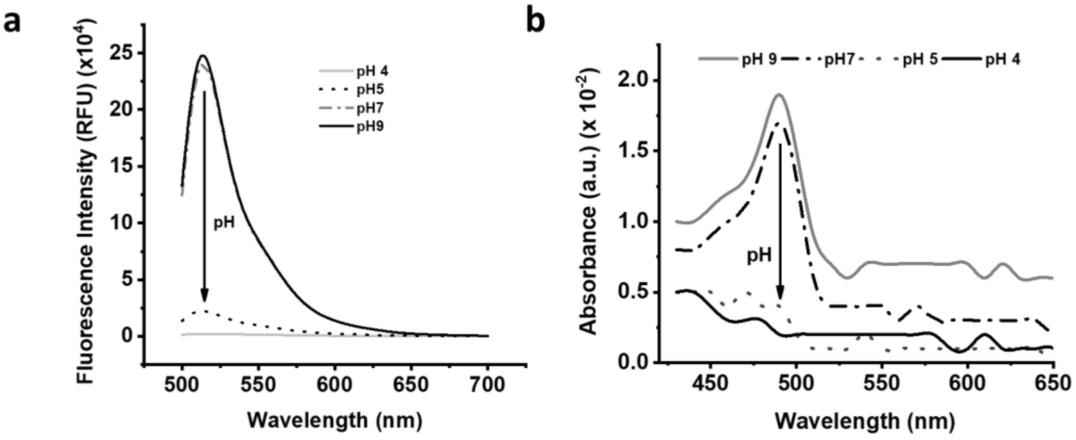

Figure 24 a) Fluorescence emission and **b)** absorption spectrum of 5-carboxyfluorescein in different pH buffers (pH's 4, 5, 7 or 9).

The pH dependency of fluorescein has been understood for some time, with several experimental studies reported to better understand the effect of the different protonation states of the fluorophore on its photophysical properties. When evaluating the quantum yields of the different protonation species of fluorescein, the dianion has the highest quantum yield (Φ = 0.9-1.0) for emission at 510 nm, the quantum yield of the mono anion is estimated to be 0.2 to 0.3 (at pH 5.5) with the neutral forms even lower. At acidic pH's a cation with a blue shift in emission is formed, with a maximum emission at 475 nm. [89]

The neutral and mono-anionic forms of fluorescein coexist with their corresponding lactone form, that results from cyclization with the carboxylic acid leading to a non-conjugated and therefore non-fluorescent compound (Figure 20). [86]

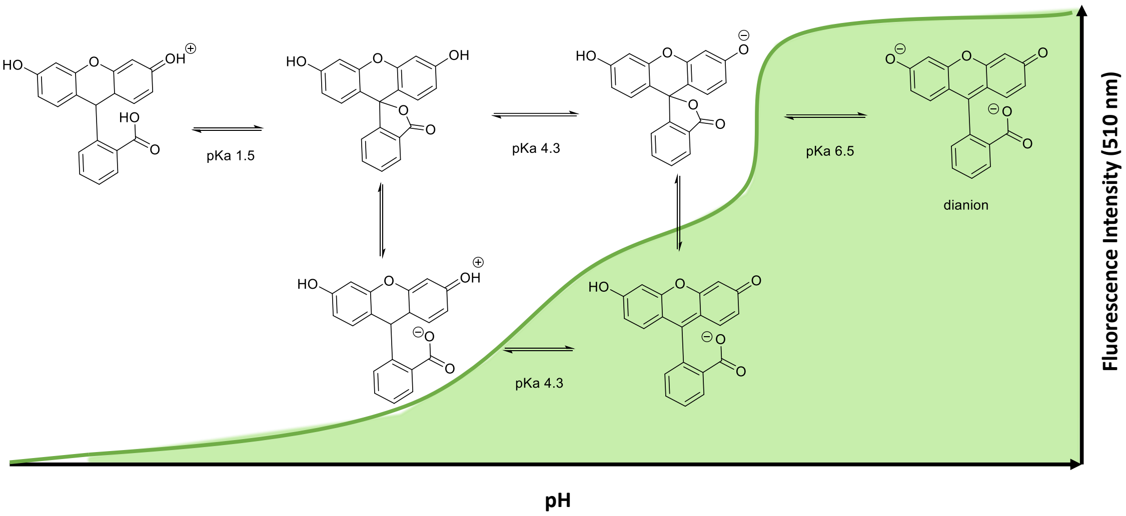

Figure 25 Fluorescein protonation states at different pH and their relative fluorescence intensities. Adapted from reference 88 with permission from MDPI, Basel, Switzerland. [88]

The effect of pH on the fluorescence signal of **HNE-FQ** (**11**) was assessed by evaluating the fluorescence emission of cleaved and uncleaved probe. The fluorescence intensity, as expected due to the pH sensitive nature of the dye, decreased with pH (Figure 26). The fluorescence signal changes were also evaluated in different biological microenvironments by analysis of the intact or activated probe in reaction buffer (control), complete cell media, 10% fetal bovine serum (FBS) or HeLa cell lysate. The fluorescence signal of the activated probe was not affected over time under these conditions and, similarly, the intact probe was not activated or switched-on in any of the media evaluated in absence of hNE.

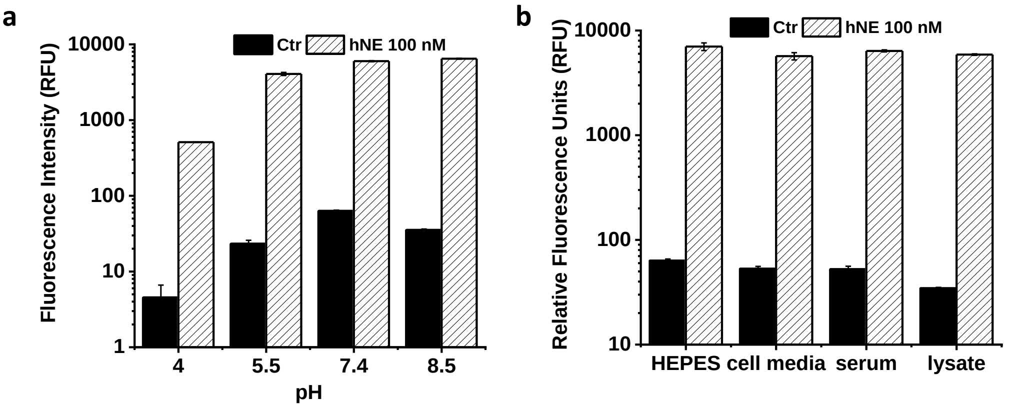

Figure 26 a) Effect of pH on the fluorescence signal of the cleaved and uncleaved probe. Stocks of cleaved and uncleaved probe were generated by incubating the probe (85 µM) in 50 mM HEPES pH 7.4, in a final volume of 200 µL, with or without hNE (100 nM). Cleaved or uncleaved probe solutions (15 µM) were added to the different pH buffers (4.0, 5.5, 7.4 and 8.5) and fluorescent intensities measured using a fluorescence microplate reader, n = 3. **b)** The effect of different biological microenvironment on the fluorescence signal was evaluated by incubating intact or hNE cleaved probe (15 µM) in HEPES buffer (control), complete cell media , 10% Fetal Bovine Serum (FBS) or Hela cell lysate) and incubated for 2 hours at 37°C in a final volume of 50 µL. Fluorescence intensities were read using a fluorescence microplate reader (for the Hela cell lysate cells, a T25 at confluency was used, cells were resuspended in sterile water (5 mL), approximately 1 million cells/mL, and incubated for 30 min at 37°C). The resulting lysate was centrifuged at 13000 g for 10 min and the supernatant collected and used immediately. Ctr: Control, no hNE, n =3.

Finally, to prove that **HNE-FQ** provides a significantly higher amplification capacity compared to the previously designed probes, the activation profiles of the different probes were compared. The probe (5 µM), when incubated in presence of the hNE, provided a 22-fold increase in signal within one hour of incubation, while that increase was only about 6-fold for **NES** (**2**) and 3.7-fold for **NAP** (**1**).

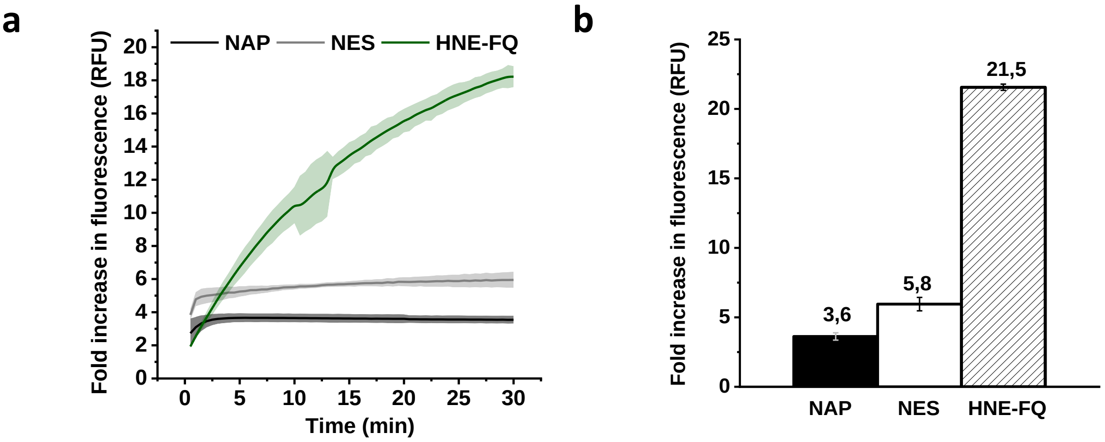

Figure 27 a) NAP (**1**), **NES** (**2**) or **HNE-FQ** (**11**) (all at 5 µM in 50 mM HEPES buffer pH 7.5) were exposed to hNE (100 nM) and activation was monitored over 30 minutes at 37°C. **b)** Bar plot showing the maximum fold increase observed upon activation of all three probes. **NAP** n = 3; **NES** n = 2; **HNE-FQ** n = 3.

The optimised design in **HNE-FQ** (**11**) tackles the limitations of the two previous designs by reorienting the FRET pair labels on the peptide sequence (5-carboxyfluorescein on the N-terminus and Methyl Red on the C-terminus), allowing full release of three carboxyfluorescein fluorophores. This rearrangement resulted in a significant improvement in the signal amplification upon probe activation (22-fold).

Taken together, optimisation of the previous elastase probes led to probe **HNE-FQ**, which showed a significant improvement in fluorescence signal amplification and a major reduction in background fluorescent levels.

- **Detection of elastase in activated neutrophils by flow cytometry**

To evaluate if **HNE-FQ** was able to detect hNE in neutrophils, primary human neutrophils were isolated from healthy patients (and activated by exposure to calcium ionophore A23187[82] or chemoattractant fMLF). [90] fMLF is a bacterial peptide that acts on receptors FPR, FPRL1[90], and leads to release of Ca^{2+} from the endoplasmatic reticulum via phospholipase C signal transduction pathway. Both fMlF and A23187 result in high levels of intracellular Ca^{2+} that trigger activation of neutrophils. [83]

When primary human neutrophils were exposed to fMlf or the calcium ionophore A23187 and stained with HNE-FQ, an increase in fluorescence intensity was detected in flow cytometry, whilst control neutrophils (quiescent), or neutrophils pre-treated with the elastase inhibitor sivelestat, showed reduced or negligible levels of fluorescence. The increase in fluorescence upon activation was modest in neutrophils activated with calcium ionophore A23187, whilst those activated by fMLF showed a significant increase. These results suggest that **HNE-FQ** (**11**) can detect activation of neutrophils, and that the fluorescence signal comes specifically from elastase detection, since inhibition of the protease with Sivelestat significantly neutralises the signal (Figure 28a). Besides, no fluorescence emission at the probe's emission wavelength could be detected in activated neutrophils that were not stained without probe (Figure 28b).

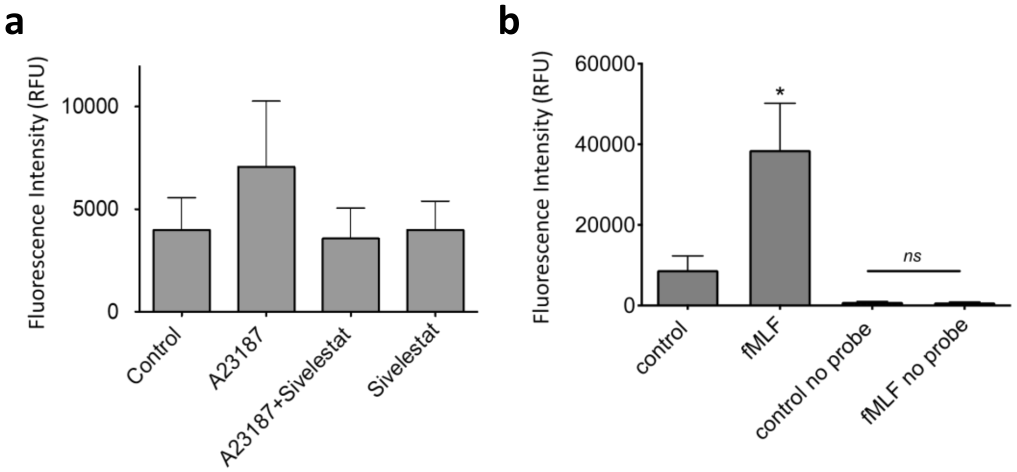

Figure 28 Flow cytometry assays of primary human neutrophils stained with the **HNE-FQ** exposed to different activators. **a)** Neutrophil activation was induced by exposure to calcium ionophore A23187 (10 μM), followed by incubation with **HNE-FQ** (**11**, 5 μM) in presence or absence of Sivelestat (100 μM) n=2. Control neutrophils and neutrophils preincubated with sivelestat showed low levels of activation when compared to those activated by A23187; **b)** Neutrophils were activated with fMLF (10 μM) and incubated with **HNE-FQ**. Controls showed negligible fluorescence when compared to activated neutrophils. Detection wavelengths: green channel (**HNE-FQ**) λ_{ex} 488 nm / λ_{em} 530/30 nm. Data from G. Rinaldi.

To further evaluate the capacity of the probe for monitoring neutrophil activation by flow cytometry the human promyelocytic the cell line HL-60 was used. This cell line is a valid cell culture model to study neutrophil differentiation[91], activation and NETs generation. To validate **HNE-FQ** (**11**), cells were stimulated with the vitamin A derivate all-*trans*-

retinoic acid (ATRA, 2 µM) for 4 days to induce a neutrophil-like phenotype. A quantitative nitro-blue tetrazolium (NBT) assay[92] was used to confirm differentiation into the neutrophil phenotype (experimental section, Figure 102).

Next, HL-60 differentiated neutrophils were stained with an antibody directed against the CD11b antigen, a well-known marker of neutrophil activation [82], and the probe **HNE-FQ** in the presence or absence of phorbol marismat acetate (PMA). [93] PMA is an activator of protein kinase C (PKC), which, like fMlf, increases levels of intracellular Ca^{2+} with activation of neutrophils. Under PMA exposure, an increase in the fluorescence intensity of neutrophils labeled with **HNE-FQ** was observed. In parallel, an increase in fluorescence intensity of $CD11b^+$ HL-60-derived neutrophils when treated with PMA was observed. The upper panels show the fluorescence profile of control and PMA-activated HL60 cells after staining with **HNE-FQ** (**11**) (blue) and CD11b (green). As shown by the overlay of the signals obtained in the presence of PMA, **HNE-FQ** probe was able to detect NETs formation in the flow cytometry assay (Figure 29)

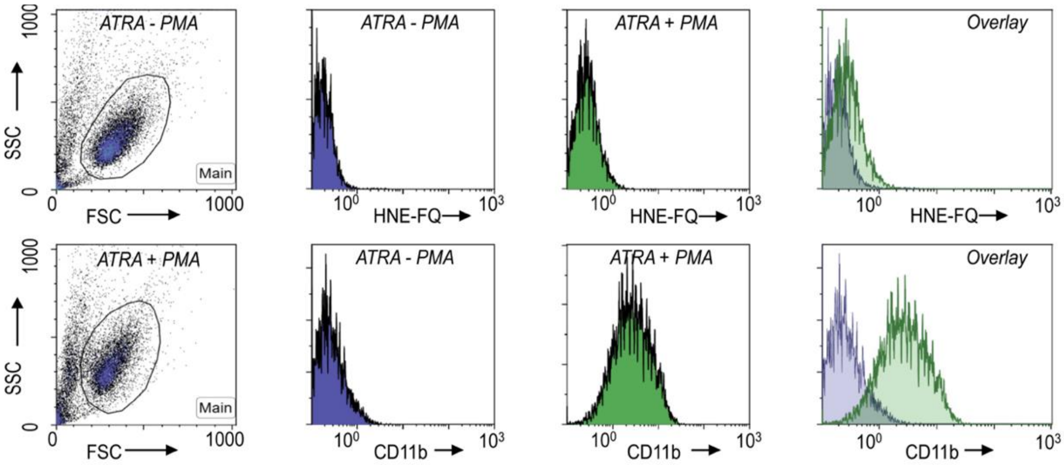

Figure 29 Detection of activated neutrophils by flow cytometry. Fluorescence profile of control (blue peak) or activated HL60 cells activated by PMA (100 nM, green peak). Upper panels, cells stained with the probe (5 µM). Lower panels: Cells stained with allophycocyanin labelled anti-CD11b Ab. Detection wavelengths: green channel (**11**, HNE-FQ) λ_{ex}: 488 nm / λ_{em}: 530/30 nm. Red channel (Cd11b-Ab) λ_{ex}: 633 nm / λ_{em}: 660/20 nm. Reproduced from reference 94 with permission from the Royal Society of Chemistry©. Data by G. Garoffolo. [94]

- **Imaging elastase in activated neutrophils and neutrophil extracellular traps**

The capabilities of the probe to image elastase activity in cells by fluorescence microscopy were evaluated in live cells. Primary human neutrophils were exposed to fMLF (10 µM) for 30 min and stained with nuclear DNA stain Hoescht and probe **HNE-FQ** (5 µM). An increase in fluorescence in the green channel was observed following activation with fMLF, while untreated neutrophils showed negligible fluorescence emission by **HNE-FQ** (Figure 30).

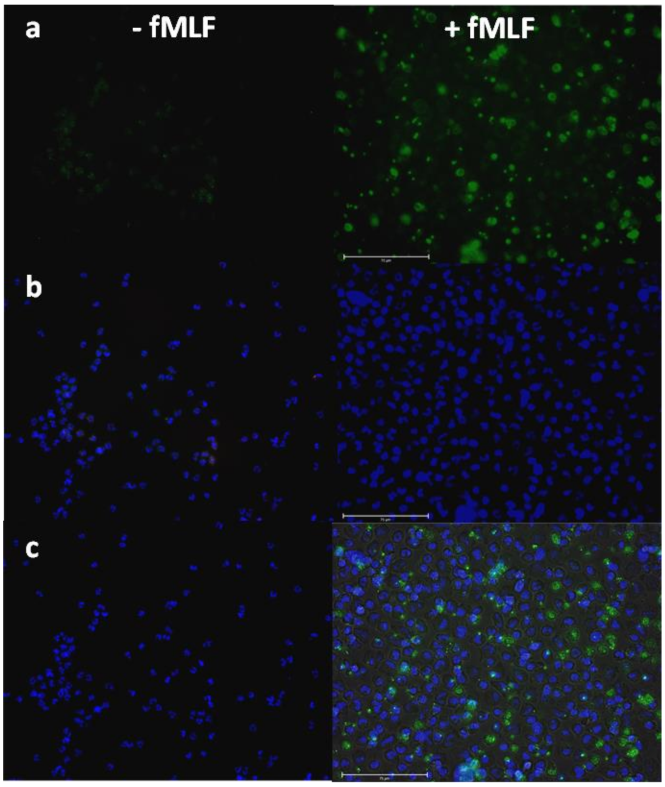

Figure 30 Fluorescence microscopy images of primary human neutrophils stained with Hoechst 33342 (100 nM, blue) and HNE-FQ (5 µM, green). Left: Control untreated neutrophils. Right: Neutrophils were exposed to fMLF (10 µM) and HNE-FQ for 30 min, followed by incubation with Hoescht (10 nM) for 30 min before acquiring the images. **a)** green channel (λ_{ex}: 447-494 nm / λ_{em}: 500-554 nm) **b)** blue channel (λ_{ex}: 340-395 nm / λ_{em}: 430-505 nm) **c)** merged. Data from G. Rinaldi. Imaged on an EVOS FL AUTO2 Cell Imaging System

PMA is a potent NETotic inducer. [95] In order to visualise NETs using **HNE-FQ**, primary human neutrophils were activated with PMA for 3 hours. An increase in fluorescence signal from **HNE-FQ** activation was observed in neutrophils activated with PMA, whilst negligible levels of fluorescence were observed in control neutrophils. To further evaluate specificity of the probe, neutrophils were pretreated with the elastase inhibitor Sivelestat. Pre-treatment with the inhibitor not only resulted in a reduced fluorescent signal in the green channel (from inhibition of elastase), but also a reduction in NET production, with no clear "NEtotic" structures observed (Figure 31). These results support that **HNE-FQ** (**11**) is specifically activated by hNE (with inhibition of the protease preventing probe activation) and that hNE is required for the production of NETs. [56]

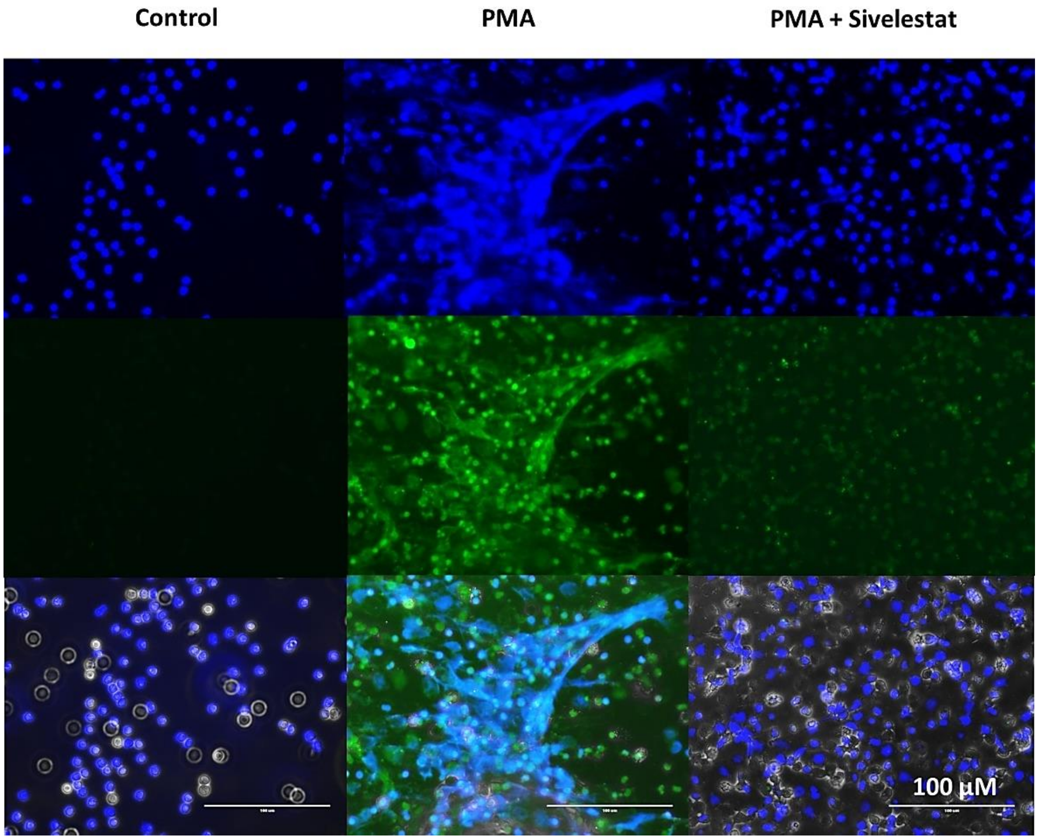

Figure 31 Fluorescence confocal microscopy images of primary human neutrophils stained with Hoechst 33342 (100 nM, blue) and **HNE-FQ** (5 µM, green). **Control:** neutrophils incubated with probe only for 3 h; **PMA:** PMA (10 nM) and probe for 3 h; **PMA + Sivelestat:** neutrophils preincubated with Sivelestat (100 µM) for 30 min and then with PMA (10 nM) and probe for 3 h. Following incubation, the nuclei was stained with Hoescht (100 nM, 30 min) before acquiring the images. Excitation and emission filters: green channel (probe) λ_{ex}: 447-494 nm / λ_{em}: 500-554 nm; blue channel (Hoechst) λ_{ex}: 340-395 nm / λ_{em}: 430-505 nm. Data from G. Rinaldi. Imaged on an EVOS FL AUTO2 Cell Imaging System.

The NETotic mechanism was further evaluated in HL-60 neutrophils. Neutrophils were treated with PMA to induce NETosis. To verify whether the treatments induced NET production, PMA treated cells were incubated with micrococcal nuclease, which disrupts and releases the DNA of NETs into the supernatant. Extracellular DNA was quantified using a Sytox orange assay, Sytox Orange (a DNA intercalating red emitting fluorophore that has high affinity for DNA but is membrane impermeable, so it can only penetrate cells with compromised plasma membranes). An increase in extracellular DNA was detected in cells that were treated with PMA (Figure 32f).

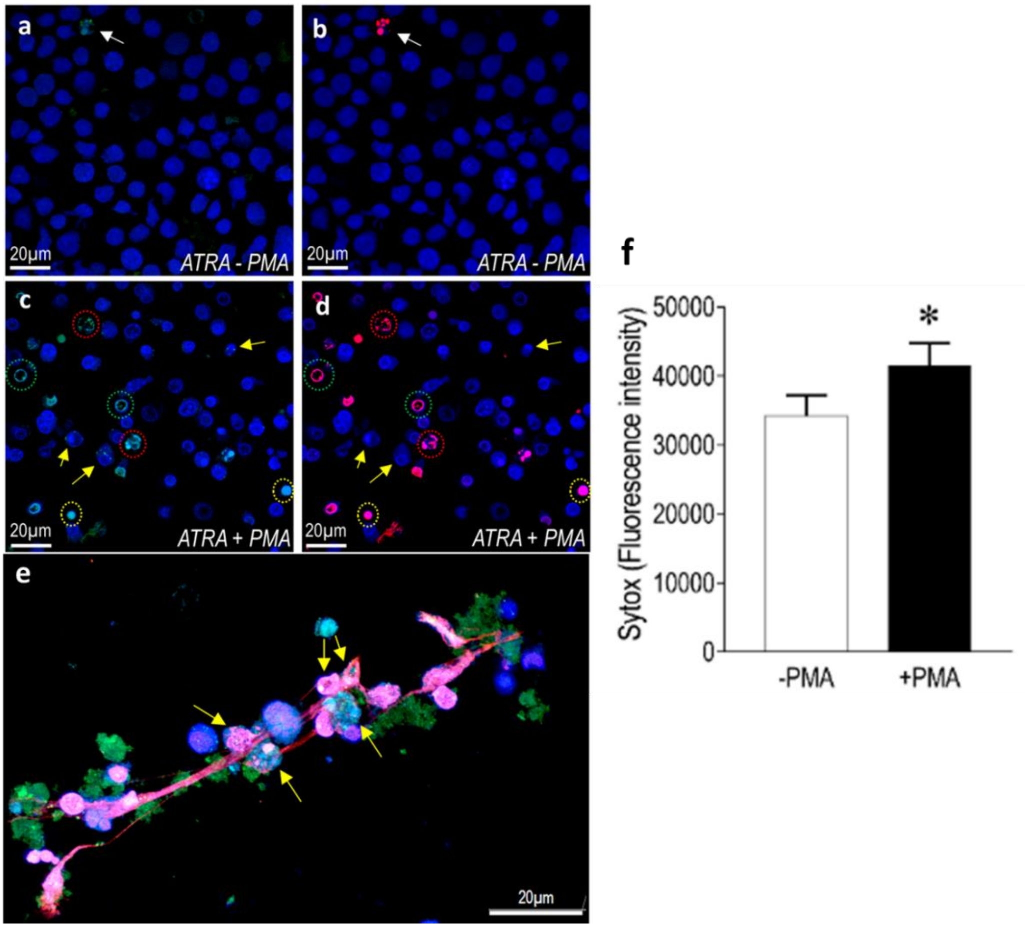

Figure 32 Fluorescence microscopy images of HL-60 cells stained with DAPI (0.2 mM, blue), **HNE-FQ** (5 µM, green) and SYTOX Orange (5 µM, red). Top row left: Control HL-60 neutrophils in the absence of PMA. **a)** Blue/Green channels; **b)** Blue/Red channels. Bottom row left: HL-60 neutrophils stimulated with PMA; **c)** Blue/Green channels; **d)** Blue/Red channels. Yellow arrows indicate cells expressing low hNE (likely at the beginning of the NETosis process) while those encircled in green, red and yellow are cells at different stages of NETosis; **e)** 3D image of a slice of a typical NET (stained as in the panels on the left). Arrows indicate chromatin studded with **HNE-FQ**, indicative of chromatin release by activated cells. Excitation and emission filters: green channel (probe) λ_{ex}: 488 nm / λ_{em}: 503-530 nm; blue channel (DAPI) λ_{ex}: 405 nm / λ_{em}: 430-505 nm red channel (Sytox orange) λ_{ex}: 540 nm / λ_{em}: 560-615 nm. **f)** Quantification of extracellular DNA release by NETotic neutrophils by a SYTOX Orange assay (5 μM). * Indicates $P < 0.05$ by paired Student's t-test (n=3). Data by G. Garoffolo. Zeiss LSM710 confocal microscope. Reproduced from reference 94 with permission from the Royal Society of Chemistry. [94]

To visualise NETs using microscopy, cells were stained with the probe **HNE-FQ** (**11**) to image elastase activity and with the nuclear DNA stain DAPI and extracellular DNA stain SYTOX Orange and imaged by confocal microscopy. PMA treated cells exhibited four different morphological stages of NETosis, based on nuclear morphology and hNE distribution. Early stages of neutrophil activation exhibited a small and rounded nucleus with hNE co-localized with condensed chromatin (stage 1; yellow circles) [96]. At later stages, chromatin decondensation led to spherical (stage 2; green circles) or more "cloud-like spread" shapes (stage 3; red circles). In the final stage, neutrophils formed extracellular chromatin filaments composed by cytoplasmic granules and hNE (stage 4; Figure 32) [97].

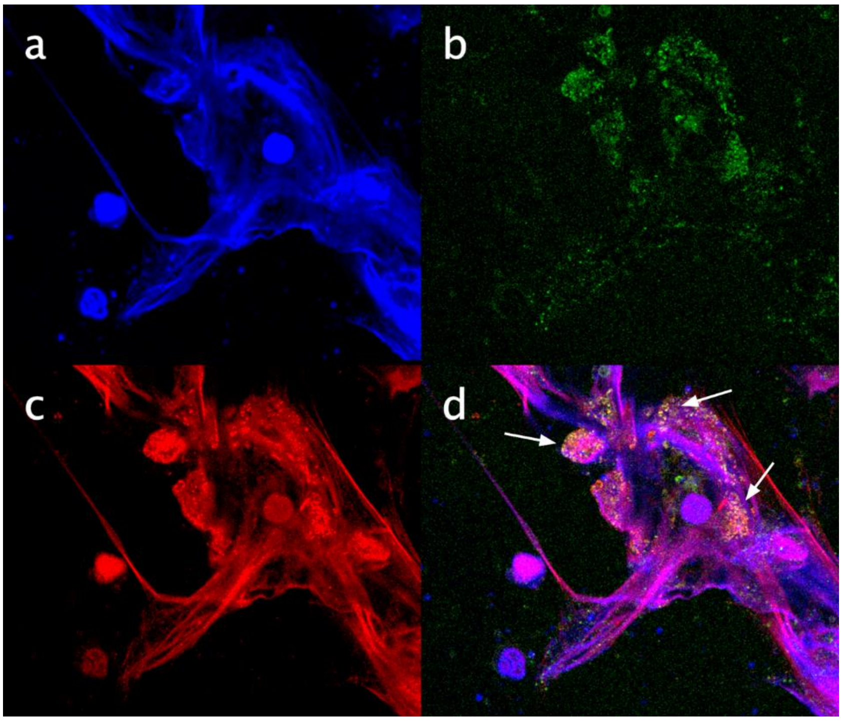

Figure 33. hNE can be detected with **HNE-FQ** on NETs produced by primary human neutrophils. Representative images of neutrophils activated with PMA (10 nM) and stained with **HNE-FQ** (5 μM) for 3 h. Cells were fixed with PFA (2% in PBS), stained with SYTOX orange (1 μM) and Hoechst 33342 (100 nM) for 30 min. NETs images were acquired on a Leica SP8 confocal microscope. **a)** Red channel, SYTOX Orange; **b)** Blue channel, Hoechst; **c)** Green channel, **HNE-FQ**; **d)** Merged. Arrows indicate chromatin studded with **HNE-FQ**. Detection wavelengths: blue channel (Hoechst) λ_{ex}: 405 nm / λ_{em}: 420-500 nm; green channel (probe): λ_{ex}: 488 nm / λ_{em}: 500-550 nm; red channel (Sytox Orange) λ_{ex}: 633 nm / λ_{em}: 650-710 nm. Data from G. Rinaldi. Imaged with SP8 confocal microscope. Reproduced from reference 94 with permission from the Royal Society of Chemistry. [94]

The capacity to detect elastase activity in NETs by probe **HNE-FQ** (**11**) was also evaluated in a different cell model, using primary human neutrophils. Following co-incubation with PMA and **HNE-FQ**, cells were fixed, washed and stained with SYTOX orange. Similar results to those previously obtained were observed, where signal from Hoescht, Sytox Orange and **HNE-FQ** colocalising along the NETs (Figure 33).

Next, NETs produced by primary human neutrophils were analyzed by flow cytometry. NETotic structures were produced by exposure to PMA as previously described and exposed to **HNE-FQ.** An increase in fluorescence signal of **HNE-FQ** was observed in PMA induced NETotic neutrophils by flow cytometry (Figure 34a), whilst no increases in fluorescence signal were observed in untreated neutrophils or neutrophils that were pre-treated with NAD(P)H oxidase inhibitor diphenyleneiodonium (DPI) or protein kinase C inhibitor Rho 31-820.

To confirm that the activation by PMA produced NETs, the presence of extracellular histones was confirmed by antibody co-staining of Histones 1 and 2. [98] High levels of double positive neutrophils (positive for both histone labels) were observed, indicating presence of high levels of extracellular histones in the cells (Figure 34b). Next, NETs were co-stained with a single Histone 1 labelling antibody and **HNE-FQ** and results showed high levels of “double positive” cells in PMA induced NETotic neutrophils (Figure 34c). In both experiments, non-NETotic (PMA untreated) neutrophils showed negligible levels of fluorescence for the histone stains or the probe, and the levels of double positive cells were significantly reduced in presence of inhibitors (DPI or Rho 31-820). The inhibitors themselves, had no effect on the signal from either the histone antibody stains or the probe.

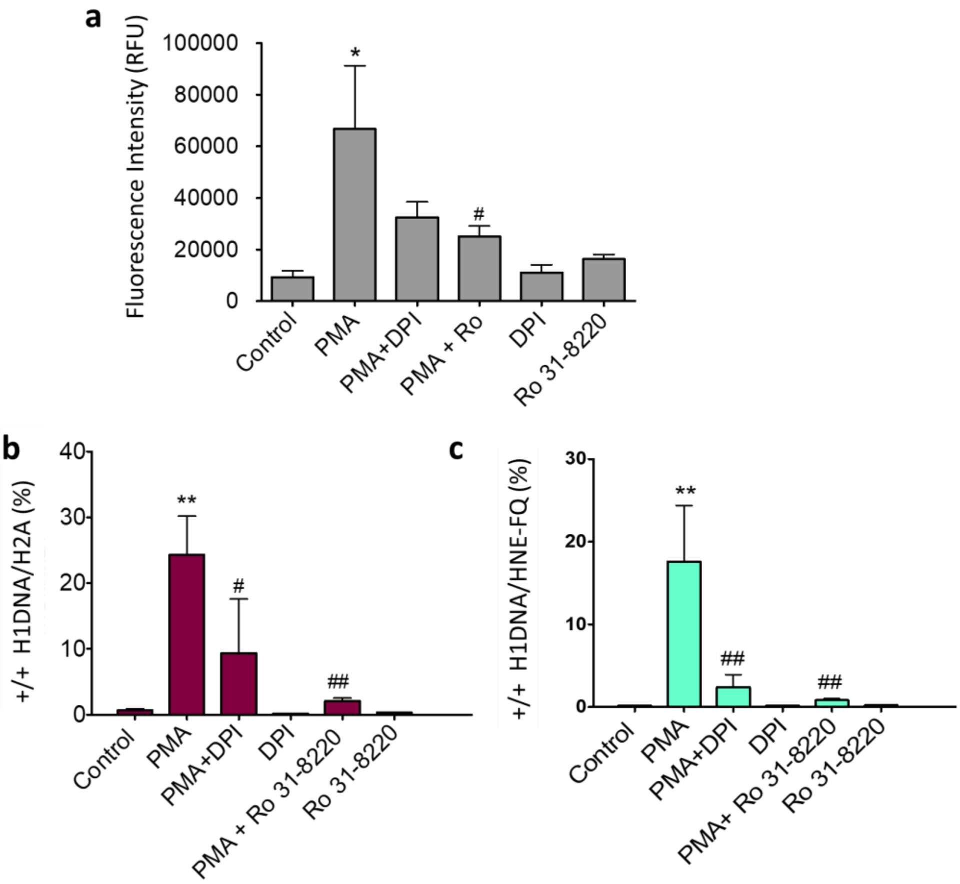

Figure 34 Flow cytometry assays of primary human neutrophils co-stained with probe **11** (green) or/and histone 1 or/and histone 2 fluorescent antibodies. Neutrophil activation was induced by exposure to PMA (10 nM), followed by incubation with **HNE-FQ** (**11**) and/or pre-incubated in presence or absence of inhibitors DPI (10 µM) or Rho 31-8220 (1 µM). **a)** Fluorescence intensity from the **HNE-FQ** in presence or absence of inhibitors**; b)** Percentage of cells with co-labelling of Histone 1 and Histone 2 antibodies; **c)** Percentage of cells with co-labelling of Histone 1 antibody and **HNE-FQ**. Detection wavelengths: (green channel (HNE-FQ) λ_{ex}: 488 nm / λ_{ex}: 530/30 nm, blue channel (H1A) λ_{ex}: 405 nm / λ_{ex}: 445/45 nm, red channel (H2A) λ_{ex}: 640 nm / λ_{em}: 660/20 Data *,** compared to control. $^{\#,\#\#}$ compared to PMA treated neutrophils. from G. Rinaldi.

To test **HNE-FQ** (**11**) in the context of NETosis in more a more complex model, HL-60 neutrophils were differentiated as previously described and exposed to serum from COVID positive patients in the presence of the probe. An increase in elastase activity was observed following exposure to the COVID+ serum, whilst the control (neutrophils incubated with probe only), showed negligible levels of elastase activity. A control where neutrophils were exposed to PMA was used as a control for NETotic neutrophils (Figure 35).

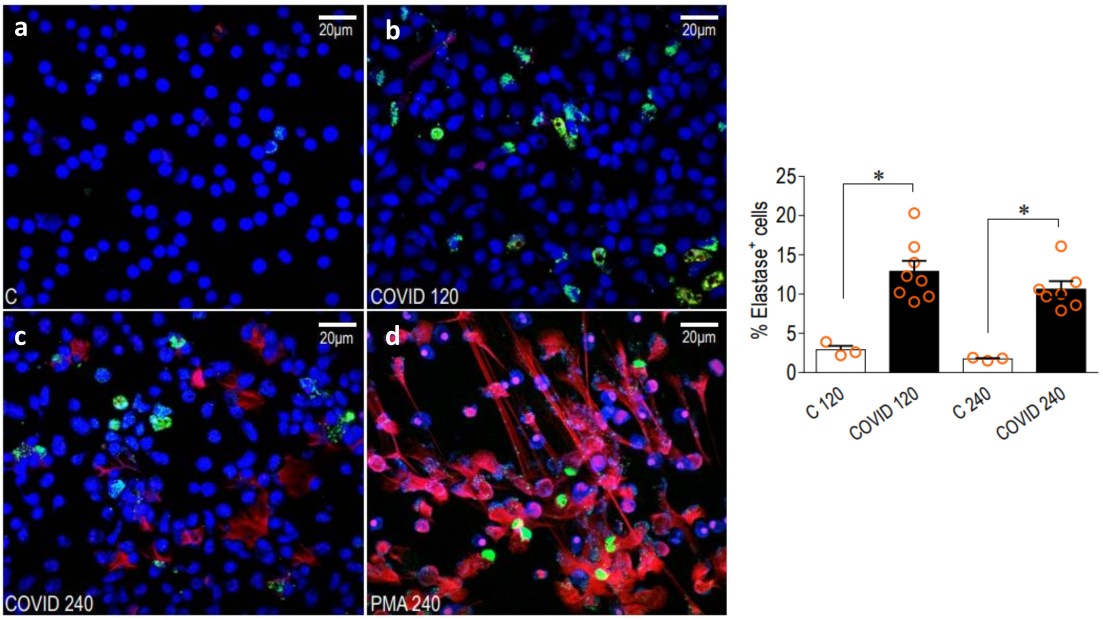

Figure 35 . Confocal imaging of primary human neutrophils stained with DAPI (0.2 mM), Sytox Orange (1 μM) and probe **HNE-FQ** (5 μM) **a)** Control, untreated neutrophils; neutrophils exposed to serum isolated from COVID + patients for 120 min or **b)** 240 min **d)** NETotic neutrophils control, neutrophils exposed to PMA (15 nM). The bar graph (right) shows the quantification of the Elastase positive cells. Excitation and emission filters: green channel (probe) λ_{ex}: 488 nm / λ_{em}: 503-530 nm; blue channel (DAPI) λ_{ex}: 405 nm / λ_{em}: 430-505 nm red channel (Sytox orange) λ_{ex}: 540 nm / λ_{em}: 560-615 nm. Data by G. Garoffolo. Zeiss LSM710 confocal microscope

Interleukin 8 (IL-8) is a cytokine produced by macrophages that is involved in the recruitment of neutrophils to the site of damage or infection; in a process called chemotaxis and it also mediates activation of these cells once recruited.

Ladaraxin is an inhibitor of the IL-8 receptor that is currently in phase 3 clinical trials (NCT04628481) for treatment of Diabetes Mellitus type 1[99], to reduce infiltration of neutrophils into beta-pancreatic cells. Neutrophilia and infiltration of neutrophils into the lung is a hallmark of COVID-19 infection, and IL-8 plasma levels are elevated in COVID + patients with mild and severe symptoms, serving as a biomarker for the prediction of disease severity and survival of COVID-19. [100] Thus, Ladaraxin could serve as a treatment for severe cases of COVID-19 infection by reducing neutrophil recruitment and activation. To evaluate the capacity of Ladaraxin to inhibit neutrophil activation, neutrophils were treated with IL8 or IL8 + Ladarixin and stained with probe **HNE-FQ** (**11**) and imaged by fluorescence microscopy. An increase in activated neutrophils, with elastase granules displayed on the membrane were observed upon exposure to IL-8, while inhibition of the release of elastase was achieved when neutrophils were pretreated with Ladarixin (Figure 36).

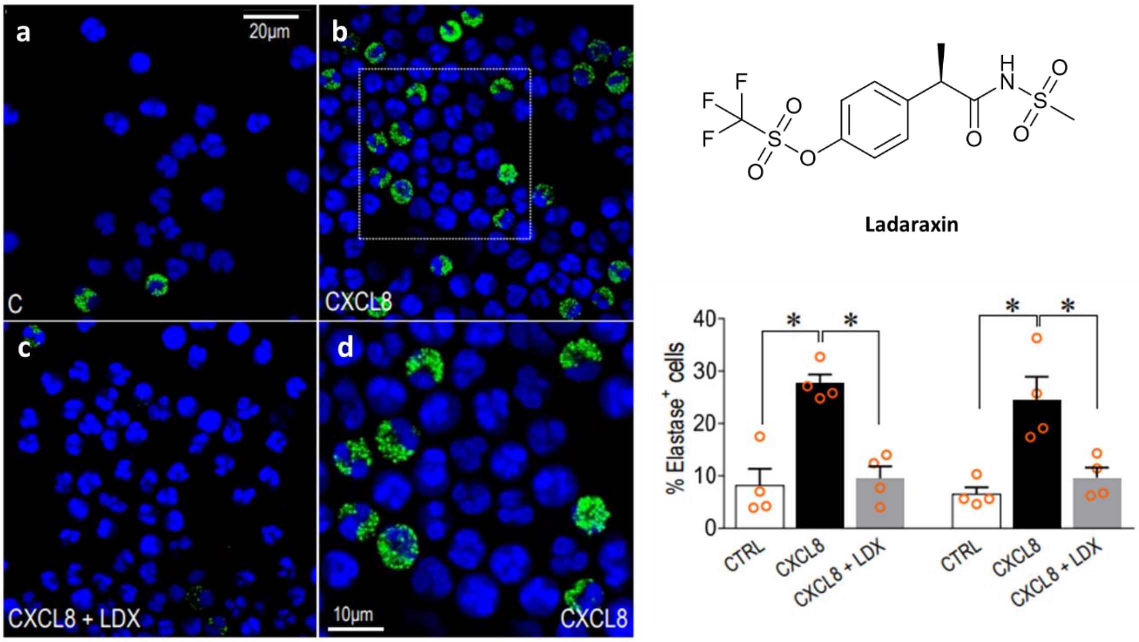

Figure 36. Confocal imaging of human neutrophils stained with DAPI (0.2 mM) and probe **HNE-FQ** (5 µM)**.** **a)** Untreated neutrophils**; b)** neutrophils exposed to IL-8 **c)** neutrophils pretreated Ladaraxin (160 µM) were exposed to IL-8 (100 ng/ml). The bar graph (right) shows the quantification of the Elastase positive cells and the inhibition by Ladarixin®. **d)** zoomed region of **b.*** indicate $P < 0.01$ in comparisons using, for each incubation time, one-way ANOVA with Dunnet post-hoc. Excitation and emission filters: green channel (probe) λ_{ex}: 488 nm / λ_{em}: 503-530 nm; blue channel (DAPI) λ_{ex}: 405 nm / λ_{em}: 430-505 nm red channel (Sytox orange) λ_{ex}: 540 nm / λ_{em}: 560-615 nm. Data by G. Garoffolo. Zeiss LSM710 confocal microscope

IL-8 can trigger production of NETs in neutrophils. [101] To evaluate the capacity of IL-8 to induce production of NETs, neutrophils were exposed to IL-8 or PMA (positive control) and NETs were stained with extracellular DNA stain Sytox Orange and elastase was labelled with **HNE-FQ** (**11**). Upon IL-8 exposure, increased levels of elastase containing granules were observed in neutrophils and inhibition of neutrophil activation with Ladaraxin resulted in reduced levels elastase production as previously observed. The positive control, where NETs were produced by exposure to PMA, showed well defined NETs with elastase co-localised throughout the DNA skeleton. These results confirm the previous results that IL-8 can induce neutrophil activation and results in increased levels of elastase, and that this activation, can be inhibited by treatment with Ladaraxin. However, no clear NETotic structures could be observed following IL-8 exposure (Figure 37), where the elastase appeared contained in granules and low levels of extracellular DNA were detected, indicating absence of NETotic structures.

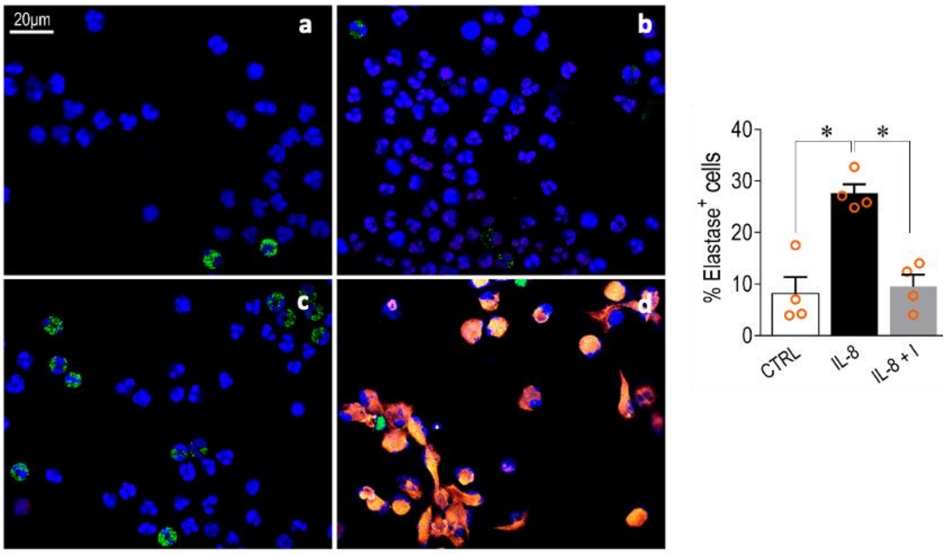

Figure 37. Confocal imaging of primary human neutrophils exposed to IL-8 or IL-8 + Ladaraxin for 2 h. Neutrophils were stained with DAPI (0.2 mM), Sytox Orange (1 µM) and probe **HNE-FQ** (5 µM). **a)** Control, untreated neutrophils **b)** neutrophils exposed to IL-8 (100 ng/ml) pretreated with Ladaraxin (160 µM) **c)** neutrophils exposed to IL-8 **d)** NETotic neutrophil control, neutrophils exposed to PMA (15 nM) without Il-8 or Ladaraxin. The bar graph (right) shows the quantification of the Elastase positive cells and the inhibition by Ladarixin. * Indicate *P* < 0.01 in comparisons using, for each incubation time, one-way ANOVA with Dunnet post-hoc. Excitation and emission filters: green channel (probe) λ_{ex}: 488 nm / λ_{em}: 503-530 nm; blue channel (DAPI) λ_{ex}: 405 nm / λ_{em}: 430-505 nm red channel (Sytox orange) λ_{ex}: 540 nm / λ_{em}: 560-615 nm. Data by G. Garoffolo. Zeiss LSM710 confocal microscope.

- **Fluorescence lifetime experiments**

Fluorescence lifetime is the time a fluorophore spends in the excited state before returning to the ground state by emitting a photon. The lifetime of fluorophores (τ) can range from picoseconds to hundreds of nanoseconds. For fluorescein, the reported lifetime is 4-5 ns. [102] FRET can reduce the fluorescence lifetime of the donor fluorophore through energy transfer to the dark quencher and therefore, a significant change in lifetime upon activation of the probe was expected. Thus, the changes in fluorescence lifetime of the probe upon activation was evaluated. The "super-silent" character of the probe in its inactive form resulted in a short fluorescence lifetime of 1.3 ns, whilst, in its activated form, the fluorescence lifetime measured was 5.0 ns (Figure 38).

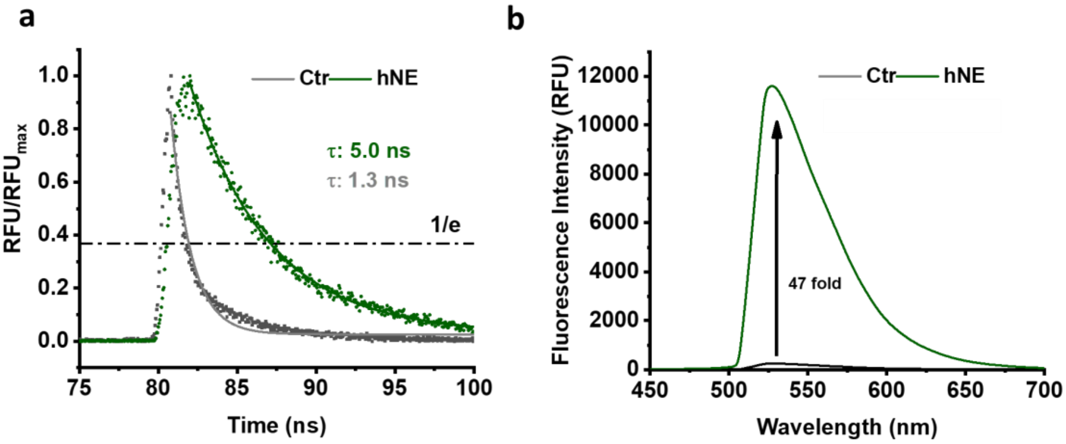

Figure 38 a) Fluorescence lifetime of the probe (at 5 µM) before and after incubation with hNE for 1 h (100 nM), n = 2. Fluorescence lifetime is calculated by measuring the time it takes the intensity to decrease to 1/e from the moment the pulse of light is emitted (t_0 = 80 s). The intensity was normalized (RFU/RFUmax) to allow comparison between cleaved and uncleaved probe. **b)** Corresponding increase in fluorescence upon exposure to hNE (100 nM), n = 2. Data obtained with Caitlin Tay.

The change in lifetime was also monitored over 45 min, with measurement taken manually every few min following exposure of the probe to the enzyme. A clear increasing trend in lifetime was observed with time, with the most significant changes observed during the first 5 min of exposure to elastase, and although fluorescence intensity kept increasing, changes in lifetime values were less pronounced.

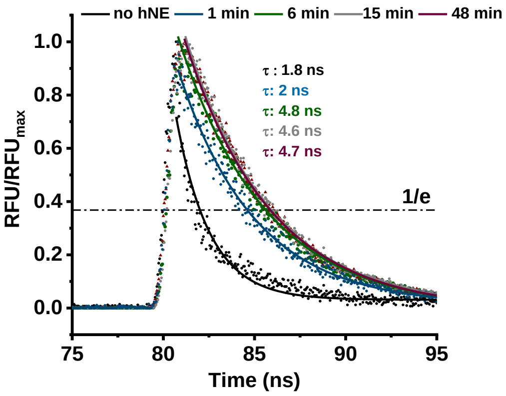

Figure 39 Normalized intensity (RFU/RFU$_{max}$) at different timepoints upon hNE exposure. Fluorescence lifetime of the probe (5 µM) was monitored over time upon exposure to hNE for 1 h (100 nM) in reaction buffer. Fluorescence lifetime increased rapidly over the first min, reaching a maximum fluorescence lifetime of 4.8 ns at 6 min, remaining constant on subsequent timepoints. Fluorescence lifetime is calculated by measuring the time it takes the intensity to decrease to 1/e from the moment the pulse of light is emitted (t_0 = 80 s). Data obtained with Caitlin Tay.

3.3 Conclusions

Human neutrophil elastase (hNE) is a serine protease implicated in the pathogenesis of acute and chronic inflammatory diseases and is secreted by inflammatory neutrophils to destroy pathogens. Activated neutrophils are pivotal actors in many diseases. Herein I reported on an optimised fluorogenic probe for detection of hNE in activated neutrophils and Neutrophil Extracellular Traps (NETs).

The probe was optimized from previous tribranched probes for elastase detection that used self-quenching and FRET substrates for elastase detection but that suffered from high background fluorescence or low specificity, respectively, and that proved unsuccessful for labelling elastase activity in NETs.

The probe is a tri-branched activatable fluorescent hNE compound that allows the rapid, specific and sensitive detection of hNE in activated neutrophils and NETs. The green emitting probe is based on a multivalent scaffold combined with three copies of a FRET-labelled peptide using Fluorescein and Methyl-Red as fluorophore and quencher, respectively. The synthesis of the optimized probe is carried out with a combination of solution and solid phase chemistries. The synthesis starts with the construction of a tribranched scaffold with three terminal amino groups that was inmobilised into a solid support to then build the peptide sequences using standard Fmoc SPPS.

The multivalent scaffold approach enables "self-quenching", making the probe super-silent under physiological conditions and offering excellent signal amplification upon substrate cleavage (>20-fold). The probe was found to be specifically cleaved by HNE, with no cleavage by related proteases. Activated human neutrophils and NETs were successfully labelled with the probe under inflammation-induced conditions, allowing visualisation of different stages of NETosis and activation could be monitored by flow cytometry.

The behaviour of **HNE-FQ** (**11**) was compared to the previous probes **NAP** (**1**) and **NES** (**2**) to prove that **HNE-FQ** provides a significantly higher amplification capacity compared to previously designed probes, with **HNE-FQ** providing a 22-fold increase in signal within one h of incubation, while that increase was only about 6-fold for **NES** and 3.7-fold for **NAP**.

Elastase activity was detected with the probe in neutrophils activated by fMLF. The fluorescence signal from the probe could be detected by flow cytometry and by fluorescence microscopy in live cells. The probe successfully labelled elastase in NETs produced *in vitro* by exposing neutrophils to PMA, a stablished NETotic inducer. Inhibition of the protease resulted in a significant decrease in signal and was correlated to a reduced level production of NETs, suggesting that elastase plays a key role in NET production. Different stages of NETosis could be differentiated in HL-60 neutrophils incubated with PMA and the colocalization of elastase with extracellular DNA confirmed the presence of well-defined NETs after 3 h exposure to PMA.

To highlight the potential of **HNE-FQ** as a diagnostic tool to detect NETosis and activated neutrophils in more relevant and complex models, the probe was used to detect the production of NETs by HL-60 neutrophils exposed to serum from COVID + patients, and to assess the efficiency of Ladaraxin to inhibit NETotic events as a potential treatment for COVID patients.

Finally, the potential as a fluorescence lifetime imaging tool was assessed by monitoring the lifetime changes of the probe upon activation that demonstrated a clear change in fluorescence in lifetime, of approximately 5-fold, upon incubation with elastase.

Chapter 4 Moving into the NIR

4.1 Introduction

The applicability of fluorescence imaging *in vivo* is compromised when using wavelengths in the visible spectrum.[103, 104] Both resolution and contrast decrease with increasing tissue depths due to factors such as photon scattering, photon absorption and high levels of tissue autofluorescence from endogenous fluorophores.

Thus, as shown in Scheme 1, incident photons can be scattered, reflected back at the surface of the tissue or in rare cases penetrate through it. The photon, once it penetrates tissue, can undergo further light scattering, or can be absorbed by endogenous chromophores or excite endogenous fluorophores leading to autofluorescence. All these contribute to the limited excitation of the targeted fluorophore.[103]

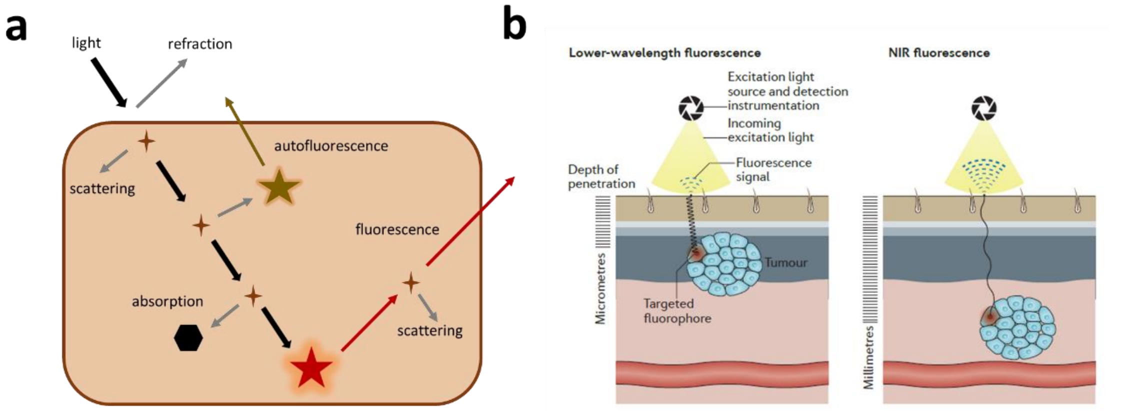

Figure 40 a) Light scattering events on an incident light source on and in biological tissue. Light can be lost by reflection by the skin or scattered by biological components (grey arrows) or absorbed by endogenous molecules (black shape) or excite endogenous fluorophores leading to autofluorescence (brown star and arrow). These events dramatically affect the efficiency of excitation and fluorescent emission from the desired fluorophore (red). Reproduced from reference 103 with permission from the Springer Nature©. **b)** NIR fluorescence has reduced scattering ($1/\lambda^4$) thus better tissue penetration and lower fluorescent background compared to shorter wavelength fluorescence, allowing imaging at deeper locations. Reproduced from reference 104 with permission from the Elsevier Inc©.

4.1.1 Light attenuation coefficients of tissue

The attenuation coefficient (μ) of a tissue is the sum of absorption coefficients (μ_a) and scattering coefficients (μ_s) of the components of that given tissue. A large coefficient value represents high attenuation of light as it passes through a tissue. [105]

$$\mu = \mu_a + \mu_s$$

Equation 1 Light attenuation coefficient

The attenuation or extinction coefficient in complex biological tissue is lowest in the optical range from 650 nm to 900 nm, the so-called NIR region, where there is reduced light scattering and minimal absorption by endogenous biomolecules making this region ideal for *in vivo* imaging.

- **Light scattering (μ_s)**

Photon scattering occurs because of the macroscopic and microscopic variations in refractive index in biological tissue meaning photons follow diverted paths. [106] Tissues are complex heterogeneous systems with many variations in structure and therefore many scattering centres. Thus, photons that penetrate into the tissue will be subject to a multitude of scattering events depending on the specific composition of a given tissue and the refractive indices of its different components. Therefore, the scattering properties of tissue govern how deep light can penetrate. High scattering of light by tissue leads to attenuation of fluorescent signal, greatly limiting the depth imaging (or therapeutic potential) of a given optical technique.

Light scattering in biological tissue is denoted by the scattering coefficient which is defined as the probability of photon scattering in tissue per unit path length with attenuation of light in tissue by scattering dominated by Rayleigh scattering ($1/\lambda^4$) (Figure 41).[105]

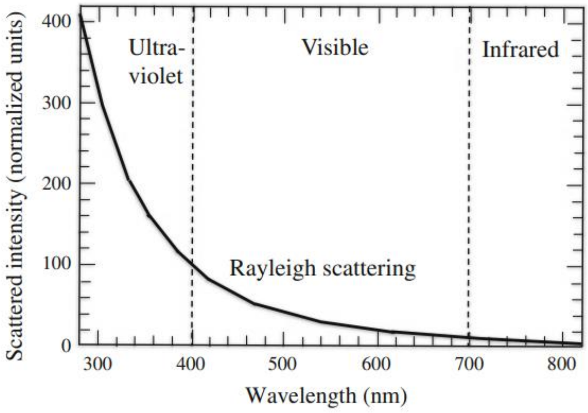

Figure 41 Light scattering is inversely proportional to wavelength. Reproduced from reference 105 with permission from Springer Science Business Media Singapore.[105]

- **Absorption from endogenous biomolecules absorption coefficient (μ_a)**

The number and type of chromophore in a material dictates its absorption coefficient (μ_a). Naturally occurring chromophores in biological tissue include oxy- and deoxyhemoglobin, and melanin as well as water and fat (although these do so mainly below or above the NIR window 650-900nm (Figure 42)).[107]

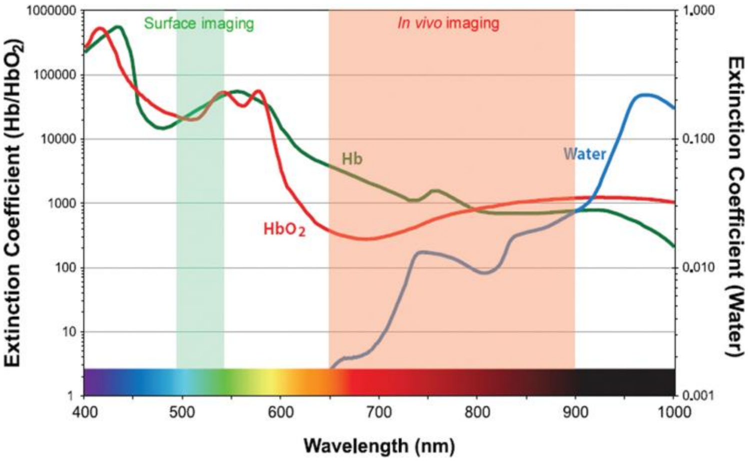

Figure 42 Endogenous biomolecules such as oxy- and deoxyhaemoglobin absorb light significantly at wavelengths below 650 nm and water does above 900 nm. Reproduced from reference 107 with permission from American Chemical Society ©.[107]

4.1.2 Tissue autofluorescence

Tissue autofluorescence affects the signal to background ratios in the blue and green regions of the wavelength spectrum (below 650 nm), where the emission of many endogenous fluorophores such as protoporphyrin, aromatic amino acids or NAD(P) fall. Autofluorescence at longer wavelengths is reduced, with fewer endogenous fluorophores in this region (Figure 43b). [106]

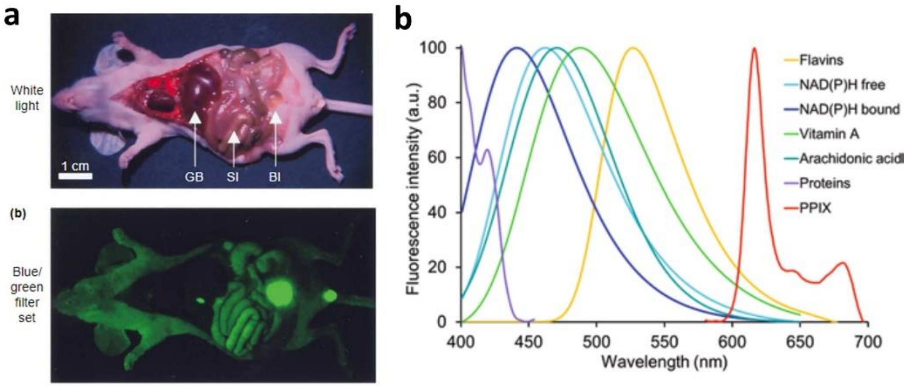

Figure 43 Tissue autofluorescence. **a)** An example of autofluorescence from tissue. [106] **Upper**: white light image or **Lower**: under a blue/green fluorescent filter (460–500 nm/505–560 nm). Reproduced from reference 106 with permission from Elsevier Ltd.© **b)** Fluorescence emission spectrum of biologically abundant biomolecules, excited at their appropriate λ_{max} (PPIX stands for Protoporphyrin IX). Reproduced from reference 108 with permission from Springer ©.[108]

The NIR region (650 - 900 nm) is therefore an ideal spectral window for biomedical imaging since it shows reduced light scattering, minimum absorption and negligible autofluorescence, offering higher signal-to-background ratios with increases in signal transduction (due to reduced scattering and absorption) and reduced background (decreased autofluorescence).

4.1.3 Fluorescence imaging *in vivo,* why NIR light

For many decades, fluorescence imaging has been used as a method to visualise biological processes at a molecular level, and it is a useful tool for monitoring abnormal biological processes in different disease states. Fluorescein is a green emitting fluorophore that has been used since the 1960s by opticians to assess eye health, allowing to observe corneal injuries or abnormal tear production as well as for diagnosis of ophthalmic pathologies such as blepharitis. [109] Another widely used fluorophore, is Indocyanine green (ICG) with emission in the NIR, that was approved by the FDA more than half a century ago. It has been used since as a cost-effective imaging modality for analysis of blood flow, assessment of cancer tissue such as oral squamous cell carcinoma[110] and for endoscopic marking of colorectal tumours. [111] Methylene blue, is a fluorophore and photodynamic agent that was FDA approved in 2016 for injection for i.v. as ProvayBlue® , for use in patients with acquired methemoglobinemia (blood disorder in which an abnormal amount of methemoglobin is produced), and it has been used for the visualization of anatomical features such as ureters[112] or for imaging of fibrous tumours in the pancreas [112] and breast cancer. [113] Another FDA approved "contrast agent" is the precursor to protoporphyrin IX, 5-aminolevulinic acid (5 ALA), a keto amino acid that is metabolised via the heme-synthesis pathway to produce protoporphyrin IX. 5-ALA has been approved in Europe, Canada, and Japan for use in fluorescence guided surgery of glioblastoma[114] and 5-ALA has been applied for intraoperative imaging of cancers and premalignant lesions. [115]

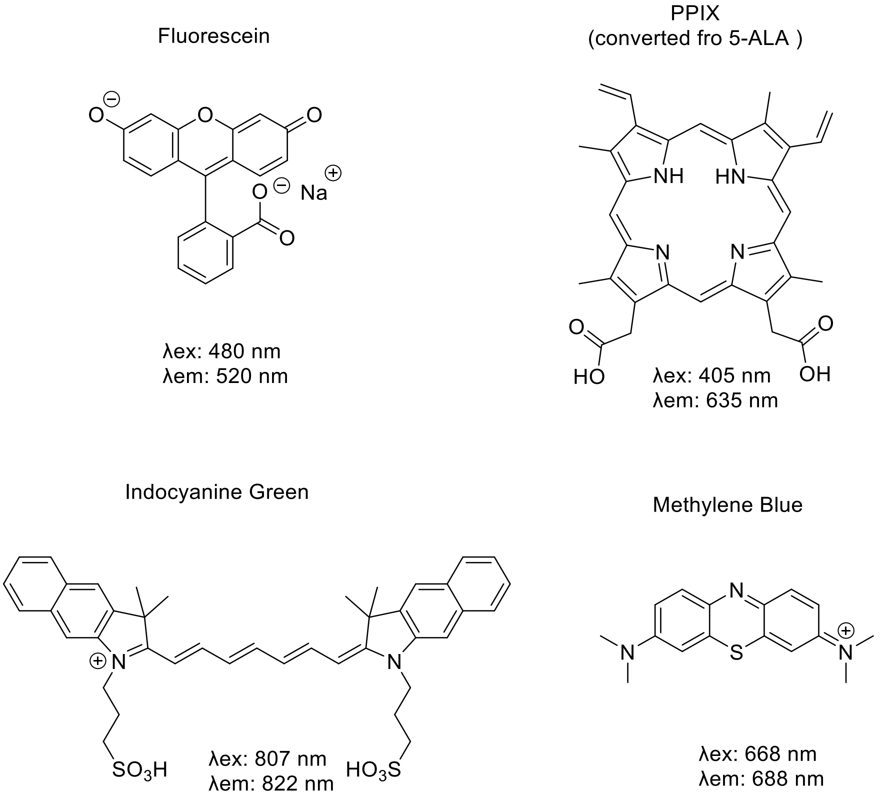

Figure 44 Examples of non-targeted NIR fluorophores used in the clinic.

4.1.4 NIR fluorescent probes

Attaching fluorophores to targeting agents enables the expansion of fluorescence imaging in clinical settings improving their sensitivity and specificity of detection. Some targeted NIR fluorescent probes are currently being used for optical-guided-surgery, examples include the FDA approved Cytalux (OTL38) that targets the folate receptor alpha and has been used for imaging of gastric adenocarcinoma[116] or the tyrosine kinase MET receptor targeting probe for colon cancer[117] or thyroid cancer. [118] Some antibody fluorophore conjugates with NIR emission have also entered clinical studies in the last decade, for example for VEGF-targeted fluorescent detection of lesions in breast cancer (NCT0150857) or head and neck cancer using an ICG variant labelled cetuximab (NCT01987375).

In the area of protease detection, targeted probes have also been developed with emission in the NIR.[119] Examples include the activity based probe for cathepsin detection VGT-309, that was used to guide surgical removal of a tumour in a mouse model[120] (Figure 45) while another cathepsin-activated imaging probe LUM015 has entered clinical studies for breast cancer intraoperative detection (see page 10, compound **1**).[121]

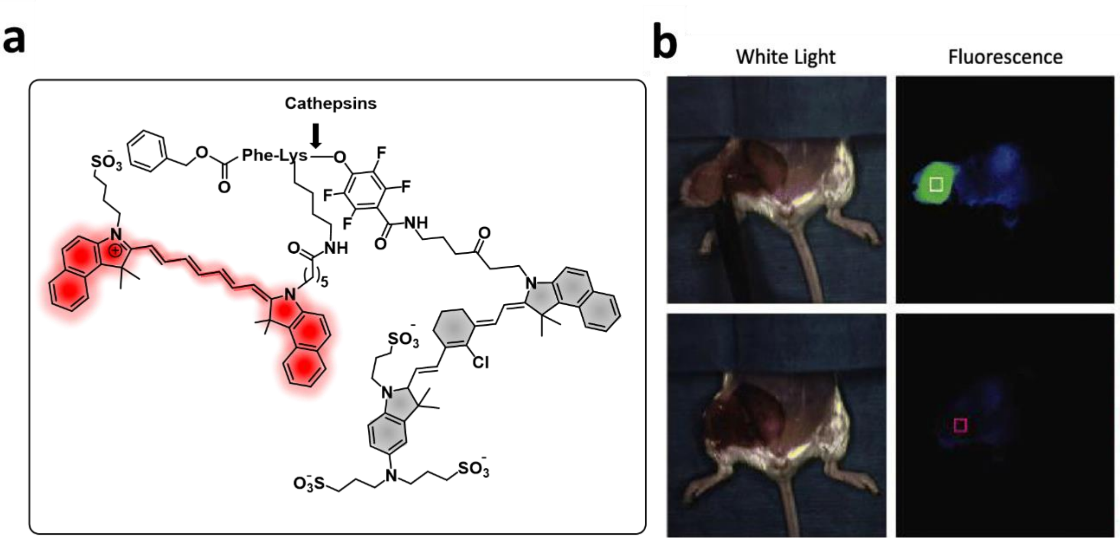

Figure 45 a) Structure of VGT-309 probe**. b)** Imaging of a tumour in a mouse using the cathepsin detection probe VGT-309. White light (left) and fluorescent (right) images of the surgical field before (upper) and after (lower) tumor removal using the Novadaq Spy Elite imaging system. Reproduced from reference 120 with permission from Springer ©.[120]

In the area of neutrophil elastase detection, one example of targeted activatable NIR probes includes a non peptidic pentafluoropropanoic acid caged hemicyanine recognised by hNE.[122] Activity based probes emitting in the NIR have been developed for human and murine elastase[123, 124], both with "always on" and fluorogenic character, as well as substrate-based probes such as NE680, that uses a specific substrate of murine elastase, labelled with multiple copies of the so-called VivoTag-S680 dye and is based on self-quenching (Figure 46). Most of the available probes for detection of human neutrophil elastase, however, have limited specificity, with many of them cross-reacting with the closely related proteases Cathepsin G or Proteinase 3, or have high levels of background fluorescence.[65]

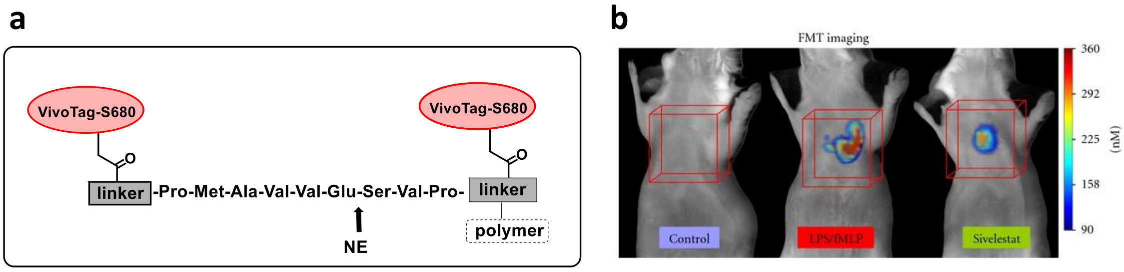

Figure 46 Imaging and quantification of NE680 activation *in vivo*; **a)** generic structure of the probe; **b)** CD-1 mice were challenged with LPS and fMLP. Mice received an intranasal instillation of 200 nM LPS in PBS, PBS only of 200 nM LPS and 4 nmol NE680. A subset of mice was also treated with the NE inhibitor sivelestat 15 min prior to fMLP and NE680 addition and the mice were imaged 5 h later by FMT 2500. Representative volume rendering projections taken at the same color gating as left: control, middle: LPS/fMLP and right: LPS/fMLP mice which had been treated with sivelestat. Reproduced from reference 65 with permission from Sylvie Kossodo et al.©

4.2 Synthesis of NIR fluorogenic probes for detection of neutrophil elastase

4.2.1 Synthesis of a sulfonated cyanine 5 fluorophore.

Over the past few decades, there has been extensive work in the development of NIR-I fluorophores with cyanine fluorophores remaining the most popular due to their favourable safety profiles, tunable fluorescence characteristics, good solubility (when sulfonated), and their synthetic and commercial availability. [125]

Cyanine dyes consist of two heterocyclic “head groups” that are connected by an odd (n) number of methine groups (Figure 47). Cyanine dyes are named depending on the number of carbon atoms in the polymethine chain with n = 0, 1, 3, 5 or 7, the mono-, tri- (cyanine 3), penta (cyanine 5), or heptamethine (cyanine 7) cyanine’s respectively and their emission properties can be tuned to cover a broad region of the electromagnetic spectrum (500-900 nm) by extending the polymethine chain with the addition of vinylene groups or aromatic rings. The addition of functional groups such as carboxylic acids within the structure allows conjugation to biomolecules.

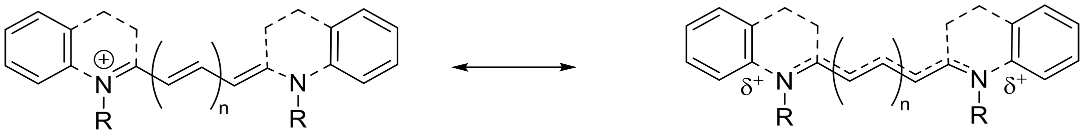

Figure 47 Generic resonance structure of cyanine dyes through delocalisation of electrons along the conjugated system.

The sulfonated NIR cyanine sulfoCy5 (**12**), previously reported in our group[126], was chosen as the NIR fluorophore here, due to its high water solubility (from the sulfonate and pyridine groups) and the carboxylic acid handle that allows conjugation to a peptide via an amide bond. The compound was synthesised by reacting 1,2,3,3-tetramethyl-3H-indolium 5-sulfonate with 2-(3-hydroxycarbonyl-6-pyridyl)malondialdehyde in the presence of sodium acetate at 120 °C in a mixture of acetic anhydride/acetic acid (1:1) as solvent under microwave irradiation (Figure 49). The product could be precipitated and washed thoroughly with diethyl ether without the need of reverse phase chromatography. The carboxylic acid was activated *in situ* using the activating agent dipyrrolidino (N-succinimidyloxy)carbenium hexafluorophosphate (HSPyU) in the presence of base (DIPEA) for coupling to amino groups. This fluorophore is efficiently excited (Φ = 0.22[127]) at 640 nm and had a maximum fluorescence emission at 660 nm (Figure 48).

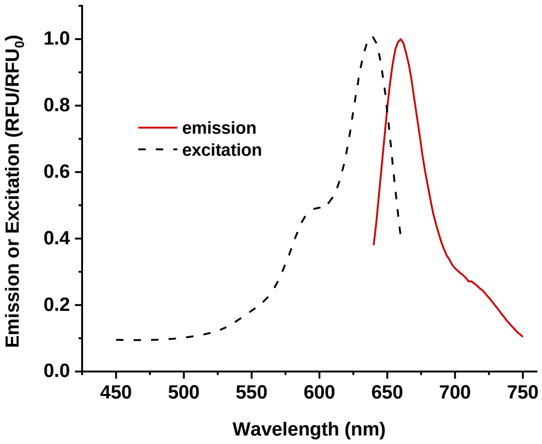

Figure 48 Excitation and emission of the sulfonated cyanine 5 (12). The excitation spectrum (dashed line) shows the excitation maxima at 640 nm (λem 660 nm). The emission spectrum (red solid line) shows the maximum emission wavelength at 660 nm (λex 630 nm).

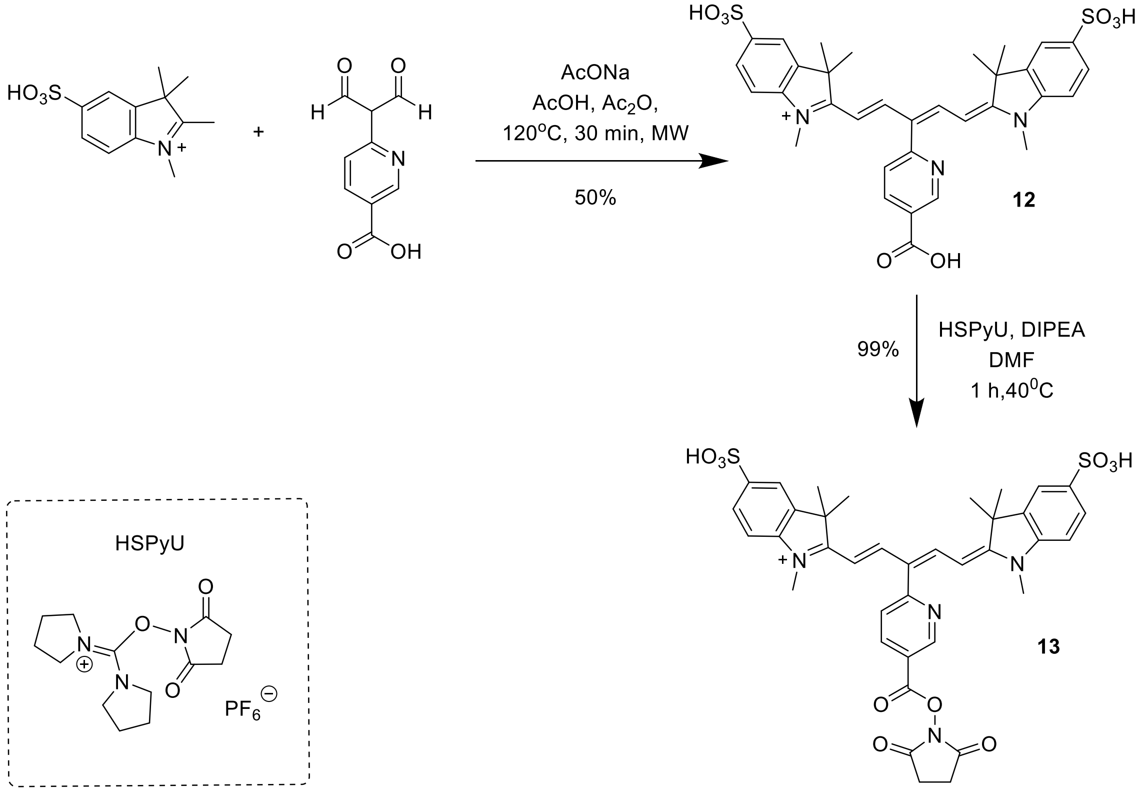

Figure 49 Synthesis of sulfonated Cyanine 5 (**12**). [34] 1,2,3,3-tetramethyl-3H-indolium 5-sulfonate was reacted with 2-(3-hydroxycarbonyl-6-pyridyl)malondialdehyde (2:1) and heated in a microwave for 30 min at 120° C to give the corresponding hemicyanine (**12**) that can be activated in situ to the corresponding NHS ester using HSPyU.

4.2.2 Synthesis of the quencher QSY21-NHS.

Quenching of fluorescence by dark quenchers has been used extensively in the development of fluorogenic probes. [128] The most commonly used quenchers are azo-based compounds such as Dabcyl or Methyl Red, used in combination with fluorophores such as fluorescein, Rhodamine, EDANS, or Cyanine 3 to give highly efficient FRET pairs. [129]

Quenchers that absorb fluorescence in the NIR region of the spectrum are, however, less well known and typically require a more complex synthesis. Two main classes are used, (i) azo-based quenchers[130-132] with an extended conjugation (includes a series of red shifted dark quenchers (so-called Black Hole Quenchers (BHQ)) and (ii) QSY quenchers, based on a rhodamine scaffold bearing anilines on the aromatic rings at positions 3,6-positions of the xanthene moiety. These show no fluorescence emission, irrespective of solvent polarity and pH (Figure 50).[129]

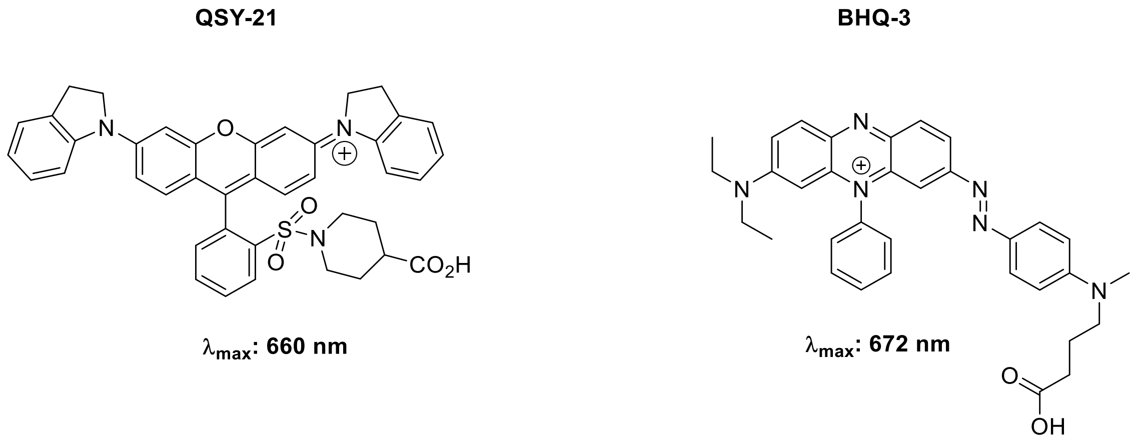

Figure 50 NIR dark quenchers based on rhodamine (QSY21) and azo-based compounds (BHQ-3).

QSY-21 was chosen as the dark quencher here for the synthesis of the NIR probe based on its absorption spectrum to absorb and its ability to quench the fluorescence emitted by the sulfoCy5 fluorophore (Figure 52). The quencher was synthesised using a previously reported procedure (Figure 51)[133] starting from commercially available sulfonfluorescein (**14**), with the phenolic groups substituted in the presence of sulfonyl chloride and a catalytic amount of DMF under reflux to give the corresponding sulfonfluorescein bis-chloride (**15**). This formed a precipitate that was isolated by filtration. Nucleophilic aromatic substitution on **15** in the presence of 2,3-dihydroindole under reflux gave the sulfonate (**16**) that was isolated by liquid-liquid extraction and taken forward without further purification. Next, the cyclic sulfonate was converted into a sulfonyl chloride using phosphoryl chloride and reacted with ethyl isonipecotate to give the sulfonamide (**17**), purification by flash chromatography and hydrolysis of the ethyl ester with NaOH gave the carboxylic acid (**18**) in high yield. Activation of the carboxylic acid with TSTU gave the isolable NHS ester (**19**) that was used for direct attachment on the peptide.

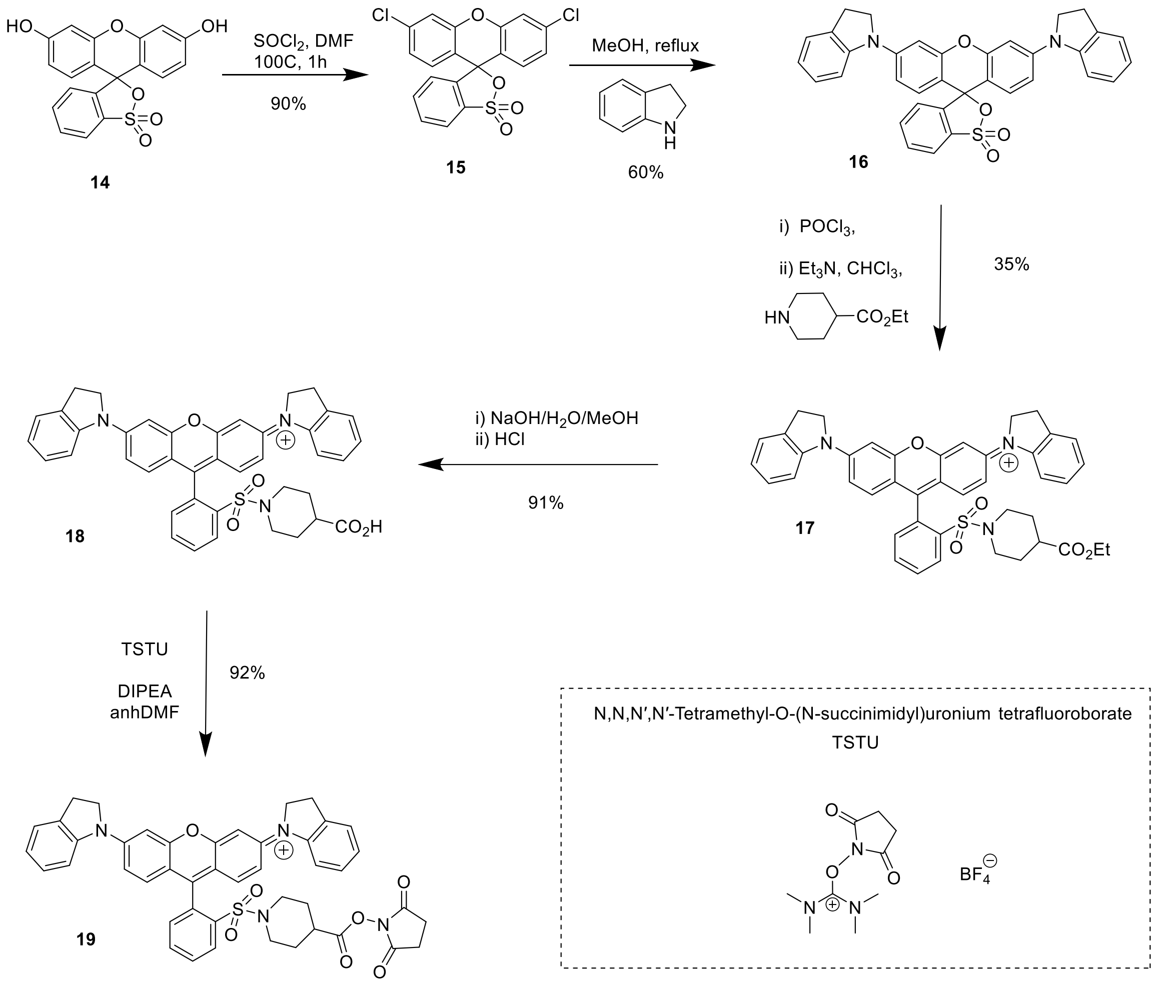

Figure 51 Synthesis of the NHS ester of the xanthene-based dark quencher QSY21 (**19**) starting from sulfonfluorescein (**14**) in 5 steps with an overall yield of 15%.

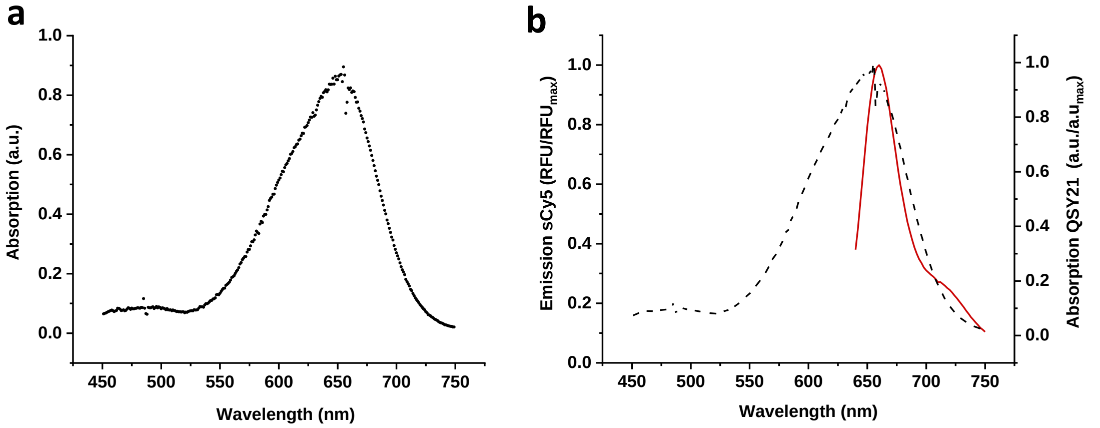

Figure 52 a) Absorption spectrum of QSY21 (**18); b)** Spectral overlap between the emission (red line) of the fluorophore sulfoCy5 (**12**) and absorption of quencher QSY21 (black dotted line).

4.2.3 Stability of the dyes under SPPS conditions

The stability of both QSY21-COOH (**18**) and sulfoCy5 (**12**) under commonly used Fmoc and Dde deprotecting conditions was evaluated. For this, dyes were dissolved in solutions of 20% piperidine, 2% DBU, 2% hydrazine or imidazole·HCl/NH_2OH/NMP and their stability monitored by analytical HPLC and LC-MS after 1 h of incubation. Appearance of secondary absorption or mass (m/z) peaks in the chromatogram or spectrum were monitored. Analysis of HPLC traces was done at 650 nm, at lower wavelengths (242 nm, 350 nm and 495 nm) the spectra showed absence of or similar traces to those at 650 nm. MS analysis was done in the range of 100 to 1000 m/z using a LC-MS system and the mass list obtained at the retention time of the corresponding peaks in the Vis window.

QSY21-COOH (**18**) was stable under all tested conditions, and although treatment with 2% hydrazine led to a loss of colour, this was reversible upon addition of a mixture of ACN/H_2O (50/50) with 0.1% FA. Under all evaluated conditions, the HPLC chromatogram remained unchanged with no side-peaks appearing and the corresponding m/z of $[M]^+$ detected by LC-MS. A clear change of colour was observed for every evaluated condition in the case of sulfoCy5 (**12**), from dark blue to dark orange/yellow. The colour change was reversible in all cases except when sulfoCy5 was exposed to 2% hydrazine. Here HPLC chromatograms of **12** in presence of 20% piperidine and 2% hydrazine showed the appearance of a second peak. The corresponding m/z of $[M]^+$ was still detected by in all cases by LC-MS, but new masses were also detected.

These results suggest that Fmoc and Dde protecting groups in QSY21 containing peptides can be cleaved using the whole range of tested conditions. In sulfoCy5 containing peptides, deprotection of Fmoc with 20% piperidine and 2% hydrazine should be avoided, Fmoc cleavage can be achieved using 2% DBU while Dde protecting groups can be removed using mild conditions (imidazole·HCl/NH_2OH/NMP).

4.2.4 Synthesis on solid phase of the linear NIR FRET peptide HNE-1F1Q

The first NIR FRET labelled peptide **HNE-1F1Q** (**21**) was synthesised using the sulfoCy5/QSY21 pair on opposite sides of the hNE cleavable peptide sequence used in the "green" versions of the probe (Figure 53).[66, 134]

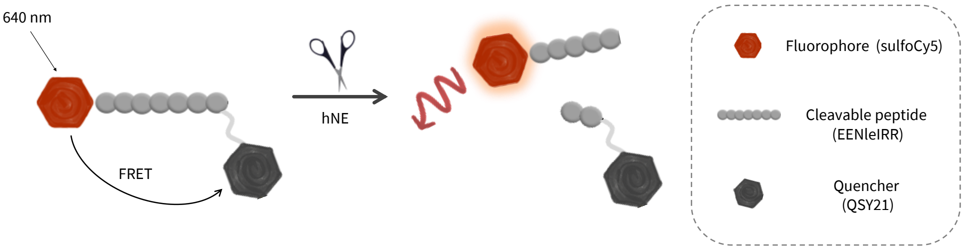

Figure 53 FRET linear NIR probe **HNE-1F1Q.** Cleavage by hNE stops the FRET quenching between the sulfonated Cy5 fluorophore and the QSY21 quencher and results in a switch-on of fluorescence.

For dual labelling of the peptides on solid support, orthogonal protection of reactive groups was required. Here, the Dde protecting group was used for Ɛ-amino group protection on the C-terminal lysine to allow late incorporation of the dyes onto the peptide with orthogonal labelling on the α-amino terminus (hence the stability of the dyes under Dde and Fmoc deprotecting conditions was crucial).

The FRET peptide was synthesised by standard Fmoc/tBu solid phase synthesis using a Dde protected lysine **9** (Fmoc-Lys(Dde)-OH).[85] Following all amino acid couplings, the Dde protected peptide was selectively deprotected on the resin using mild conditions (imidazole/NH_2OH/NMP)[85] and the activated NHS ester of QSY21 (**19**) was coupled at that position, followed by deprotection of the remaining Fmoc group using 20% piperidine and coupling the activated ester of the sulfoCy5 fluorophore on the N-terminus as the final resin-based. Deprotection of acid labile sidechain protecting groups and cleavage from the resin were achieved under acidic conditions (TFA/H_2O/TIS (95/2.5/2.5)) and the peptide subsequently purified by semipreparative reverse phase HPLC.

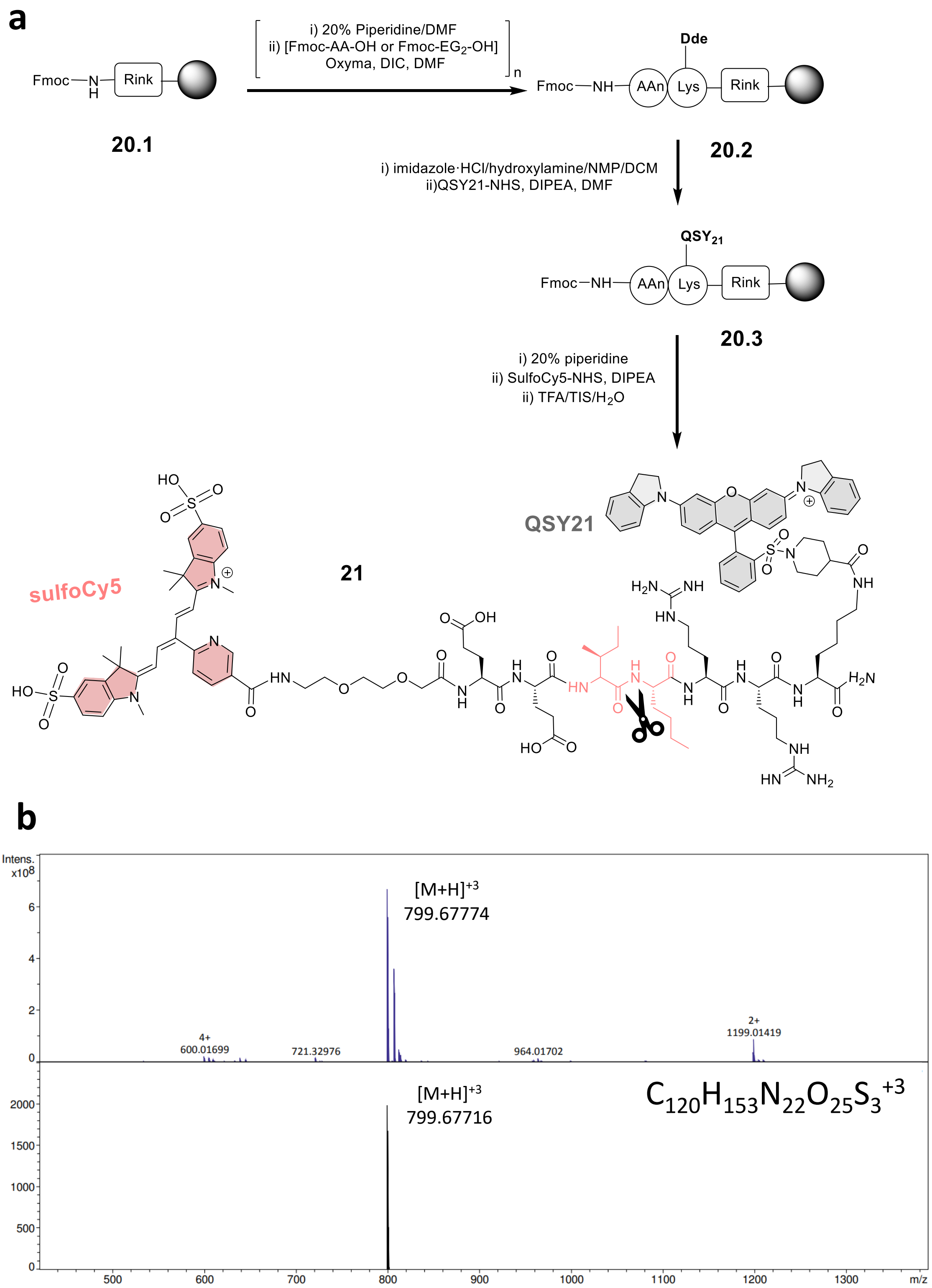

Figure 54 a) Synthesis of **HNE-1F1Q** (**21**) using standard Fmoc solid-phase approach on a Rink amide linker with orthogonal Dde deprotection. Coupling of the sulfoCy5 ester was the final resin-based step before resin cleavage and removal or remaining protecting groups and linker cleavage. **b) FT-MS** analysis of compound **HNE-1F1Q**. Calculated m/z for $C_{120}H_{153}N_{22}O_{25}S_3^{+3}$ $[M+H]^{+3}$ Expected: 799.67716 Found: 799.67774.

Partial deprotection of the Fmoc group was observed on the stored Fmoc/Dde protected peptide scaffold (**20.3**) and a different order of couplings was required. In this scenario and based on the results previously obtained on the stability of the dyes, the pre-activated sulfoCy5 ester (**13**) was coupled first on the N-terminus of the peptide, following full Dde deprotection, again under mild conditions (imidazole·HCl/NH_2OH/NMP).

- ***In vitro* evaluation**

Surprisingly (in view of the number of charges in the molecule), the NIR linear FRET probe (**21**) showed poor water solubility and slow activation kinetics, even at low concentrations and when DMSO as co-solvent.

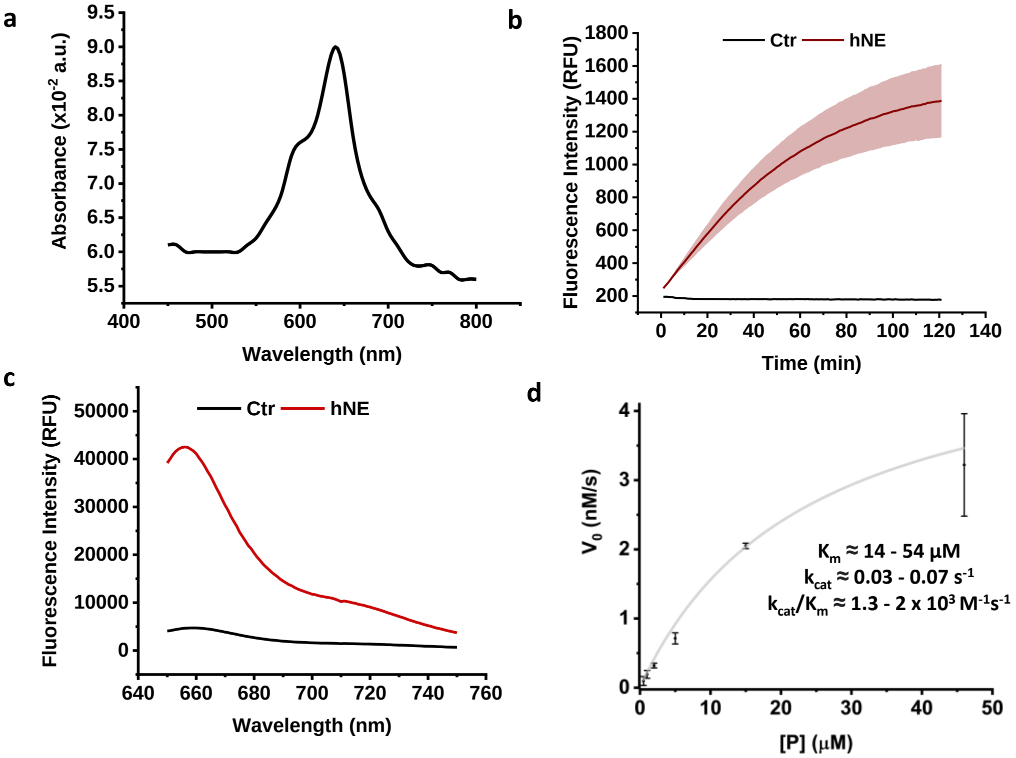

Figure 55 HNE-1F1Q (**21**) characterisation**. a)** Absorption spectrum of **HNE-1F1Q** (38 µM); **b)** Time course of activation of **HNE-1F1Q** (38 µM) by hNE (100 nM), n=3; **c)** Emission spectrum of the probe (38 µM) in the presence or absence of hNE (100 nM)**,** n=3; **d)** Michaelis–Menten plot was generated from calculated initial velocities over the first 15 minutes of reaction at increasing concentrations of **HNE-1F1Q** in the presence of a constant concentration of hNE (100 nM). The kinetic values displayed in **d** were calculated by analysing the Michaelis-Menten saturation curve, LinewaverBurk and Eadie-Hofstee plots. Ctr: Control, no hNE, n = 3.

When the probe (38 µM) was exposed to hNE (100 nM), cleavage took >2 h for full activation and generated limited signal amplification (5-fold). The slow activation was potentially caused by the bulky quencher affecting enzyme access to the cleavage site and the poor solubility of the construct (indeed precipitation was observed in aqueous buffer, even at low concentrations).

Absorption and fluorescence emission were consistent with the expected spectrums for sulfonated Cy5 and K_m and k_{cat}/K_m were calculated from the Michaelis Menten saturation curves, Eadie-Hofstee and LinewaverBurk plots (Figure 55 and experimental section).

4.2.5 Novel strategy for the synthesis of an NIR tribranched probes for human elastase analysis

The strategy initially used for the synthesis of the probe **NES** (**2**, see page 63) was attempted to build a tribranched NIR FRET probe equivalent, bearing three copies of the NIR FRET peptide (**21**). However, incorporation the QSY21 quencher at such a hindered position of the tribranched Fmoc/Dde protected scaffold proved unsuccessful (Figure 56). Therefore, based on the initial results from the linear probe (**21**) and the complexity of the solid phase synthesis, a new synthetic approach was proposed.

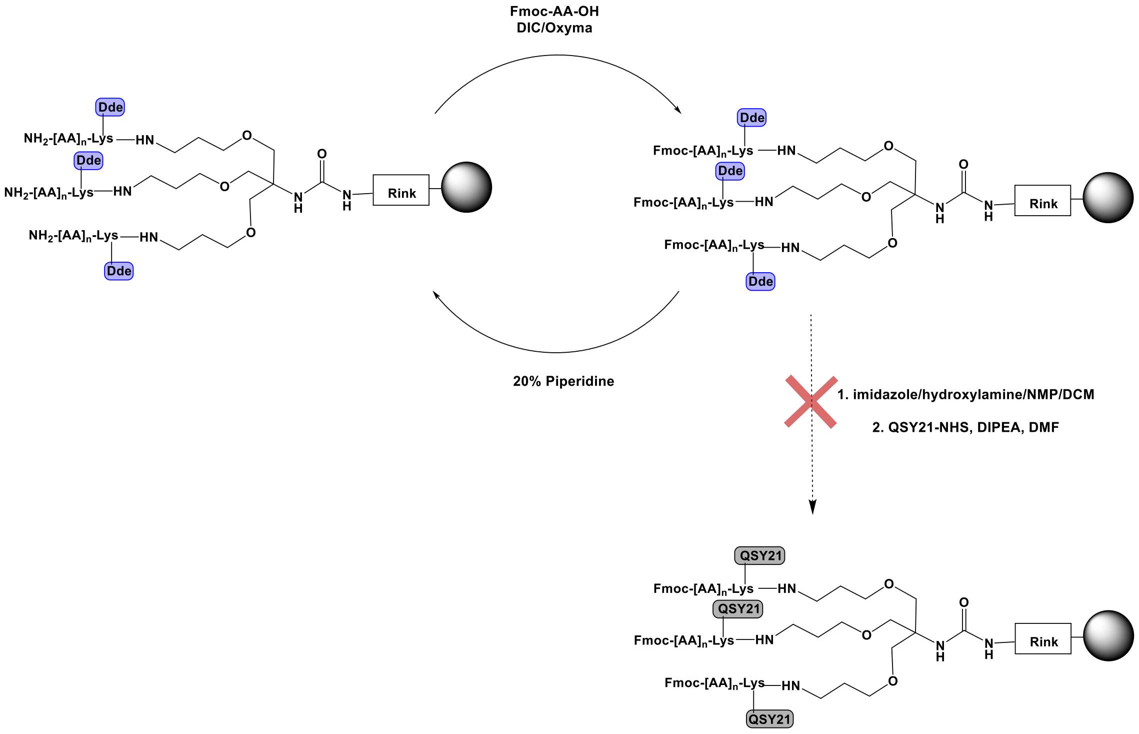

Figure 56 Attempted strategy for the synthesis of tribranched NIR compounds on solid phase as previously described for the "green" probes (chapter 2). Triple incorporation of the QSY21 proved impossible.

This approach targeted a more convergent copper catalysed click chemistry (CuAAc) synthesis for a NIR tribranched probe. The CuAAc was first discovered two decades ago by Meldal and Sharpless. [135, 136] Copper catalysed azide-alkyne cycloaddition transforms organic azides and terminal alkynes exclusively into the corresponding 1,4-disubstituted 1,2,3-triazoles (Figure 57). In contrast, the uncatalyzed reaction, requires much higher temperatures and provides mixtures of 1,4- and 1,5-triazole regioisomers. [137]

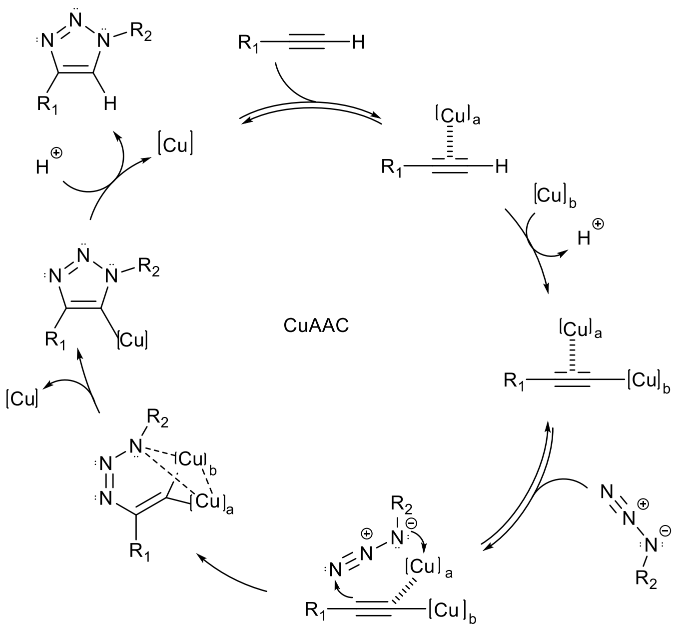

Figure 57 Mechanistic details of the CuAAC as currently proposed.

Addition of external ligands such as THPTA or TBTA (Figure 58) can be used to accelerate the reaction by forming a complex with copper(I) allowing better control of the active species within the reaction media and preventing the formation of ROS species preventing Cu(I) from oxidation. These ligands can also act as a base to promote the initial copper(I)-acetylide formation, thus accelerating the CuAAC. Furthermore, these ligands can enhance the solubility of copper(I) in the desired media.

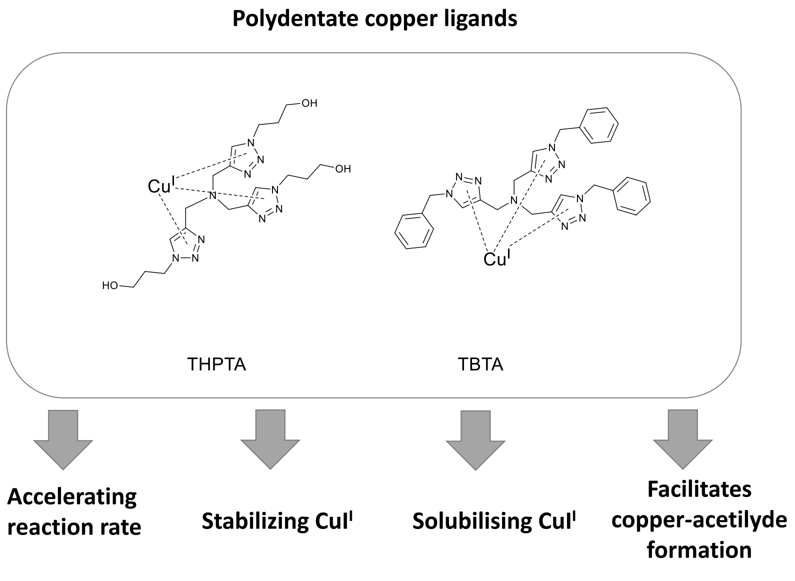

Figure 58 Examples of polydentate copper ligands and their benefits in the CuAAC.

The proposed strategy to build the NIR tribranched probes using CuAAC required two main building blocks: An azide functionalised peptide (three copies) and a tribranched scaffold containing three terminal alkyne groups (Figure 59).

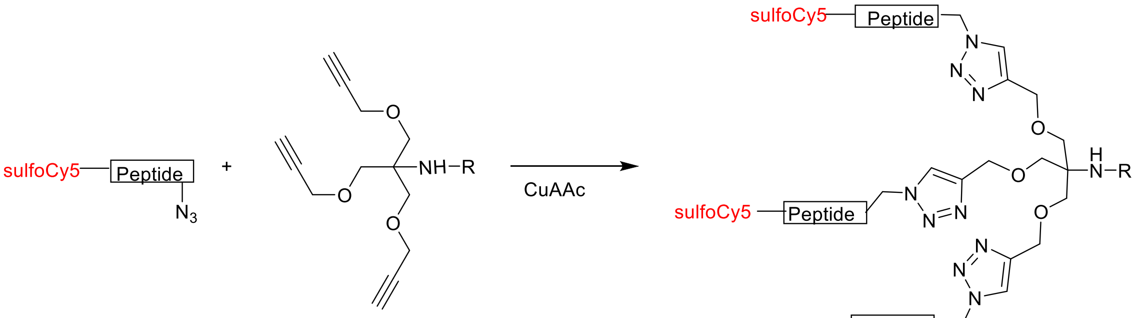

Figure 59 Synthetic strategy for the convergent synthesis of the tribranched NIR probes. sulfoCy5 (fluorophore); R = H or quencher.

In the new design, the quencher (**R**) is distal to the cleavage site to improve cleavage kinetics. This compound thus incorporated a single QSY21 quencher (**18**) on a tribranched scaffold with three copies of the sulfonated-Cy5-peptide (**22**).

The azide building block hNE peptide substrate (**22,** Figure 60) was used, bearing the same cleavable sequence previously used in other probes, capped with sulfoCy5 at the amino-terminus and functionalised with an azide lysine derivative at its C-terminus. The peptide was synthesised using standard Fmoc SPPS, without the need for orthogonal deprotection, improving the overall yield and simplifying the subsequent purification. The azide group survived the TFA/TIS deprotection conditions without problems. In contrast to the linear FRET peptide (**21**), the sulfoCy5 labelled hNE peptide (**22**) was freely water soluble.

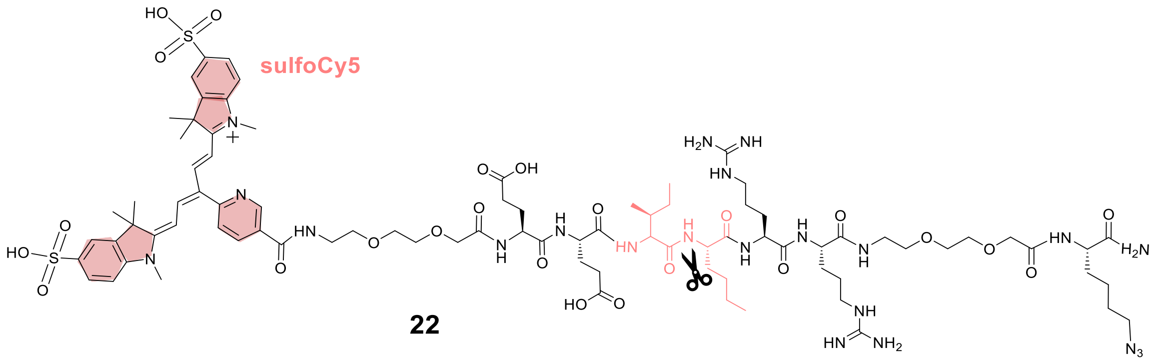

22

Figure 60 Structure of sulfo-Cy5 azide peptide (**22**). The peptide was labelled with a sulfo-Cy5 at the N-terminus and an azide group was incorporated at the C terminus. The Ile↑Nle cleavage site is high-lighted.

The alkyne building block was prepared from *tris*-hydroxymethyl-aminomethane, following a previously reported procedure[138] (Figure 61) to obtain the corresponding Boc protected propargylated scaffold (**23**). This was purified by column chromatography and deprotected with 20% TFA to give the corresponding free amino propargylated scaffold (**24**). Direct modification of the free amino group in **24** with the NHS ester (**19**) did not work (presumably too sterically hindered). Instead, the quencher was conjugated via a bis-ethylene glycol spacer (**25**). The spacer both helps the incorporation of the bulky quencher and improves water solubility.

The bis-polyethylene glycol spacer was attached using a highly reactive acyl fluoride (**25,** Boc-amino-EG$_2$-COF) to help overcome the poor reactivity of the hindered amino group in **24**. Once the bis-ethylene glycol was attached, deprotection of the Boc group under acidic conditions allowed subsequent facile incorporation of the QSY21 NHS ester (**19**) to give the quencher containing alkyne (**27**, see Figure 61).

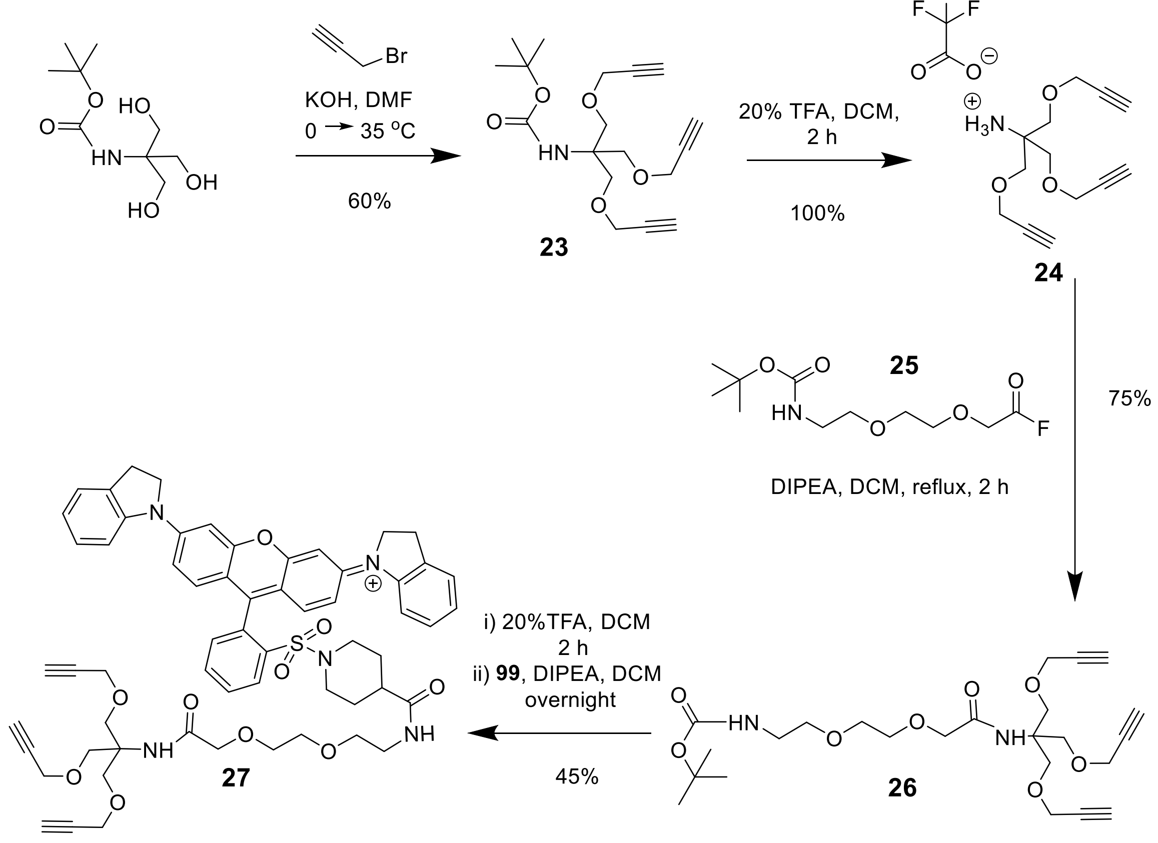

Figure 61 Tribranched scaffold synthesis. The quencher containing alkyne **27** was synthesised from tris-hydroxymethyl aminomethane in 6 steps, with an overall yield of 20%.

The Boc protected bis-ethylene glycol acyl fluoride (**25**) was prepared using a mixture of cyanuric fluoride and pyridine in DCM (Figure 62).[139] Acyl fluoride formation was monitored by generating the corresponding methyl ester *in situ* by dissolving a small amount of crude from the reaction mixture in anhydrous MeOH and the mass change was monitored by LC-MS. The product was used immediately after preparation.

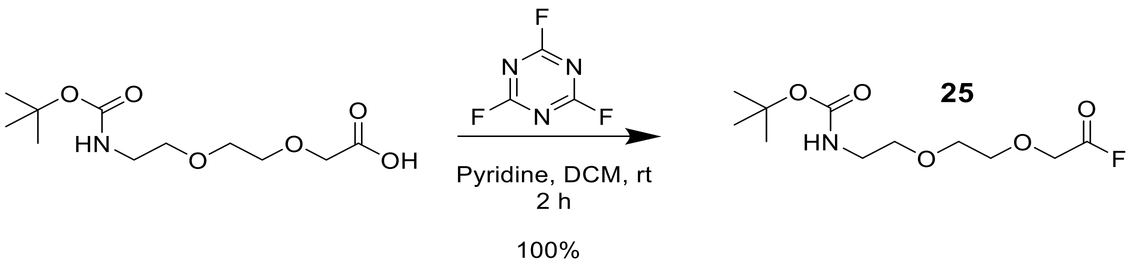

Figure 62 Acyl fluoride synthesis. bis-ethylene glycol acyl fluoride **25** was generated by reacting the corresponding carboxylic acid in the presence of cyanuric fluoride (2 eq) and pyridine (2 eq) in DCM.

- **A self-quenching triple-labelled NIR probe HNE-3F0Q**

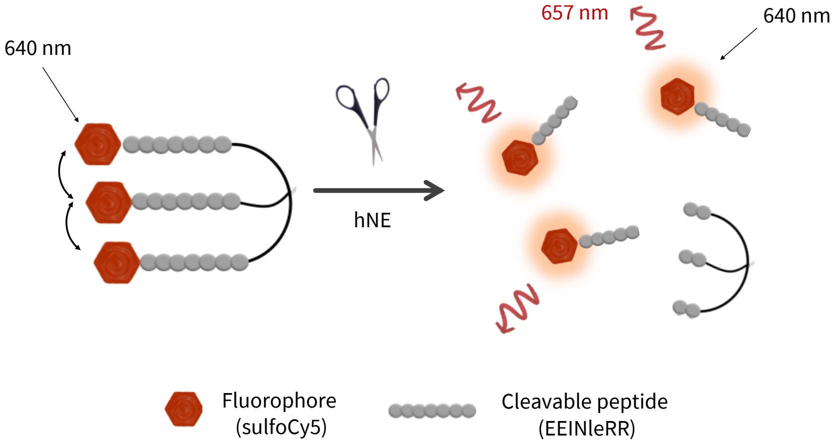

Figure 63 Self-quenching NIR probe**.** Activation by hNE liberates the fluorophores and stops the linear quenching resulting in a switch-on of fluorescence.

The feasibility of the click strategy was tested in a simple model. The NIR tribranched compound (**28**) was assembled that contained three of the sulfoCy5 capped hNE specific peptide **22** utilising the tris alkyne (**24**)**.** This compound served not only as a model reaction, but also, as a "self-quenching" control, where the "linear" quenching effect on the three dyes could be assessed, in the absence of any quencher (Figure 63).

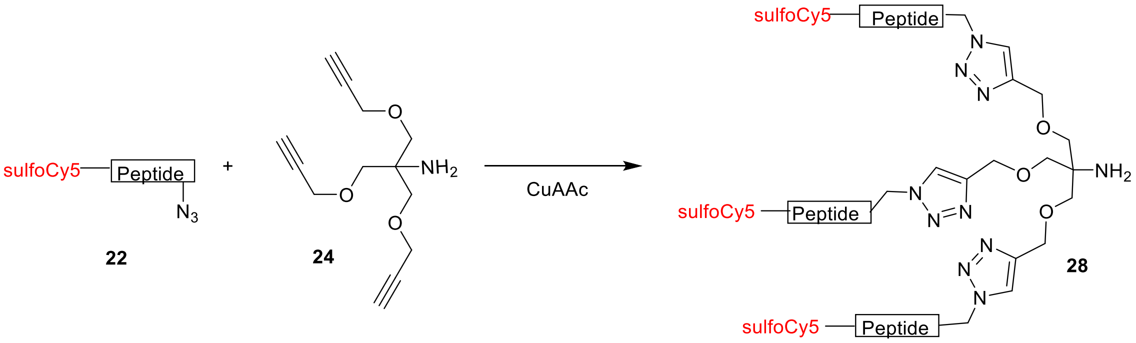

Figure 64 Synthetic strategy for assembly of self-quenching probe HNE-3F0Q (28).

Bioconjugation using CuAAC becomes more challenging in cases involving biomolecules such as peptides, proteins or polynucleotides due to the low concentrations at which these biomolecules are often manipulated which presents significant challenges. [140-143] The bioconjugation becomes even more complex when attempting "dendrimeric" or multibranched click reactions, where several groups in the same molecule need to react. [138]

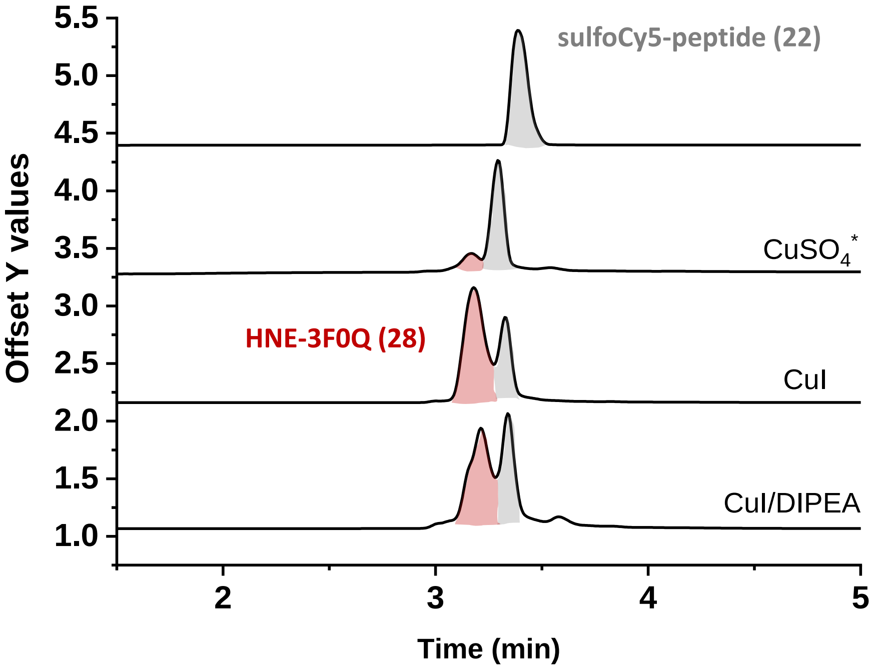

Figure 65 Synthetic conditions evaluated to generate **HNE-3F0Q** (**28**, red peak). Monitoring was done by RP-HPLC at 650 nm eluting with a gradient of ACN/H_2O 0.1% FA over 6 min and based on changes in the sulfoCy5-peptide (**22**) peak (grey**,** the excess of peptide 22, 1 equivalent, will remain after 100% conversion of the alkyne). *$CuSO_4$ /THPTA/aminoguadinide/NaAsc in *t*-BuOH/H_2O.

Based on previous optimised methods for bioconjugation of peptides and dendrimers, different conditions were tested to synthesise the self-quenching probe **HNE-3F0Q** using four equivalents of the sulfoCy5 labelled peptide (**22**) per alkyne (**24**). Conditions tested included $CuSO_4$ /NaAsc in presence of the ligand THPTA and aminoguanidine in tBuOH/H_2O[144] , CuI only, or CuI in presence of base with DMF as solvent. When the $CuSO_4$ /NaAsc conditions were used[138, 144], conversion into the product was poor whilst high conversion was observed in the presence in conditions using copper iodide, [138] with minor traces of the mono- and bibranched intermediates (Figure 65). Since the addition of base did not result in an improvement in reaction rate or yield, the condition using CuI in DMF was selected for the synthesis of **HNE-3F0Q** (Figure 66).

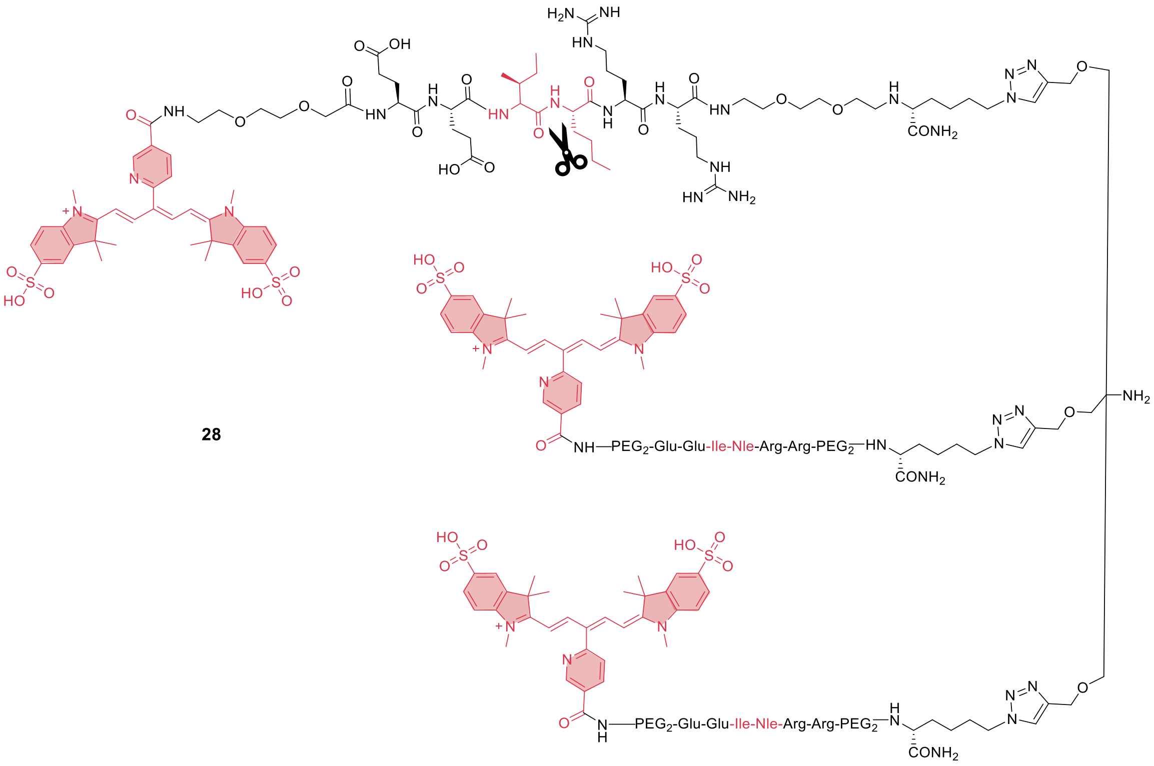
28

Figure 66 Self-quenching NIR probe **HNE-3F0Q** (**28**) containing three copies of the highly specific hNE sequence labelled with sulfoCy5 on their amino terminus.

The non-quencher containing probe relies solely on the linear self-quenching effect between the three dyes and therefore the amplification of signal would be expected to be limited. The fluorogenic capacity of **HNE-3F0Q** (**28,** 12 µM) was evaluated *in vitro*, and a 2-fold amplification upon exposure to elastase (100 nM), was observed (Figure 67). This limited amplification is consistent with the results observed previously in previous self-quenching probes such as the green probe **NAP** (**1**). Absorption and fluorescence emission were consistent with the expected spectra for sulfoCy5 and kinetic parameters K_m and k_{cat}/K_m were calculated from the Michaelis Menten saturation curves, LinewaverBurk and Eadie-Hofstee plots (Figure 67 and experimental section).

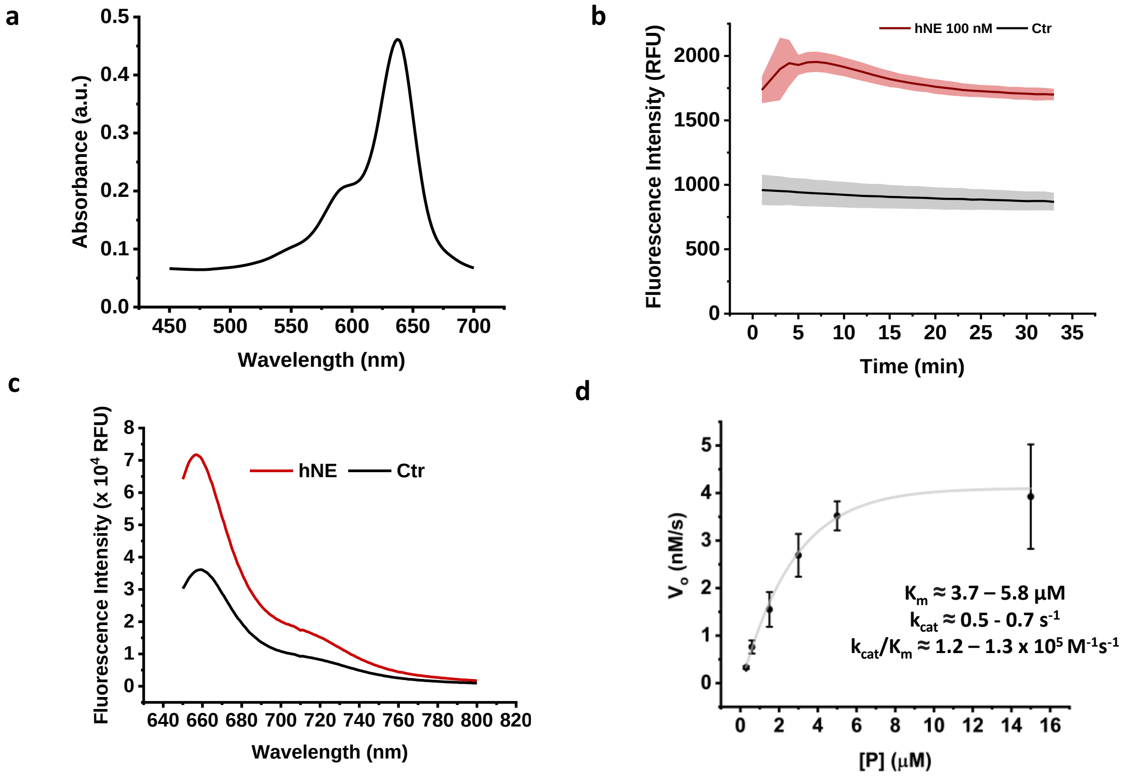

$K_m \approx 3.7 - 5.8\ \mu M$

$k_{cat} \approx 0.5 - 0.7\ s^{-1}$

$k_{cat}/K_m \approx 1.2 - 1.3 \times 10^5\ M^{-1}s^{-1}$

Figure 67 HNE-3F0Q (**28**) characterisation. **a)** Absorption spectrum of **HNE-3F0Q** (12 µM) shows a maximum absorption at 640 nm**; b)** Activation of **HNE-3F0Q** (12 µM) happens within seconds in presence of hNE (100 nM) but the background fluorescence of the uncleaved probe is high, only achieving an approximately 2-fold increase in signal; **c)** Fluorescence emission of **HNE-3F0Q** (**28**) in the presence and absence of hNE (100 nM) (maximum emission at 657 nm); **d)** Michaelis–Menten saturation curve for activation of increasing concentrations of **HNE-3F0Q** in the presence of hNE (10 nM). Kinetic values were calculated by analysing the Michaelis-Menten saturation curve, LinewaverBurk and Eadie-Hofstee plots. Ctr: Control, no hNE.

4.2.6 A triple-labelled one-quencher containing FRET NIR probe

To improve the signal-to-noise ratio of the probe, incorporation of a single quencher was targeted to obtain the “three-fluorophore-one-quencher” tribranched probe **HNE-3F1Q** (**29**). In this design, the quencher molecule enhances the overall silencing effect via FRET and the solubility of the overall compound would be less affected compared to the NIR linear FRET peptide (**21**).

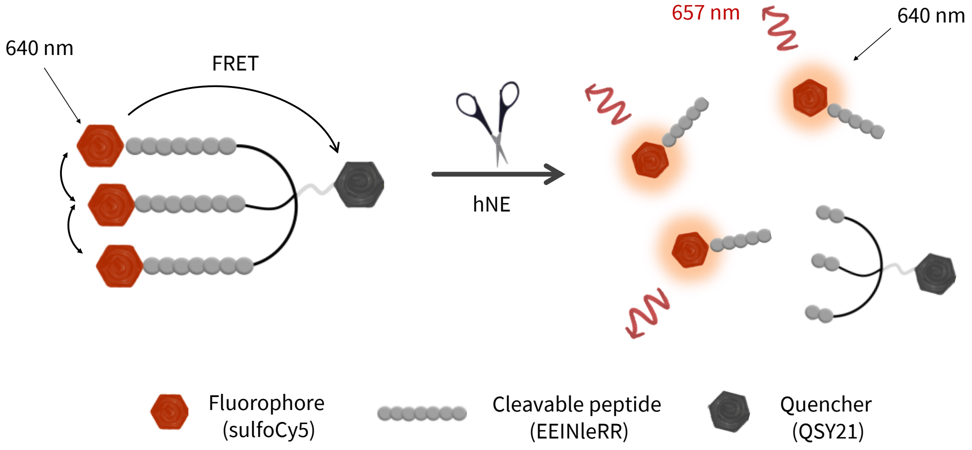

Figure 68 Super-silent NIR probe combines FRET quenching between the sulfoCy5 fluorophores and the QSY21 quencher and self-quenching of the three sulfoCy5 fluorophores between themselves in the tribranched structure.

The probe was constructed from alkyne (**27**), by reacting with the azide peptide (**22**) to obtain **HNE-3F1Q** (1:4, alkyne:azide). Initial attempts, using the CuAAC conditions previously used for the synthesis of the self-quenching probe (**28**), showed poor conversion, and this had to be optimised.

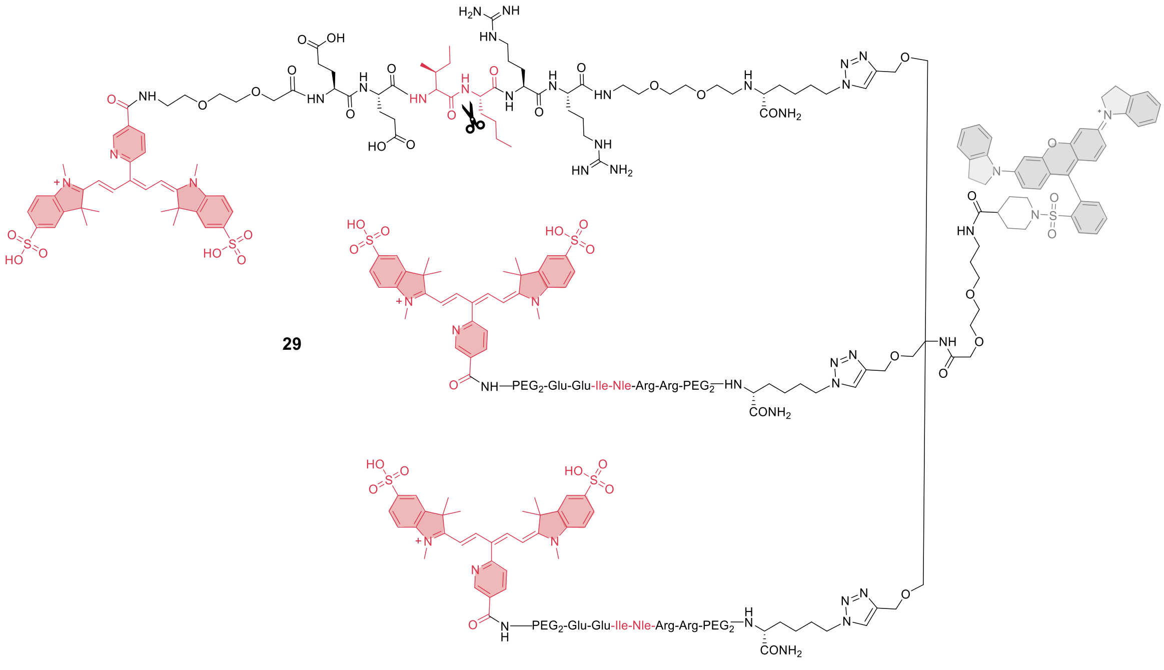

29

Figure 69 Probe **HNE-3F1Q** (**29**) that incorporates one quencher and three dyes, with the quencher located distally from the cleavage site.

- **Optimisation of the cycloaddition conditions**

Conditions for the CuAAC were optimised using a different peptide model (Figure 70) due to the limited availability of the NIR building blocks. Alkyne (**24**) was used as the tribranched scaffold, and a bulky azide peptide, bearing a FRET label (**30**) (previously synthesised) were reacted using different reaction conditions.

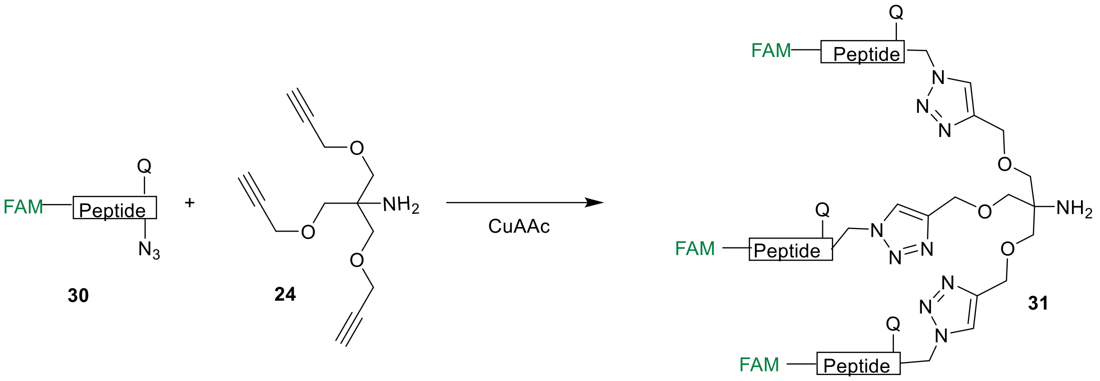

Figure 70 CuAAC optimisation conditions with a model peptide (**30**) and the tris alkyne (**24**). FAM = fluorophore; Q = quencher.

The reaction conditions evaluated (Table 3 and Figure 71) included the previously tested $CuSO_4$/NaAsc conditions as well as copper iodide, in the presence or absence of the copper ligand (THPTA). When the reaction was run in the presence of $CuSO_4$/NaAsc/THPTA/aminoguadine, similar results to those previously obtained were observed, with mono- and bibranched probes appearance and minimal conversion into the tri-branched product. The use of CuI in DMF gave good conversion into the desired product (as previously observed in the synthesis of probe **HNE-3F0Q**) with minimal amounts of mono- or bibranched products observed. The addition of the ligand THPTA in the presence of CuI helped solubilising the CuI (otherwise insoluble in DMF). The ligand was added in 5-fold excess with respect to CuI and the combination was premixed prior to addition to the reaction. When the THPTA ligand was used, the reaction rate was accelerated, with full conversion achieved within 1 h of reaction while addition of DIPEA in this case was detrimental. Based on the results obtained, the conditions using CuI/THPTA in DMF were used for the synthesis of **HNE-3F1Q** (**29**).

Table 3 Conditions for the CuAAc evaluated. Temperature: 40 ^{0}C, atm: N_2. Conversion percentages were calculated based on integration from analytical HPLC traces (495 nm) of the crude. *Based on conversion of ¾ of the area of peptide-azide original peak.

[Alkyne/azide]	Solvent	Cu source	Additive	Time	Conversion*
Alkyne (0.5 mM) Azide (2 mM)	*t*-BuOH/H_2O (1:2)	$CuSO_4$ (2 mM)	THPTA (10 mM) NaAsc (80 mM) Aminoguanidine (80 mM)	24 h	<10%
	Anh DMF	CuI (1 mM)	--	24 h	100%
			DIPEA (4 mM)	24 h	<10%
			THPTA (5 mM)	1 h	100%

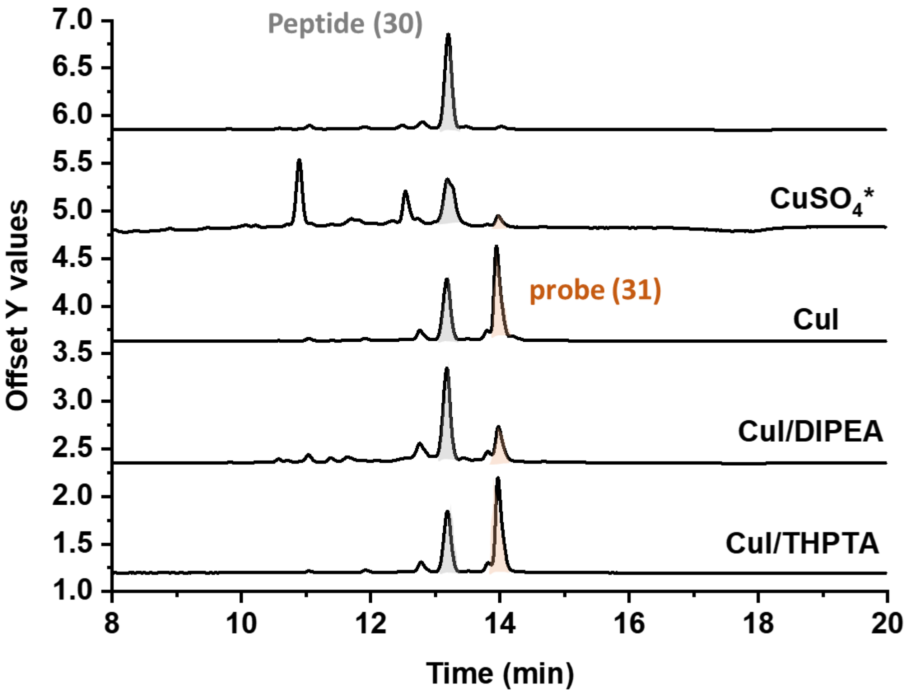

Figure 71 Representative HPLC traces of the different conditions for CuAAC. The reaction was monitored by RP-HPLC eluting with ACN/H_2O 0.1% FA over 20 min and detection at 495 nm. **Top trace:** pure starting peptide (**30**). Other traces show conditions screened. Grey peak corresponds to starting FRET peptide (**30**) and the orange peak corresponds to the tri-branched product (**31**). All conditions show the trace after 24 h except for CuI/THPTA, that shows the trace after 1 h. (the excess of peptide 30, 1 equivalent, will remain after 100% conversion of the alkyne). * $CuSO_4$/THPTA/NaAsc/Aminoguanidine.

- **Synthesis of probe HNE-3F1Q (29)**

Using the optimised conditions, **HNE-3F1Q**, containing a single quencher and three fluorophores was successfully synthesised (Figure 72). Disappearance of the alkyne (**27**) peak was rapid, within the first hour of reaction (fast disappearance is to be expected since each molecule contains three reactive sites and will form the monobranched construct quickly). However, consumption of the sulfoCy5 peptide (**22**) was slower, with maximal consumption achieved after 24 h. The crude product from the reaction was purified using RP HPLC to give probe **HNE-3F1Q** (**29**) as a blue lyophilised powder.

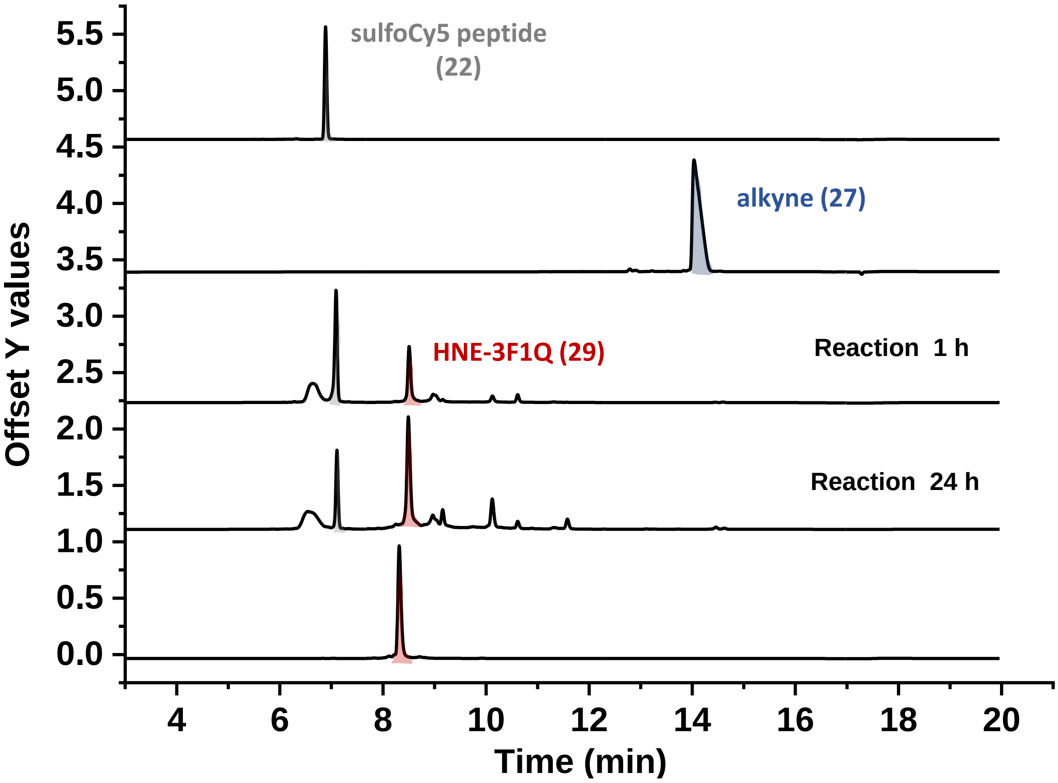

Figure 72 Reaction monitoring for the synthesis of HNE-3F1Q (**29**, red peak). Monitored by RP HPLC (650 nm). Four equivalents of sulfoCy5 labelled peptide (**22**, grey peak) were reacted with 1 equivalent of the alkyne (**27,** blue peak) in the presence of CuI/THPTA. The progress was monitored by the changes in the sulfoCy5 peptide peak (grey peak), which is consumed over time (the excess, 1 equivalent, will remain after 100% conversion of the alkyne). As the peptide is consumed, the appearance of a new peak corresponding to the HNE3F1Q product (black box) is observed.

Excess copper remaining following synthesis can be problematic since copper ions are toxic to cells. [145] Here, the excess copper in the final probe was removed using a thiol functionalised resin. [146, 147] The scavenger resin was synthesised in house and copper removal monitored by ICP-MS. For the resin, mercaptobenzoic azid (4-MBA) was coupled using DIC/Oxyma onto an aminomethyl polysterene resin with couplings monitored by a ninhydrin test.

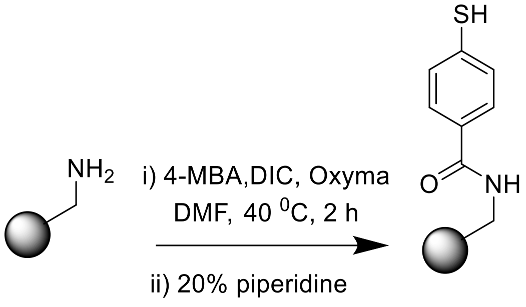

32

Figure 73 Synthesis of the thiol-resin. The scavenger resin contains a thiol group that can bind to copper.

Thus, for resin treatment, after HPLC purification, resin **32** was added to the pure combined fractions (in ACN/H_2O) and the solution shaken for 30 min. The beads were filtered off and the resulting elutant, lyophilised to give the product. Samples for ICP-MS were prepared by dissolving the lyophilised product in deionised water containing a small amount of nitric acid to help solubility. Results showed efficient removal of copper by resin treatment, with a Cu concentration of 236 µg/l in the lyophilised sample that was not treated with the scavenging resin, whilst in the sample that was treated with resin **32**, the Cu concentration was reduced to 0.04 µg/l (a 5900 fold reduction)

• *In vitro* evaluation

A rapid increase in fluorescence signal from **HNE-3F1Q** (**29**) was observed within seconds when hNE was added (100 nM), with up to 15-fold signal amplification (at 12 µM of probe), and the fluorescence background of the uncleaved form was negligible (Figure 74b). These results suggest that a single QSY21 quencher can efficiently quench the three fluorophores within the compound. The excitation and emission spectrum of the probe showed that the maximum excitation wavelength (λ_{ex}) was observed at 640 nm and maximum emission (λ_{em}) at 657 nm, consistent with the optical properties of the incorporated sulfoCy5 (Figure 74a) (akin to the linear and self-quenching probes). Activation of the probe was fully inhibited in the presence of the elastase inhibitor Sivelestat (100 µM) (Figure 74c).

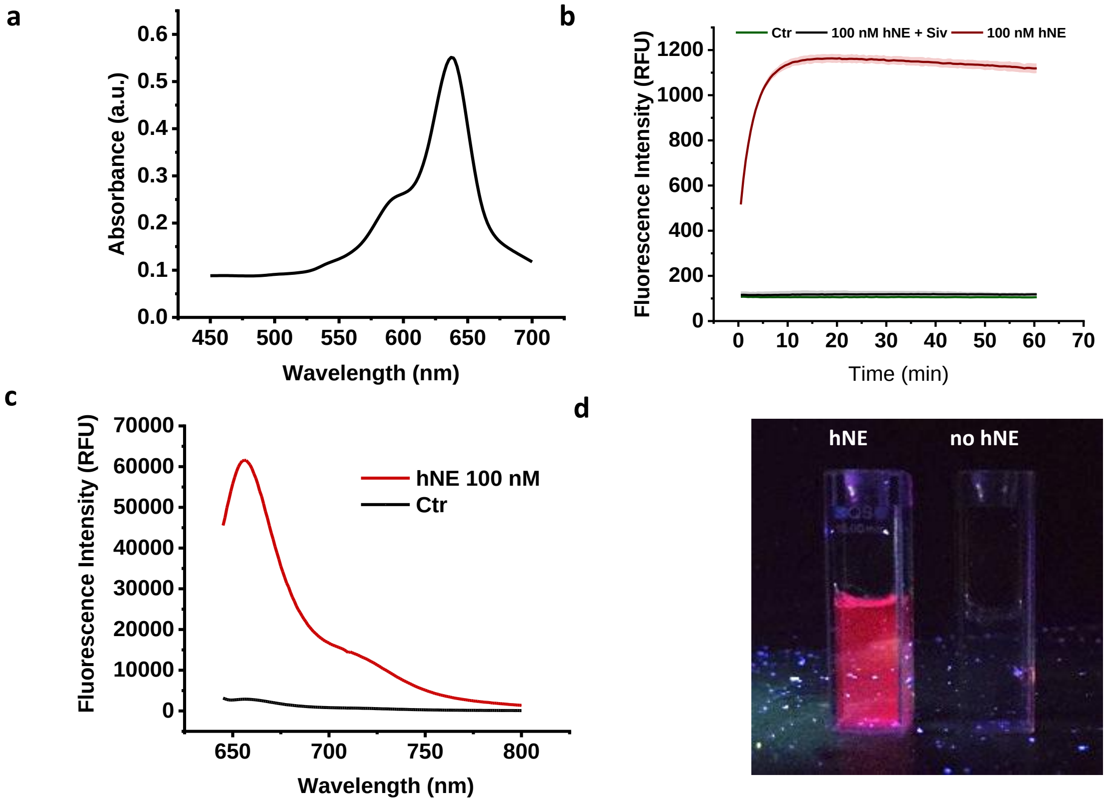

Figure 74 Activation in presence of hNE and probe's specificity. **a)** Absorption profile of **HNE-3F1Q** (**29**, 12 µM) n=2; **b)** Activation of probe (12 µM) is fully prevented in the presence of the elastase inhibitor Sivelestat (100 µM) n=3; **c)** Fluorescence emission of HNE-3F1Q (29) in the presence and absence of the protease n = 3; **d)** Fluorescent signal under irradiation by a 590/15 nm lamp of stocks of activated and non-activated probe (10 µM).

The specific hydrolytic cleavage between Ile↑Nle was confirmed following **HNE-3F1Q** (12 µM) incubation with hNE (100 nM) and analysis of the reaction mixture by MALDI-TOF MS confirmed the appearance of peaks with the expected masses (Figure 75). No other cleavage sites were identified, indicating a sequence specific cleavage by elastase of this probe. The non-prime (N-terminal fragment), sulfoCy5 containing fragment was clearly detected as well as the fully cleaved prime fragment (C-terminal fragment) containing the QSY21 fragment (Figure 75). In the spectrum. A small MS peak corresponding to the partially cleaved probe, with an intact single branch and two cleaved peptides was also detected, but no intact probe or the two branched probe were seen. These results suggest an efficient cleavage of the probe by the protease and confirm specific cleavage between the expected residues (Ile↑Nle).

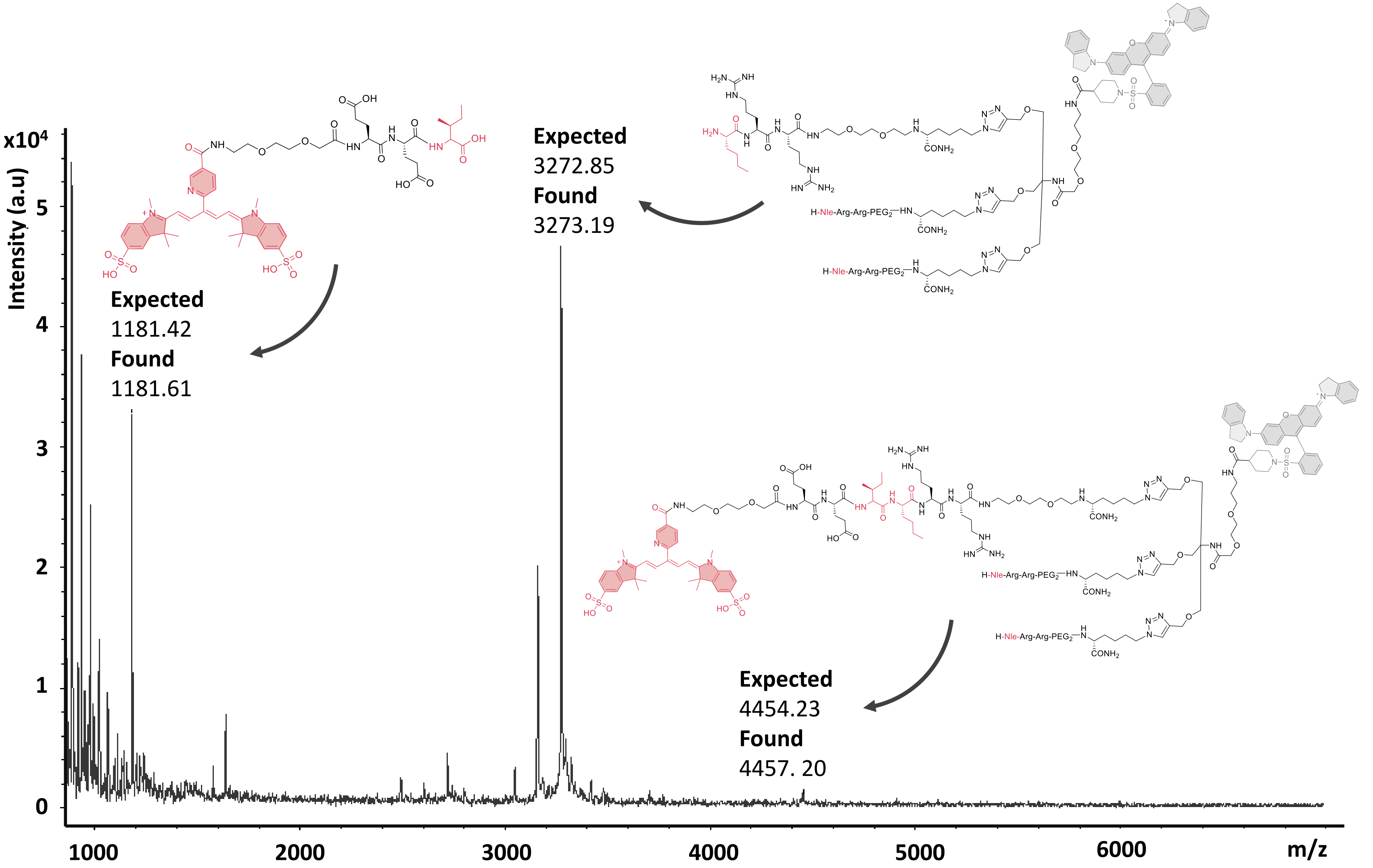

Figure 75 MALDI-TOF MS analysis of the reaction mixture confirmed the presence of the fully cleaved C-terminal prime fragment of **HNE-3F1Q** (m/z 3273.2) and the non-prime fragment (m/z 1181.6) and the probe with one remaining branch intact (m/z 4457.2) were also found in the spectra.

The previous green emitting probes **NAP** (**1**) and **HNE-FQ** (**11**) showed high specificity for hNE, using a similar peptide sequence, thus specificity for the protease was expected for **HNE-3F1Q** (**29**) and this was confirmed by incubation in presence of the relevant proteases Proteinase 3 and Cathepsin G, which resulted in negligible cleavage.

The stability of the fluorescence of **HNE-3F1Q** is important for *in vivo* applications, where biological environments have increased complexity when compared to *in vitro* set-ups. Therefore, the fluorescence stability of the probe was tested in a variety of environments (Figure 76). The probe's fluorescence was (as expected) pH independent and incubation of the probe in 10% fetal bovine serum, HeLa cell lysate or complete cell media showed no effect on the fluorescence signal (on the unactivated or activated probe).

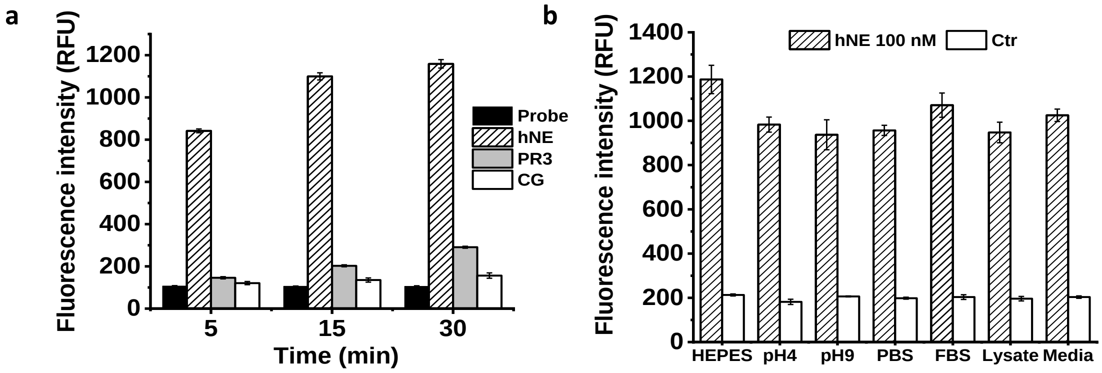

Figure 76 a) Probe **HNE-3F1Q** (12 µM) is only cleaved by hNE (100 nM), with negligible cleavage by closely related proteases Cathepsin G (100 nM) and Proteinase 3 (100 nM); **b)** Stability of probe (concentration on well 10 µM) in different complex biological environments. The fluorescence of the cleaved and uncleaved probe was monitored in either 10% FBS, complete cell media or a Hela cell lysate for 2 hours at 37°C in a final volume of 50 µL. Results demonstrate no activation of the uncleaved probe in absence of the protease in the different environments, with fluorescence intensities unaltered over time. PR3: Proteinase 3, CG: Cathepsin G, Ctr: Control.

Kinetic parameters were obtained for **HNE-3F1Q** as previously described, with the initial velocities plotted using Michaelis Menten, Lineweaver Burk or Eadie Hofstee graphs to obtain the corresponding kinetic parameters (Figure 77) of K_m (that ranged between 2 and 7 µM), k_{cat} (that ranged between 0.2 and 0.3 s^{-1}) and catalytic efficiency (k_{cat}/K_m) that was $3.5 \times 10^4\ M^{-1}s^{-1}$.

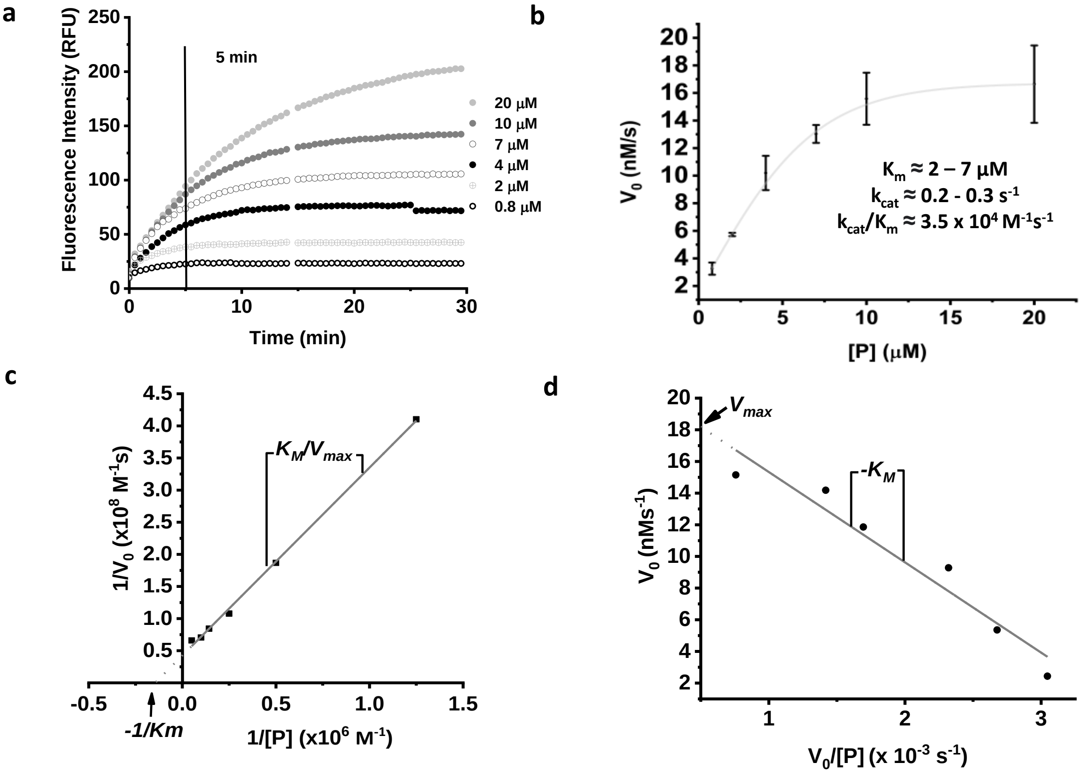

Figure 77 a) Activation at increasing concentrations of probe **HNE-3F1Q** (0.8 µM to 20 µM) in presence of a constant concentration of protease hNE (100 nM) allows calculation of initial velocities based on the linear increase in fluorescence intensity over the first 5 minutes of incubation. **b)** Michaelis Menten curve generated from the initial velocities calculated in the range of 0.8 to 20 µM. Linearisation of the data allows generation of **c)** Lineweaver Burk plot (1/V vs 1/[P]) or **d)** Eadie Hofstee plot (V vs V/[P]). All datapoints are n=3.

- **Neutrophil imaging**

To evaluate if **HNE-3F1Q** was able to detect hNE in neutrophils, primary human neutrophils were activated by exposure to fMLF or PMA. An increase in fluorescence from the probe was observed in activated neutrophils when compared to untreated controls. A clear difference between formyl-MLF and PMA activation was observed. The formyl-MLF activated neutrophils had intact nuclei while PMA activated cells formed "cloud-like" structures, with the DNA signal diffusing into the extracellular environment and co-localised with the NIR signal of 10, indicating co-localisation of DNA and hNE in these neutrophil extracellular traps (NETs).

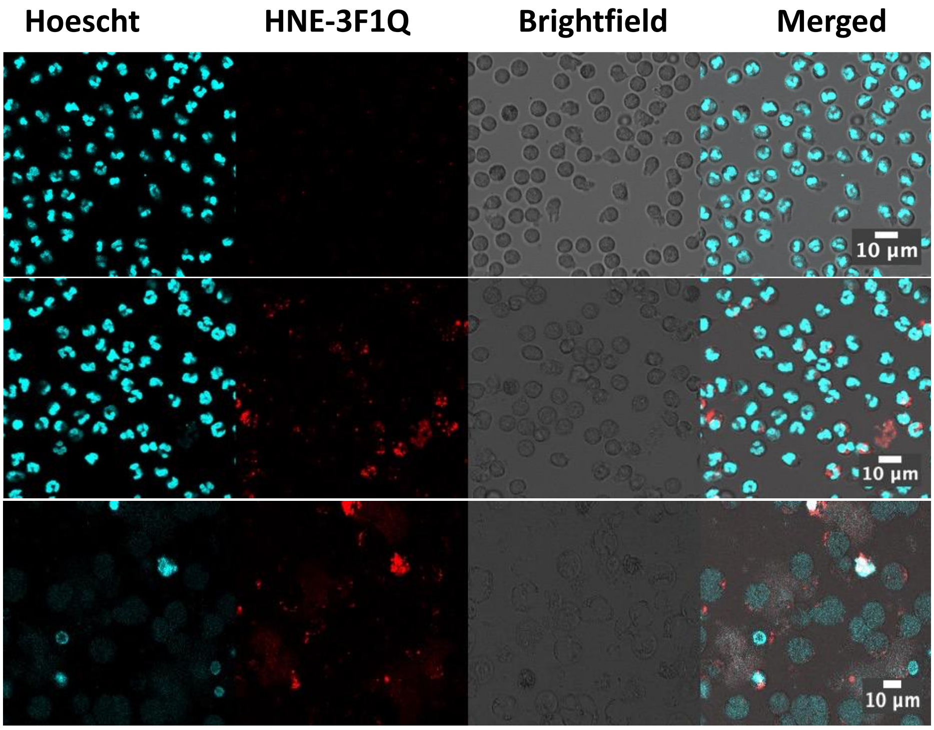

Figure 78. Fluorescence microscopy images of neutrophils activated with fMLF or PMA after incubation with **HNE-3F1Q** (5 µM) for 3 hours, followed by nuclear staining with Hoechst 33342 (10 nM). Detection wavelengths: blue channel (Hoechst) λ_{ex}: 405 nm / λ_{em}: 420-500 nm; red channel (probe) λ_{ex}: 633 nm / λ_{em}: 650-710 nm.

- **Comparative studies of NIR probes**

Activation profiles of all three probes were compared side-to-side. For the comparison, the fold increase in fluorescence signal at each timepoint of the time-dependent activation profiles were calculated by dividing the fluorescence signal by the background fluorescence of the intact probe (concentrations were approximately 12 µM for the tribranched probes and 35 µM for **HNE-1F1Q**). The best results in terms of signal amplification were obtained with the tribranched probe **HNE-3F1Q** (**29**), that showed a 10-fold increase in signal whilst the linear NIR FRET peptide and the self-quenching probes showed limited amplification (6- and a 2-fold, respectively). The activation profile also showed rapid activation for **HNE-3F1Q**, like the self-quenching probe **HNE-3F0Q**, that also had a rapid increase in signal with NIR fluorescence emission, as opposed to the linear FRET peptide, which was very slowly activated (Figure 79).

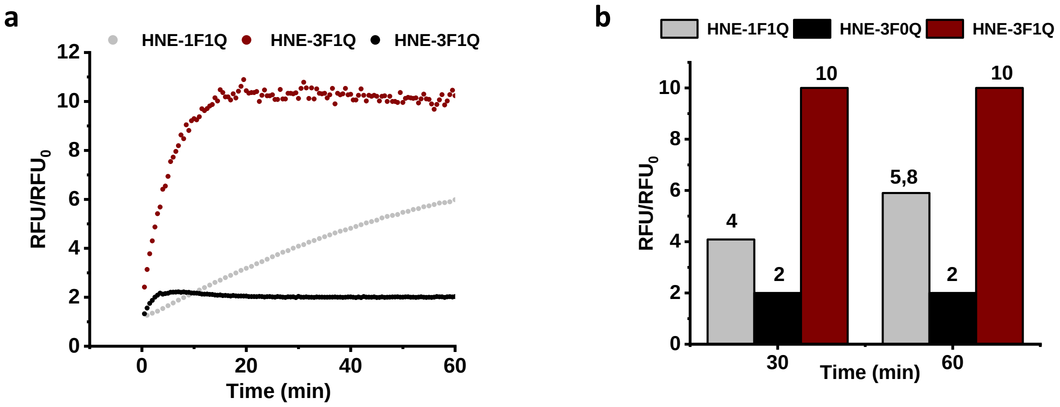

Figure 79 Comparison of activation profiles of self-quenching probe **HNE-3F0Q** (**28**, 12 µM), the super silent probe **HNE-3F1Q** (**29**, 12 µM) and linear FRET peptide **HNE-1F1Q** (**21,** 35 µM) in the presence of hNE (100 nM); **a)** Probes activation in the presence of hNE (100 nM). Fluorescence intensity signals for each of the probes were normalised by dividing by the background fluorescence (uncleaved probe); **b)** Fold increase in fluorescence signal of the probes following 30 or 60 min incubation with hNE (100 nM).

Kinetic parameters comparison shows that **HNE-1F1Q** (**21**), with a slow activation profile has high K_m values and low k_{cat}, resulting in a low catalytic efficiency (k_{cat}/K_{m}, 2×10^3 $M^{-1}s^{-1}$). The fastest activation was observed in the self-quenching probe **HNE-3F0Q** (**28**), having a low K_m and high turnover number and resulting in the highest catalytic efficiency (k_{cat}/K_m, 1.5 × 10^5 $M^{-1}s^{-1}$) of all three probes. The longer activation time required by **HNE-3F1Q** (**29**) resulted in a lower catalytic efficiency compared to the self-quenching probe (1.5 × 10^4 $M^{-1}s^{-1}$), but higher than the linear FRET substrate. The comparison on both the activation profile and kinetic parameters for all three probes is summarised in Table 4.

Table 4 Comparison of **HNE-1F1Q** (**21**), and probes **HNE-3F0Q** (**28**) self-quenching, **HNE-3F1Q** (**29**), three fluorophores and one quencher). Table summarises the relevant kinetic values of all three probes. *at 12 µM (probes **28** or **29**) or 35 µM (probe **21**) and 100 nM of hNE.

Probe	Structure	Quenching type	Activation time*	Fold$_{max}$ (RFU/RFU$_0$)	k_{cat} (s^{-1})	k_{cat}/K_m ($M^{-1}s^{-1}$)
HNE-1F1Q	Linear	FRET	2 h	6	0.03-0.07	2 × 10^3
HNE-3F0Q	Tribranch	Self-quenching	5 min	2	0.5-0.7	1.5 × 10^5
HNE-3F1Q	Tribranch	FRET and self-quenching	15 min	10	0.2-0.3	3.5 × 10^4

Taken together, comparative results demonstrate that **HNE-3F1Q (29)** is an excellent probe for NIR fluorescence detection of elastase *in vitro*, providing the greatest signal amplification of all three probes synthesised. The fluorescence background was negligible when the probe was inactive, a problem that the self-quenching probe **HNE-3F0Q (28)** suffers from. The activation of the probe was rapid and the catalytic efficiency was within an appropriate range for *in vitro* applications. Work is undergoing for biological validation of the probe in neutrophils.

4.3 Conclusions

A series of FRET NIR probes for the detection of hNE have been synthesised with emission in the NIR region of the spectrum, where within biological samples the endogenous biomolecules present reduced light scattering coefficients, decreased absorbance, and minimal autofluorescence.

The highly water-soluble sulfonated Cyanine 5 was chosen as the fluorophore for NIR emission, with emission maximum at 660 nm. QSY21 was selected as the appropriate quencher, with full spectral overlap, capable of absorbing the light emitted by the fluorophore by FRET quenching when close in space. The first design consisted of a linear FRET substrate that resulted to be a poor substrate for elastase, with poor water solubility and very slow cleavage kinetics, which could be due to the presence of the bulky and poorly soluble quencher near the cleavage site. Based on these results, a new approach was developed, whereby a tribranched NIR probe was synthesised.

Previously reported synthetic methods used for the synthesis of the green emitting tribranched probes for elastase proved unsuccessful and a novel synthetic approach was proposed, using a more convergent assembly method utilising copper catalysed azide-alkyne cycloaddition (CuAAc). In the new design, three copies of a sulfoCy5 N-terminal labelled elastase substrates, bearing an azide at the C-terminus, were clicked by CuAAc with a tribranched scaffold bearing three terminal alkyne groups. The scaffold also incorporated a single copy of the quencher. This strategy allows for the quencher to be placed far from the cleavage site and that proved to be key for efficient probe activation.

A self-quenching control, without any added quencher molecule was synthesised to evaluate the self-quenching effect of the fluorophores on the tribranch scaffold. Indeed, self-quenching of the probe allowed for a 2-fold increase in signal upon a rapid activation, but the background fluorescence remained high.

The final design, incorporating a single quencher, presented an excellent optimised probe, with much improved signal amplification when compared to the linear FRET substrate and the self-quenching probe. Activation of the probe was significantly faster than the linear version, consistent with that of the control where no quencher was present. I hypothesise that the presence of the quencher in close proximity to the cleavage site hindered access of elastase and relocation of the quencher lead to a significant improvement in signal amplification and activation velocity.

Chapter 5 A Fluorogenic Probe for the detection of Cathepsin D

5.1 Introduction

Monocytes are a group of cells found in the bone marrow, spleen and circulating blood. These pluripotent immune cells leave the bone marrow and remain in circulation for up to 1–2 days and, during this time, they can be recruited into tissues and differentiate into macrophages to replenish counts of tissue-specific resident macrophages or to face an inflammatory challenge. If they have not been recruited into a tissue facing a danger within 1–2 days, they die and are cleared by other phagocytes. Once in tissue, depending on the stimuli received, macrophages can then be polarised to two phenotypes that have different functions, they can contribute to homeostatic functions, or help in the inflammatory response during an infection (Figure 80).[148]

Classically activated or M1 macrophages, or so-called “fighting” macrophages, are essential for fighting infection (via pathogen phagocytosis) and for the maintenance of tissue homeostasis. They produce nitric oxide (NO) and other reactive oxygen species to help destroy invading bacteria and viruses. During the initial stages of bacterial infection, M1 macrophages are responsible for fighting bacterial infection and are largely responsible for bacterial clearance, together with neutrophils.[149] Clearance of bacteria by macrophages involves internalization of the microorganisms into the phagosomes, which are then delivered to endo-lysosomes, the resulting phagosome (phagolysosome) is now acidic, by the contribution of the highly acidic environment of the fused lysosome, leading to activation of proteases with capacity for enzymatic degradation of the bacteria.

M2 macrophages, or “fixing” macrophages, are anti-inflammatory and produce either polyamines to induce cell proliferation, or proline to induce collagen production. These macrophages are believed to be associated with wound healing and tissue repair. M2 macrophages are responsible for functions such as clearing neutrophils during inflammatory processes. [150] They can stimulate the proliferation, differentiation, and activation of fibroblasts, epithelial cells, endothelial cells, and stem and progenitor cells that facilitate tissue repair. [151, 152]

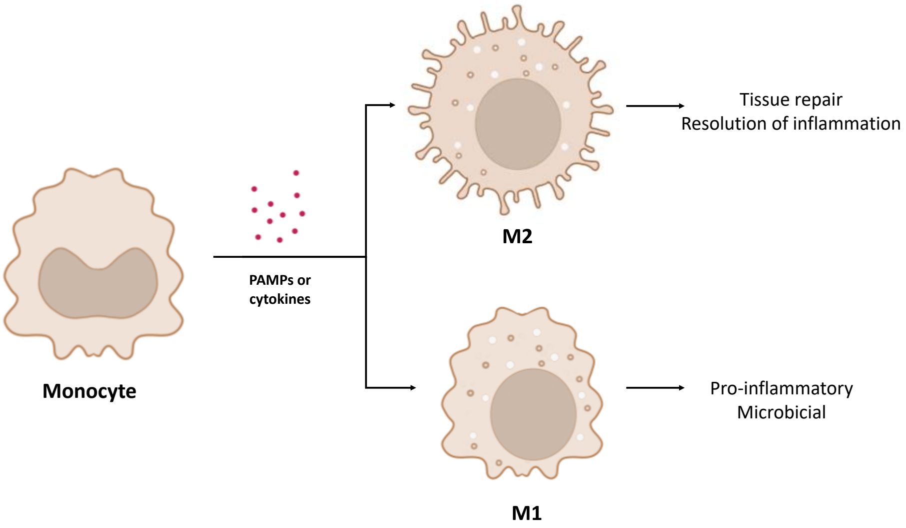

Figure 80 Monocytes are differentiated into macrophages. Depending on the stimuli, the macrophages can be differentiated into M1 (involved in the pro-inflammatory response) or M2 (responsible for the resolution of inflammation and tissue repair) macrophages. PAMPS: pathogen-associated molecular patterns.

5.1.1 Immune escape by bacteria in macrophages

Certain bacterial strains are known to have developed mechanisms to escape standard bacterial killing strategies by macrophages. *Mycobacterium tuberculosis* has been shown to have a variety of mechanisms for immune escape, including inhibition of macrophage phagocytosis, prevention of lysosome maturation, avert phagolysosome acidification and can also resist oxidative stress. [153] Another example is *Staphylococcus aureus* (*S. aureus)* that can use a macrophage as a reservoir and replicate within it following adaptation to the phagosome and preventing it from fusing to the lysosome. There, bacteria can survive and replicate, and, eventually, bacterial replication will lead to the loss of the integrity of the cell membrane (potentially by expression of pore-forming toxins) and bacteria gets into the cytosol leading to macrophage whole cell lysis (Figure 81).[154] Following cell lysis, a burst of live *S. aureus* can be observed outside the cell that contributes to fast dissemination of the pathogen. Interestingly, macrophages appear healthy until the plasma membrane integrity is compromised.[155]

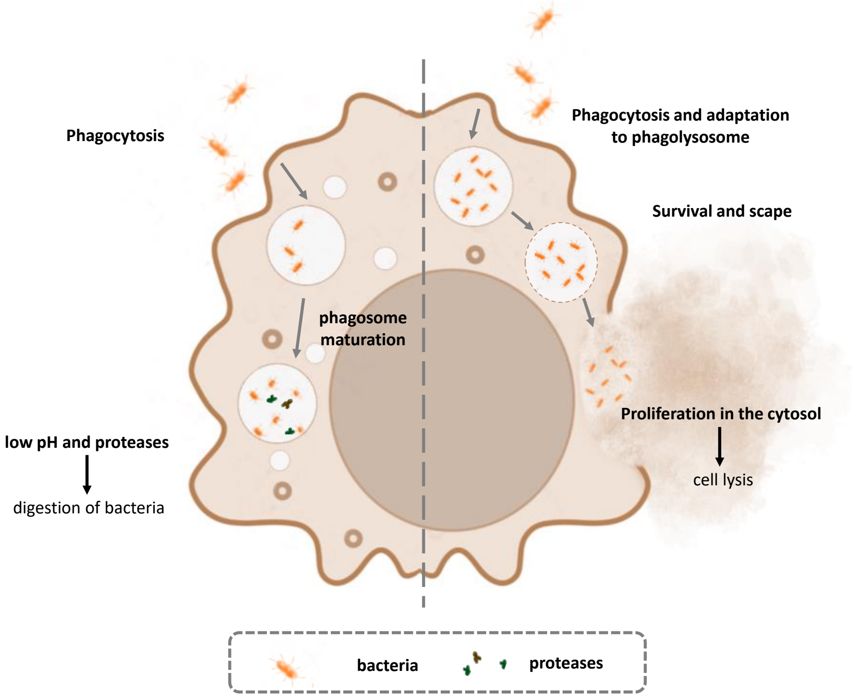

Figure 81 Macrophage killing mechanism and *S. aureus* evasion. Macrophages engulf bacteria in the phagosome that fuses with the lysosome to mature into the phagolysosome, a highly acidic compartment where degradation of pathogens by proteolytic enzymes and reactive oxygen species happens. *S. aureus* can evade killing by adapting to the phagosomal environment and preventing fusion with the lysosome. Bacteria replicates in the phagosome until they burst the compartments leading to cell lysis. Figure adapted from reference 154 Copyright © 2021 Pidwill, Gibson, Cole, Renshaw and Foster.[154]

5.1.2 Alveolar macrophages and *S. pneumoniae*

Alveolar macrophages are believed to originate from either the replication of resident macrophages or through the migration of bone marrow and peripheral blood monocytes in circulation. Alveolar macrophages are very long-lived cells that may live for prolonged periods in the steady state and then can be differentiated into M1 or M2 macrophages, into which phenotype they polarise is dictated by the environment. Under physiological conditions, alveolar macrophages are believed to be predominantly M2, they produce low levels of inflammatory cytokines, maintain high phagocytic activity (sampling the environment and removing cell debris), and generally suppress inflammation and adaptive immunity. Upon a bacterial challenge, alveolar macrophages can be differentiated into M1 or fighting macrophages and play crucial role in innate immunity against bacteria and are key orchestrators of the inflammatory response. They can recruit neutrophils, induce apoptosis in target cells and down-regulate the pro-inflammatory cytokines by communicating with M2 macrophages to resolve inflammation. However, there is still limited understanding of how these macrophages kill bacteria. [156]

Community-acquired pneumonia, commonly caused by *Streptococcus pneumoniae (S. pneumoniae)*, is a leading cause of global mortality[157] and presents challenges in the efficacy of treatments. *S. pneumoniae* express several proteins that help to cope with oxidative stress in the phagosome. For example, *S. pneumoniae* expresses a specific *nox* protein (SpNOX) that is an enzyme that transforms molecular oxygen into hydrogen peroxide (H_2O_2). Simultaneously, *S. pneumoniae* can also express proteins that help resist the presence of H_2O_2 such as heat shock-stimulated serine proteases (caseinolytic peptidase P and high temperature requirement protein). H_2O_2 can inhibit the production of the radical ROS produced in the phagolysosome by macrophages, depleting intracellular iron (required by NAPH oxidase to produce ROS), oxidizing and inactivating redox-sensitive proteins, and promoting an antioxidant response. Besides, S. pneumoniae can evade the complement system recognition by releasing extracellular toxin pneumolysin and expressing pneummococcal surface antigen A, although the exact mechanism of this evasion is not yet clear. [158]

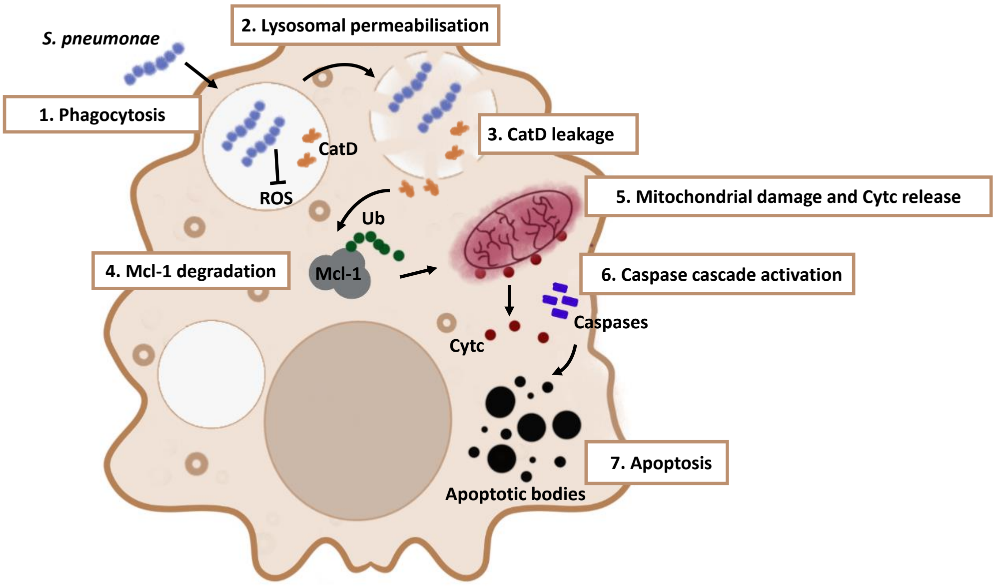

Figure 82 Apoptotic bacterial killing in macrophages. *S. pneumoniae* evades killing by oxidative stress produced by macrophages. Overwhelmed by bacteria, the phagolysomal membrane is compromised and starts leaking and the protease CatD gains access the cytosol that gets acidified. Cytosolic CatD triggers proteosomal degradation of antiapoptic myeloid leukemia 1 protein (Mcl-1) by ubiquitin ligase E3. Following Mcl-1 degradation, mitochondrial outer membrane permeabilization and cytochrome c (Cytc) release leads to the caspase cascade activation and cell apoptosis. Figure adapted from reference 159 with permission from the British Society for Immunology ©.

The capacity of alveolar macrophages to clear bacteria is finite, and high abundancy of bacteria can lead to a point where macrophages can no longer control the intracellular levels of engulfed bacteria. The intracellular killing capacity of macrophages can then become "exhausted", with bacteria replicating at a higher rate than the macrophage can kill. This, taken together with the range of survival strategies developed by the bacteria to evade killing, means that additional mechanisms are required to effectively kill phagocyted bacteria. A mechanism has been discovered whereby macrophages undergo apoptosis to enhance bacterial killing (so-called apoptosis-associated-bacterial killing). Induction of apoptosis-associated killing is believed to be a key component of the host's defence, which combines bacterial clearance with relatively modest inflammation and represents an important component of host defence when initial phagolysosomal killing is exhausted. [159]

The apoptosis-associated-bacterial killing mechanism has been extensively studied in *S. pneumoniae* infection models. The pathway is understood to start with phagocytosis of *S. pneumoniae* that is capable of withstanding oxidative steps by several mechanisms, with survival of the bacteria and replication leading to exhaustion of the phagocytic pathway. The phagolysosomal membrane is compromised and starts leaking, releasing a variety of proteases into the cytosol, among those, Cathepsin D, an aspartic protease involved in several regulatory processes in the cell. Cathepsin D can engage in a non-proteolityc (or glueing) way with Mcl-1 to promote interaction with its corresponding ligase Mule, leading to ubiquitination and proteosomal degradation of Mcl-1. Mcl-1 is an antiapoptotic protein that blocks the progression of apoptosis by binding and sequestering the pro-apoptotic proteins Bcl-2 homologous antagonist killer (Bak) and Bcl-2-associated protein X (Bax). In the absence of Mcl-1, Bak and Bax are capable of forming pores in the mitochondrial membrane, allowing the release of cytochrome c into the cytoplasm, that forms a complex with Apaf-1 and caspase-9, called the **"**apoptosome**,**", which is a critical activator of the effector caspases. (Figure 82).

This mechanism has been proved to enhance killing of bacteria. [160] The antimicrobial effects of this mechanism and how apoptosis contributes to antimicrobial killing is yet to be fully understood but it has been speculated that induction of apoptosis contributes to limit bacterial spread by allowing containment of bacteria when the phagolysosomal antimicrobial capacity is 'exhausted' and prevents bacterial persistence within subcellular compartments. Apoptotic macrophages are then cleared by M2 macrophages to resolve inflammation, resulting in a reduction of inflammation by reducing the neutrophil recruitment and pro-inflammatory cytokine release.

It is important to highlight that not all bacteria trigger this mechanism to enhance killing. For example, *S. aureus* does not use this mechanism, potentially because containing phagosomes fail to mature appropriately and the required CatD activation is not achieved for Mcl-1 proteasomal degradation. [161]

5.1.3 Cathepsin D

Cathepsin D (CatD) is a lysosomal aspartic protease,[162] which contains two aspartic acids at its active site that allow protonation of the amide bond, deprotonation and attack by water, leading to hydrolysis of the amide bond (Figure 83). This protease is ubiquitously distributed in all tissues and organs, and it is involved in a variety of cellular functions, including activation of other proteins, such as prolactin[163] and osteopontin[164] and modulating their functions. CatD degrades cystatin C, which results in enhancement of cysteine cathepsin activity[165], and cleaves several chemokines.[166] Inactivation of chemokines is believed to be an important mechanism to fight cancer. Cathepsin D can also directly degrade pathogens in the lysosome.

Due to its highly destructive nature, CatD is tightly regulated, and is expressed as a zymogen in the endoplasmic reticulum and transported to the lysosome, with an acidic environment required for maturation into the active form. [167] The protease constitutively expressed in nearly all cells, constituting up to a 10% of the lysosome protein content, with concentration of CatD in lysosomes as high as 0.7 mM. In physiological conditions its activity is limited to the lysosome, due to its pH dependency. [168, 169]

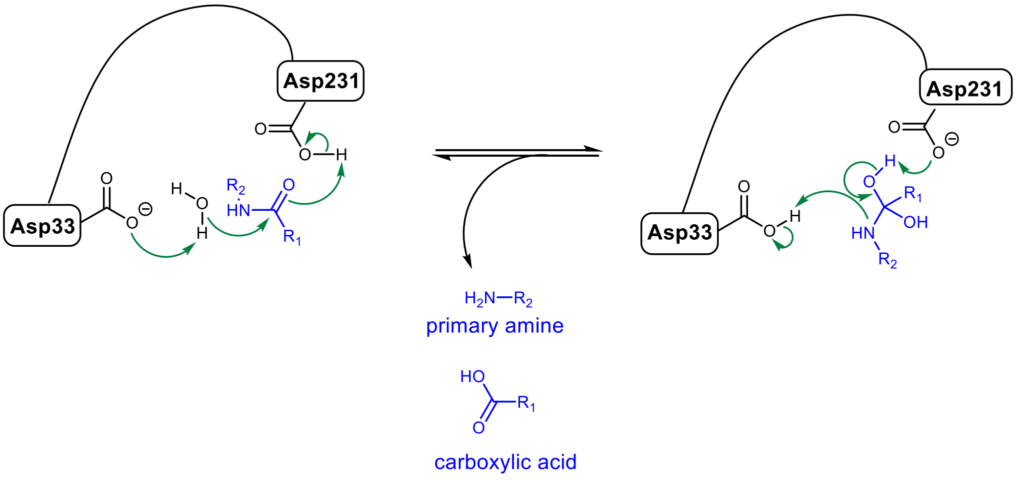

Figure 83 Mechanism of CatD mediated proteolysis. Two aspartic acids in the active site mediate the transfer of protons that promote the nucleophilic attack by a molecule of water leading to ultimate cleavage of the amide bond.

Deficiency of CatD has been associated with several pathologies, for example CatD knock-out mice presented with intestinal atrophy and died of anorexia on week 3, suggesting its regulatory role in cell growth and homeostasis. [170] CatD absence has also been associated with neurodegenerative diseases in humans. [171] Overactivation of CatD has also been linked to breast cancer and has been increased tumour invasiveness[172, 173] and with a variety of chronic inflammatory diseases such as bowel disease. [174]

Extensive work has focused on CatD specificity and its close similarity to other aspartic acid proteases such as pepsin or renin that makes finding an optimal substrate for CatD a challenge.[175] Substrate screening assays have identified several substrates for CatD cleavage rates, but the substrate preference and specificity of each subsite seems to be related to the particular interactions with the peptide sequence, with different amino acids accepted in each subsite. [176]

Several studies have been carried out to better understand substrate specificity of CatD. Mayer[177] used modified pepstatin inhibitors and modified several positions (P4, P3, P1, P2′, and P3′, see page 1). Scarborough[178] used synthetic FRET substrates to study the preference of the enzyme on its S2 and S3 pockets by modifying the P2 and P3 positions of the substrate. Beyer[179] and Arnold[180] studied the prime side subsite specificity by modification in the P2′ and P3′ on synthetic substrates and assessing degradation of natural substrates on positions P1-P4′, respectively. Pimenta performed a systematic study using a library of modified substrates derived from kallistatin. [176] Those results were generally consistent with previous findings with hydrophobic residues preferred at P1 and P1′, with Phe, Leu or Met combinations showing the best cleavages and P1′ having a greater influence in effective cleavage over P1. The P2 preferred Ala, Leu or Glu, and this residue was, in fact, a key modification within the kallistatin library study (modification of this residue lead to the best substrate). The P3 and P3′ sites also prefer hydrophobic residues. Interestingly, the P2′ site showed different results in different studies, with Beyer[179] reporting preference for large positively charged amino acids (Lys or Arg) while Pimenta[176] showed preference of Ser; however, in both studies, various other residues were tolerated at this position (for instance Asp and Ala mutants showed similar kinetic parameters), a finding that was reported by other authors. [180] The S2 pocket is a hydrophobic pocket, but it is hypothesised that long chain charged residues can "stick out" of the pocket and be exposed to solvent.

- **Optical probes for the detection of Cathepsin D**

Current CatD detection methods mostly rely on the use of labelled antibodies[181] or chromogenic substrates, [182] which are limited to *in vitro* use. [183] Only a limited number of optical probes have been reported for CatD. Examples include a dual MRI contrast probe[184] additionally decorated with a pH sensitive Oregon Green fluorophore and a BODIPY-labelled suicide inhibitor based on Pepstatin A, which has been used to distinguish active CatD from its inactive form in macrophages. [185] However, inhibitor-based probes have no signal amplification due to irreversible enzyme inhibition and so suffer from low signal-to-noise ratios (the fluorescence is also "always on"). In addition, Pepstatin A is a generic aspartic acid protease inhibitor, so selectivity is a problem. In contrast, fluorogenic, substrate-based CatD probes would allow for better signal-to-noise ratio and the amplification of the fluorescence signal with thousands of copies of the probe activated by a single enzyme molecule. Early examples of FRET-based fluorogenic substrates for CatD have been reported but in the blue region (350-495 nm) limiting their use for *in vitro* applications. [159, 175, 186]

5.2 Synthesis and validation of a pH insensitive, water soluble CatD FRET probe

Herein, I report the optimisation of a substrate based fluorogenic probe, based on a specific substrate for CatD, that provides an OFF→ON signal upon activation by the protease with a good signal amplification. When choosing a substrate to build an optical probe to be used in cells and potentially *in vivo*, cross-selectivities are important and it is important to design a specific substrate that is not cleaved by related proteases. One of the most abundant and active proteases in the lysosome is Cathepsin B, which prefers substrates bearing Phe-Arg or Arg-Arg sequences at their P2-P1 sites. Previously reported substrates for CatD, reported highly efficient cleavable substrates bearing the sequence Phe-Arg (P1'-P2' for CatD), which would be cleaved by Cathepsin B. The optimal substrate reported by Pimenta based on the natural substrate kallistatin was chosen for its high catalytic efficiency high affinity for the protease [Ala-Ile-Ala-Phe↑Phe-Ser-Arg-Gln] (K_m=0.27 µM, k_{cat} = 16.25 s^{-1}).[187] Besides, this substrate inserts a Ser residue in the P2' that should help towards reducing Cathepsin B cross-activation. The substrate was selected here as the peptide substrate and FRET labelled with a BODIPY fluorophore at its N-terminus, while the Gln residue was replaced with a Lys residue capped with a quencher group (Methyl Red). A carboxyl functionalised BODIPY derivate, $\lambda_{ex/em}$ 503/516 nm) was selected as an appropriate fluorophore since it has stable and bright fluorescence [188] (Φ = 0.6) and is not pH sensitive (unlike carboxyfluorescein[189]).

The first substrate-based probe **CatD-P1** (**33**) was synthesised using a combination of solid and solution-phase synthesis (Figure 84). The Methyl Red quencher was incorporated by coupling Fmoc-Lys(MR)-OH (**10**, see page 68)[190] firstly onto a Rink-amide functionalised polystyrene resin (0.7 mmol/g, 100-200 mesh, 1% DVB), followed by the substrate sequence (Ala-Ile-Ala-Phe↑Phe-Ser-Arg), using DIC and Oxyma as the coupling combination (Fmoc/tBu strategy). A short PEG spacer was introduced between the last amino acid and the BODIPY dye to increase hydrophilicity and promote aqueous solubility.

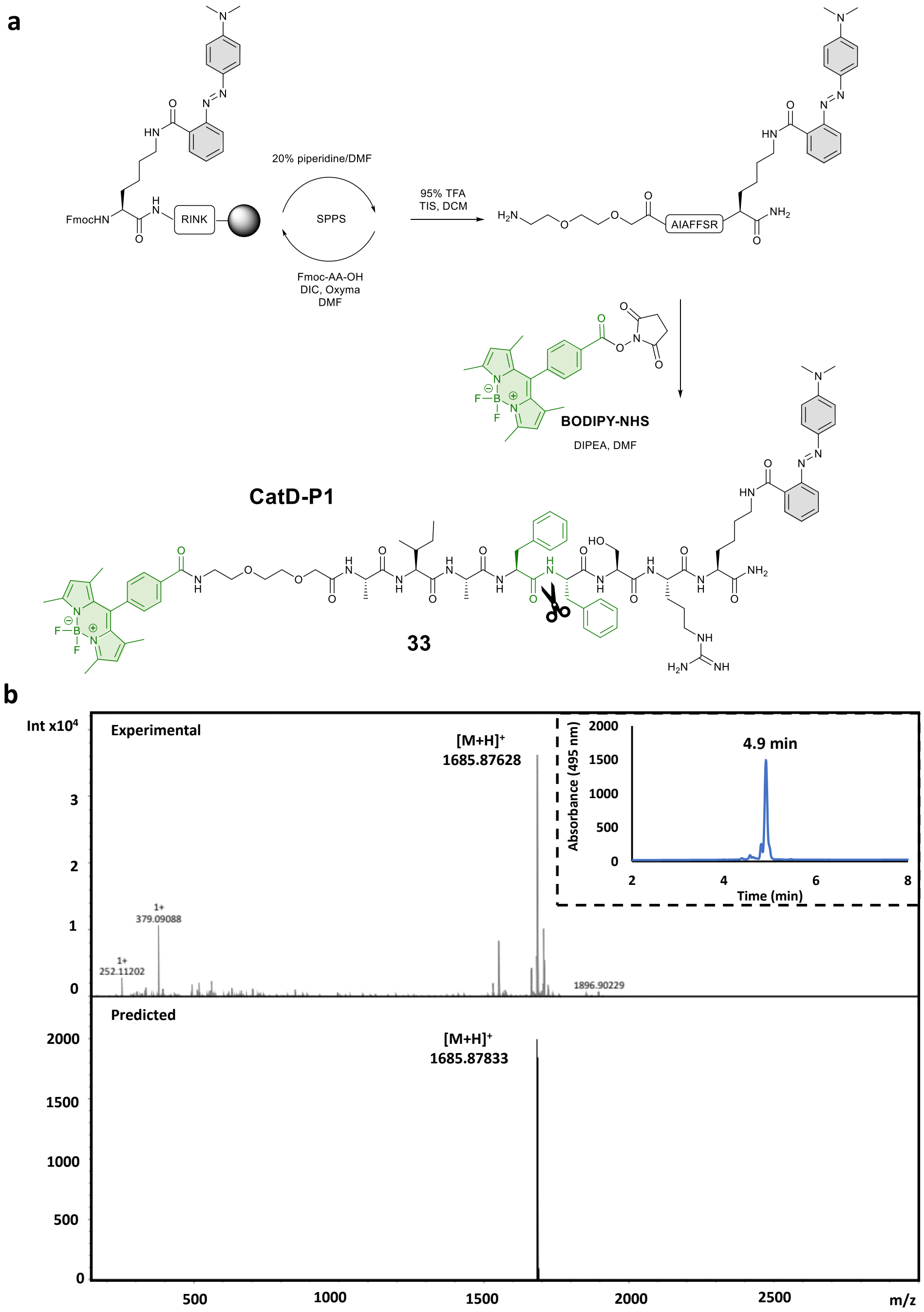

Figure 84 The design of the first fluorogenic, FRET-based CatD probe **CatD-P1** (**33**). **a)** Synthesis and full structure of **CatD-P1** (**33**), which incorporates a BODIPY dye (highlighted green, ▯ex/em 503/516 nm) as the fluorescence donor and a Methyl Red (highlighted red, ▯$_{max}$ 500 nm) as the quencher/acceptor, with CatD cleaving the substrate sequence between the two phenylalanine residues (shown in green). **b)** Characterisation of probe by FT-HRMS Calculated m/z for $C_{86}H_{114}BF_2N_{19}O_{14}^+$ $[M+H]^+$: 1685.8783 Found: 1685.8763 and RP-HPLC-UV (495 nm) shows the retention time at 4.9 min (over a gradient of 6 min ACN/H_2O 0.1% FA). Probe synthesised by MSc student Zhengqi.

The BODIPY fluorophore was not stable to strong acids such as TFA [191] which is commonly used in the global peptide deprotection and cleavage off the resin. Thus, the MR containing peptide was first cleaved off the resin using acidic conditions and after that, the BODIPY NHS-ester[192] was coupled to the N-terminus in solution. The probe **CatD-P1** (**33**) was purified by semipreparative RP-HPLC and characterised by MALDI-TOF and LC-MS.

The probe **CatD-P1** (20 µM) was incubated with CatD to evaluate if it can act as a substrate for the enzyme. No significant increase in fluorescence was observed when **CatD-P1** (**33**) was treated with CatD (50–300 nM) in pH 4 NaOAc buffer with 1–10% DMSO (the addition of DMSO in the assay buffer was required due the low aqueous solubility of **CatD-P1**. Indeed, precipitation was observed during the incubation in all cases, with the poor water solubility limiting the concentration of the probe even with high levels of DMSO in the reaction buffer.

5.2.1 Improving water solubility of the compound

PEGylation of drugs and other biologically relevant molecules is a widely used approach to improve solubility and PEGylation has been reported to reduce immunogenicity, prolong bioavailability, and reduce renal clearance. [193] Two PEGylated versions of this FRET probe were designed, with the first synthesised by coupling, on the solid-support, whereby three consecutive Fmoc-$(EG)_2$-COOH moieties to the C-terminus of the sequence to give probe **CatD-P2** (Figure 85).

CatD-P2 (**34**), with a short PEG at the C-terminus (Figure 85), proved more water soluble than **CatD-P1** (**33**), but the addition of DMSO was still required for the enzymatic assays. The maximum probe concentration in 1% DMSO/buffer was only 7-8 µM. An approximately 30-fold increase in fluorescence was seen with **CatD-P2** (20 µM) after incubation with CatD (50 nM) for 1 h, with a 3% DMSO required in the reaction buffer to solubilise the probe.

The next probe was designed to have a 5 KDa PEG moiety introduced via an azide functionalised side chain at the C-terminus. Thus, **CatD-P3** was synthesised by coupling Fmoc-Lys(N_3)-OH onto the Rink-amide linker on a PS resin, which was followed by coupling a short $(EG)_2$ spacer and the FRET probe construct as described above. Following the cleavage off the resin and BODIPY coupling, copper-catalysed azide–alkyne cycloaddition [135, 194] allowed incorporation of the 5 KDa PEG-alkyne unit (Figure 86a). For the subsequent click reaction, the azide peptide (**35**) was dissolved in anhydrous DMF and the 5 KDa PEG-alkyne (1.1 eq) added followed by addition of a mixture of CuI/THPTA and the reaction was stirred 24 h at 40° C under a N_2 atmosphere to obtain the PEGylated probe **CatD-P3** (**36**) (the reaction was monitored by RP HPLC-UV). **CatD-P3** was isolated by semipreparative RP-HPLC (Figure 86b). MS analysis of **CatD-P3** showed a Gaussian distribution of masses due to the nature of the 5 kDa PEG unit (ranging from 6000 to 8000 m/z), but the average increase of m/z in approximately 2000 units (azide peptide 1984 mol/g) confirmed the formation of a triazole and the success of the click reaction (Figure 86c).

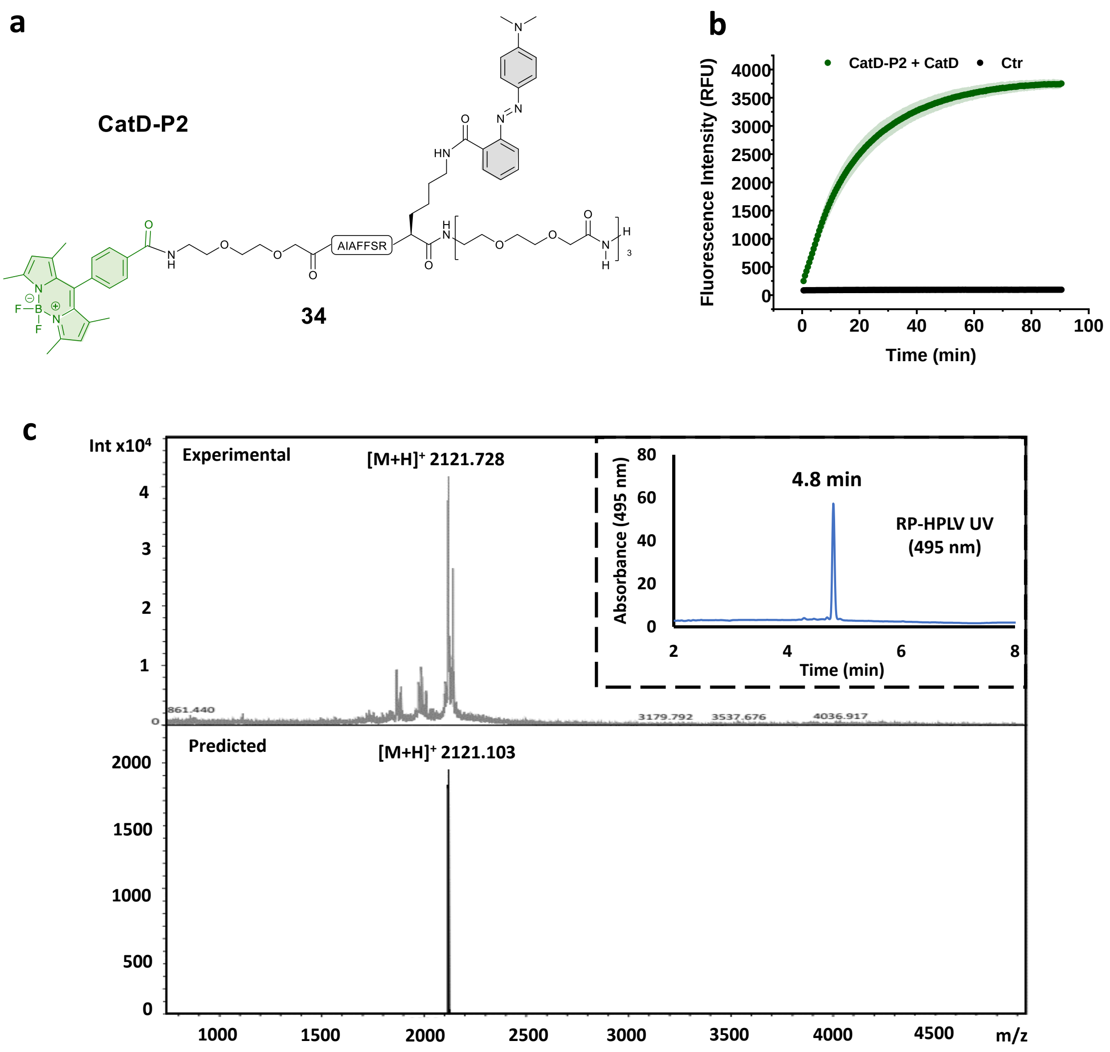

Figure 85 FRET-based CatD probe **CatD-P2. a)** The probe contains three bis-ethylene glycol units on its C-terminus; **b) CatD-P2** (20 µM) was exposed to the enzyme CatD (50 nM) and the increase of fluorescence monitored over time, the probe in absence of enzyme was used as a control for the background fluorescence. **c) MALDI-TOF** calculated m/z for $C_{104}H_{147}BF_2N_{22}O_{23}Na_2$ MALDI-TOF expected: 2121.134; found: 2121.728 and **RP-HPLC-UV (495 nm)** shows the retention time at 4.8 min (over a gradient of 6 min ACN/H_2O 0.1% FA). Probe synthesised by MSc student Zhengqi.

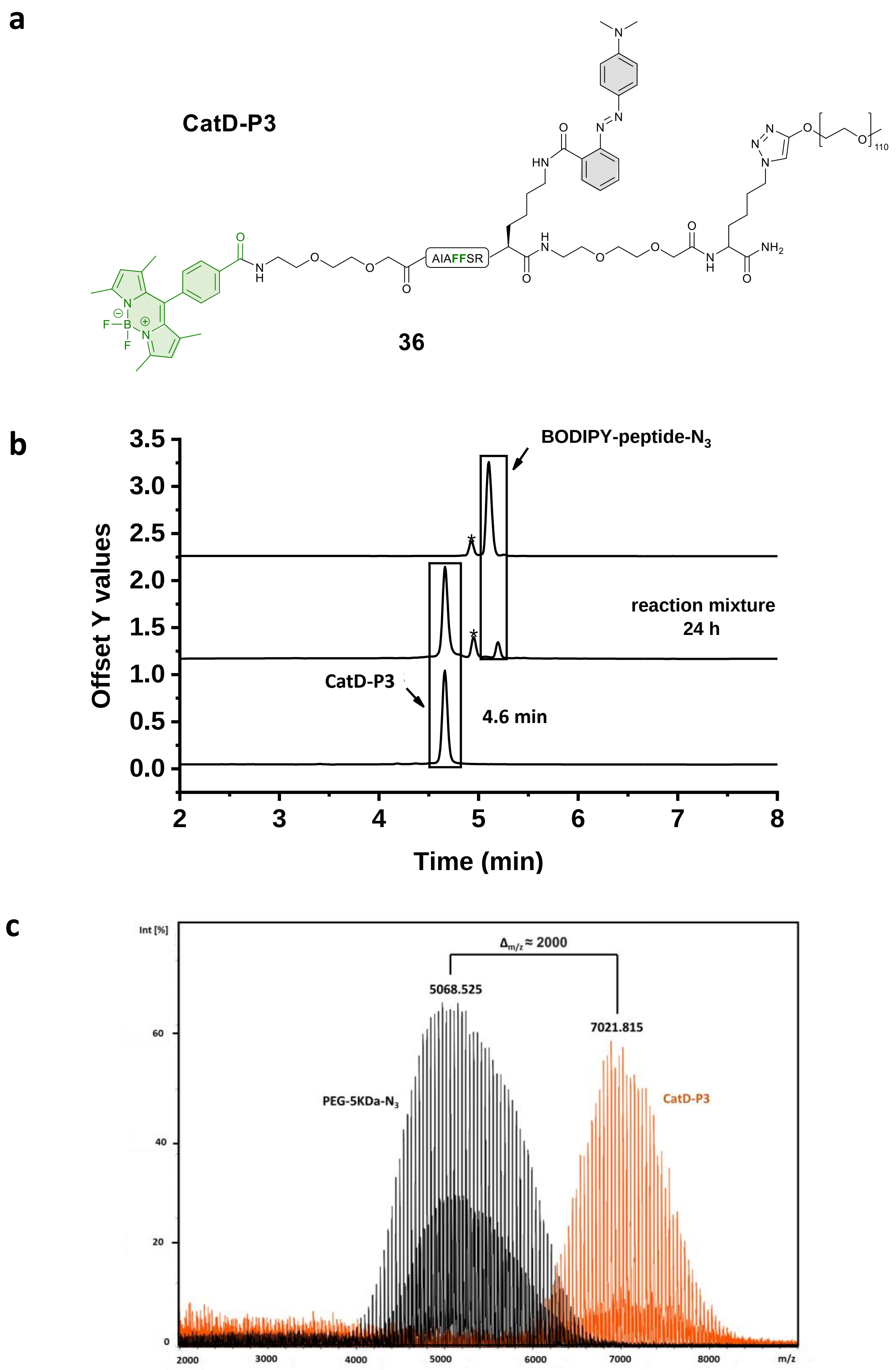

Figure 86 FRET-based CatD probe **CatD-P3 a)** Full structure includes a long PEG 5K tail on its C-terminus. **b)** CuAAC reaction was monitored by RP-HPLC (495 nm) over 6 min using a gradient of ACN/H_2O 0.1% FA. * Indicates for the trace of BODIPY-COOH dye from the prior conjugation of the peptide azide building block. **c)** MALDI-TOF MS analysis of 5 KDa PEG-alkyne (black spectrum) and purified **CatD-P3** probe (red spectrum) average mass found (m/z) Mn: 7096.471.

5.2.2 *In vitro* validation of probe CatD-P3

Probe **CatD-P3** (**36**, 20 µM) with the 5 KDa PEG, was fully water soluble, and was rapidly activated by CatD (50 nM) resulting in 26-fold increase fluorescence after 1 h (Figure 87a). The fluorescence signal of the intact or activated **CatD-P3** was not affected by different pH's (pH 4–9.2, (Figure 87b), suggesting that the probe would allow detection of Cat D in any cellular compartment.

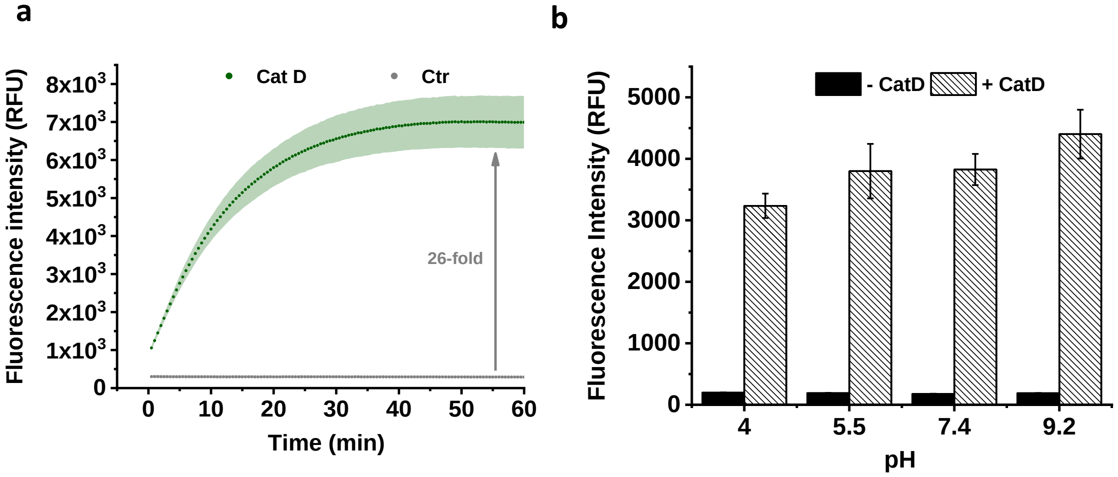

Figure 87 a) Activation profile of **CatD-P3** (20 µM) in reaction buffer in presence or absence of CatD (50 nM), Ctr: no enzyme, n=3. **b)** The fluorescence of cleaved and uncleaved probe (20 µM) at different pH's (1.5 h incubation with the enzyme), n=3.

In order to compare the activation profile of **CatD-P2** (**34**) and **CatD-P3** (**36**), stocks of both probes were prepared (60 µM of probe in 10 % DMSO in water or 100% ultrapure water, respectively) and diluted in reaction buffer to a final concentration of 20 µM. Probes were exposed to CatD (50 nM) and activation monitored over 1.5 h. Both peptides showed comparable activation profiles, with **CatD-P3** showing a slightly higher background fluorescence (Figure 88).

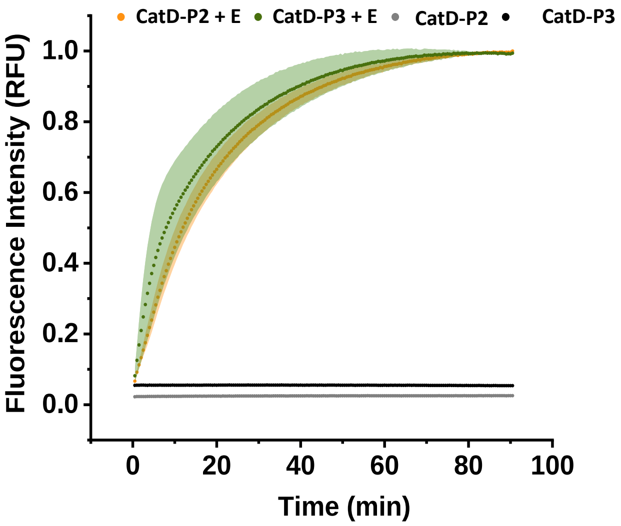

Figure 88 Comparative activation of **CatD-P2** and **CatD-P3** (20 µM) in presence or absence of CatD (50 nM) in reaction buffer (50 mM NaOAc pH 4,). The **CatD-P2** assay required addition of 10 % DMSO whilst the **CatD-P3** assay was done in absence of DMSO, n=3.

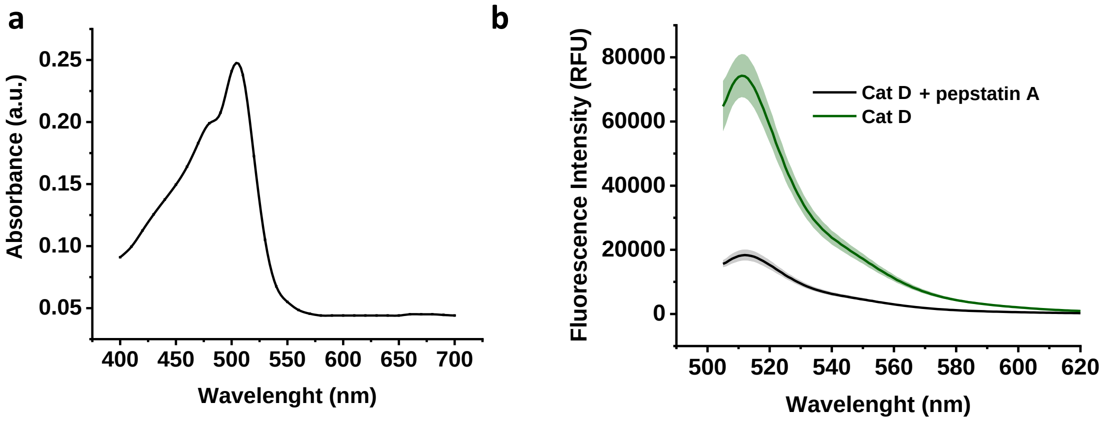

Figure 89 a) Absorption spectrum of probe **CatD-P3 b)** CatD (50 nM) mediated an increase in the fluorescence intensity of **CatD-P3** (5 µM) with and without the inhibitor Pepstatin A (20 µM), n = 3.

The absorption and fluorescence emission spectrum showed a maximum absorption (λ_{abs}) at 505 nm and fluorescence emission (λ_{em}) at 515 nm (Figure 89a). Activation of **CatD-P3** (**36**) was efficiently inhibited in the presence of pepstatin A (20 µM) (Figure 89b). Kinetic profiling of the probe gave a K_m of 6×10^{-6} M and a catalytic efficiency (k_{cat}/K_m) of 1.3×10^5 $M^{-1}s^{-1}$ (Figure 90c). The probe was also characterised by its fluorescence lifetime. A moderate increase in fluorescence lifetime, of approximately 1 ns was observed upon probe activation (Figure 90b).

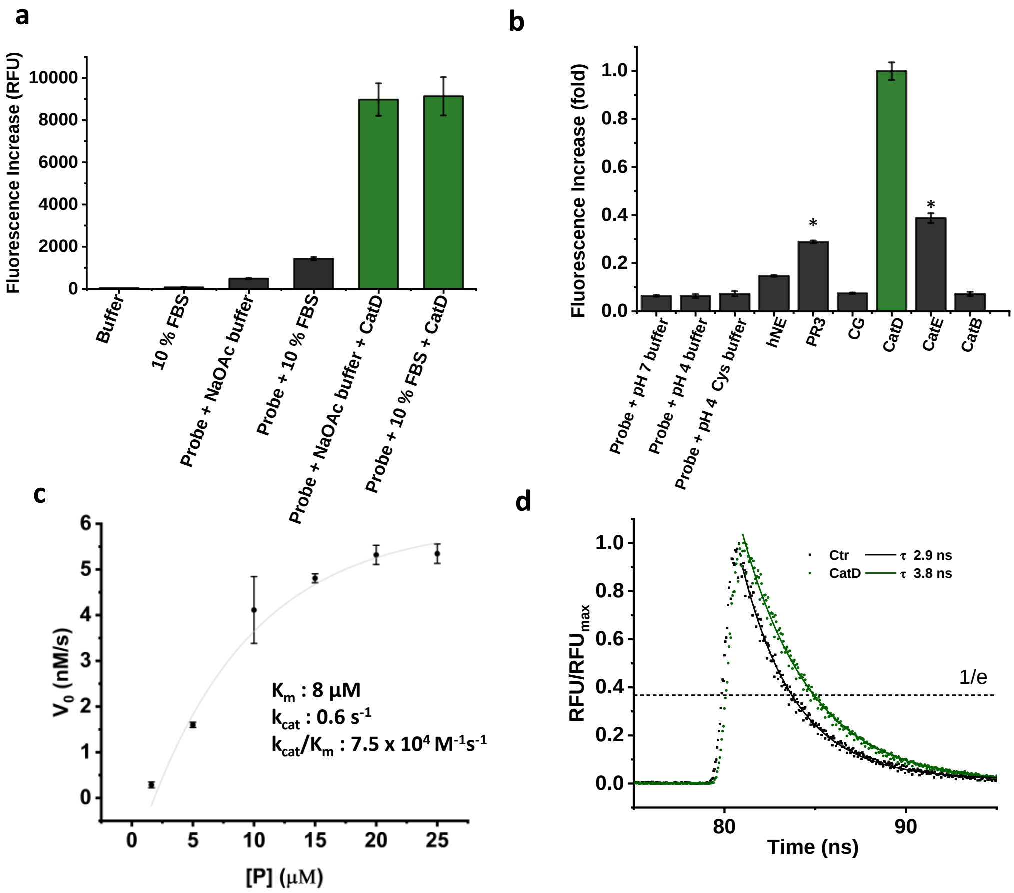

Figure 90 **a)** Activation of the probe was monitored in reaction buffer and in pH 4 adjusted 10% fetal bovine serum, fluorescence signal amplification was comparable in both conditions, with slightly higher background fluorescence in the 10% FBS media. **b)** Specificity of probe **CatD-P3** was evaluated in the presence of other immune proteases, cleavage preference (signal was normalized to the maximum signal in each buffer) *indicates where other proteases have relatively high cleavage. **c)** Michaelis-Menten plot. **d)** The fluorescence lifetime of the probe was monitored before and after 1.5 h incubation with the enzyme. All experiments n=3. Ctr: Control, no enzyme.

CatD-P3 (**36**) was efficiently activated by CatD in serum (10% FBS), showing a similar activation profile as in reaction buffer, and the intact probe showed stability in serum for at least 2 h (Figure 90a). **CatD-P3** showed good specificity for CatD over other proteases present in macrophages, Cathepsin G and B, and other inflammatory proteases human Neutrophil Elastase and Proteinase 3. [195] Proteinase 3 is a very promiscuous protease with a broad substrate specificity, however, the presence of proteinase 3 should be specific to neutrophils and not present in macrophages. Similarly, Cathepsin E cleaved partially the probe due to both proteases sharing very similar substrate specificity. Despite their similarity, there was a faster rate of cleavage of the substrate by CatD (Figure 90b). [196, 197]

Analysis of the of the enzymatic reaction by MALDI-TOF MS confirmed that the probe was cleaved by CatD between the two phenylalanine residues (Figure 91). Specific hydrolytic cleavage between Phe↑Phe was confirmed following probe (10 µM) incubation with Cat D (50 nM) for 90 min at 37°C following analysis of the reaction mixture by MALDI-TOF MS confirming the appearance of mass peaks of the expected fragments. The BODIPY fragment ion showed a variation of mass of -19, consistent with the loss of a fluorine ion $[M-F]^+$ from the boronate salt (this ion was not observed when the compound was analysed by LC-MS, suggesting this is a result of the ionisation method, which is consistent with previously reported analysis of BODIPY by mass spectrometry). [198]

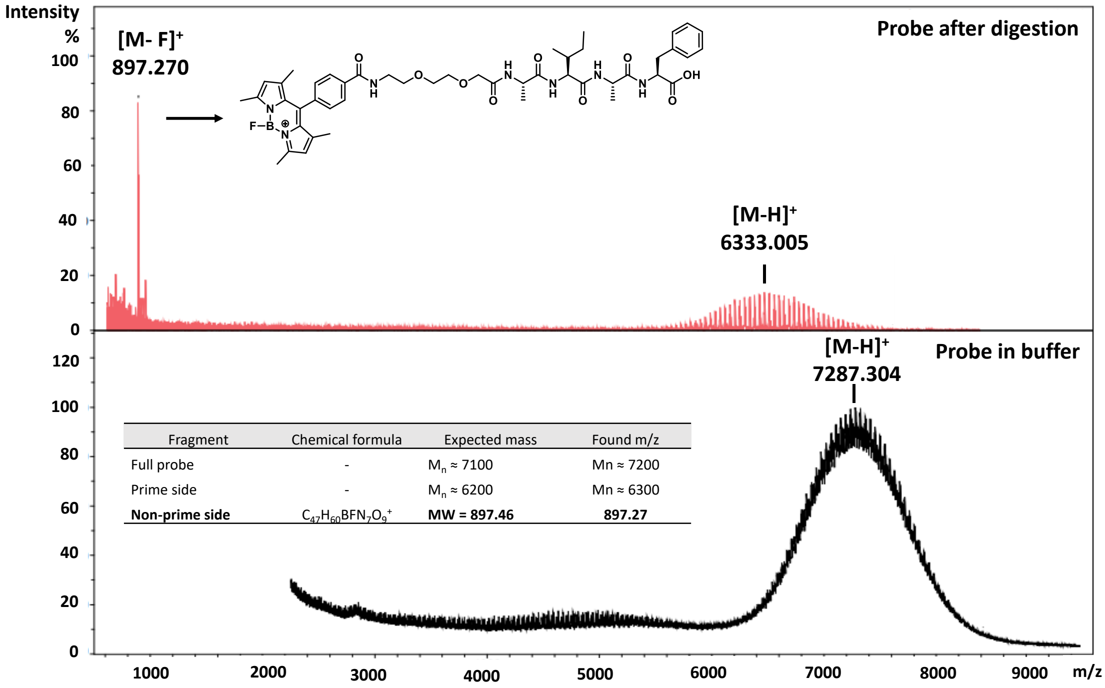

Fragment	Chemical formula	Expected mass	Found m/z
Full probe	-	$M_n \approx 7100$	Mn ≈ 7200
Prime side	-	$M_n \approx 6200$	Mn ≈ 6300
Non-prime side	$C_{47}H_{60}BFN_7O_9^+$	**MW = 897.46**	**897.27**

Figure 91 MALDI-TOF MS analysis following exposure of the probe to the enzyme. The amino terminal BODIPY containing fragment confirms the cleavage site happens between Phenylalanines: $[M-F]^+$ Expected: 897.46 found: 897.27

5.2.3 CatD detection in in primary human macrophages infected with *S. pneumoniae*

Finally, **CatD-P3** (**36**) was assessed for imaging CatD activity in macrophages. Human Monocyte-derived Macrophages (MDM) obtained from peripheral blood were incubated with *S. pneumoniae* at a multiplicity of infection of 10 (ratio of *S pneumoniae* agents to number of macrophage cells) for 10 h to induce active CatD release from phagolysosomes. [150] Macrophages were first allowed to phagocytose bacteria for 4 h initially, after which external bacteria were removed by washing, and the macrophages were incubated with **CatD-P3** (10 µM) for 6 h. Cells were subsequently fixed with 2% paraformaldehyde. Confocal microscopy images of the macrophages showed activation of the probe with clear fluorescence signal observed from *S. pneumonia*-challenged macrophages compared to only a low background signal observed in the cytosol from uninfected macrophages (Figure 92).

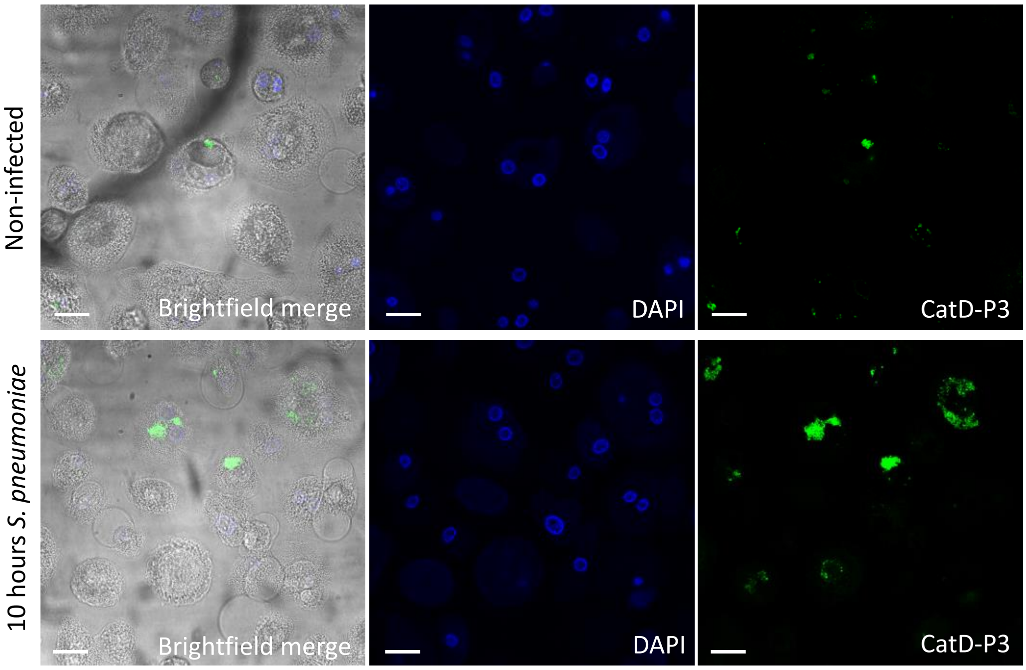

Figure 92 Confocal fluorescence microscopy images of macrophages with and without *S. pneumoniae* versus challenge incubated with the fluorogenic CatD probe (10 µM, 6 h, λ_{ex}: 488, λ_{em}: 512 nm). CatD release was induced by incubating the macrophages for 10 h in the presence of *S. pneumoniae*. The cells were fixed and stained with nuclear stain (DAPI, λ_{ex}: 405, λ_{em}: 461 nm) Scale bar = 10µm. Images were obtained in a Leica SP5 confocal microscope by Dr. Brian McHugh.

Pre-treatment of macrophages with the Cathepsin D inhibitor Pepstatin A resulted in reduced fluorescent signal, indicating that the activation of the probe is specifically triggered by Cathepsin D.

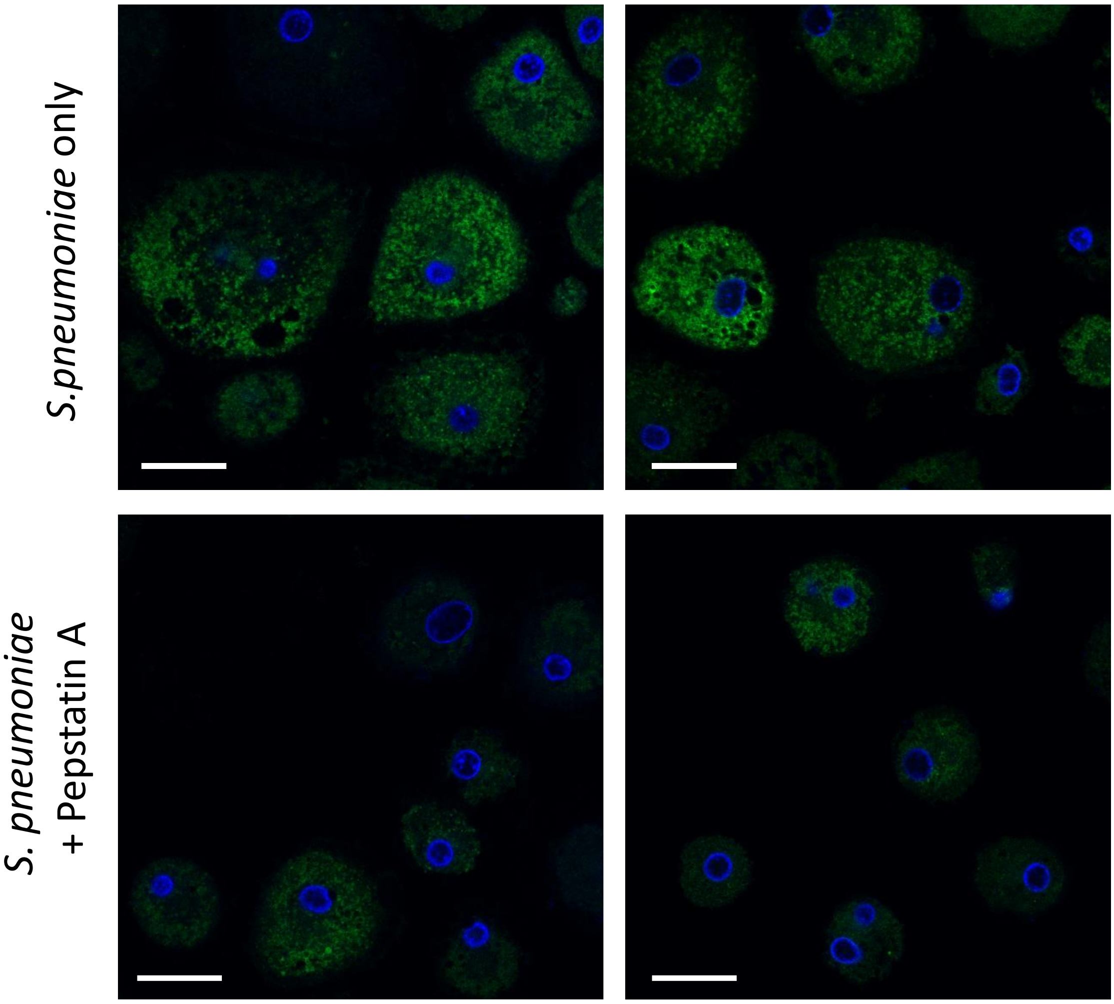

Figure 93 Confocal fluorescence microscopy images of macrophages challenged with *S. pneumoniae* versus challenge incubated with the fluorogenic CatD probe (10 µM, 6 h, λ_{ex}: 488, λem: 512 nm) in absence or presence of the inhibitor Pepstatin A. CatD release was induced by incubating the macrophages for 10 h in the presence of *S. pneumonia* with or without Pepstatin A (20 µM). The cells were fixed and stained with nuclear stain (DAPI, λex: 405, λem: 461 nm). Scale bar = 10 µm. Images were obtained from an Andor spinning disk confocal microscope by Dr. Brian McHugh.

5.3 Conclusions

In conclusion, a water soluble fluorogenic FRET probe for detection of CatD was synthesised, that allows the specific detection and imaging of CatD within acidic pH environments.

The fact that the peptide sequence is rich in aliphatic residues resulted in the initial designs being poorly water soluble. In an attempt to increase the solubility of the probes, a short and a long PEG chain were incorporated on the C-terminus of the peptide. Water solubility on the PEGylated probes improved, however, the probe bearing the short PEG tail still required DMSO as a co-solvent for dissolution. Instead, the long PEG tail made the probe fully water soluble.

The water-soluble probe **CatD-P3** was chosen as the optimal probe for cellular studies and potential *in vivo* applications and was further characterised *in vitro*. The fluorescence signal of **CatD-P3** was stable at different pHs and activation was efficient in presence of Cathepsin D, both in reaction buffer and in more complex media such as in 10% FBS. The activation was inhibited by pepstatin A (an aspartic acid protease inhibitor). The cleavage site between the two phenylalanines, was confirmed by MALDI-TOF MS. Furthermore, **CatD-P3** was tested in presence of a variety of inflammatory proteases, such as Cathepsin B, Cathepsin G, Cathepsin E, hNE and Proteinase 3 with only Cathepsin E, an aspartic protease highly related to Cathepsin D, showing cross-activation. To my knowledge, no substrates have been found that are selective for Cathepsin D over Cathepsin E, and further optimisation of the substrates for Cathepsin D are required to reach full selectivity over Cathepsin E.

The probe was successfully used to detect Cathepsin D activity in macrophages challenged by exposure to bacteria. Upon exposure to *S. pneumoniae*, release of Cathepsin D into the cytosol by lysosomal leakage or partial rupture was detected in macrophages that were exposed to bacteria for 10 hours, while in “mock” macrophages, unexposed to the pathogen, the fluorescence signal was reduced and localised into the lysosomes. Pre-treatment of macrophages with Pepstatin A, a CatD inhibitor, resulted in a significant decrease in fluorescence signal. Next plans for cellular imaging assays will focus on performing co-staining experiments with bacterial labelling to confirm presence of bacteria in the cell and testing the probe in more complex environments to validate the probe as a useful tool to understand the role of Cathepsin D in apoptosis-associated bacterial killing in macrophages.

Chapter 6 Thesis conclusions and future work

The work on this thesis aimed to develop a series of peptide based fluorogenic peptide substrates for monitoring proteolytic activity of inflammatory proteases hNE and CatD.

The first two chapters focus on the development of probes for hNE that overcome some of the the limitations of existing hNE sensors, such as low sensitivity and specificity as well as limited tissue penetration. The probes developed are highly specific and sensitive for hNE and provide amplification of signal thanks to their substrate nature, that is cleaved in a catalytic manner. Furthermore, a near-infrared (NIR) version of the probe was developed that showed capabilities to detect hNE in activated neutrophils and NETs and can allow deeper tissue penetration for *in vivo* use. Further investigation is needed to fully characterize the performance of the smartprobe in various *in vitro* and *in vivo* models, as well as to optimize its design for specific applications. Current studies on the green hNE sensor (Chapter 1) are focusing on detection of hNE activity and NETosis in whole blood samples and as a tool for evaluating performance of drugs such as Ladaraxin for the treatment of COVID. Further functional characterisation on the best NIR probe (Chapter 2) is required and planned experiments include evaluating the probe's capabilities for detecting hNE by flow cytometry as well as *ex vivo* tissue imaging of elastase in inflamed porcine lung tissue.

In the future, these sensors can be further optimised to generate a variety of probes, including NET specific probes, which could be developed by including a DNA binding moiety or dye (such as DAPI or Hoescht) that would label and attach the probe to the extracellular DNA of NETs. Similarly, theranostic probes can also be developed by adding a photodynamic dye that can be activated by light to produce ROS locally upon detection of probe's fluorescence.

The fourth chapter describes the synthesis of a fluorogenic, pH stable, water-soluble FRET probe for the specific detection of CatD, an aspartic protease present in macrophages that is upregulated in macrophages when fighting bacterial infections. Initial Cathepsin D substrates showed poor water solubility and high pH dependency of the fluorescence signal limiting its applications. Optimisation of initial designs lead to incorporation of a long polyethylene glycol moiety as well as a pH insensitive BODIPY fluorophore. The probe was used a tool to understand the mechanism of apoptosis associated bacterial killing by macrophages, where the activity of CatD was detected in macrophages exposed to bacteria, however, the background signal remains relatively high and further optimisation on specificity will be required.

Going forward, these type of probes and construct could be combined as orthogonal systems to obtain dual detection of proteases, allowing for simultaneous monitoring of CatD and hNE activity (and therefore neutrophil and macrophage function) using two independent FRET systems (i.e., a construct containing a sCy5-QSY21 labelled substrate for hNE detection and a BODIPY-MR CatD substrate).

Overall, this thesis provides valuable insights into the development of peptide-based fluorogenic probes for monitoring proteolytic activity of inflammatory proteases, and the results have significant implications for the diagnosis and treatment of inflammatory diseases and for better understanding of protease's roles and functions. The optimized probes described in this work offer several advantages over existing probes, such as improved specificity, sensitivity, and tissue penetration, and have the potential for further optimization and development for specific applications.

Chapter 7 Experimental Procedures

General methods

All Fmoc-amino acids, Methyl Red, 5-carboxyfluorescein, DIC, Oxyma and Aminomethyl ChemMatrix Resin (1 mmol/g), aminomethyl polysterene resin (0.75 mmol/g) and Fmoc-Rink Amide Linker were purchased from GL Biochem, Sigma, Fluorochem or Apollo Scientific and used without further purification. 5-carboxyfluorescein diacetate NHS ester was provided by Shuo Zhang. Electrospray ionization mass spectrometry (ESI–MS) analyses were carried out on an Agilent Technologies LC/MSD quadrupole 1100 series mass spectrometer (QMS) in an ESI mode. High-resolution mass spectra (HR-MS) were recorded on a Bruker SolariX Fourier transform ion cyclotron resonance mass spectrometer (FT-MS). MALDI-TOF spectra were acquired on a Bruker Ultraflextreme MALDI TOF/TOF with a matrix solution of sinapic acid (10 mg/mL) in $H_2O/CH_3CN/TFA$ (69.9/30/0.1) or α-cyano-4-hydroxycinnamic acid (10 mg/mL) in $H_2O/CH_3CN/TFA$ (49.9/50/0.1). NMR spectra were recorded using Bruker AC spectrometers operating at 500 MHz for 1H and 13C NMR. Chemical shifts are reported on the δ scale in ppm and are referenced to residual non-deuterated solvent resonances.

Analytical reverse-phase high-performance liquid chromatography (RP HPLC) was performed on an HP1100 system equipped with a Kinetex 5 μm XB-C18 reverse-phase column (5 cm × 4.6 mm, 5 μm) with a flow rate of 1 mL/min and eluting with $H_2O/CH_3CN/HCOOH$ (95/5/0.1) to $H_2O/CH_3CN/HCOOH$ (5/95/0.1). Method A was used as default unless otherwise stated.

- Method A: 10 minutes. With a gradient from 5 % to 95% CH_3CN over the first 6 min then holding at 95% for 3 min, with detection at 495 and/or 650 nm and by evaporative light scattering.
- Method B: 15 minutes. With a gradient from 5 % to 95% CH_3CN over the first 12 min then holding at 95% for 2 min, with detection at 495 and/or 650 nm and by evaporative light scattering.

- Method C: 20 minutes. With a gradient from 5 % to 95% CH_3CN over the first 15 min then holding at 95% for 4 min, with detection at 495 and/or 650 nm and by evaporative light scattering.

Peptide purifications were performed on semipreparative or preparative reverse-phase high-performance liquid chromatography (RP HPLC) systems.

- The preparative system was equipped with a Kinetex 5 µm XB-C18 100 Å, reverse-phase column (150 × 21.2 mm, AXIA packed). The separation was achieved with a method with a flow rate of 10 mL/min and eluting with $H_2O/CH_3CN/HCOOH$ (95/5/0.1) to $H_2O/CH_3CN/HCOOH$ (5/95/0.1) over a gradient of 21 minutes.
- The semipreparative system was equipped with an Aeris 5 µm XB-C18 100 Å, reverse-phase column (250 × 10 mm). The separation was achieved with a method with a flow rate of 10 mL/min and eluting with $H_2O/CH_3CN/HCOOH$ (95/5/0.1) to $H_2O/CH_3CN/HCOOH$ (5/95/0.1) over a gradient of 30 or 35 minutes.

[2-Amino-3-(2-cyano-ethoxy)-2-(2-cyano-ethoxymethyl)-propoxy]propionitrile (3) [78]

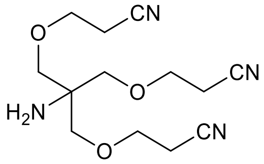

To a solution of tris(hydroxymethyl)aminomethane (6.0 g, 49 mmol) in THF (100 mL), 40% KOH aqueous solution (2 mL) and acrylonitrile (12.9 mL, 200 mmol) were added sequentially, and the resulting solution stirred overnight. The solvent was removed *in vacuo* and water (100 mL) added to the crude. The aqueous layer was extracted with DCM (3 × 100 mL), and the organic layer was dried with Na_2SO_4. The organic solvent was evaporated *in vacuo* to give the product as a colourless oil (7.4 g, 54%), used in the next step without further purification. The data was in good agreement with the literature. [78]

^{1}H-NMR (500 MHz, Chloroform-*d*) δ 3.67 (t, *J* = 6.1 Hz, 6H, OCH_2), 3.42 (s, 6H, CH_2O), 2.60 (t, *J* = 6.0 Hz, 6H, CH_2CN), 1.61 (br, 2H, NH_2). **^{13}C-NMR** (126MHz Chloroform-*d*) δ 118.10 72.6, 65.8, 56.2, 19.0. **LC-MS (ESI)** 303.2 $[M+Na]^+$ **HPLC-ELSD: t_R** 0.96 min, purity 92%.

[2-(2-cyano-ethoxy)-1,1-bis-(2-cyano-ethoxymethyl)-ethyl]-carbamic acid tert-butyl ester (4) [78]

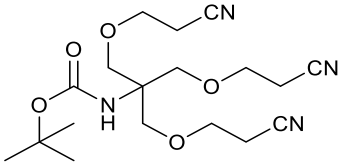

To a stirred solution of *tris*-nitrile (**3**), (7.43 g, 26.5 mmol, 1 eq) in THF (100 mL), a solution of di-*tert*-butyl dicarbonate was added (8.7 g, 39.8 mmol, 1.5 eq) in THF (30 mL) at 0 °C followed by the addition of DIPEA (6.93 mL, 39.8 mmol, 1.5 eq). The reaction was allowed to warm to room temperature and was stirred overnight. The THF was evaporated *in vacuo* and the residue was dissolved in ethyl acetate (250 mL). The organic layer was washed with 1N $KHSO_4$ (100 mL), saturated $NaHCO_3$ (100 mL) and brine (100 mL), dried over Na_2SO_4 and the solvent was evaporated to give the compound **4** as a colourless oil (12.8 g, 100%). The data was in good agreement with the literature. [78]

^{1}H NMR (500 MHz, Chloroform-*d*) δ 4.88 (s, 1H, N*H*), 3.80 (s, 6H, C*H*$_2$O), 3.72 (t, J = 6.1 Hz, 6H, OC*H*$_2$), 2.63 (t, J = 6.1 Hz, 6H, C*H*$_2$CN), 1.46 (s, 9H, C*H*$_3$) **^{13}C NMR (**126 MHz, Chloroform-*d*) δ 154.7, 118.0, 69.4, 65.8, 58.5, 28.3, 18.8. **LC-MS (ESI):** $[M+Na]^{+1}$ 403.3 **HPLC-ELSD: t$_R$** 4.49 min, purity 98.9%.

[2-(3-Amino-propoxy)-1,1-bis-(3-amino-propoxymethyl)-ethyl]-carbamic acid tert-butyl ester (5) [78]

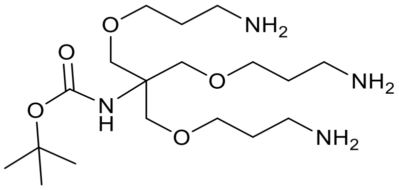

To a stirred solution of the Boc protected tris-nitrile (**4**) (4.5 g, 12 mmol, 1 eq) in anhydrous THF (50 mL) BH_3-THF complex (1M in THF, 72 mmol, 72mL, 6 eq) was added and the resulting mixture was stirred at 55 °C for 5h. Following cooling, 2M HCl was added to give a pH between 1-2. The mixture was neutralized with 1M NaOH and the solvent was removed *in vacuo* to give the Boc protected tris amine **5** as a colourless oil (5.0 g, 100%). The crude product was used without purification for the next step. The data was in good agreement with literature. [78]

^{1}H NMR (500 MHz, MeOD-*d*) δ 3.67 (s, 6H, CH_2O), 3.59 (t, *J* = 6.0 Hz, 6H, OCH_2), 2.97 (m, 6H CH_2N), 1.90 (quint, *J* = 6.2 Hz, 6H, CH_2), 1.46 (s, 9H, CH_3, Boc). **LC-MS (ESI)**: $[M+Na]^+$ 405.4 **HPLC-ELSD: t_R** 0.69 min.

[2-{3-[1-(4, 4-Dimethyl-2,6-dioxocyclohexylidene)ethylamino]propoxy- 1,1-bis-[3-[1-(4,4-dimethyl-2,6 - dioxocyclohexylidene)ethylamino]propoxymethyl]-ethyl]-carbamic acid tert-butyl ester (6) [71]

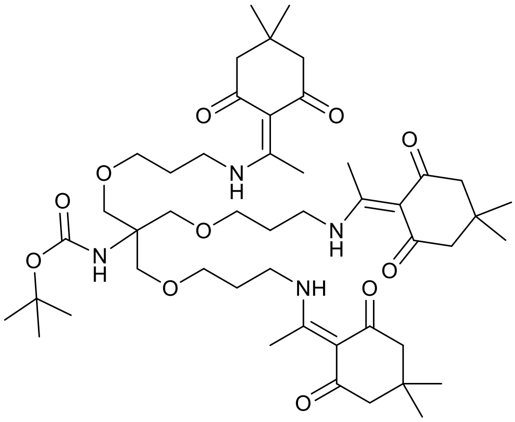

The crude product (**5**) (4.05g, 10.2mmol, 1 eq) was dissolved in MeOH (75 mL) and DIPEA (2.13 mL, 12.24 mmol, 1.2 eq) was added. A solution of 2-acetyl-dimedone (DdeOH, 6.5g, 35.7 mmol, 3.5 eq) in DCM (40 mL) was added and the resulting mixture was stirred overnight. The solvents were removed *in vacuo* and the residue was purified by column chromatography (eluting with DCM:MeOH 9:1) to give the product (**6**) as a yellow oil (6.1 g, 69%). The data was in good agreement with the literature. [71]

^{1}H-NMR (500 MHz, Chloroform-*d*) δ 3.66 (s, 6H, CH_2O), 3.56 – 3.45 (m, 12H, OCH_2/CH_2N), 2.56 (s, 9H, CH_3, Dde), 2.36 (s, 12H, CH_2, Dde), 1.92 (quint, 6H, *J* = 6.2 Hz, CH_2), 1.40 (s, 9H, CH_3, Boc), 1.03 (s, 18H, CH_3, Dde). **^{13}C NMR** (126 MHz, Chloroform-*d*) δ 173.5, 156.0, 154.9, 107.9, 79.1, 69.8, 68.3, 67.8, 58.5, 40.6, 30.1, 29.3, 28.4, 28.3, 17.8. **LC-MS (ESI)**: $[M+H]^{+1}$ 885.5 **HPLC-ELSD: t_R** 5.39 min, purity 97%.

[2-[3-[1-(4, 4-Dimethyl-2,6-dioxocyclohexylidene)ethylamino]propoxy]- 1,1-bis-[3-[1-(4,4-dimethyl-2,6- dioxocyclohexylidene)ethylamino]propoxymethyl]-ethyl]amine (6.1) [71]

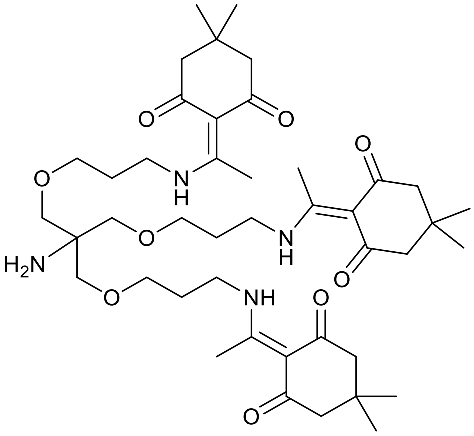

The protected amine (**6**) (2.6 g, 2.9 mmol) was dissolved in 20% TFA in DCM (40 mL) and the resulting mixture was stirred for 2h at room temperature. The solvent was removed *in vacuo* and the residue was dissolved in DCM (150 mL) and washed with saturated aqueous $NaHCO_3$ (75 mL) and water (75 mL). The organic layer was dried with Na_2SO_4 and the solvents removed *in vacuo* to obtain the amine **6.1** as a yellow oil (1.9 g, 83%). The data was in good agreement with the literature. [71]

^{1}H-NMR (500 MHz, Chloroform-*d*) δ 3.52 (m, 12H, OCH_2/CH_2N), 3.37 (s, 6H, CH_2O), 2.59 (s, 9H, CH_3, Dde), 2.38 (s, 12H, CH_2, Dde), 1.95 (quint, 6H, *J* = 6.2 Hz, CH_2), 1.05 (s, 18H, CH_3, Dde) **^{13}C NMR** (126 MHz, Chloroform-*d*) δ 198.3, 173.5, 107.9, 72.7, 68.7, 56.3, 52.9, 40.9, 30.1, 29.2, 28.3, 17.8 **LC-MS (ESI):** $[M+H]^+$ 785.5; **HPLC-ELSD: t_R** 3.93 min purity 84%.

[2-[3-[1-(4, 4-Dimethyl-2,6-dioxocyclohexylidene)ethylamino]propoxy]- 1,1-bis-[3-[1-(4,4-dimethyl-2,6 - dioxocyclohexylidene)ethylamino]propoxymethyl]-ethyl] isocyanate (7) [71]

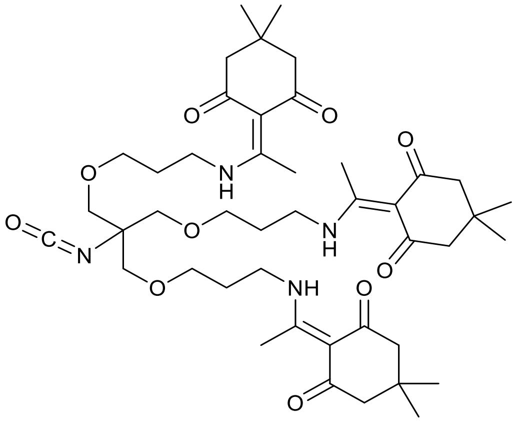

To a mixture of amine (5) (0.9 g, 1.15 mmol, 1 eq) and DMAP (0.16 g, 1.27 mmol, 1.1 eq) in anhydrous DCM (20 mL) was added, dropwise, a solution of Boc$_2$O (0.31g, 1.44 mmol, 1.25 eq) in anhydrous DCM (10 mL) and the reaction mixture was stirred for 1 h (conversion was monitored by HPLC). The solvent was removed *in vacuo* to give the isocyanate **6** that was used immediately. The data were in good agreement with the literature. [71]

LC-MS (ESI): $[M+H]^{+1}$ 811.4 ; **IR (neat)** ν (cm^{-1}): 2954, 2868, 2244, 1636, 1572, 1463, 1388, 1108, 805; **HPLC-ELSD**: **t_R** 5.77 min purity 97 %.

Dde-OH (8) [199]

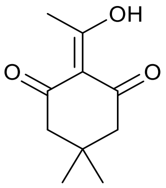

Dimedone (7.07 g, 50.4 mmol, 1 eq), DMAP (6.46 g, 52.9 mmol, 1.05 eq.) and 1-(3-dimethylaminopropyl)-3-ethylcarbodiimide hydrochloride (EDC·HCl, 10.1 g, 52.9 mmol, 1.05 eq) were dissolved in DMF (50 mL). Acetic acid (3.02 mL, 52.9 mmol, 1.05 eq) was added and the reaction stirred overnight. The DMF was removed *in vacuo*, the residue was dissolved in EtOAc (50 mL) and washed with 1 M HCl (2 × 100 mL) and water (2 × 100 mL). The organic layer was dried with MgSO4, filtered, concentrated and dried *in vacuo* to give the target compound **8** (6.7 g, 73%). Data in good agreement with literature. [199]

^{1}H NMR (500 MHz, Chloroform-*d*) δ 2.63 (s, 3H, CH_3), 2.55 (s, 2H, CH_2), 2.38 (s, 2H, CH_2), 1.10 (s, 6H, CH_3). **^{13}C NMR** (126 MHz, Chloroform-*d*) δ 202.5, 197.9, 195.2, 112.4, 52.5, 46.9, 30.7, 30.5, 28.5, 28.2. **LC-MS (ESI)**: $[M+H]^{+1}$ 183.1 **HPLC-UV (252 nm): t_R** 4.44 min, purity 94%.

Fmoc-Lys(Dde)-OH (9) [200]

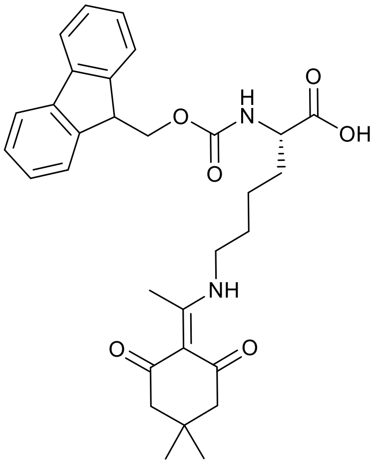

Fmoc-Lys-OH·HCl (10.2 g, 25.2 mmol, 1 eq) was dissolved in H_2O (100 mL) and DIPEA (4.8 mL, 27.7 mmol, 1.1 eq) was added and the reaction was stirred for a few minutes until a white precipitate formed. The resulting solid was collected by filtration and dried in a vacuum oven at 40° C overnight to give the free amine (9.1 g, 95%). To a stirred suspension of Fmoc-Lys-OH (6.77 g, 18.4 mmol, 1 eq) in EtOH (250 mL), Dde-OH **8** (6.7 g, 36.8 mmol, 2 eq) and TFA (100 µL, 1.84 mmol, 0.1 eq) were added. The reaction mixture was refluxed for 60 h. After cooling to room temperature, the solvent was removed *in vacuo* and the residue was dissolved in EtOAc (300 mL), washed with 1M $KHSO_4$ (2 × 200 mL) and 1M HCl (2 × 200 mL). The organic phase was dried over $MgSO_4$, filtered, and evaporated *in vacuo*. The product was isolated by flash column chromatography (eluting with 5% AcOH / EtOAc) and solvent evaporated *in vacuo* to give compound **9** as a white powder (6.5 g, 66%). The data was in good agreement with the literature. [200]

^{1}H NMR (500 MHz, Chloroform-*d*) δ 7.77 (d, *J* = 7.6, 2H), 7.61 (t, *J* = 7.9 Hz, 2H), 7.41 (t, *J* = 7.5 Hz, 2H), 7.34 – 7.27 (m, 2H), 5.73 (d, *J* = 8.1 Hz, 1H), 4.47 (q, *J* = 7.6 Hz, 1H), 4.40 (d, *J* = 8.0 Hz, 2H), 4.23 (t, *J* = 7.0 Hz, 1H), 3.42 (q, *J* = 6.3 Hz, 2H), 2.57 (s, 3H), 2.38 (s, 4H), 2.03 – 1.90 (m, 1H), 1.73 (m, 3H), 1.55 (m, 2H), 1.03 (s, 6H). **^{13}C NMR** (126 MHz, Chloroform-*d*) δ 175.5, 174.8, 174.0, 156.1, 143.9, 143.8, 141.3, 127.7, 127.1, 125.1, 120.0, 120.0, 107.9, 67.1, 53.4, 52.5, 47.2, 43.2, 31.9, 30.2, 28.3, 28.2, 22.4, 20.6, 18.1. **LC-MS (ESI):** $[M+H]^{+1}$ 533.3 **HPLC-ELSD: t_R** 5.4 min, purity 100 %. **FT-HRMS:** Calculated *m/z* for $C_{31}H_{37}N_2O_6$ $[M+Na]^{+1}$: 555.24656 Found: 555.2460

Fmoc-Lys-(MR)-OH (10) [94]

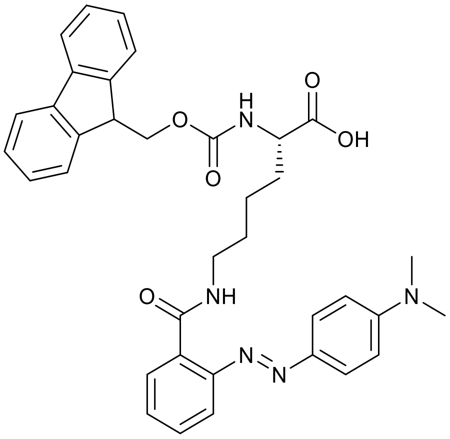

Methyl Red (2.50 g, 9.30 mmol, 1 eq) was dissolved in THF (60 mL) and cooled to 0° C in an ice-bath. DCC (2.21 g, 10.7 mmol, 1.15 eq) was added followed by NHS (1.14 g, 9.87 mmol, 1.06 eq). The reaction mixture was stirred 2 h at 0° C followed by overnight at rt. The reaction mixture was filtered and the red precipitate was collected. The precipitate was dissolved in anydrous. DMF (15 mL) and added dropwise to a solution of Fmoc-Lys-OH·HCl (4.89 g, 12.0 mmol, 1.3 eq) in anhydrous DMF (20 mL) and DIPEA (4.8 mL, 27.6 mmol, 3 eq), and the reaction mixture stirred for 3 h. The solvent was evaporated *in vacuo* and the crude product purified by column chromatography on silica gel (DCM:MeOH 15:1 as an eluent) to generate compound **10** as a red solid (2.40 g, 32%).[94]

^{1}H NMR (500 MHz, DMSO-d) δ 8.55 (t, J = 5.6 Hz, 1H), 7.89 (d, J = 7.6 Hz, 2H), 7.76 (d, J=8.9 Hz, 2H), 7.71 (d, J = 7.7 Hz, 2H), 7.67 (d, J = 8.0 Hz, 1H), 7.62 (d, J = 8.1 Hz, 1H), 7.53 (t, J = 7.6 Hz, 1H), 7.46 (t, J = 7.3 Hz, 1H), 7.42 (td, J = 7.5, 2.8 Hz, 2H), 7.32 (t, J = 7.4 Hz, 2H), 6.86 (d, J = 9.0 Hz, 2H), 4.27 (d, J = 7.1 Hz, 2H), 4.21 (t, J = 7.2 Hz, 1H), 3.94 (m, 1H), 3.06 (s, 6H), 2.61 (m, 2H), 1.76 (m, 1H), 1.67 (m, 1H), 1.56 (m, 2H), 1.44 (m, 2H). **^{13}C NMR** (500 MHz, Chloroform-d) δ 174.1, 171.1, 167.0, 156.4, 153.3, 150.6, 143.9, 143.8, 143.4, 141.3, 131.9, 131.4, 129.6, 128.9, 127.7, 127.1, 127.1, 125.8, 125.2, 119.9, 116.0, 111.7, 67.1, 53.7, 47.3, 40.3, 39.5, 31.4, 29.7, 22.5 **LC-MS (ESI):** $[M+H]^+$ 620.3 **HPLC-ELSD: t_R** 6.4 min, purity 90.5%. **FT-HRMS**: calculated m/z for $C_{36}H_{38}O_5N_5$ $[M+H]^+$ 620.2867; found, 620.2876

Rink amide linker attachment to ChemMatrix or polysterene resin: The Fmoc-Rink-amide linker (3 eq) was dissolved in DMF (10 mL) and Oxyma (3 eq) was added and the mixture was stirred for 10 min. DIC (3 eq) was added and the mixture was stirred for further 1 min. The solution was added to the resin (0.7 mmol/g PS or 1 mmol/g CM, 1 eq, pre-swollen in DCM) and shaken for 2 h. The resin was washed with DMF (3 × 10 mL), DCM (3 × 10 mL) and MeOH (3 × 10 mL). The coupling reaction was monitored by a Kaiser test.

Isocyanate coupling: A solution of isocyanate **7** (3 eq), DIPEA (3.1 eq) and DMAP (0.06 eq) in a 1:1 mixture of DCM/DMF (4 mL) was added to the resin (1 eq, pre-swollen in DCM) and the mixture was shaken overnight (the reaction was monitored by a Kaiser test). The solution was drained and the resin was washed with DMF (3 × 20 mL), DCM (3 × 20 mL), MeOH (3 × 20 mL) and ether (3 × 20 mL).

Dde deprotection: To the resin (pre-swollen in DCM), 2% hydrazine in DMF was added and the reaction mixture was shaken for 2h. The resin was filtered and washed with DMF (3 × 20 mL), DCM (3 × 20 mL) and MeOH (3 × 20 mL). Dde deprotection in the Fmoc or sulfoCy5 containing peptides was achieved with a solution containing imidazole (1.35 mmol) and hydroxylamine hydrochloride (1.80 mmol) in NMP (5 mL). After complete dissolution 5 volumes of this solution were diluted with 1 volume of CH_2Cl_2 and the resin was treated with the final mixture for 3 h at room temperature. The solution was drained and the resin washed with DMF (3 × 10 mL), DCM (3 × 10 mL) and MeOH (3 × 10 mL).

Fmoc deprotection: To the resin (pre-swollen in DCM), 20% piperidine in DMF was added and the reaction mixture was shaken for 10 min. The solution was drained and the resin was washed with DMF (3 × 10 mL), DCM (3 × 10 mL) and MeOH (3 × 10 mL). This procedure was reaped twice.

Amino acid and dye couplings: A solution of the *N*-Fmoc-protected amino acid, 5-Carboxyfluorescein, Fmoc-$(EG)_2$-OH (4.3 eq), Fmoc-Lys(Dde)-OH or Fmoc-Lys(MR)-OH (1.7 eq) with Oxyma (4.3 eq or 1.7 eq) in DMF (0.07 M) was stirred for 10 min. DIC (4.3 eq or 1.7 eq) was added and the solution was stirred for further 1 min. The solution was added to the resin (3 eq, pre-swollen in DCM) and the reaction mixture was shaken for 30 min at 50° C, except for Fmoc-Lys(MR)-OH that was shaken for 1 h at 50° C. The solution was drained and the resin washed with DMF (3 × 10 mL), DCM (3 × 10 mL) and MeOH (3 × 10 mL). Following the last coupling with 5-Carboxyfluorescein, the resin was washed with 20 % piperidine to cleave any esters formed. The coupling reactions were monitored by a Kaiser test.

N-terminal capping with sulfo-Cy5 dye: A solution containing sulfo-Cy5 (1.0 eq per amine) in anhydrous DMF (10 mg/mL) was activated with *N,N,N',N'*-bis(tetramethylene)-*O*-(*N*-succinimidyl)uranium hexafluorophosphate (HSPyU) (1.0 eq) and DIPEA (3 eq) at 40^0 C for 1 h. Once the activation was complete the solution was added to the resin together with DIPEA (3 eq) and shaken overnight. The solution was drained and the resin washed with DMF until the wash solution was colourless, then DCM (3 × 5 mL) and MeOH (3 × 5 mL).

QSY21 coupling: QSY21 succynimil ester (**19**) (1.0 eq per amine) was coupled in anhydrous DMF (0.1 M) containing DIPEA (3 eq) for 12 h. The solution was drained and the resin washed with DMF until the wash solution was colourless, then DCM (3 × 5 mL), MeOH (3 × 5 mL) and finally ether (3 × 5 mL)

Coupling of N-hydroxysuccinimide ester of 5-carboxyfluorescein diacetate[2]: A solution of the *N*-hydroxysuccinimide ester of 5-carboxyfluorescein diacetate (1.7 eq) in DMF (0.07 M) were stirred for 10 min and added to the resin followed by addition of DIPEA (1 eq) and the mixture was shaken for 30 min at 50° C followed by shaking at room temperature overnight. The solution was drained and the resin washed with DMF (3 × 10 mL), DCM (3 × 10 mL) and MeOH (3 × 10 mL). The coupling reaction was monitored by a Kaiser test. The resin was washed with 20 % piperidine to remove any esters.

Cleavage and deprotection: The resin (pre-swollen in DCM) was shaken 3 h in TFA/TIS/DCM (95:2.5:2.5, 5 mL). The solution was collected by filtration and the resin was washed with the cleavage cocktail. The combined filtrates were added to ice-cold ether, and the precipitated solid was collected by centrifugation, and washed repeatedly with cold ether (3 × 50 mL).

NES (2)

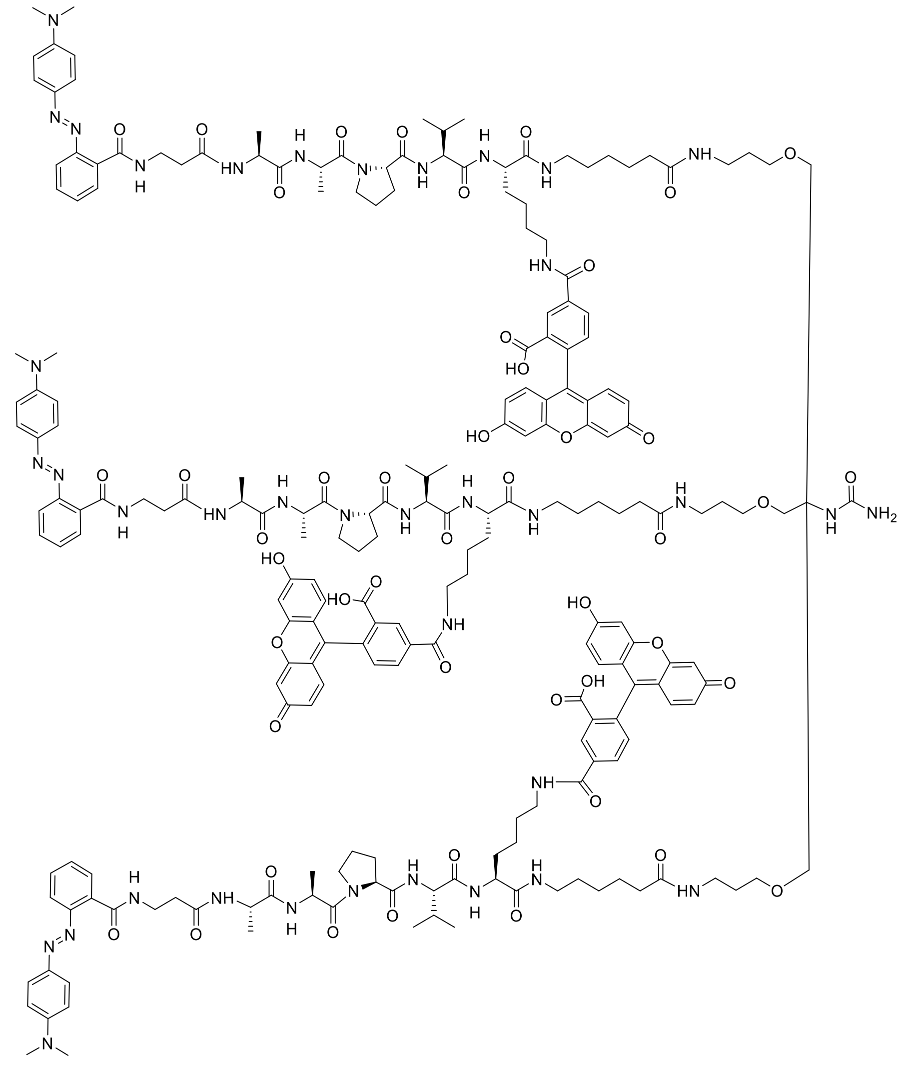

All amino acids and Methyl Red were coupled following the general solid-phase coupling procedure. The 5-carboxyfluorescein was incorporated following Dde deprotection of the Lysine sidechain (**9**), using 4.3 eq. (0.1 M) of 5-carboxyfluorescein per amino group of the sidechain. Purification of the probe was performed on the semi-preparative HPLC system with a gradient of 5 to 95% B over 35 min (t_R = 23 min). Fractions containing the product were combined and the solvent removed by freeze-drying to give **NES** as an orange solid. (2 mg, 2%). Data in good agreement with literature. [77]

LC-MS (ESI): $[M+6H]^{+6}$ 824.2. **FT-HRMS:** $C_{215}H_{267}N_{38}NaO_{46}^{4+}$ $[M+3H+1Na]^{4+}$ Expected: 1035.4915 Found: 1035.4909. **HPLC (495 nm):** **t_R** 5.40 min, purity 98%. **λ_{abs}** 500 nm (max) **λ_{em}** 520 nm (max).

HNE-FQ (11)

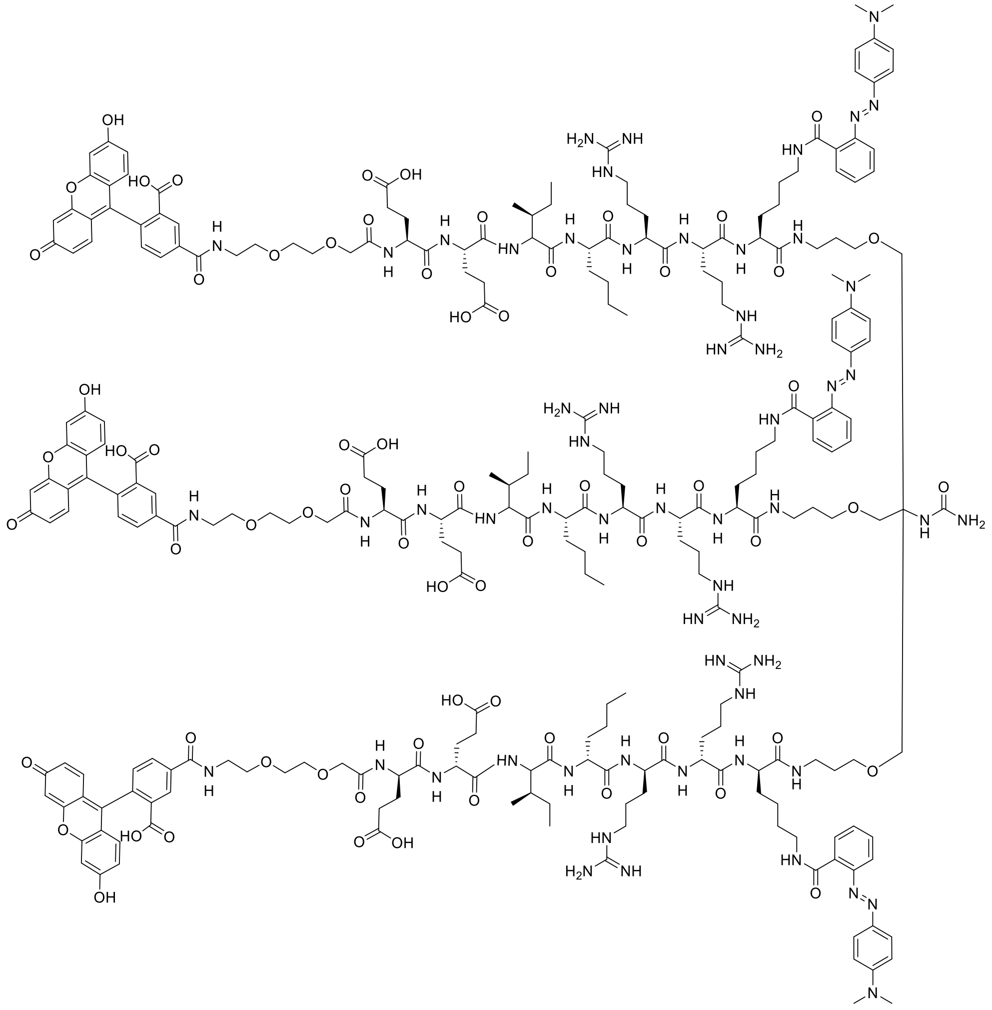

All amino acids 5-carboxyfluorescein (or the NHS ester of 5-carboxyfluorescein diacetate ester) and Fmoc-Lys(MR)-OH (**10**) were coupled following the general solid-phase coupling procedures described above. Purification of the probe was performed on the semi-preparative HPLC system with a gradient of 5 to 95% B over 35 min (t_R = 24.4 min). Fractions containing the product were combined and the solvent removed *via* freeze-drying to give HNE-FQ as an orange solid. (20 mg, 15 %). Data in good agreement with literature. [94]

LC-MS (ESI): $[M+5H]^{+5}$ 1075.6**.** **FT-HRMS:** Calculated m/z for $C_{260}H_{357}N_{59}O_{67}$ $[M+6H]^{+6}$ 896.7733 Found: 896.7710 **MALDI-TOF MS:** $[M+H]^+$ Expected: 5375.603 Found: 5375.789. **HPLC:** (495 nm) (lower) **t_R** 4.0 min, purity 97% **λ_{abs}** 500 nm (max) **λ_{em}** 520 nm (max).

SulfoCy5-OH (12)

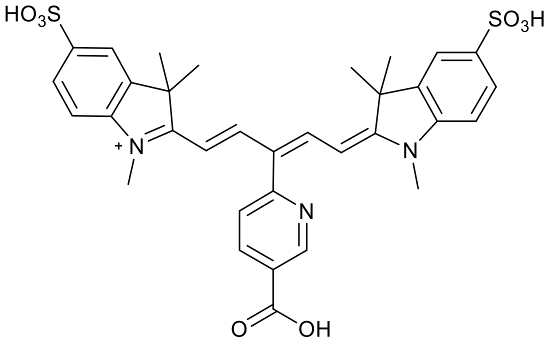

A solution of 1,2,3,3-tetramethyl-3H-indolium 5-sulfonate (372 mg, 1.47 mmol, 2.2 eq), 6-(1-formyl-2-oxoethyl)-3-pyridinecarboxylic acid (129 mg, 0.67 mmol, 1.0 eq) and sodium acetate (346 mg, 4.22 mmol, 6.3 eq) in Ac_2O/AcOH (1:1, 10 mL) were added to a microwave vial and heated at 120°C for 30 min in a microwave. The mixture was cooled to room temperature and the solvents were removed *in vacuo*. Cold diethyl ether was added and the solid collected by centrifugation (3 x 15 mL). The obtained solid was dried under vacuum to give a dark blue solid, (200 mg, 45%). Data is in good agreement with literature. [34]

^{1}H NMR (601 MHz, MeOD-*d*) δ 9.28 (s, 1H), 8.50 (dd, *J* = 7.9, 2.0 Hz, 1H), 8.45 (d, *J* = 14.3 Hz, 2H), 7.92 (s, 2H), 7.88 (dd, *J* = 8.2, 1.7 Hz, 2H), 7.58 (d, *J* = 8.0 Hz, 1H), 7.32 (d, *J* = 8.3 Hz, 2H), 5.83 (d, *J* = 14.3 Hz, 2H), 3.42 (s, 6H), 1.81 (s, 12H) **^{13}C NMR** (126 MHz, MeOD-*d*) δ 175.4, 168.7, 155.7, 153.3, 150.8, 144.0, 143.0, 142.3, 141.2, 138.5, 137.8, 127.6, 125.4, 119.9, 110.4, 101.3, 49.4, 30.3, 26.2. **LC-MS (ESI)**: $[M+Na]^+$ 685.9. **MALDI-TOF MS**: calculated for $C_{33}H_{34}N_3O_8S_2^+$ $[M+H]^+$ m/z 664.2. Found 664.3. **HPLC** (650 nm) **t_R** = 3.00 min, purity 100 %

Spiro[3H-2,1-benzoxathiole-3,9′-[9H]xanthene]-6-carboxylic acid, 3′,6′-dichloro-, 1,1-dioxide (15)

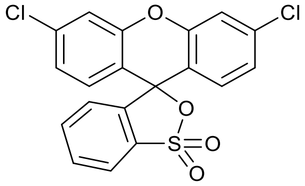

DMF (280 µL, 3.6 mmol, 0.9 eq) was added to $SOCl_2$ (10.66 mL). Sulfonfluorescein (1.9 g, 3.9 mmol, 1 eq) was added in small portions under stirring. The mixture was heated under reflux for 4 h, then cooled to rt and slowly poured into 300 mL iced water with continuous stirring. The resulting precipitate was collected by filtration, washed with water and dried *in vacuo* to give the product as a brown powder (2.2 g, 90 %). The crude was used without further purification. Data in agreement with literature. [133]

LC-MS (ESI) $[M+H]^+$: 405.1 **HPLC (252 nm): t_R** 6.25 min.

Spiro[3H-2,1-benzoxathiole-3,9'-[9H]xanthene], 3',6'-bis(2,3-dihydro-1H-indol-1-yl)-, 1,1-dioxide (16)

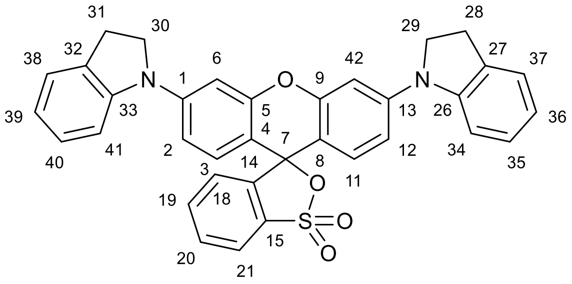

Compound **15** (2.0 g, 5 mmol, 1 eq) was dissolved in MeOH (80 mL), indoline (2.5 g, 20 mmol, 4 eq) was added, and the reaction mixture refluxed for 5 h. After cooling to rt, the solvent was evaporated *in vacuo*. DCM (100 mL) was added and the organic layer washed with 1M HCl (2 × 150 mL) and brine (200 mL). After drying over Na_2SO_4 the solvent was evaporated *in vacuo* to give the product as a dark blue film (1.9 g, 60%). The compound was used without further purification. Data in good agreement with literature. [133]

^{1}H NMR (500 MHz, Chloroform-*d*) δ 8.44 (dd, J = 8.1, 1.2 Hz, 1H, H_{21}), 7.73 – 7.66 (m, 1H, H_{18}), 7.57 (m, 2H, H, $H_{19,20}$), 7.49 (m, 2H, $H_{35,40}$), 7.43 (d, J = 8.2 Hz, 2H, $H_{3,11}$), 7.32 – 7.29 (m, 1H), 7.28 – 7.24 (m, 2H), 7.22 – 7.16 (m, 4H), 7.15 – 7.11 (m, 1H), 7.05 (d, J = 7.8 Hz, 2H, $H_{6,42}$), 4.07 (t, J = 8.3 Hz, 4H, $H_{29,30}$), 3.17 (t, J = 8.2 Hz, 4H, $H_{31,28}$) **LC-MS (ESI):** $[M+H]^+$ 571.0; **HPLC (650 nm): t_R** 5.7 min, purity 96%.

1-[2-[3-(1,3-dihydroisoindol-2-ium-2-ylidene)-6-(1,3-dihydroisoindol-2-yl)xanthen-9-yl]phenyl] sulfonylpiperidine-4-carboxylate ester (17)

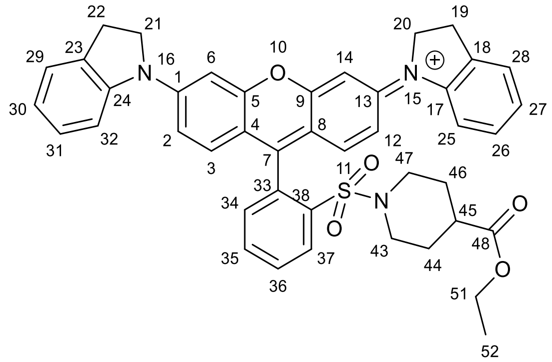

Compound **17** (1.7 g, 3 mmol, 1 eq) was dissolved in $POCl_3$ (28 mL) and heated at reflux for 5h under N_2. After cooling to room temperature, the solvent was evaporated *in vacuo*. The resulting crude was dissolved in chloroform (50 mL) and a solution containing ethyl isonipecotate (4.8 mL, 41 mmol, 12.5 eq) and Et_3N (3.4 mL) in chloroform (14 mL) was added dropwise and the reaction mixture stirred overnight. DCM (150 mL) was added and the organic layer washed with 2M HCl (2 × 120 mL), brine (120 mL) and dried over Na_2SO_4. The product was purified by column chromatography (elution with 9:1 DCM:MeOH) to give a dark blue film (990 mg, 35%). Data in good agreement with literature. [133]

^{1}H NMR (500 MHz, Chloroform-*d*) 8.16 (dd, *J* = 8.0, 1.4 Hz, 1H, H_{37}), 7.93 (td, *J* = 7.5, 1.3 Hz, 1H, H_{35}), 7.87 (td, *J* = 7.8, 1.4 Hz, 1H, H_{36}), 7.63 – 7.59 (m, 2H), 7.58 (d, *J* = 8.1 Hz, 2H, $H_{3,11}$), 7.54 (d, *J* = 2.3 Hz, 2H), 7.52 (dd, *J* = 7.5, 1.4 Hz, 1H, H_{34}), 7.49 – 7.41 (m, 1H), 7.37 (dd, *J* = 7.5, 1.3 Hz, 2H), 7.32 – 7.29 (m, 2H), 7.24 – 7.17 (m, 1H), 7.14 (m, 2H), 4.49 – 4.36 (m, 4H), 4.22 – 4.10 (m, 1H), 4.05 (quint, *J* = 7.1 Hz, 2H, H_{52}), 3.41 – 3.25 (m, 6H), 2.76 –2.66 (m, 2H), 2.42 (m, 1H), 1.56 (m, 2H, $H_{44,46}$), 1.32 – 1.23 (m, 2H, $H_{44,46}$), 1.18 (t, *J* = 7.1 Hz, 3H, H_{51}).**^{13}C NMR** (126 MHz, Chloroform-*d*) δ 173.8, 157.7, 156.0, 152.5, 142.3, 138.9, 134.9, 133.4, 132.1, 131.5, 131.0, 130.6, 129.7, 127.6, 126.3, 125.1, 117.9, 116.9, 113.8, 100.4, 60.7, 53.5, 44.7, 39.7, 28.2, 27.6, 14.1. **LC-MS (ESI)** $[M]^+$: 710.3 found: 710.3 **HPLC (650 nm): t_R** 5.32, purity 93%.

QSY21 carboxylic acid (18)

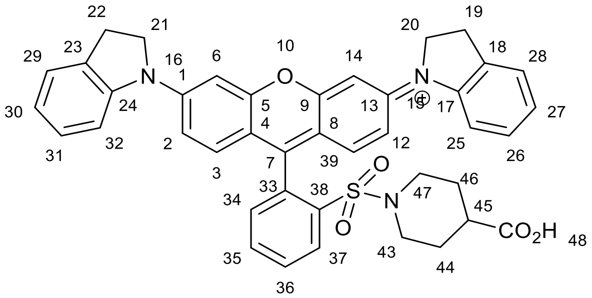

Compound **17** (0.86 g, 1.21 mmol) was dissolved in MeOH/THF (1:2, 30 mL) and 1M NaOH (aq, 10 mL) was added and the reaction mixture stirred for 2h. The solvent was partially evaporated under vacuum. The organic layer was washed with 2M HCl (120 mL), brine (120 mL). The organic phase was dried over Na_2SO_4 and solvent evaporated under vacuum to give a blue powder (0.8 g, 100%). Data in good agreement with literature. [133]

^{1}H NMR (500 MHz, Chloroform-*d*) δ 8.19 (dd, *J* = 5.5, 2.0 Hz, 1H, H_{37}), 7.92 – 7.81 (m, 2H, $H_{35,36}$), 7.60 (m, 2H), 7.56 – 7.52 (m, 2H), 7.48 (d, *J* = 2.2 Hz, 2H), 7.43 (dd, *J* = 5.2, 2.1 Hz, 1H, H_{34}), 7.36 (dd, *J* = 7.5, 1.2 Hz, 2H), 7.34 – 7.24 (m, 3H), 7.14 (t, *J* = 7.4 Hz, 2H), 4.55 – 4.27 (m, 4H, $H_{20,21}$), 3.34 (m, 4H, $H_{19,22}$), 3.17 – 3.03 (m, 2H, $H_{43,47}$), 2.81 – 2.64 (m, 3H, $H_{43,47,45}$), 1.90 – 1.78 (m, 2H, $H_{44,46}$), 1.67 – 1.53 (m, 2H, $H_{44,46}$). **^{13}C NMR** (126 MHz, Chloroform-*d*) δ 175.4, 157.5, 155.9, 152.5, 142.2, 138.7, 135.0, 133.1, 132.2, 131.1, 131.1, 130.7, 130.4, 127.7, 126.3, 125.2, 118.1, 116.9, 113.9, 99.9, 53.4, 44.5, 39.3, 28.2, 27.5. **LC-MS (ESI)** $[M]^+$: 682.0 **HPLC (650 nm): t_R** 4.78 min, purity 90%.

QSY21 succynimil ester (19)

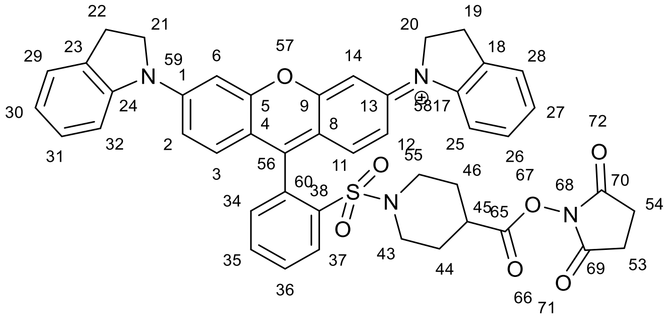

Compound **18** (0.25 g, 0.36 mmol) was dissolved in anhydrous DMF (12 mL). TSTU [*N*,*N*,*N*′,*N*′-Tetramethyl-*O*-(*N*-succinimidyl)uronium tetrafluoroborate] (165 mg, 1.5 eq) and DIPEA (0.19 mL, 3 eq) were added and the solution stirred overnight. The solvent evaporated under vacuum and chloroform (100 mL) was added. The organic layer washed with 1M HCl (2 × 100 mL), were dried over Na_2SO_4 and evaporated under vacuum to give a blue powder (200 mg, 71%). Data in good agreement with literature. [133]

^{1}H NMR (500 MHz, Chloroform-*d*) δ 8.21 (d, *J* = 7.8 Hz, 1H, H_{37}), 7.91 – 7.81 (m, 2H, $H_{35,36}$), 7.64 – 7.48 (m, 6H), 7.42 (m, 1H, H_{34}), 7.36 (m, 2H), 7.34 – 7.29 (m, 3H), 7.14 (td, *J* = 7.4, 4.9 Hz, 2H), 4.54 – 4.25 (m, 4H, $H_{20,21}$), 3.34 (m, 4H, H $_{19,22}$), 3.20 – 3.03 (m, 2H, $H_{43,47}$), 2.80 – 2.71 (m, 2H, $H_{43,47}$) , 2.67 (s, 4H, $H_{44,46}$), 2.45 – 2.33 (m, 1H, H_{45}), 2.03 – 1.68 (m, 4H, $H_{53,54}$). **LC-MS (ESI)** $[M]^+$ 779.0 **HPLC (650 nm): t$_R$** 4.99 min, purity 92 %.

Carbamic acid, *N*-[2-(2-propyn-1-yloxy)-1,1-bis[(2-propyn-1-yloxy)methyl]ethyl]-, 1,1-dimethylethyl ester (23)

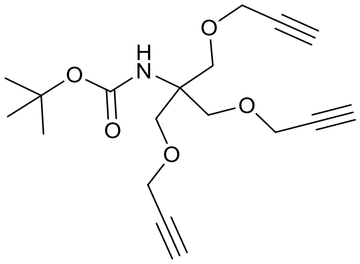

A solution of N-(tert-butyloxycarbonyl)tris(hydroxymethyl)aminomethane (500 mg, 2.26 mmol, 1 eq) in anhydrous DMF (6 mL) was stirred at 0° and small portions of finely ground KOH (951 mg, 16.4 mmol , 7.25 eq) were added over a period of 15 min. Propargyl bromide (80 wt.% in toluene, 1.76 mL , 15.8 mmol, 7 eq) was added dropwise and the reaction mixture was then heated to 35°C and stirred for 24 h under N_2 atmosphere. To resulting brown mixture ethyl acetate (50 mL) was added and the organic layer was washed with water (3x30 mL), dried over Na_2SO_4 and concentrated to dryness *in vacuo*. Purification by column chromatography on silica gel (eluting with hexanes/EtOAc 95:5 to 90:10) gave the title compound (190 mg, 60%). The data were in good agreement with the literature. [201]

^{1}H NMR (500 MHz, Chloroform-*d*) δ 4.94 (br, 1H, N*H*), 4.18 (d, *J* = 2.4 Hz, 6H, OC*H₂*), 3.81 (s, 6H, C*H₂*O), 2.45 (t, *J* = 2.4 Hz, 3H, C≡C*H*), 1.45 (s, 9H, *Boc*). **^{13}C NMR** (126 MHz, Chloroform-*d*) δ 154.8, 79.6, 79.3, 74.5, 68.9, 58.7, 58.1, 28.4. **LC-MS (ESI)** $[M+H]^+$ 336.2, $[M +Na]^+$ 358.2 $[M+K]^+$; **FT-HRMS :** calculated for $C_{18}H_{25}NO_5$ $[M+H]^+$ m/z 336.18055 Found: $[M+Na]^+$ 358.1626; **HPLC-ELSD: t$_R$** 5.80 min, purity 100%.

1,3-Bis(2-propyn-1-yloxy)-2-[(2-propyn-1-yloxy)methyl]-2-propanamonium 2,2,2-trifluoroacetate (24)

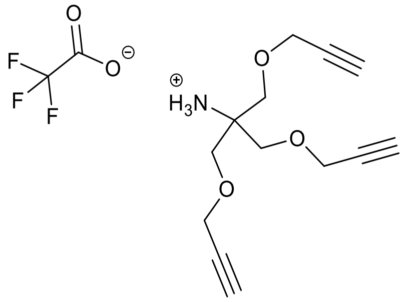

A solution of N-(tert-Butyloxycarbonyl)tris(hydroxymethyl)propargyl (80 mg, 0.3 mmol, 1 eq) was stirred in 20% TFA/DCM (5 mL) for 1 h and the reaction was monitored by TLC and HPLC. The solvent was removed *in vacuo* to give the product as a colourless oil (75 mg, 100%).

^{1}H NMR (500 MHz, Chloroform-*d*) δ 4.20 (d, J = 2.4 Hz, 6H, OC*H₂*), 3.73 (s, 6H, CH_2O), 2.50 (t, J = 2.3 Hz, 3H, C≡C*H*). **^{13}C NMR** (500 MHz, Chloroform-*d*) δ 78.2, 76.1, 67.0, 60.3, 59.0. **LC-MS (ESI)** $[M+H]^+$ 236.2 $[M+Na]^+$ 258.1 ; **FT-HRMS :** calculated for $C_{13}H_{18}NO_3$ $[M+H]^+$ 236.12812 Found: $[M+H]^+$ 236.1279; HPLC-**ELSD:** 2.7 min, purity 100%. The data were in good agreement with the literature. [201]

N-Boc-3-[2-(2-aminoethoxy)ethoxy]ethanoic acid fluoride **(25)**

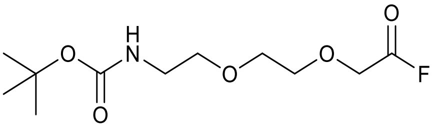

8-Tert-butyloxycarbonylamino-3,6-dioxaoctanoic acid (264 mg, 1 mmol, 1 eq) was dissolved in anhydrous DCM (5 mL) and cyanuric fluoride (172 µL, 2 eq, 2 mmol) was added followed by pyridine (81 µL, 2 eq, 2 mmol) and reaction stirred for 2 h. Conversion was monitored by TLC (MeOH:DCM 1:9) and LC-MS by adding a small amount of the reaction mixture into anhydrous MeOH to form the corresponding methyl ester and analysis). Upon completion ice water was added to the reaction mixture and the organic layer was dried with $MgSO_4$ and evaporated *in vacuo*. The product was used immediately without further purification (223 mg, 80%).

^{1}H NMR (500 MHz, Chloroform-*d*) δ 5.1 (s, 1H) 4.34 (d, *J* = 3.5 Hz, 2H), 4.16 (s, 2H), 3.79 – 3.73 (m, 2H), 3.68 – 3.63 (m, 2H), 3.53 (t, J = 5.2 Hz, 2H), 1.44 (s, 9H). **^{13}C NMR** (126 MHz, Chloroform-*d*) δ 162.2, 159.3, 156.2, 79.5, 71.5, 71.4, 70.5, 66.8, 66.3, 40.5, 28.4. **LC-MS (ESI)**: calculated for $C_{12}H_{23}NO_6$ (methyl ester) $[M+OMe+Na]^+$ 300.1, found 300.1 HPLC-ELSD (MeOH/H_2O, 15 min): 6.9 min, purity 85 %.

N-Boc-2-[2-(2-aminoethoxy)ethoxy]ethanamide, *N*-[2-(2-propyn-1-yloxy)-1,1-bis[(2-propyn-1-yloxy)methyl]ethyl] (26)

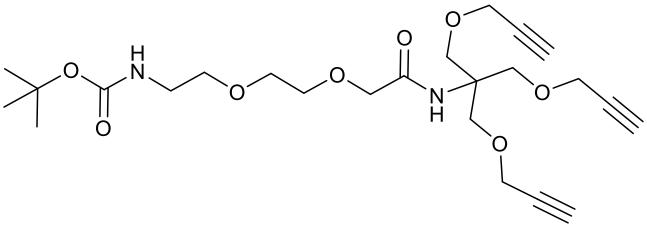

8-*tert*-butyloxycarbonylamino-3,6-dioxaoctanoic acyl fluoride (70 mg, 0.3 mmol) was dissolved in anhydrous DMF (5 mL) and DIPEA (0.5 mL, 3 eq. 3 mmol) was added followed by tris(hydroxymethyl)propargyl **25** (80 mg, 1 eq, 0.3 mmol) and the reaction stirred overnight. Conversion was monitored by TLC and RP-HPLC. The solvent was evaporated *in vacuo* and the product was purified by column chromatography (eluted with DCM:MeOH 9:1) (110 mg, 75 %).

^{1}H NMR (500 MHz, Chloroform-*d*) δ 6.84 (br, 1H, NH, *Tris*), 5.03 (br, 1H, NH, *Boc*), 4.17 (d, 6H, CH_2O, *Tris*), 3.92 (s, 2H, $COCH_2$, *PEG),* 3.88 (s, 6H, OCH_2, *Tris*), 3.69 – 3.59 (m, 4H, OCH_2/CH_2O, *PEG*), 3.56 (t, *J* = 5.2 Hz, 2H, OCH_2/CH_2O, *PEG*), 3.34 (quint, *J* = 5.4 Hz, 2H, CH_2*N*H *PEG*), 2.45 (t, *J* = 2.4 Hz, 3H, C≡C*H, Tris*), 1.46 (s, 9H, CH_3 *Boc*). **^{13}C NMR** (126 MHz, Chloroform-*d*) δ 169.6, 156.0, 79.6, 79.3, 74.7, 71.0, 70.9, 70.5, 70.1, 68.5, 59.1, 58.7, 40.4, 28.4. **LC-MS (ESI)** $[M + Na]^+$ m/z 503.1; **FT-HRMS :** calculated for $C_{24}H_{37}N_2O_8$ $[M+H]^+$ m/z 481.25444 Found: $[M+H]^+$ 503.23639**; HPLC-ELSD: t_R** 5.08 min, purity 86 %.

2-[2-(2-aminoethoxy)ethoxy]-ethanamide, *N*-[2-(2-propyn-1-yloxy)-1,1-bis[(2-propyn-1-yloxy)methyl]ethyl] (26.1)

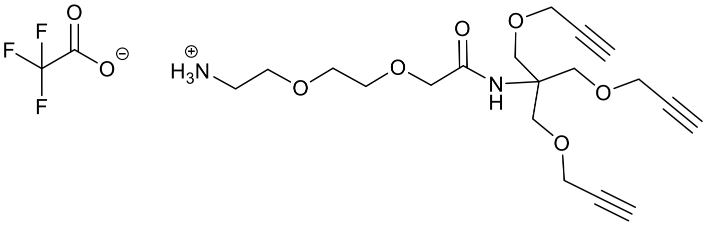

8-*tert*-butyloxycarbonylamino-3,6-dioxaoctanoic-tris(hydroxymethyl)propargyl (110 mg, 0.28 mmol) was dissolved in 20% TFA in DCM (5 mL) and stirred for 2. The solvent was evaporated under vacuum and the product used without further purification. (90 mg, 100%).

^{1}H NMR (500 MHz, MeOD-*d*) δ 4.19 (d, *J* = 2.4 Hz, 6H, CH_2O, *Tris*), 3.98 (s, 2H, $COCH_2$, *PEG*), 3.85 (s, 6H, , OCH_2, *Tris)* 3.79 – 3.75 (m, 2H OCH_2/CH_2O, *PEG*), 3.74 (d, 4H, OCH_2, *PEG*), 3.19 – 3.13 (m, 2H, OCH_2/CH_2O, *PEG*), 2.89 (t, *J* = 2.4 Hz, 3H, C≡C*H, Tris*), 1.31 (br s, 3H, N*H$_3$*).**^{13}C NMR** (126 MHz, MeOD-*d*) δ 170.7, 79.1, 74.8, 70.5, 70.0, 69.9, 67.9, 66.6, 59.3, 58.1, 39.3. **LC-MS (ESI):** [M + Na]$^+$ 403.1; **FT-HRMS:** calculated for $C_{19}H_{29}N_2O_6$ [M+H]$^+$ m/z 381.20201 Found: [M+H]$^+$ 381.2022; **HPLC-ELSD:** 3.29 min, purity 93 %.

N-QSY21-2-[2-(2-ethoxiamide)ethoxy]-ethanamide, N-[2-(2-propyn-1-yloxy)-1,1-bis[(2-propyn-1-yloxy)methyl]ethyl] (27)

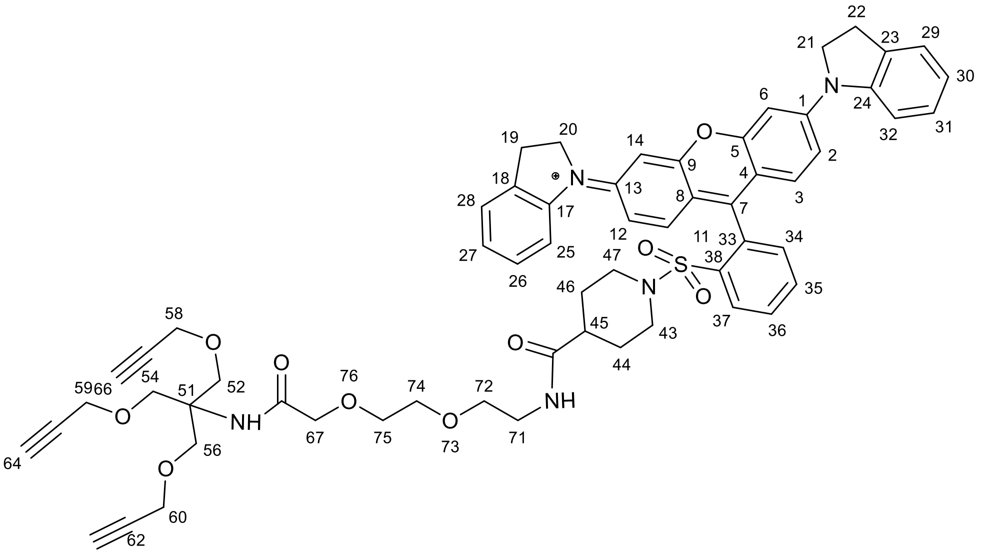

QSY21-NHS (**19**) (130 mg, 1 eq, 0.17 mmol) was dissolved in anhydrous DMF and amino-3,6-dioxaoctanoic-tris(hydroxymethyl)propargyl (**18**, 90 mg, 1.5 eq, 0.23 mmol) was added followed by DIPEA (100 µL, 2.5 eq, 0.42 mmol), and the reaction stirred at 50 ^{o} C for 6 h. Conversion was monitored by TLC and RP-HPLC. The solvent was removed *in vacuo* and the mixture was purified by column chromatography (eluting with DCM:MeOH 9:1) to give the product **27** as a dark blue film (80 mg, 45%).

^{1}H NMR (600 MHz, Chloroform-*d*) δ 8.65 (br, 1H), 8.17 (d, *J* = 7.4 Hz, 1H, H_{37}), 7.96 – 7.84 (m, 2H, $H_{35,36}$), 7.61 (d, *J* = 8.1 Hz, 1H), 7.55 (d, *J* = 9.3 Hz, 1H), 7.48 – 7.41 (m, 2H,), 7.38 (d, *J* = 7.4 Hz, 1H, H_{34}), 7.36 – 7.29 (m, 1H), 7.22 (d, *J* = 8.0 Hz, 1H), 7.19 – 7.14 (m, 2H), 7.10 (t, *J* = 8.9 Hz, 1H), 6.97 (d, 1H), 6.88 (dd, *J* = 8.5, 2.3 Hz, 1H), 6.86 – 6.81 (m, 1H), 6.77 (t, *J* = 7.3 Hz, 1H), 6.40 – 6.33 (m, 1H), 6.25 (br ,1H), 4.40 (q, *J* = 8.2 Hz, 1H), 4.31 (q, *J* = 8.2 Hz, 1H), 4.16 (dd, *J* = 9.2, 2.3 Hz, 6H), 4.01 – 3.91 (m, 4H), 3.87 (d, *J* = 13.2 Hz, 6H), 3.72 – 3.68 (m, 1H), 3.68 – 3.60 (m, 3H), 3.58 (t, J = 5.2 Hz, 1H), 3.55 (t, J = 6.0 Hz, 1H), 3.49 (q, J = 5.3 Hz, 1H), 3.43 (d, J = 12.1 Hz, 1H), 3.38 (q, *J* = 5.6 Hz, 1H), 3.33 (t, *J* = 7.9 Hz, 2H), 3.13 (t, *J* = 8.4 Hz, 3H), 3.10 – 3.03 (m, 1H), 2.65 – 2.56 (m, 1H), 2.47 (dt, *J* = 11.5, 2.3 Hz, 3H), 2.45 – 2.38 (m, 1H), 2.05 – 2.00 (m, 1H), 1.99 – 1.92 (m, 1H), 1.82 – 1.76 (m, 1H), 1.61 (qd, J = 12.1, 4.1 Hz, 1H). **^{13}C NMR** (126 MHz, Chloroform-*d*) δ 173.9, 169.9, 157.6, 152.5, 151.3, 146.5, 143.9, 142.2, 136.6, 134.7, 133.9, 132.3, 131.3, 130.7, 128.4, 127.8, 127.1, 126.3, 125.2, 125.0, 119.1, 116.5, 113.9, 99.9, 79.6, 79.5, 74.8, 71.0, 70.9, 70.8, 70.3, 69.9, 69.8, 68.5, 59.2, 59.1, 58.7, 53.2, 52.0, 45.4, 45.0, 39.2, 38.8, 37.3, 29.7. **LC-MS (ESI):** $[M+2H]^{+2}$ 522.9.; **FT-HRMS:** calculated for $C_{60}H_{62}N_5O_{10}S$ $[M+H]^+$ m/z 1044.42119 Found: $[M+H]^+$ 1044.42; **MALDI-TOF MS:** calculated for $C_{60}H_{62}N_5O_{10}S$ $[M]^+$ m/z 1046.42 Found: $[M]^+$ 1046.77; **HPLC-ELSD: t$_R$** 7.63 min, purity 92 %.

HNE-1F1Q (21)

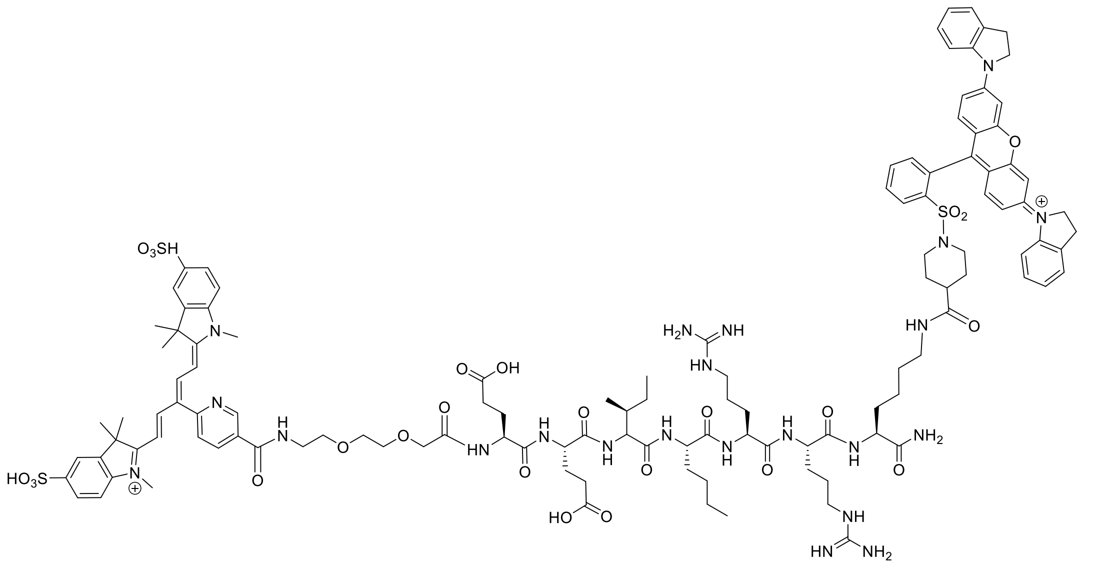

All amino acids, sulfoCy5 and QSY21 were coupled following the solid-phase coupling procedures described above. **LC-MS (ESI):** $[M+H]^{+3}$ 799.7; **FT-HRMS:** Calculated m/z for $C_{120}H_{151}N_{21}O_{26}S_3^{+3}$ $[M+H]^{+3}$ Expected: 799.67716 Found: 799.67774; **HPLC** (650 nm): **t$_R$** of 3.9 min, purity 97 %; **⍰$_{abs}$** 640 nm (max) **⍰$_{em}$** 657 nm (max). Purification of the probe was performed on the semi-preparative HPLC system with a gradient of 5 to 95% B over 30 min (t_r = 16 min).

HNE-1F0Q (22)

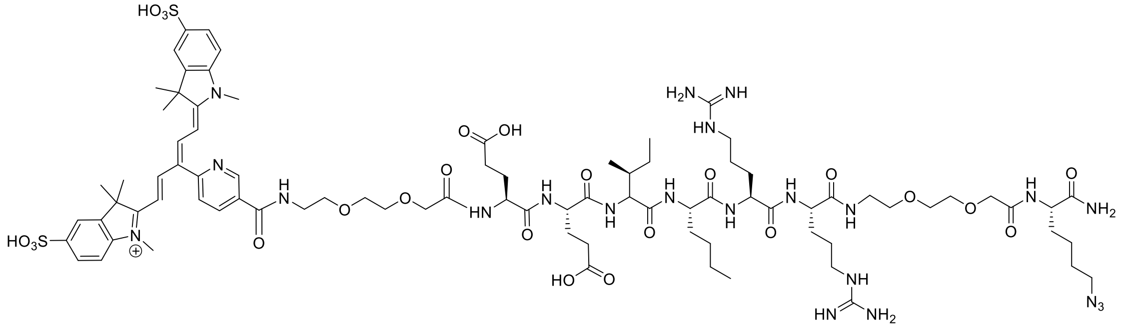

Purification of the probe was performed on the preparative HPLC system with a gradient of 5 to 95% B over 21 min with detection at 650 nm (t_R = 12 min). **LC-MS (ESI):** $[M+H]^{+2}$ 952.8 **FT-HRMS:** calculated m/z for $C_{85}H_{128}N_{22}O_{24}S_2^{+2}$ $[M+H]^{+2}$ Expected: 952.94654 Found: 952.44512; **HPLC** (650 nm, method A): **t_R** of 3.4 min, purity 100 %; **HPLC** (650 nm, method C): **t_R** of 6.9 min λ_{abs} 640 nm (max) λ_{em} 657 nm (max).

Procedure for Click Chemistry:

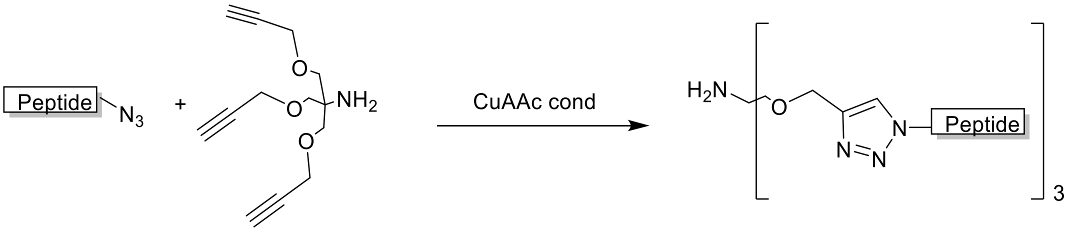

CuI or CuI/THPTA as catalyst

The azide-peptide **22** (3 to 5 eq, final concentration 2 to 4 mM), and alkynes **24** or **27** (1 eq, final concentration 0.7 mM) were dissolved in anhydrous DMF and a solution of CuI (0.5 eq) or CuI/THPTA (0.5/2.5 eq, final concentration 1.4 mM/7.1 mM) added. The reaction was allowed to proceed at 50^{o}C overnight, under N_2. Monitoring was carried out by RP-HPLC until reaction completion. The solvent was evaporated under vacuum and the resulting product purified by semipreparative RP-HPLC.

$CuSO_4$/THPTA/Aminoguanidine/NaAsc as catalyst

In an eppendorf, the azide-peptide **22** (4 eq, final concentration 2.8 mM), and alkynes **24** or **27** (1 eq, final concentration 0.7 mM) were dissolved in a mixture of tBu/H_2O and a solution of premixed $CuSO_4$/THPTA (0.5/2.5 eq, final concentration 2 mM/10 mM) was added, followed by addition of aminoguanidine hydrochloride (final concentration 80 mM) and NaAsc (final concentration 80 mM), were added. The reaction was allowed to proceed at 40^{o}C overnight. Monitoring was carried out by RP-HPLC until reaction completion. The solvent was evaporated under vacuum and the resulting product purified by semipreparative RP-HPLC.

HNE-3F0Q (28)

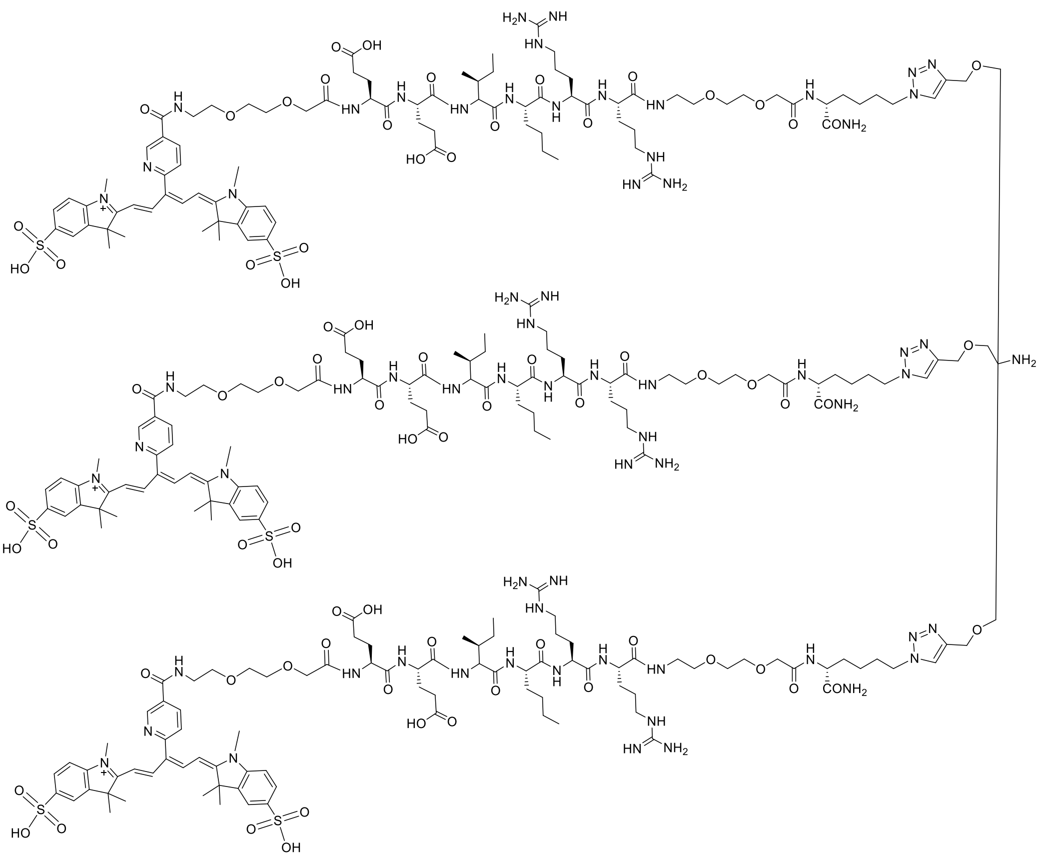

Purification of the probe was performed on the semi-preparative HPLC system with a gradient of 5 to 95% B over 30 min with detection at 650 nm (t_R = 12.8 min). **LC-MS (ESI)**: $[M+3H]^{6+}$ 992.1; **FT-HRMS:** Calculated m/z for $C_{268}H_{340}N_{67}O_{75}S_6$ $[M+2H]^{5+}$: 1190.358308 Found: 1190.356672. **HPLC** (650 nm, method C) **t_R** of 3.2 min **HPLC** (650 nm, method C) **t_R** of 6.6 min, purity 100 %; **λ_{abs}** 640 nm (max) **λ_{em}** 657 nm (max).

HNE-F31Q (29)

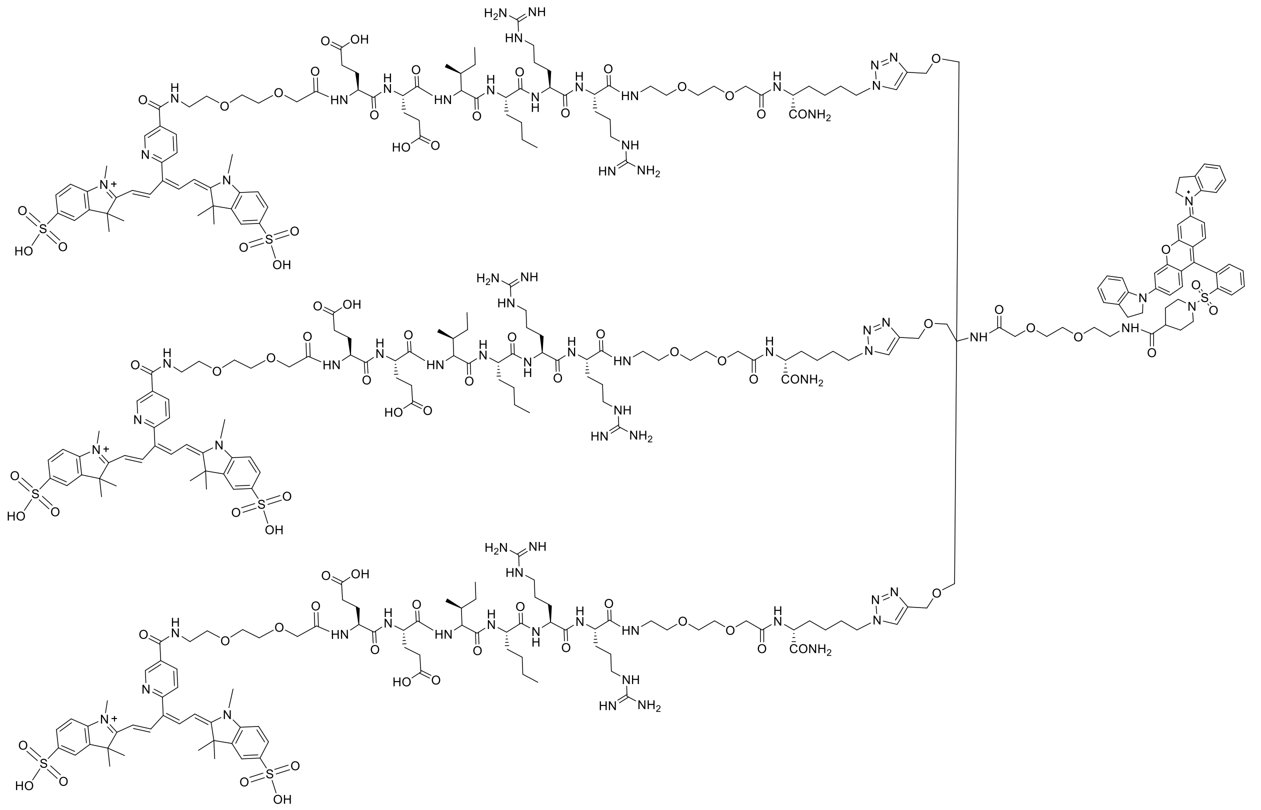

Purification of the probe was performed on the semi-preparative HPLC system with a gradient of 5 to 95% B over 30 min with detection at 650 nm (t_R = 15 min). **LC-MS (ESI):** $[M+2H]^{6+}$ 1126.9; **FT-HRMS:** Calculated m/z for $C_{315}H_{439}N_{71}O_{82}S_7$ $[M+H]^{5+}$ Expected: 1352.21737 Found: 1352.22055; **HPLC** (650 nm, method C): **t_R** of 8.5 min, purity 98 %; **λ_{abs}** 640 nm (max) **λ_{em}** 657 nm (max).

Azide peptide for model reaction (**30**)

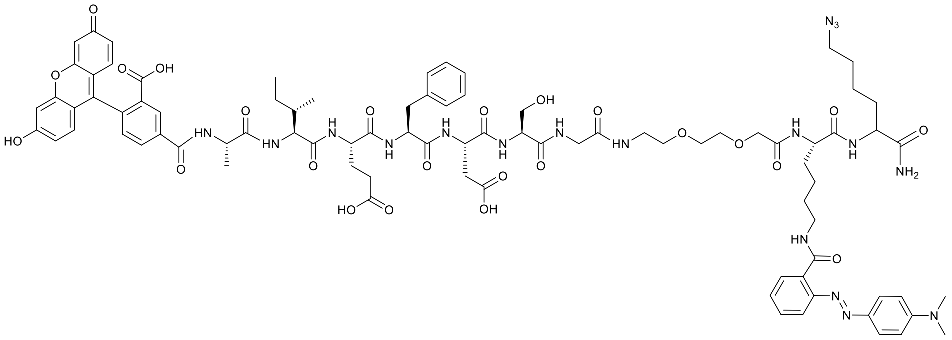

LC-MS (ESI): [M+H]$^+$ 1774.6; **HPLC** (495 nm, method C): **t_R** of 13.2 min; **λ_{abs}** 490 nm (max) **λ_{em}** 520 nm (max).

Tribranched peptide from model reaction (**31**)

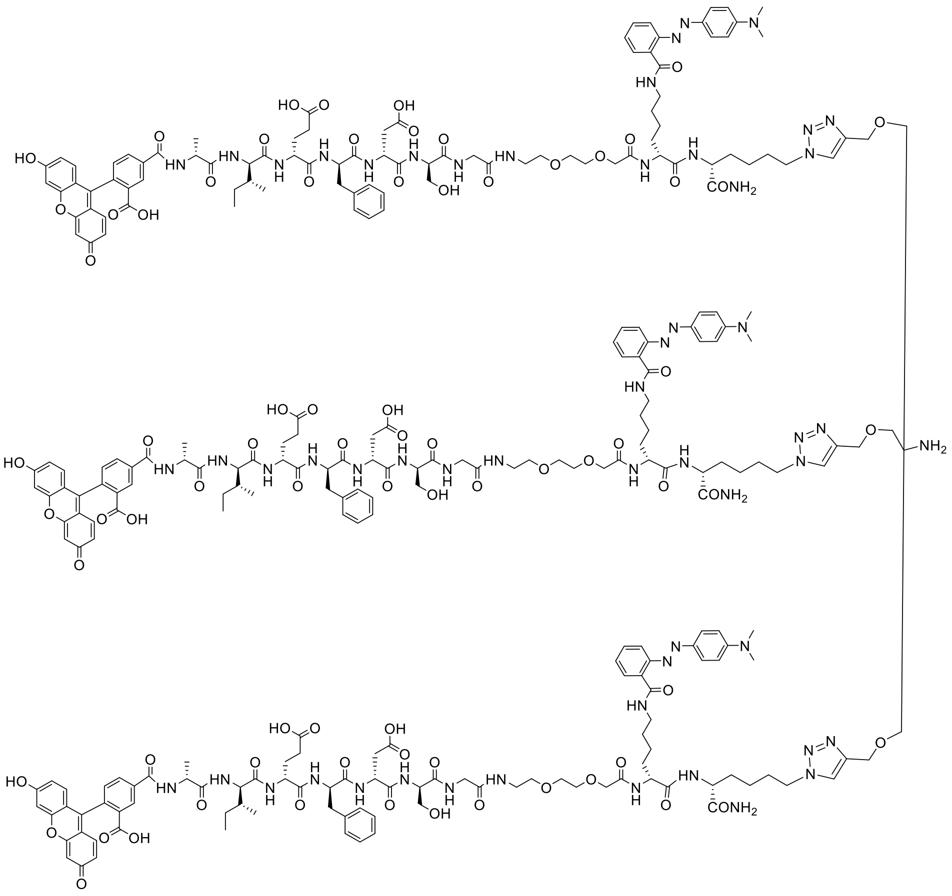

MALDI-TOF MS: $C_{271}H_{332}N_{55}O_{65}$ [M+3H]$^{3+}$ Expected: 1853.130927 Found: 1853.123866; **HPLC** (495 nm, method C): **t_R** of 14.0 min; **λ_{abs}** 490 nm (max) **λ_{em}** 520 nm (max).

BODIPY-NHS (37)

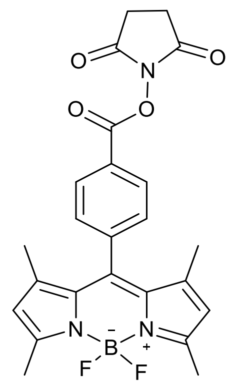

BODIPY (140 mg, 0.38 mmol, 1 eq), EDC HCl (160 mg, 0.83 mmol, 2.2 eq), NHS (95.5 mg, 0.83 mmol, 2.2 eq) were dissolved in DCM (90 mL), and the reaction mixture was stirred overnight under N_2. The solvent was evaporated in vacuo and the crude purified by column chromatography (eluting with DCM: MeOH, 95:5). The data were in good agreement with the literature. [192]

^{1}H NMR (500 MHz, Chloroform-*d*) δ 8.27 (d, *J* = 8.4 Hz, 2H), 7.50 (d, *J* = 8.4 Hz, 2H), 6.01 (s, 2H), 2.94 (s, 4H), 2.56 (s, 6H), 1.38 (s, 6H). **LC-MS (ESI)**: $[M+H]^+$ 466.1; **HPLC-ELSD:** 5.79, purity 89.33 % Data were in good agreement with the literature.

Procedure for BODIPY-NHS (37) attachment: The crude peptide, carrying a free amino group, was dissolved in anhydrous DMF (1 eq, 10 mM), DIPEA (1 eq, 10 mM) was added, followed by the addition of BODIPY-NHS (1.5 eq, 15 mM). The reaction was stirred overnight at 40 °C under N_2. The solvent was removed *in vacuo* and the mixture washed with cold ether to remove excess/unreacted BODIPY. The resulting product was either purified by semi-preparative HPLC or used without further purification in subsequent reactions.

CatD-P1 (33)

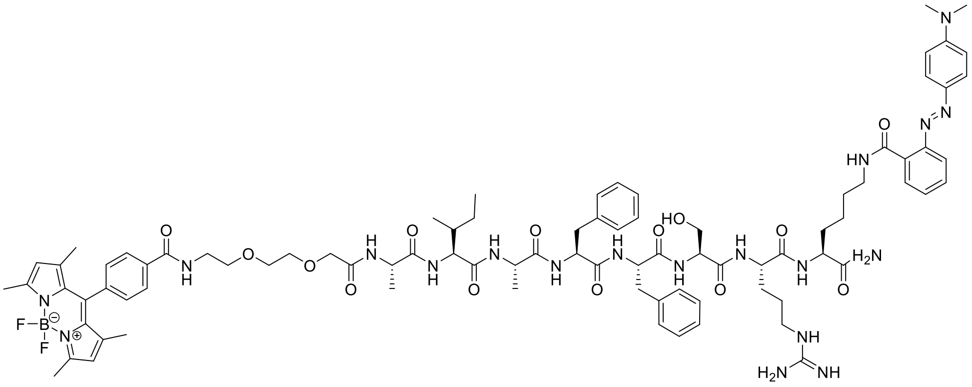

All amino acids were coupled following the solid-phase coupling procedures described above. The BODIPY was coupled as described above.

LC-MS (ESI): $[M+3H]^{3+}$ 563.3; **FT-HRMS:** Calculated m/z for $C_{86}H_{114}BF_2N_{19}O_{14}^+$ $[M+H]^+$ Expected: 1685.88073 Found: 1685.87628 . **HPLC** (495 nm): **t_R** of 4.9 min; **λ_{abs}** 500 nm (max) **λ_{em}** 520 nm (max).

CatD-P2 (34)

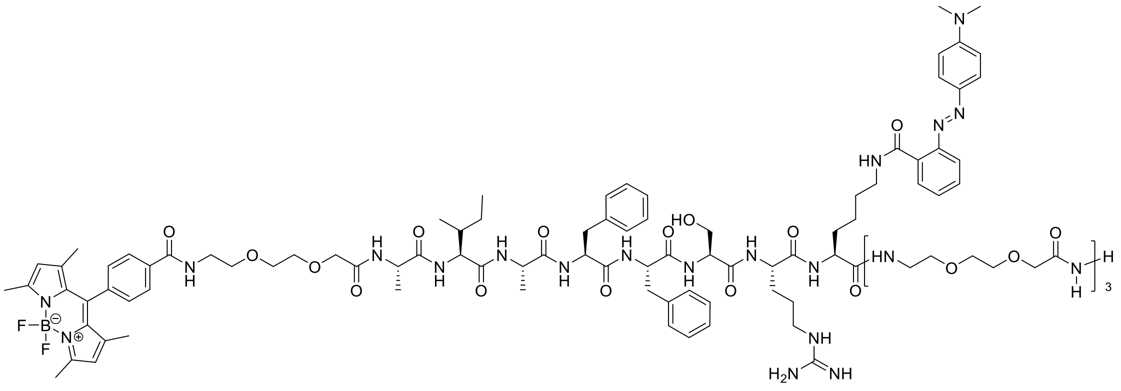

All amino acids and bis-ethylene glycol residues were coupled following the solid-phase coupling procedures described above. BODIPY was coupled as described above.

LC-MS (ESI) $[M+2H]^{2+}$ 1060.5; **MALDI-TOF MS:** m/z expected: 2121.104; found: 2121.302**; HPLC (495 nm, method B**): t_R of 6.7 min, purity 98 %; **λ_{abs}** 500 nm (max) **λ_{em}** 520 nm (max).

Azide-BODIPY-peptide (35)

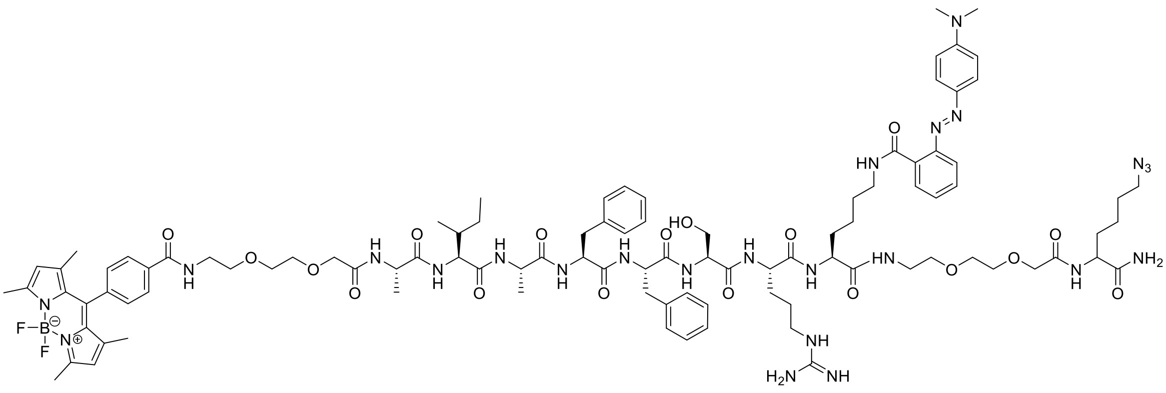

All amino acids, including Fmoc-Lys(MR)-OH and Fmoc-Lys(N_3)-OH and bis-polyethylene glycol residues were coupled following the solid phase coupling procedure described above, BODIPY-NHS was coupled as described above.

LC-MS (ESI) $[M+2H]^{2+}$: 655.4 **FT-HRMS: Calculated** m/z for $C_{98}H_{133}B_1N_{24}F_4O_{18}$ $[M+H]^+$ Expected: 1985.0401 Found: 1985.0386. HPLC-UV (495 nm): $\mathbf{t_R}$ of 5.1 min, purity 100 %; $\mathbf{\lambda_{abs}}$ 500 nm (max**)** $\mathbf{\lambda_{em}}$ 520 nm (max)

CatD-P3 (36)

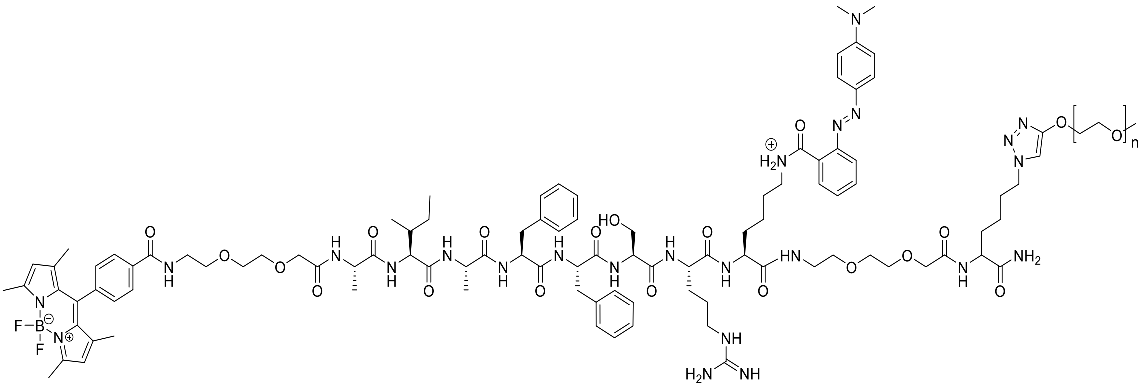

Azide-peptide **35** (19 mg, 1.5 eq, 16 mM), was dissolved in anhydrous DMF and alkyne-PEG(5K)-OMe (38 mg, 1 eq, 15 mM) was added, followed by a pre-mixed solution of CuI/THPTA (0.5/2.5 eq, final concentration 2 mM/10 mM). The reaction was allowed to proceed at 50⁰C overnight, under a N_2 atmosphere. Monitoring was done by HPLC until completion. The solvent was evaporated under vacuum and the resulting product purified by semipreparative HPLC.

HPLC-UV (495 nm): $\mathbf{t_R}$ of 4.6 min, purity 100 % λ_{abs} 500 nm (max) λ_{em} 520 nm (max). **MALDI-TOF MS:** calculated m/z for $\mathbf{C_{329}H_{594}BF_2N_{24}O_{133}^+}$ $[M+H]^+$ 7059.051 found 7059.070 (for n=114)

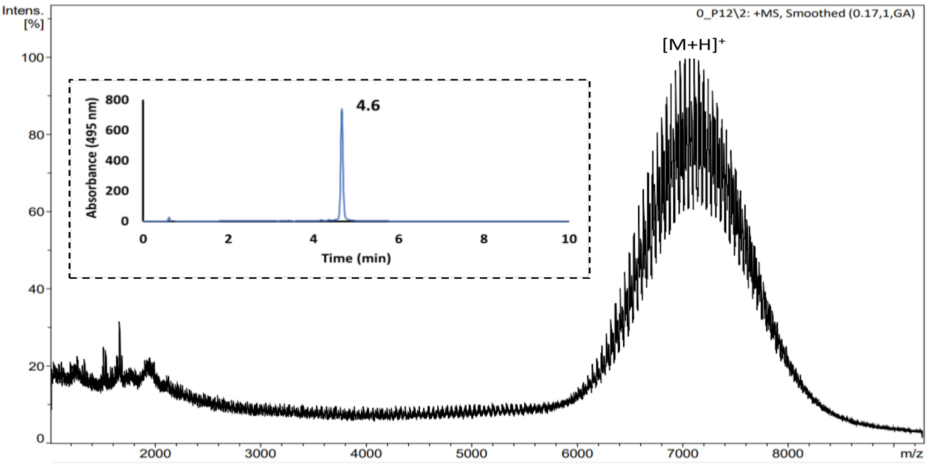

Figure 94 Pure probe **CatD-P3**. HPLC (495 nm) trace and MALDI-TOF MS spectrum.

Biological evaluation

For experiments using human neutrophil elastase, Cathepsin G or Proteinase 3 (Athenas Research and Technology or Enzo) were performed in 50 mM HEPES buffer, pH 7.4, 0.75 M NaCl, 0.05% Igepal CA-630 (v/v). Experiments using CatD or E were done in the reaction buffer with composition 50 mM NaOAc, pH 4.5 while for Cathepsin B, the reaction buffer was 50mM NaOAc, pH 5.5, EDTA 1 mM, 4 mM Cys. Activity of purchased proteases was tested when appropriate, using commercial substrates AAPV-pNA (for hNE and Proteinase 3), AAPF-pNA (for Cathepsin G), FR-pNA (Cathepsin B) following the protocols provided.

- **Plate reader experiments**

Probes were incubated with proteases in the appropriate reaction buffer in a final volume of 50 μL in a 96-well plate (Life Technologies). The time-dependent increase in fluorescence was monitored over 1.5 h using a fluorescence microplate reader (Biotek Synergy HT multi-mode reader) at 37°C. Buffer, enzymes and inhibitor where appropriate were incubated in the wells for 30 min at 37ºC before adding the probe. Readings were taken immediately after addition of the probe every 30 seconds and the plate was shaken for 1 to 10 seconds before the start of the readings. Data was normalised to buffer alone and the fold-change in signal (Relative Fluorescent Units) compared to enzyme-free controls was calculated. Data was plotted using Prism5 (GraphPad Software Inc., La Jolla, CA, USA).

- **Absorbance spectrum**

Probes were incubated in the appropriate in a final volume of 50 μL in a 96-well plate (Life Technologies) and absorbance was measured across the wavelength spectrum range 300 to 700 nm.

- **Fluorometric experiments**

Probes were incubated with or without protease, in reaction in a final volume of 150 μL in a quartz cuvette. Emission spectrum readings were recorded in a spectrofluorimetric range from 500 to 700 nm after 40 min incubation, with the appropriate excitation wavelength.

- **Effect of pH on fluorescence signal.**

A stock of cleaved and uncleaved probes was generated by incubating the probe with or without hNE respectively, in reaction buffer in a final volume of 200 µL for 1.5 h. Intact or cleaved probe solutions were added to different pH buffers (4, 5.5, 7.4 and 8.5).

- **Effect of different biological microenvironments on the fluorescence signal.**

The effect of different biological microenvironment on the fluorescence signal was evaluated by incubating intact cleaved probes in reaction buffer (control), complete cell media, 10% Fetal Bovine Serum (FBS) or HeLa cell lysate and incubated for 2 h at 37°C in a final volume of 50 µL. Fluorescence intensities were read using a fluorescence microplate reader.

Fort the HeLa cell lysate, trypsin (x 10, 1 mL) was added to a culture of adhered Hela cells 100% confluent cells and incubated for 5 min at 37°C, detachment of the cells was monitored by microscopic observations. Complete cell media was added (4 mL) and the resulting suspension transferred into a 50 mL falcon tube and spun down at 350 g for 5 min. The resulting pellet was washed with water three times. Cells were resuspended in sterile water (5 mL) and incubated for 30 min at 37°C. The resulting lysate was spun down at 13000 g for 10 min and the supernatant collected was used immediately.

- **Probe's kinetic parameters determination (K_m, k_{cat}, k_{cat}/K_m)**

General procedure: Proteases (hNE or CD) were added to solutions of increasing concentrations of the probes in a 96-well plate (n=3) and fluorescence intensity values monitored every 30 second or 1 min recorded on a Biotek Synergy HT multi-mode reader. Control samples (n=3) had the same composition but no enzyme, control RFU values were either subtracted or used as t = 0. The fluorescence intensity values were plotted against time (min) to obtain initial velocity values (V_o) on the first 5, 10 or 15 min of reaction (where best fit r^2>0.95). Velocity units (RFU/s) were converted to M/s by the factor[P]/RFU_{max}. Eadie-Hofstee and or Lineweaver Burk plots were built (when possible) to obtain values of K_m, V_{max} and k_{cat}/K_m.

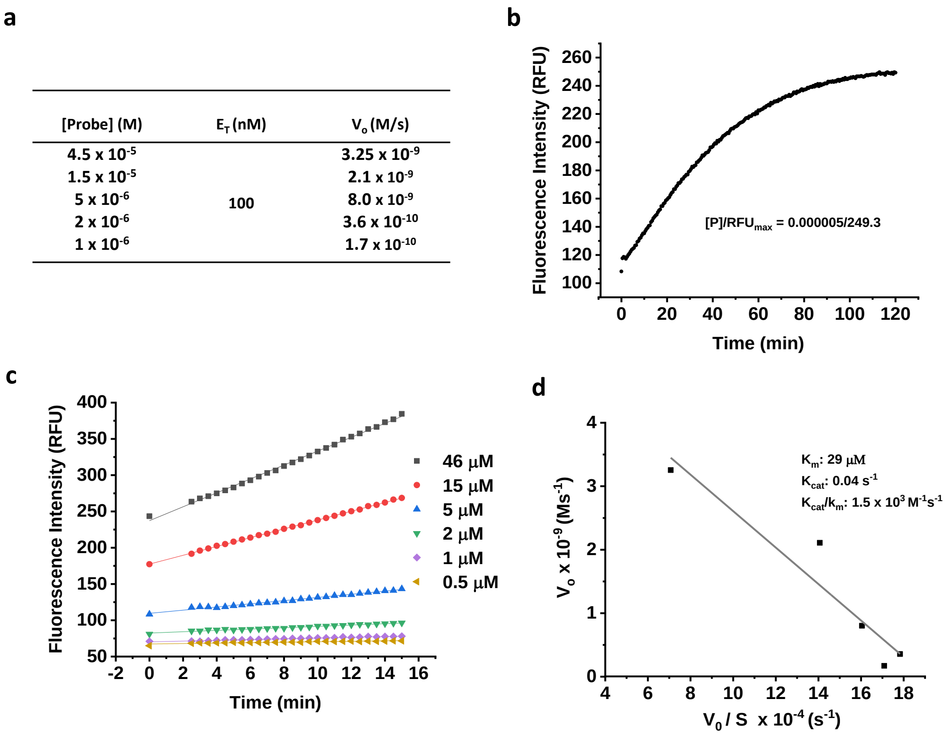

a

[Probe] (M)	E_T (nM)	V_o (M/s)
4.5×10^{-5}	100	3.25×10^{-9}
1.5×10^{-5}		2.1×10^{-9}
5×10^{-6}		8.0×10^{-9}
2×10^{-6}		3.6×10^{-10}
1×10^{-6}		1.7×10^{-10}

Figure 95. Kinetic parameter determination for linear NIR FRET probe **HNE-1F1Q** (**21**). **a)** the table shows the initial velocities obtained at increasing concentrations of probe at a constant concentration of enzyme of 100 nM. **b)** Normalisation factor ([P]/RFU_{max}) was obtained from the activation profile of the probe at 5 µM, where RFU_{max} was 249.3. **c)** Initial velocity plots at increasing concentrations of the **HNE-1F1Q**. **d)** Eadie-Hofstee plot provided a K_m value of 29 µM and a turnover number (k_{cat}) of 0.04 s^{-1}. Values of fluorescence were obtained with a Biotek Synergy HT multi-mode reader with 30 seconds intervals during 15 min, λ_{ex} = 640/10, λ_{em} = 680/20 (with a fluorescence gain of 50).

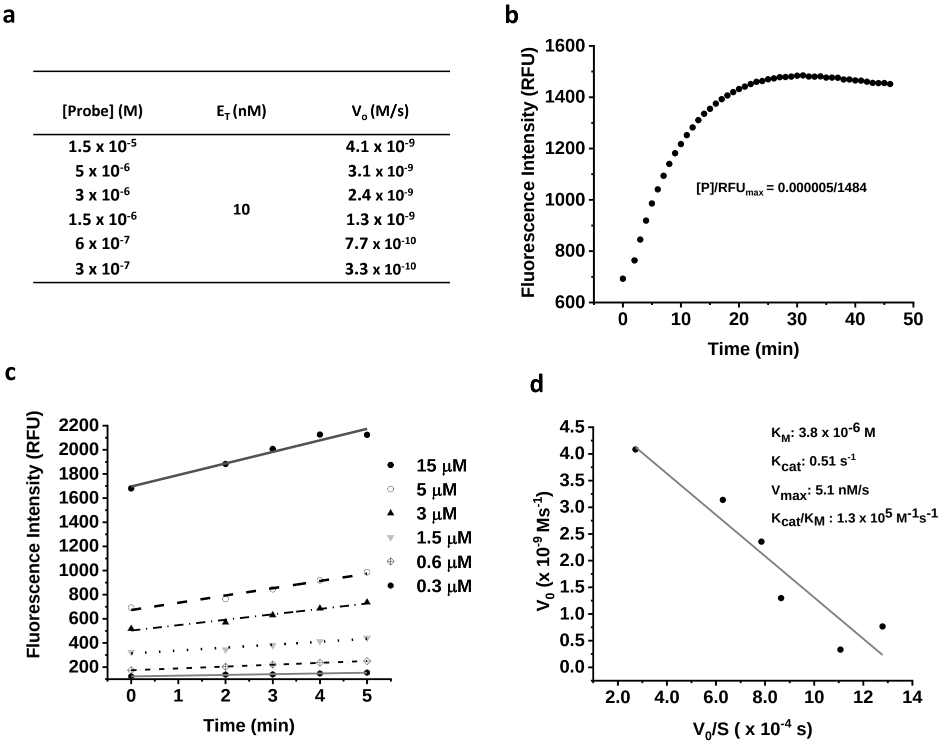

a

[Probe] (M)	E_T (nM)	V_o (M/s)
1.5×10^{-5}	10	4.1×10^{-9}
5×10^{-6}		3.1×10^{-9}
3×10^{-6}		2.4×10^{-9}
1.5×10^{-6}		1.3×10^{-9}
6×10^{-7}		7.7×10^{-10}
3×10^{-7}		3.3×10^{-10}

Figure 96. Kinetic parameter determination for NIR probe **HNE-3F0Q** (**28**). **a)** the table shows the initial velocities obtained at increasing concentrations of probe at a constant concentration of hNE at 10 nM. **b)** Normalisation factor ([P]/RFU_{max}) was obtained from the activation profile of the probe at 5 µM, where RFU_{max} was 1484. **c)** Initial velocity plots at increasing concentrations of the **HNE-3F0Q**. **d)** Eadie-Hofstee plot provided a K_m value of 3.8 µM and a turnover number (k_{cat}) of 0.51 s^{-1}. Values of fluorescence were obtained with a Biotek Synergy HT multi-mode reader with 1 min intervals during 5 min, λ_{ex} = 640/10, λ_{em} = 680/20 (with a fluorescence gain 50).

a

[Probe] (M)	E_T (nM)	V_o (M/s)
2×10^{-5}	100	1.5×10^{-8}
1×10^{-5}		1.4×10^{-8}
7×10^{-6}		1.2×10^{-8}
4×10^{-6}		9.2×10^{-9}
2×10^{-6}		5.4×10^{-9}
8×10^{-7}		2.4×10^{-9}

b

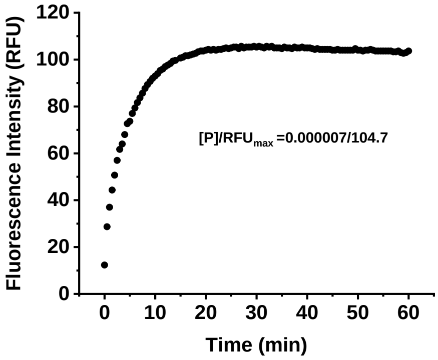

Figure 97. Kinetic parameter determination for NIR probe **HNE-3F1Q** (**29**). **a)** the table shows the initial velocities obtained at increasing concentrations of probe at a constant concentration of enzyme of 100 nM. **b)** Normalisation factor ([P]/RFU$_{max}$) was obtained from the activation profile of the probe at 7 µM, where RFU$_{max}$ was 1484. Values of fluorescence were obtained with a Biotek Synergy HT multi-mode reader, with 1 min intervals during 10 min and λ_{ex} = 640/10, λ_{em} = 680/20 (with a fluorescence gain 35).

a

	E_T (nM)	V_o (nM/s)
3.3×10^{-5}	10	4.4
2.5×10^{-5}		5.3
2.0×10^{-5}		5.3
1.5×10^{-5}		4.8
1.0×10^{-5}		4.1
5×10^{-6}		1.6
1.6×10^{-6}		0.3
8×10^{-7}		0.1

b

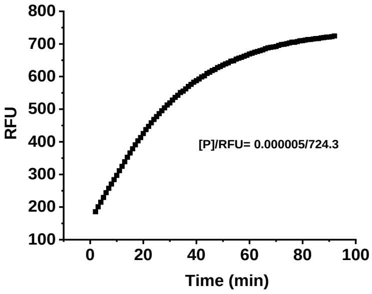

c

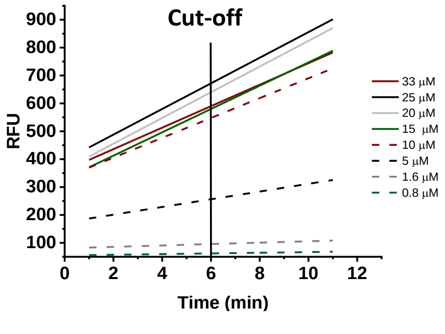

Figure 98 Kinetic parameter determination for linear **CatD-P3** probe (**36**). **a)** the table shows the initial velocities obtained at increasing concentrations of probe at a constant concentration of enzyme of 10 nM. **b)** Normalisation factor ([P]/RFU$_{max}$) was obtained from the activation profile of the probe at 5 µM, where RFU$_{max}$ was 1484. **c)** Initial velocity plots, fluorescence increase over the first ten min of reaction. Values of fluorescence were obtained with a Biotek Synergy HT multi-mode reader, with 1 min intervals during 5 min and λ_{ex} = 485/20, λ_{em} = 528/20 (with a fluorescence gain 50).

- **Calibration curves for concentration calculations**

NES (2) and **HNE-FQ (11)** contain three FRET-pairs (FAM/MR) per molecule. The absorbance spectrum of the probes and free fluorophores/quenchers showed comparable absorbance, with a maximum absorbance at 495 nm. A calibration curve using FAM or FAM/MR at 0 to 375 µM (n = 3) was built. When calculating the concentration, the obtained value from the calibration curve was divided by three to get the concentration of the probe (since three FRET-pairs are contained per probe).

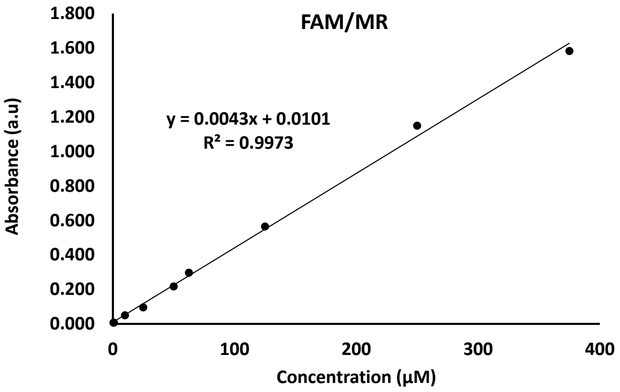

Figure 99 . Calibration curve for concentration calculation of probes **NES** (**2**) and **HNE-FQ** (**11**). Increasing concentrations of a 1:1 solution of 5-FAM/MR were plotted against absorbance. Solutions (50 µL) of the increasing concentrations were added to a 96-well plate and 490 nm absorbance values were obtained using a plate reader (Biotek HT Synergy). n=3.

The NIR probes **HNE-1F1Q** (**21**), **HNE-3F0Q** (**28**) and **HNE-3F1Q** (**29**) contain different rations of dyes per molecule. Comparable maximum absorbance was at 640 nm in probes and dyes. Calibration curves were built using a solution of sCy5 only, or a mixture of 1:1 or 3:1 sCy5/QSY21, in the range of concentrations from 0 to 150 µM (n = 3).

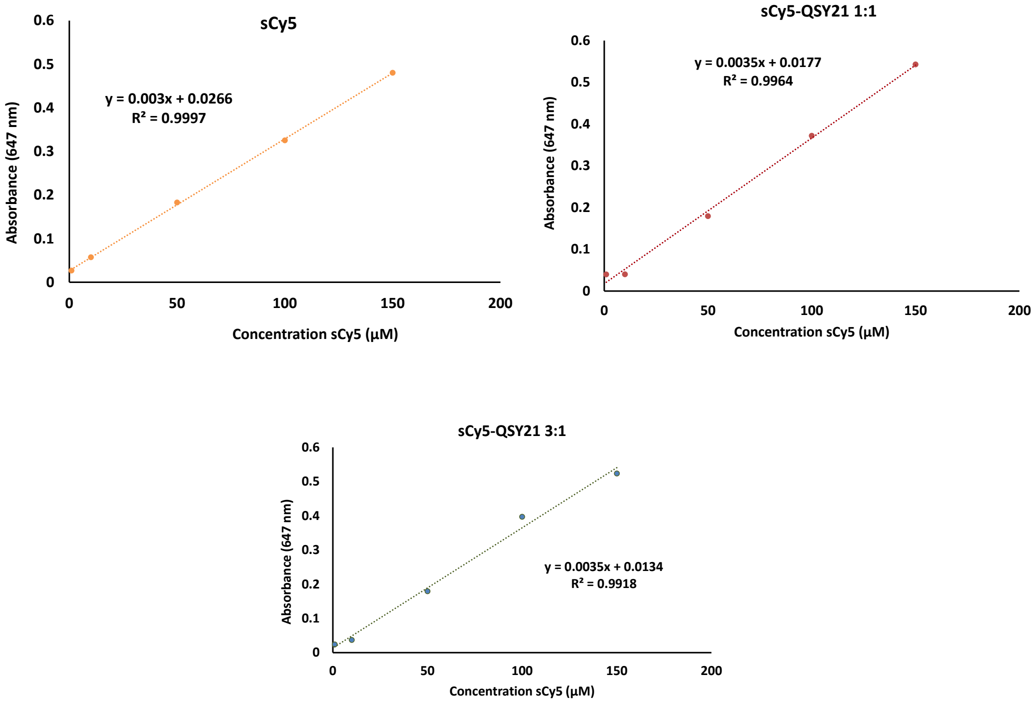

Figure 100 . Calibration curve for concentration calculation of probes **HNE-1F1Q** (**21**), **HNE-3F0Q** (**28**) and **HNE-3F1Q** (**29**). Increasing concentrations of a 1:0, 1:1 or 3:1 solution of sCy5/QSY21 were plotted against absorbance. Solutions (50 µL) of the increasing concentrations were added to a 96-well plate and 647 nm absorbance values were obtained using a plate reader (Biotek HT Synergy). n=3.

The corresponding BODIPY/MR calibration curve was built using a similar procedure, for calculation of concentrations in probes **CatD-P1** (**33**), **CatD-P2** (**34**) and **CatD-P3** (**36**).

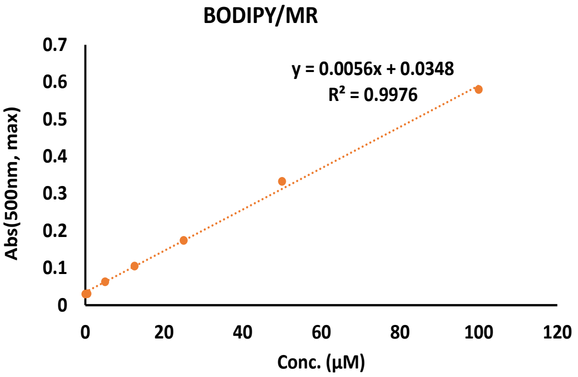

Figure 101 . Calibration curve for concentration calculation of probes **CatD-P1** (**33**), **CatD-P2** (**34**) and **CatD-P3** (**36**). Increasing concentrations of a 1:1 solution of BODIPY/MR were plotted against absorbance. Solutions (50 µL) of the increasing concentrations were added to a 96-well plate and 500 nm absorbance values were obtained using a plate reader (Biotek HT Synergy). n=3.

- **HL-60 differentiation and fluorescence microscopy of activated neutrophils and NETs - Gloria Garoffolo.**

HL-60 cells were grown in RPMI-1640 medium with 10% FBS at 37°C in a humidified atmosphere (95% air, 5% CO_2). Cells, at the density of 2 × 10^5/mL, were treated with all-trans retinoic acid (ATRA) (2 μM) for 5 days to induce neutrophil-like differentiation. Differentiation into neutrophils was assessed by an NBT assay. After 3 h of incubation, NBT (1 mM) was dissolved in 90% (v/v) DMSO, 0.1% (v/v) SDS and optical density (550 nm) was measured using an Infinite M200 PRO reader (Tecan). NET formation was monitored by SYTOX Orange quantification. In brief, after PMA treatment, cells were collected and incubated with micrococcal nuclease[4] (0.5 U/ml) for 10 min at 37°C. EDTA (5 mM) was used to stop the reaction. Finally, supernatants containing NET-associated DNA were incubated with SYTOX Orange (5 μM) for 15 min at room temperature and fluorescence intensities were read using Infinite M200 PRO reader. Imaging of HL-60 NETS was performed with a Zeiss LSM710 confocal microscope, using cells cultured into chambered glass coverslips.

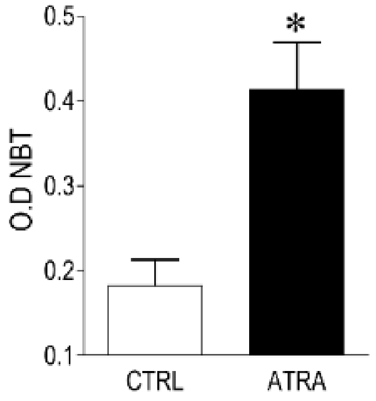

Figure 102 Quantification of HL-60 cell line differentiation into neutrophils and neutrophil activation as detected by nitro-blue tetrazolium (NBT, 1 mM) * indicates P < 0.05 by paired Student’s t-test (n=6 for NBT). Data by G. Garoffolo

- **Primary human neutrophils and fluorescence microscopy. IL-8 exposure and Ladaraxin - Gloria Garoffolo.**

Human neutrophils were isolated from whole blood, after platelet-rich plasma separation, by dextran sedimentation and Ficoll-Paque density gradient, as previously described. [202] Neutrophils were resuspended in RPMI-1640 medium with 10% FBS and seeded into µ-Slide 8 well (ibidi) coated with Poly-D-lysine (100 µg/mL). After 1 h adhesion at 37°C in a humidified atmosphere (95% air, 5% CO_2), cells were stimulated with IL-8 (100 ng/mL), with or without pre-treatment with Ladaraxin (160 µM) for 30 min, or PMA (25 nM) for 120 and 240 min in the presence of HNE-FQ probe (5 µM). After treatment, neutrophils were incubated with SYTOX Orange (5 µM) for 15 min and fixed with 4% PFA for fluorescence imaging. Image acquisition was performed with a Zeiss LSM710 confocal microscope, while fluorescent cells were quantified using and ImageJ software.

- **Flow cytometry method HL-60 differentiated neutrophils – Gloria Garoffolo**

Differentiated HL-60 cells were treated with phorbol 12-myristate 13-acetate (PMA; 100 nM) and the probe (5 µM) for 3 h. Cell suspensions were then incubated with an allophycocyanin-conjugated antibody against CD11b and the corresponding Isotype antibody (all from BD Bioscience) for 15 min at room temperature in the dark. Data were acquired with FACS Aria flow cytometry (BD Biosciences) and analysed with flow cytometric sorting Diva software (BD Biosciences).

- **Flow cytometry method primary human neutrophils – Giulia Rinaldi**

5×10^5 neutrophils were cultured in Eppendorf in RPMI + 5% FBS +/- stimulators and inhibitors for 30 min and/or 3 h and stained with HNE-FQ (5 µM). Cells were treated with phorbol 12-myristate 13-acetate (PMA; 10 nM), FMLf (10 µM) or calcium ionophore

A23187 (10 µM) for 3 h, in presence or absence of inhibitors Sivelestat (10 µM), DPI (10 µM) or Ro 31-8220 (1 µM). Cell suspensions were then incubated with a fluorochrome-conjugated antibody against Histone 1 (H1-DNA-Pacific Blue-H) or Histone 2 (H2A-647-H). Data were acquired with NovoCyte flow cytometer and analysed with NovoExpress software. A representative example of the relevant gating of neutrophils can be found below, corresponding to the gating used for flow cytometry analysis in Figure 103.

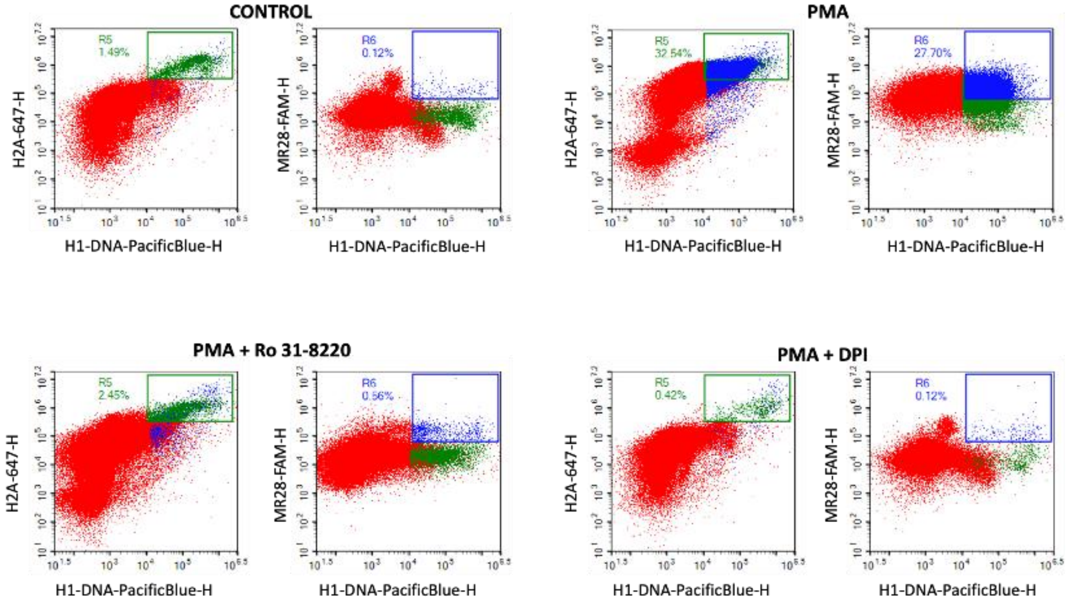

Figure 103. Representative flow cytometry gates on primary neutrophils incubated with the **HNE-FQ** (5 µM). Control: untreated neutrophils. PMA: neutrophils exposed to PMA (10 nM) for 3 h. PMA + Ro 31-88220: neutrophils exposed to PMA (10 nM) for 3 h and with inhibitor Ro 31-8220 (1 µM). PMA + DPI: neutrophils exposed to PMA (10 nM) for 3 h and with inhibitor DPI (10 µM). Giulia Rinaldi

- **Confocal images of NETosis in primary human neutrophils – Giulia Rinaldi**

Neutrophils from healthy volunteers were isolated using a protocol approved by the Accredited Medical Regional Ethics Committee (AMREC, reference number 15-HV-013)[5], (5×10^4) and **NES** (5 μM) or HNE-FQ (5 μM) were cultured in RPMI media with 5% FBS media and stimulated with PMA (10 nM), FMLf (10 μM) or calcium ionophore A23187 (10 µM) in monolayer in an ibidi μ-Slide 8 well (3 h, 37°C, 5% CO_2) or in chamber slides. After culture, media was removed and live cells were taken forward or fixed with 2% PFA (30 min, RT) and washed with PBS. Cells were then stained with SYTOX orange (1 μM) to stain extracellular DNA and Hoechst 33342 (100 nM) to stain the nuclei (30 min, RT, protected from light). The cells were imaged on a well plate or in the cell chamber, where deconstructed following manufacturer instructions and coverslip was mounted with ProLong Gold Antifade mounting media. NETs were imaged using Confocal Leica SP8 microscope or EVOS FL AUTO2 Cell Imaging System.

- **Fluorescence Lifetime measurements - Caitlin Tye and Mike Tanner**

A 485 nm pulsed laser diode (LDH-D-C-485 with PDL 800-D driver, PicoQuant, Berlin, Germany) capable of pulsed or continuous wave (CW) operation was used for excitation and coupled into the coupling-and-collection optical system based around a dichroic beam splitter (Thorlabs, Ely, UK). For the steady state setup, the laser was operated in CW mode, triggered to operate for 100 ms at 10 µW, and the spectra recorded with a simultaneously triggered commercial spectrometer (QE-Pro VIS, Ocean Optics now Ocean Insight, Largo, FL, USA). For time-resolved measurements the laser was operated in pulsed mode at 20 MHz repetition rate. The time-resolved spectrometer was based on a 256 × 1 pixels complementary metal–oxide–semiconductor (CMOS) single-photon avalanche diode (SPAD) line sensor which allows fast histogramming of arriving photons with time-correlation single photon counting (TCSPC) triggered by the laser source. The TCSPC capable CMOS SPAD line sensor detects single photons and generates histograms according to their arrival time for 256 pixels simultaneously, each correlated to a different wavelength. An average power of 2 µW was used with an integration time of 10 s to ensure a single-photon regime, avoiding pile-up effects, and recording sufficient signal (photons) for a quantitative analysis.

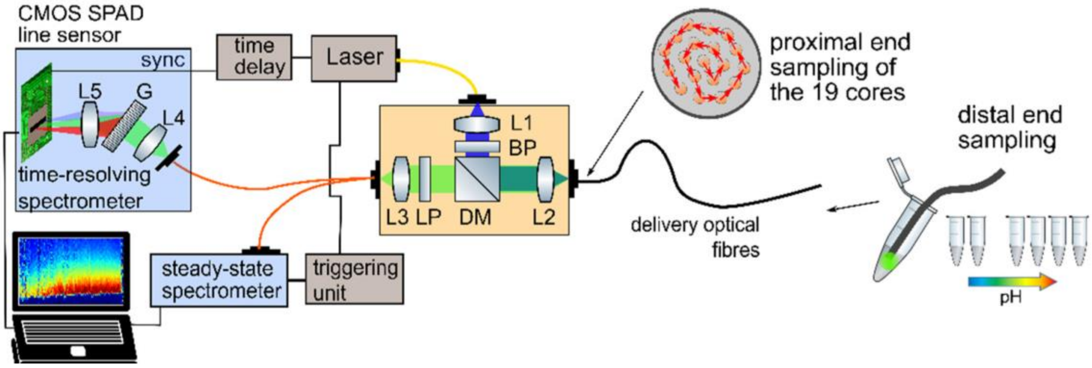

Figure 104. Scheme of work for fluorescence lifetime imaging.

- **Confocal images of human macrophages – Brian Mcugh**

Human Monocyte-derived macrophages (MDM) were matured in 24-well Corning tissue culture plates over 14 days from Peripheral Blood Mononuclear cells obtained from healthy volunteers under Ethic approval (CIR 20-HV-069). Following maturation, MDM were removed from wells by treatment with accutase (BioLegend) and re-seeded onto iBidi 8-well chamber slides for microscopy. MDM were challenged with *S. pneumoniae* strain D39 (MOI 10) for a total of 10 h, with external bacteria being removed by washing after 4 h of initial phagocytosis. After removal of external bacteria, Cat D probe was incubated with the cells at 10µM final concentration for the remaining time. At 10 h, MDM were fixed in 2% paraformaldehyde for 20 min at room temperature, followed by 3x washes in PBS. DAPI was added in the 2nd PBS wash for 10 min, at a concentration of 0.1µg/ml to counterstain cell nuclei. Slides were imaged on a Leica SP5 confocal microscope with a 63x objective, with Cat D probe imaged at 488nm wavelength and DAPI imaged at 405 nm.

References

1. M. R. Kanost and T. E. Clarke*, Compr. Mol Insect Sci*, 2005, 247-265.
2. I. Schechter, A. Berger, *Biochem Biophys Res Commun*, 1967, **27**, 157-162.
3. C. López-Otín and J. S. Bond, *J Biol Chem*, 2008, **283**, 30433-30437.
4. J. S. Bond, *J Biol Chem*, 2019, **294**, 1643-1651.
5. K. M. Heutinck, I. J. M. ten Berge, C. E. Hack, J. Hamann and A. T. Rowshani, *Mol Immunol*, 2010, **47**, 1943-1955.
6. S. Hodge, G. Hodge, J. Nairn, M. Holmes and P. N. Reynolds, *COPD*, 2006, **3**, 179-187.
7. B. Li, C. Hartono, R. Ding, V. K. Sharma, R. Ramaswamy, B. Qian, D. Serur, J. Mouradian, J. E. Schwartz and M. Suthanthiran, *N. Engl. J. Med*, 2001, **344**, 947-954.
8. I. Berdowska, *Clin. Chim. Acta*, 2004, **342**, 41-69.
9. B. M. Dunn, *Encyclop Biol Chem* , 2013, 137-140.
10. A. K. Tandon, G. M. Clark, G. C. Chamness, J. M. Chirgwin and W. L. McGuire, *N. Engl. J. Med*, 1990, **322**, 297-302.
11. R. Vassar, *Adv. Drug Deliv. Rev.*, 2002, **54**, 1589-1602.
12. A. Brik and C.-H. Wong, *Org. Biomol. Chem,* 2003, **1**, 5-14.
13. A. Scorilas, S. Fotiou, E. Tsiambas, J. Yotis, F. Kotsiandri, M. Sameni, B. F. Sloane and M. Talieri, *Biol Chem*, 2002, **383**, 1297-1303.
14. M. Warwas, H. Haczyńska, J. Gerber and M. Nowak, *Eur J Clin Chem Clin Biochem*, 1997, **35**, 301-304.
15. Y. Ikeda, T. Ikata, T. Mishiro, S. Nakano, M. Ikebe and S. Yasuoka, *J Med Invest*, 2000, **47**, 61-75.
16. T. Chai, M. Tian, X. Yang, Z. Qiu, X. Lin and L. Chen, *Front Cardiovasc Med*, 2022, **9**, 762468.
17. K. Bollavaram, T. H. Leeman, M. W. Lee, A. Kulkarni, S. G. Upshaw, J. Yang, H. Song and M. O. Platt, *Protein Science*, 2021, **30**, 1131-1143.
18. K. Tanaka, *Proc Jpn Acad Ser B Phys Biol Sci*, 2009, **85**, 12-36.
19. O. Drews and H. Taegtmeyer, *Antioxid Redox Signal*, 2014, **21**, 2322-2343.
20. Q. Zheng, T. Huang, L. Zhang, Y. Zhou, H. Luo, H. Xu and X. Wang, *Front. Aging Neurosci*, 2016, **8**.
21. P. T. Elkington, C. M. O'Kane and J. S. Friedland, *Clin Exp Immunol*, 2005, **142**, 12-20.
22. N. L. Webster and S. M. Crowe, *J. Leukoc. Biol*, 2006, **80**, 1052-1066.
23. J. Chen, W. Xu, Y. Chen, X. Xie, Y. Zhang, C. Ma, Q. Yang, Y. Han, C. Zhu, Y. Xiong, K. Wu, F. Liu, Y. Liu and J. Wu, *J Virol*, 2017, **91**.
24. D. Leung, G. Abbenante and D. P. Fairlie, *Journal of Medicinal Chemistry*, 2000, **43**, 305-341.
25. *BMJ*, 2012, **345**, e5129.
26. P. Moreau, P. G. Richardson, M. Cavo, R. Z. Orlowski, J. F. San Miguel, A. Palumbo and J.-L. Harousseau, *Blood*, 2012, **120**, 947-959.
27. P. Verdecchia, G. Reboldi, F. Angeli, R. Gattobigio, M. Bentivoglio, L. Thijs, J. A. Staessen and C. Porcellati, *Hypertension*, 2005, **46**, 386-392.

28. C. Junren, X. Xiaofang, Z. Huiqiong, L. Gangmin, Y. Yanpeng, C. Xiaoyu, G. Yuqing, L. Yanan, Z. Yue, P. Fu and P. Cheng, *Front Pharmacol*, 2021, **12**.
29. S. Keynan, N. M. Hooper, A. Felici, G. Amicosante and A. J. Turner, *Antimicrob Agents Chemother*, 1995, **39**, 1629-1631.
30. Z. Lv, Y. Chu and Y. Wang, *HIV AIDS (Auckl)*, 2015, **7**, 95-104.
31. C. Li, Y. Liu, S. Wu, G. Han, J. Tu, G. Dong, N. Liu and C. Sheng, *Eur. J. Med. Chem.*, 2020, **201**, 112515.
32. E. Burchacka, P. Pięta and A. Łupicka-Słowik, *Biomed & Pharmacot*, 2022, **146**, 112523.
33. M. J. Whitley, D. M. Cardona, A. L. Lazarides, I. Spasojevic, J. M. Ferrer, J. Cahill, C.-L. Lee, M. Snuderl, D. G. Blazer, E. S. Hwang, R. A. Greenup, P. J. Mosca, J. K. Mito, K. C. Cuneo, N. A. Larrier, E. K. O'Reilly, R. F. Riedel, W. C. Eward, D. B. Strasfeld, D. Fukumura, R. K. Jain, W. D. Lee, L. G. Griffith, M. G. Bawendi, D. G. Kirsch and B. E. Brigman, *Sci Trans Med*, 2016, **8**, 320ra324.
34. A. Megia-Fernandez, B. Mills, C. Michels, S. V. Chankeshwara, N. Krstajic, C. Haslett, K. Dhaliwal and M. Bradley, *Org Biomol Chem*, 2018, **16**, 8056-8063.
35. D. Kato, K. M. Boatright, A. B. Berger, T. Nazif, G. Blum, C. Ryan, K. A. H. Chehade, G. S. Salvesen and M. Bogyo, *Nat Chem Bio*, 2005, **1**, 33-38.
36. A.-C. Schulz-Fincke, A. S. Tikhomirov, A. Braune, T. Girbl, E. Gilberg, J. Bajorath, M. Blaut, S. Nourshargh and M. Gütschow, *Biochemistry*, 2018, **57**, 742-752.
37. N. Jugniot, P. Voisin, A. Bentaher and P. Mellet, *Cont Med Mol Imaging*, 2019, **2019**, 7417192.
38. C. T. N. Pham, *Nat Rev Immunol*, 2006, **6**, 541-550.
39. T. N. Mayadas, X. Cullere and C. A. Lowell, *Annu Rev Pathol*, 2014, **9**, 181-218.
40. E. Kolaczkowska and P. Kubes, *Nat Rev Immunol*, 2013, **13**, 159-175.
41. V. Brinkmann, U. Reichard, C. Goosmann, B. Fauler, Y. Uhlemann, D. S. Weiss, Y. Weinrauch and A. Zychlinsky, *Science*, 2004, **303**, 1532-1535.
42. G. Schonrich and M. J. Raftery, *Front Immunol*, 2016, **7**, 366.
43. E. Guiducci, C. Lemberg, N. Küng, E. Schraner, A. P. A. Theocharides and S. LeibundGut-Landmann, *Front Immunol*, 2018, **9**.
44. V. Papayannopoulos, *Nat Rev Immunol*, 2018, **18**, 134-147.
45. K. Kawabata, T. Hagio and S. Matsuoka, *Eur. J. Pharmacology*, 2002, **451**, 1-10.
46. A. Caudrillier, K. Kessenbrock, B. M. Gilliss, J. X. Nguyen, M. B. Marques, M. Monestier, P. Toy, Z. Werb and M. R. Looney, *J Clin Invest*, 2012, **122**, 2661-2671.
47. Y. Zuo, S. Yalavarthi, H. Shi, K. Gockman, M. Zuo, J. A. Madison, C. Blair, A. Weber, B. J. Barnes, M. Egeblad, R. J. Woods, Y. Kanthi and J. S. Knight, *JCI Insight*, 2020, **5**, e138999.
48. H. Ohbayashi, *Expert Opin. Investig. Drugs*, 2002, **11**, 965-980.
49. I. Bendib, L. de Chaisemartin, V. Granger, F. Schlemmer, B. Maitre, S. Hüe, M. Surenaud, A. Beldi-Ferchiou, G. Carteaux, K. Razazi, S. Chollet-Martin, A. Mekontso Dessap and N. de Prost, *Anesthesiology*, 2019, **130**, 581-591.
50. B. J. Barnes, J. M. Adrover, A. Baxter-Stoltzfus, A. Borczuk, J. Cools-Lartigue, J. M. Crawford, J. Dassler-Plenker, P. Guerci, C. Huynh, J. S. Knight, M. Loda, M. R. Looney, F. McAllister, R. Rayes, S. Renaud, S. Rousseau, S. Salvatore, R. E. Schwartz, J. D. Spicer, C. C. Yost, A. Weber, Y. Zuo and M. Egeblad, *J Exp Med*, 2020, **217**, e20200652

51. Y. Zuo, S. Yalavarthi,H. Shi,K. Gockman,M. Zuo, J.A. Madison, C. Blair A. Weber, B.J. Barnes, M. Egeblad, R. J. Woods,Y. Kanthi ,J. S. Knight, *JCI Insight*, 2020; **5**(11), e138999.
52. S. Matsumoto, S. Hidaka, K. Goto, S. Hagiwara, C. Shingu, H. Iwasaka and T. Noguchi, *J Anesth*, 2009, **23**, 288-291.
53. A. Sahebnasagh, F. Saghafi, M. Safdari, M. Khataminia, A. Sadremomtaz, Z. Talaei, H. Rezai Ghaleno, M. Bagheri, S. Habtemariam and R. Avan, *J Clin Pharm Ther*, 2020, 1515-1519
54. B. McDonald, R. Urrutia, Bryan G. Yipp, Craig N. Jenne and P. Kubes, *Cell Host Microbe*, 2012, **12**, 324-333.
55. T. O. Hirche, R. Benabid, G. Deslee, S. Gangloff, S. Achilefu, M. Guenounou, F. Lebargy, R. E. Hancock and A. Belaaouaj, *J Immunol*, 2008, **181**, 4945-4954.
56. V. Papayannopoulos, K. D. Metzler, A. Hakkim and A. Zychlinsky, *J Cell Biol*, 2010, **191**, 677-691.
57. Z. Fu, M. Thorpe, S. Akula, G. Chahal and L. T. Hellman, *Front Immunol*, 2018, **9**.
58. W. Bode, E. Meyer, Jr. and J. C. Powers, *Biochemistry*, 1989, **28**, 1951-1963.
59. C. Kuhn and R. M. Senior, *Lung*, 1978, **155**, 185-197.
60. J. Kuźniar, T. J. Kuźniar, Z. Marchewka, J. Lembas-Bogaczyk, J. Rabczyński, W. Kopeć and M. Klinger, *Scand J Urol Nephrol*, 2007, **41**, 527-534.
61. E. O. Adeyemi, R. G. Hull, V. S. Chadwick, G. R. V. Hughes and H. J. F. Hodgson, *Rheumatol Int*, 1986, **6**, 57-60.
62. B. Korkmaz, M. S. Horwitz, D. E. Jenne and F. Gauthier, *Pharmacol Rev*, 2010, **62**, 726-759.
63. P. Kasperkiewicz, Y. Altman, M. D'Angelo, G. S. Salvesen and M. Drag, *J Am Chem Soc*, 2017, **139**, 10115-10125.
64. P. Kasperkiewicz, M. Poreba, S. J. Snipas, H. Parker, C. C. Winterbourn, G. S. Salvesen and M. Drag, *Proc Natl Acad Sci U S A*, 2014, **111**, 2518-2523.
65. S. Kossodo, J. Zhang, K. Groves, G. J. Cuneo, E. Handy, J. Morin, J. Delaney, W. Yared, M. Rajopadhye and J. D. Peterson, *Int J Mol Imag*, 2011, **2011**, 581406.
66. B. Korkmaz, S. Attucci, M. A. Juliano, T. Kalupov, M. L. Jourdan, L. Juliano and F. Gauthier, *Nat Protoc*, 2008, **3**, 991-1000.
67. T. Kalupov, M. Brillard-Bourdet, S. Dade, H. Serrano, J. Wartelle, N. Guyot, L. Juliano, T. Moreau, A. Belaaouaj and F. Gauthier, *J Biol Chem*, 2009, **284**, 34084-34091.
68. J. M. Ellard, T. Zollitsch, W. J. Cummins, A. L. Hamilton and M. Bradley, *Angew Chem Int Ed Engl*, 2002, **41**, 3233-3236.
69. M. Ternon, J. J. Díaz-Mochón, A. Belsom and M. Bradley, *Tetrahedron*, 2004, **60**, 8721-8728.
70. M. Ternon, J. J. Diaz-Mochon, A. Belsom and M. Bradley, *Tetrahedron*, 2004, **60**, 8721-8728.
71. N. Avlonitis, M. Debunne, T. Aslam, N. McDonald, C. Haslett, K. Dhaliwal and M. Bradley, *Org Biomol Chem*, 2013, **11**, 4414-4418.
72. A. Megia-Fernandez, A. Marshall, A. R. Akram, B. Mills, S. V. Chankeshwara, E. Scholefield, A. Miele, B. C. McGorum, C. Michaels, N. Knighton, T. Vercauteren, F. Lacombe, V. Dentan, A. M. Bruce, J. Mair, R. Hitchcock, N. Hirani, C. Haslett, M. Bradley and K. Dhaliwal, *BME Front*, 2021, **2021**, 1-11.

73. N. Avlonitis, M. Debunne, T. Aslam, N. McDonald, C. Haslett, K. Dhaliwal and M. Bradley, *Org Biomol Chem*, 2013, **11**, 4414-4418.
74. T. H. Craven, T. Walton, A. R. Akram, E. Scholefield, N. McDonald, A. D. L. Marshall, D. C. Humphries, B. Mills, T. A. Campbell, A. Bruce, J. Mair, J. W. Dear, D. E. Newby, A. T. Hill, T. S. Walsh, C. Haslett and K. Dhaliwal, *Sci Rep*, 2021, **11**, 1-14.
75. B. Korkmaz, S. Attucci, T. Moreau, E. Godat, L. Juliano and F. Gauthier, *American Journal of Resp Cell Mol Bio*, 2004, **30**, 801-807.
76. P. W. D. Scislowski and E. J. Davis, *FEBS Lett,* 1987, **224**, 177-181.
77. T. H. Craven, N. Avlonitis, N. McDonald, T. Walton, E. Scholefield, A. R. Akram, T. S. Walsh, C. Haslett, M. Bradley and K. Dhaliwal, *Sci Rep*, 2018, **8**, 13490.
78. S. Lebreton, S. E. How, M. Buchholz, B. E. Yingyongnarongkul and M. Bradley, *Tetrahedron*, 2003, **59**, 3945-3953.
79. G. R. N. a. X. Lin, *Macromolecules,* 1991, **24**, 1443-1444
80. E. Atherton, H. Fox, D. Harkiss, C. J. Logan, R. C. Sheppard and B. J. Williams, *J Chem Soc Chem Comm*, 1978, 537-539
81. *United States Patent* 9549997*,* 2017.
82. R. Spijkerman, L. Hesselink, C. Bertinetto, C. C. Bongers, F. Hietbrink, N. Vrisekoop, L. P. Leenen, M. T. Hopman, J. J. Jansen and L. Koenderman, *J Leukoc Biol*, 2021, **109**, 833-842.
83. G. T. Nguyen, E. R. Green and J. Mecsas, *Front Cell Infect Microbiol*, 2017, **7**, 373.
84. M. R. Rios, G. Garoffolo, G. Rinaldi, A. Megia-Fernandez, S. Ferrari, C. T. Robb, A. G. Rossi, M. Pesce and M. Bradley, *Chem Commun* , 2021, **57**, 97-100.
85. L. B., J. J.Dıaz-Mochon, and Mark Bradley, *Org Lett*, 2004, **6**, 1127-1129.
86. M. M. Martin and L. Lindqvist, *J Lumin*, 1975, **10**, 381-390.
87. M. J. Doughty, *Ophthalmic Physiol Opt*, 2010, **30**, 167-174.
88. F. Le Guern, V. Mussard, A. Gaucher, M. Rottman and D. Prim, *Int J Mol Sci*, 2020, **2**, 9217
89. J. B. Birks, *J Res Natl Bur Stand A Phys Chem*, 1976, **80a**, 389-399.
90. A. G. Mahomed and R. Anderson, *Inflammation*, 2000, **24**, 559-569.
91. R. Tasseff, H. A. Jensen, J. Congleton, D. Dai, K. V. Rogers, A. Sagar, R. P. Bunaciu, A. Yen and J. D. Varner, *Sci Rep*, 2017, **7**, 14327.
92. H. S. Choi, J. W. Kim, Y. N. Cha and C. Kim, *J Immunoassay Immunochem*, 2006, **27**, 31-44.
93. H. Takei, A. Araki, H. Watanabe, A. Ichinose and F. Sendo, *J Leuk Bio*, 1996, **59**, 229-240.
94. M. R. Rios, G. Garoffolo, G. Rinaldi, A. Megia-Fernandez, S. Ferrari, C. T. Robb, A. G. Rossi, M. Pesce and M. Bradley, *Chem Commun*, 2020, **57**, 97-100.
95. T. Hoppenbrouwers, A. S. A. Autar, A. R. Sultan, T. E. Abraham, W. A. van Cappellen, A. B. Houtsmuller, W. J. B. van Wamel, H. M. M. van Beusekom, J. W. van Neck and M. P. M. de Maat, *PLoS One*, 2017, **12**, e0176472.
96. R. S. Keshari, A. Verma, M. K. Barthwal and M. Dikshit, *J Cell Biochem*, 2013, **114**, 532-540.
97. T. Kawakami, J. He, H. Morita, K. Yokoyama, H. Kaji, C. Tanaka, S. Suemori, K. Tohyama and Y. Tohyama, *PLoS One*, 2014, **9**, e84704.
98. I. Neeli and M. Radic, *Arthritis Res Ther*, 2012, **14**, 115.

99. E. Glowacka, M. Banasik, P. Lewkowicz and H. Tchorzewski, *Scand. J. Immunol*, 2002, **55**, 210-217.
100. A. Ma, L. Zhang, X. Ye, J. Chen, J. Yu, L. Zhuang, C. Weng, F. Petersen, Z. Wang and X. Yu, *Front Immunol*, 2021, **12**.
101. A. Teijeira, S. Garasa, M. D. C. Ochoa, A. Cirella, I. Olivera, J. Glez-Vaz, M. P. Andueza, I. Migueliz, M. Alvarez, M. E. Rodríguez-Ruiz, A. Rouzaut, P. Berraondo, M. F. Sanmamed, J. L. Perez Gracia and I. Melero, *Eur J Immunol*, 2021, **51**, 2274-2280.
102. X.-F. Zhang, J. Zhang and L. Liu, *J Fluoresc*, 2014, **24**, 819-826.
103. G. Hong, A. L. Antaris and H. Dai, *Nat Biomed Eng*, 2017, **1**, 0010.
104. R. R. Zhang, A. B. Schroeder, J. J. Grudzinski, E. L. Rosenthal, J. M. Warram, A. N. Pinchuk, K. W. Eliceiri, J. S. Kuo and J. P. Weichert, *Nat Rev Clin Oncol*, 2017, **14**, 347-364.
105. G. Keiser, *Biophotonics* 2016.
106. J. V. Frangioni, *Curr Opin Chem Biol*, 2003, **7**, 626-634.
107. M. O. Hisataka Kobayashi, Raphael Alford, Peter L. Choyke, and Yasuteru Urano, *Chem. Rev.*, 2010, **110**, 2620–2640.
108. M. B. Carlo Pellicciari, *Histochem*, 2017.
109. S. M. A. Ali, I. Khan, D. Khurram and I. Kozak, *JAMA Ophthalmol*, 2018, **136**, 593-594.
110. J. Pan, H. Deng, S. Hu, C. Xia, Y. Chen, J. Wang and Y. Wang, *World J Surg Oncol*, 2020, **18**, 96.
111. M. Watanabe, A. Tsunoda, K. Narita, M. Kusano and M. Miwa, *Surg Today*, 2009, **39**, 214-218.
112. F. P. Verbeek, J. R. van der Vorst, B. E. Schaafsma, R. J. Swijnenburg, K. N. Gaarenstroom, H. W. Elzevier, C. J. van de Velde, J. V. Frangioni and A. L. Vahrmeijer, *J Urol*, 2013, **190**, 574-579.
113. C. Zhang, D. Jiang, B. Huang, C. Wang, L. Zhao, X. Xie, Z. Zhang, K. Wang, J. Tian and Y. Luo, *Technol Cancer Res Treat*, 2019, **18**, 1533033819894331.
114. C. G. Hadjipanayis and W. Stummer, *J Neurooncol*, 2019, **141**, 479-486.
115. A. Hosmann, M. Millesi, L. I. Wadiura, B. Kiesel, P. A. Mercea, M. Mischkulnig, M. Borkovec, J. Furtner, T. Roetzer, S. Wolfsberger, J. J. Phillips, A. S. Berghoff, S. Hervey-Jumper, M. S. Berger and G. Widhalm, *Cancers*, 2021, **13**, 2540
116. A. D. Newton, J. D. Predina, L. G. Frenzel-Sulyok, P. S. Low, S. Singhal and R. E. Roses, *Molecular Imag Bio*, 2021, **23**, 11-17.
117. G. R. Armstrong, M. I. Khot, C. Portal, N. P. West, S. L. Perry, T. I. Maisey, J. P. Tiernan, T. A. Hughes, D. J. Tolan and D. G. Jayne, *Surg Oncol*, 2022, **40**, 101679.
118. P. K. C. Jonker, M. J. H. Metman, L. H. J. Sondorp, M. S. Sywak, A. J. Gill, L. Jansen, T. P. Links, P. J. van Diest, T. M. van Ginhoven, C. W. G. M. Löwik, A. H. Nguyen, R. P. Coppes, D. J. Robinson, G. M. van Dam, B. M. van Hemel, R. S. N. Fehrmann and S. Kruijff, *Eur J Nuc Med Mol Imag*, 2022, 3557-3570.
119. J. I. Scott, Q. Deng and M. Vendrell, *ACS Chem. Biol*, 2021, 16, 8, 1304–1317.
120. F. V. Suurs, S.-Q. Qiu, J. J. Yim, C. P. Schröder, H. Timmer-Bosscha, E. S. Bensen, J. T. Santini, E. G. E. de Vries, M. Bogyo and G. M. van Dam, *EJNMMI Research*, 2020, **10**, 111.

121. B. L. Smith, M. A. Gadd, C. R. Lanahan, U. Rai, R. Tang, T. Rice-Stitt, A. L. Merrill, D. B. Strasfeld, J. M. Ferrer, E. F. Brachtel and M. C. Specht, *Breast Cancer Res Treat*, 2018, **171**, 413-420.
122. T. Cao, Z. Teng, L. Zheng, J. Qian, H. Ma, J. Wang, W. Qin and H. Guo, *Anal Chim Acta*, 2020, **1127**, 295-302.
123. B. M. Anderson, D. P. Poole, L. Aurelio, G. Z. Ng, M. Fleischmann, P. Kasperkiewicz, C. Morissette, M. Drag, I. R. van Driel, B. L. Schmidt, S. J. Vanner, N. W. Bunnett and L. E. Edgington-Mitchell, *Sci Rep*, 2019, **9**, 13295.
124. A. C. Schulz-Fincke, M. Blaut, A. Braune and M. Gutschow, *ACS Med Chem Lett*, 2018, **9**, 345-350.
125. N. G. Medeiros, C. A. Braga, V. S. Câmara, R. C. Duarte and F. S. Rodembusch, *Asian J Org Chem*, 2022, **11**, e202200095.
126. M. Lopalco, E. N. Koini, J. K. Cho and M. Bradley, *Org Bio Chem*, 2009, **7**, 856-859.
127. N. Norouzi, PhD Thesis, Univeristy of Edinburgh, 2014.
128. M. K. Johansson and R. M. Cook, *Chemistry*, 2003, **9**, 3466-3471.
129. L. Le Reste, J. Hohlbein, K. Gryte and A. N. Kapanidis, *Biophys J*, 2012, **102**, 2658-2668.
130. A. Chevalier, P.-Y. Renard and A. Romieu, *Tetrahedron Lett,* 2014, **55**, 6759-6763.
131. A. Chevalier, C. Massif, P.-Y. Renard and A. Romieu, *Chem Eur J*, 2013, **19**, 1686-1699.
132. A. Chevalier, P.-Y. Renard and A. Romieu, *Tetrahedron Lett,* 2014, **55**, 6764-6768.
133. S. Takahashi, W. Piao, Y. Matsumura, T. Komatsu, T. Ueno, T. Terai, T. Kamachi, M. Kohno, T. Nagano and K. Hanaoka, *J Am Chem Soc*, 2012, **134**, 19588-19591.
134. B. Korkmaz, S. Attucci, E. Hazouard, M. Ferrandière, M. L. Jourdan, M. Brillard-Bourdet, L. Juliano and F. Gauthier, *J Bio Chem*, 2002, **277**, 39074-39081.
135. C. W. Tornøe, C. Christensen and M. Meldal, *J Org Chem*, 2002, **67**, 3057-3064.
136. V. V. Rostovtsev, L. G. Green, V. V. Fokin and K. B. Sharpless, *Ang Chem Int Ed*, 2002, **41**, 2596-2599.
137. S. Neumann, M. Biewend, S. Rana and W. H. Binder, *Macromol Rapid Commun*, 2020, **41**, 1900359.
138. M. Arseneault, C. Wafer and J. F. Morin, *Molecules*, 2015, **20**, 9263-9294.
139. L. A. Carpino, D. Sadat-Aalaee, H. G. Chao and R. H. DeSelms, *J Am Chem Soc*, 1990, **112**, 9651-9652.
140. X. Li, *Chem Asian J*, 2011, **6**, 2606-2616.
141. K. E. Beatty, F. Xie, Q. Wang and D. A. Tirrell, *J Am Chem Soc*, 2005, **127**, 14150-14151.
142. J. Gierlich, K. Gutsmiedl, P. M. E. Gramlich, A. Schmidt, G. A. Burley and T. Carell, *Chem Eur J*, 2007, **13**, 9486-9494.
143. A. E. Speers and B. F. Cravatt, *Chem Bio*, 2004, **11**, 535-546.
144. V. Hong, S. I. Presolski, C. Ma and M. G. Finn, *Ang Chem Int Ed*, 2009, **48**, 9879-9883.
145. K. Agarwal, A. Sharma and G. Talukder, *Chem. Biol. Interact*, 1989, **69**, 1-16.
146. H. Miyamoto, C. Sakumoto, E. Takekoshi, Y. Maeda, N. Hiramoto, T. Itoh and Y. Kato, *Org Process Res Develop*, 2015, **19**, 1054-1061.
147. T. Yamada, Y. Kobayashi, N. Ito, T. Ichikawa, K. Park, K. Kunishima, S. Ueda, M. Mizuno, T. Adachi, Y. Sawama, Y. Monguchi and H. Sajiki, *ACS Omega*, 2019, **4**, 10243-10251.

148. P. Italiani and D. Boraschi, *Front Immunol*, 2014, **5**.
149. N. Fujiwara and K. Kobayashi, *Curr drug targets Inflamm Allerg*, 2005, **4**, 281-286.
150. M. A. Bewley, H. M. Marriott, C. Tulone, S. E. Francis, T. J. Mitchell, R. C. Read, B. Chain, G. Kroemer, M. K. Whyte and D. H. Dockrell, *PLoS Pathog*, 2011, **7**, e1001262.
151. D. M. Mosser, K. Hamidzadeh and R. Goncalves, *Cellul Mol Immunol*, 2021, **18**, 579-587.
152. T. A. Wynn and K. M. Vannella, *Immunity*, 2016, **44**, 450-462.
153. W. Zhai, F. Wu, Y. Zhang, Y. Fu and Z. Liu, *Int J Mol Sci*, 2019, **20**, 340.
154. R. S. Flannagan, B. Heit and D. E. Heinrichs, *Cell Microbiol*, 2016, **18**, 514-535.
155. M. Kubica, K. Guzik, J. Koziel, M. Zarebski, W. Richter, B. Gajkowska, A. Golda, A. Maciag-Gudowska, K. Brix, L. Shaw, T. Foster and J. Potempa, *PLOS One*, 2008, **3**, e1409.
156. D. H. Dockrell and J. S. Brown, *Streptococcus Pneumoniae*, 2015, 401-422
157. B. A. Wuerth, J. P. Bonnewell, T. L. Wiemken and F. W. Arnold, *Emerg Infect Dis*, 2016, **22**, 1624-1627.
158. J. Yuste, M. Botto, J. C. Paton, D. W. Holden and J. S. Brown, *J Immunol*, 2005, **175**, 1813-1819.
159. S. V. Gulnik, L. I. Suvorov, P. Majer, J. Collins, B. P. Kane, D. G. Johnson and J. W. Erickson, *FEBS Lett,* 1997, **413**, 379-384.
160. J. A. Preston, M. A. Bewley, H. M. Marriott, A. McGarry Houghton, M. Mohasin, J. Jubrail, L. Morris, Y. L. Stephenson, S. Cross, D. R. Greaves, R. W. Craig, N. van Rooijen, C. D. Bingle, R. C. Read, T. J. Mitchell, M. K. B. Whyte, S. D. Shapiro and D. H. Dockrell, *Am J Respir Crit Care Med*, 2019, **200**, 84-97.
161. J. A. Preston, M. A. Bewley, H. M. Marriott, A. McGarry Houghton, M. Mohasin, J. Jubrail, L. Morris, Y. L. Stephenson, S. Cross, D. R. Greaves, R. W. Craig, N. van Rooijen, C. D. Bingle, R. C. Read, T. J. Mitchell, M. K. B. Whyte, S. D. Shapiro and D. H. Dockrell, *Am J Respir Crit*, 2019, **200**, 84-97.
162. A. Minarowska, M. Gacko, A. Karwowska and Ł. Minarowski, *Folia Histochem*, 2008, **46**, 23-38.
163. D. Piwnica, P. Touraine, I. Struman, S. Tabruyn, G. Bolbach, C. Clapp, J. A. Martial, P. A. Kelly and V. Goffin, *Mol Endocrinol*, 2004, **18**, 2522-2542.
164. B. Christensen, L. Schack, E. Kläning and E. S. Sørensen, *J Biol Chem*, 2010, **285**, 7929-7937.
165. V. Laurent-Matha, P. F. Huesgen, O. Masson, D. Derocq, C. Prébois, M. Gary-Bobo, F. Lecaille, B. Rebière, G. Meurice, C. Oréar, R. E. Hollingsworth, M. Abrahamson, G. Lalmanach, C. M. Overall and E. Liaudet-Coopman, *Faseb J*, 2012, **26**, 5172-5181.
166. M. Wolf, I. Clark-Lewis, C. Buri, H. Langen, M. Lis and L. Mazzucchelli, *Am J Pathol,* 2003, **162**, 1183-1190.
167. G. E. Conner, in *Handbook of Proteolytic Enzymes (Second Edition)*, 2004, 43-52.
168. R. T. Dean and A. J. Barrett, *Essays Biochem*, 1976, **12**, 1-40.
169. C. G. Knight and A. J. Barrett, *Biochem J*, 1976, **155**, 117-125.
170. P. Saftig, M. Hetman, W. Schmahl, K. Weber, L. Heine, H. Mossmann, A. Köster, B. Hess, M. Evers and K. von Figura, *EMBO Journal*, 1995, **14**, 3599-3608.
171. R. Steinfeld, K. Reinhardt, K. Schreiber, M. Hillebrand, R. Kraetzner, W. Brück, P. Saftig and J. Gärtner, *Am J Hum Genet*, 2006, **78**, 988-998.

172. C. Zhang, M. Zhang and S. Song, *Cancer Lett*, 2018, **438**, 105-115.
173. M. Glondu, E. Liaudet-Coopman, D. Derocq, N. Platet, H. Rochefort and M. Garcia, *Oncogene*, 2002, **21**, 5127-5134.
174. M. Hausmann, F. Obermeier, K. Schreiter, T. Spottl, W. Falk, J. Schölmerich, H. Herfarth, P. Saftig and G. Rogler, *Clin Exp Immunol*, 2004, **136**, 157-167.
175. Y. Yasuda, T. Kageyama, A. Akamine, M. Shibata, E. Kominami, Y. Uchiyama and K. Yamamoto, *J Biochem*, 1999, **125**, 1137-1143.
176. D. C. Pimenta, A. Oliveira, M. A. Juliano and L. Juliano, *BBA Protein Struct Mol Enzym*, 2001, **1544**, 113-122.
177. P. Majer, J. R. Collins, S. V. Gulnik and J. W. Erickson, *Prot Sci*, 1997, **6**, 1458-1466.
178. P. E. Scarborough and B. M. Dunn, *Protein Engineering, Design and Selection*, 1994, **7**, 495-502.
179. B. M. Beyer and B. M. Dunn, *Prot Sci*, 1998, **7**, 88-95.
180. D. Arnold, W. Keilholz, H. Schild, T. Dumrese, S. Stevanović and H. G. Rammensee, *Eur J Biochem*, 1997, **249**, 171-179.
181. S. R. Chinni, C. Gerçel-Taylor, G. E. Conner and D. D. Taylor, *Cancer Immunol Immunother*, 1998, **46**, 48-54.
182. P. E. Scarborough, B. M. Dunn, K. Guruprasad, C. Topham, T. L. Blundell, G. R. Richo and G. E. Conner, *Prot Sci*, 1993, **2**, 264-276.
183. I. L. H. Ong and K. L. Yang, *Analyst*, 2017, **142**, 1867-1881.
184. R. Ta, M. Suchy, J. H. Tam, A. X. Li, F. S. Martinez-Santiesteban, T. J. Scholl, R. H. Hudson, R. Bartha and S. H. Pasternak, *Contrast Media Mol Imaging*, 2013, **8**, 127-139.
185. C.-S. Chen, W.-N. U. Chen, M. Zhou, S. Arttamangkul and R. P. Haugland, *J Biochem Biophys Methods* 2000, **42**, 137–151.
186. I. Y. Filippova, E. N. Lysogorskaya, V. V. Anisimova, L. I. Suvorov, E. S. Oksenoit and V. M. Stepanov, *Anal Biochem*, 1996, **234**, 113-118.
187. A. O. Daniel C. Pimenta, Maria A. Juliano, Luiz Juliano, *Biochim Biophys Acta* 2001, **1544**, 113-122.
188. A. Cui, X. Peng, J. Fan, X. Chen, Y. Wu and B. Guo, *J Photochem Photobiol Chem*, 2007, **186**, 85-92.
189. M. M. Martin and L. Lindqvist, *J Luminesc*, 1975, **10**, 381—390.
190. M. R. Rios, G. Garoffolo, G. Rinaldi, A. Megia-Fernandez, S. Ferrari, C. T. Robb, A. G. Rossi, M. Pesce and M. Bradley, *Chem Commun*, 2021, **57**, 97-100.
191. M. Wang, M. G. H. Vicente, D. Mason and P. Bobadova-Parvanova, *ACS Omega*, 2018, **3**, 5502-5510.
192. J. M. H. Cheng, S. H. Chee, Y. Dölen, M. Verdoes, M. S. M. Timmer and B. L. Stocker, *Carbohydrate Res*, 2019, **486**, 107840.
193. G. Molineux, *Pharmacotherapy*, 2003, **23**, 3S-8S.
194. M. Meldal and C. W. Tornøe, *Chem Rev*, 2008, **108**, 2952-3015.
195. B. Korkmaz, T. Moreau and F. Gauthier, *Biochimie*, 2008, **90**, 227-242.
196. T. K. Yoshiyuki Yasuda, Akifumi Akamine, Masahiro Shibata, Eiki Kominami, Yasuo Uchiyama and Kenji Yamamoto, *J Biochem Biophys Methods*, 1999, **125**, 1137-1143.
197. W. K. Daniele Arnold, Hansjorg Schild, Than Dumrese, Stefan Stevanovic, Hans-Georg Rammensee, *Eur. J. Biochem.* , 1997, **249**, 171-179.
198. S. ÇetİndERE, S. YeŞİlot and A. KiliÇ, *Turk J, Chem*, 2020, **44**, 1-14.

199. B. P. Ross, R. A. Falconer and I. Thot, *Molbank*, 2008, **2008**, M566.

200. B. W. Bycroft, W. C. Chan, S. R. Chhabra and N. D. Hone, *J Chem Soc Chem Commun,* 1993, 778-779

201. C. C.-P. Yoann M. Chabre, Virginie Placide, Tze Chieh Shiao, and Rene Roy, *J. Org. Chem.*, 2008, **73**, 5602–5605.

202. Y. S. Tan and Y. L. Lei, *Methods Mol Biol*, 2019, **1960**, 93-99.

Appendix – probes characterisation

NES^1

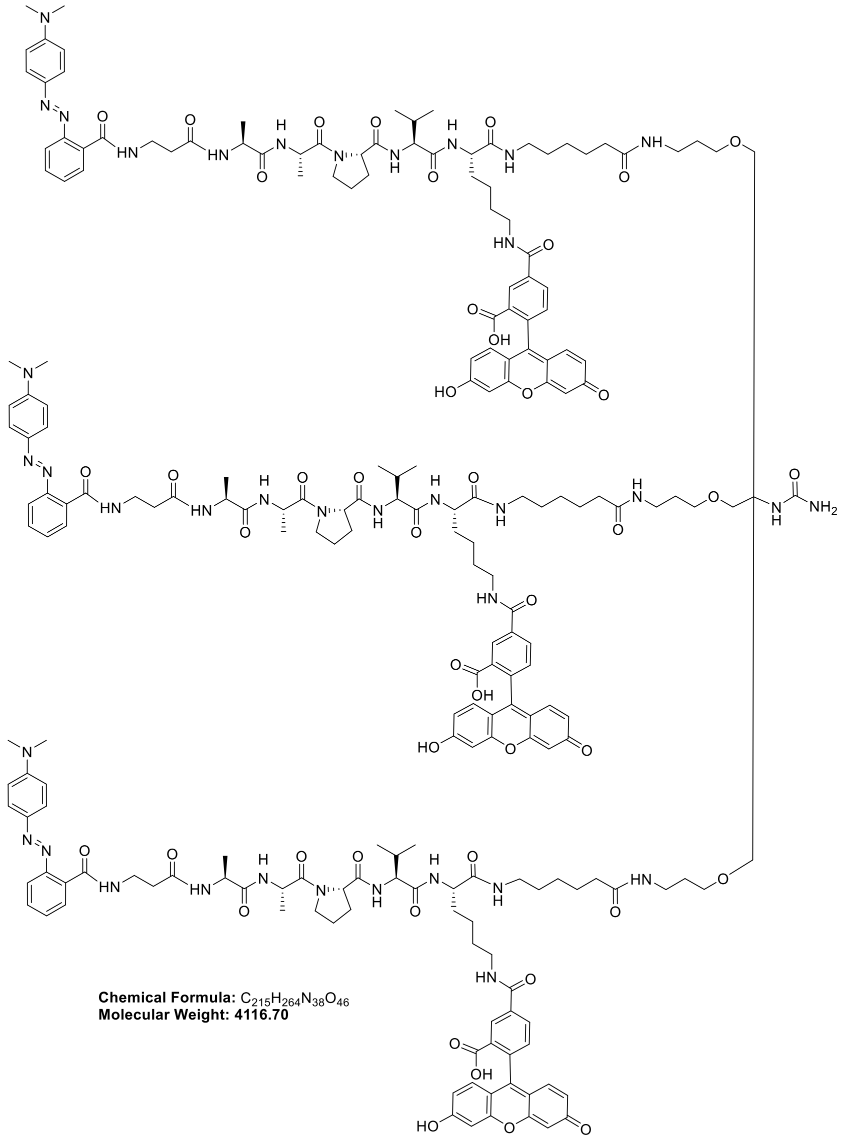

Chemical Formula: $C_{215}H_{264}N_{38}O_{46}$
Molecular Weight: 4116.70

HPLC-UV (Method A): r$_t$: 5.3 min

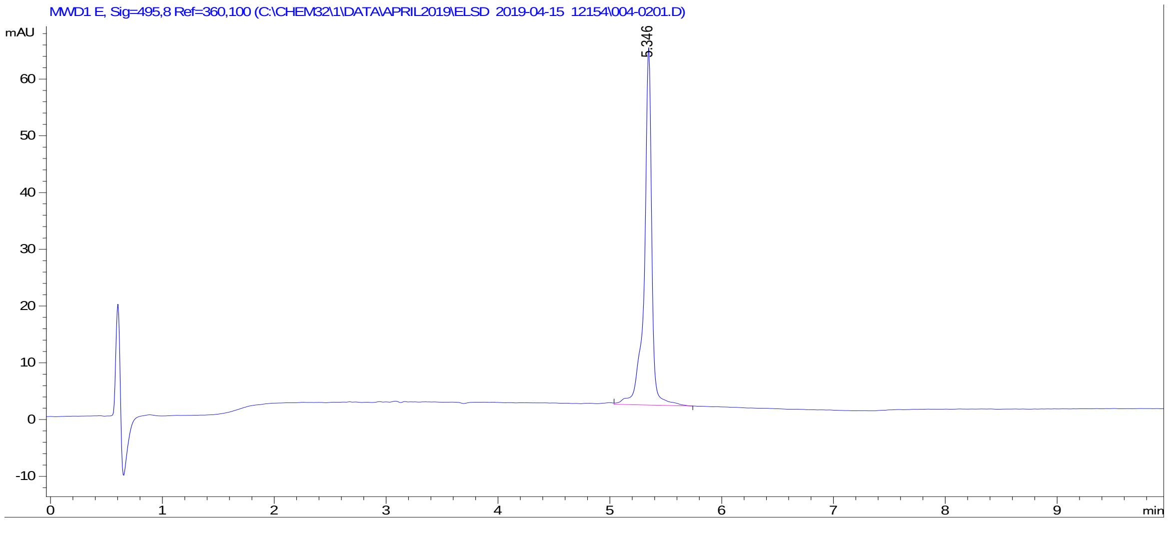

LC-MS : Found m/z $[M+4H]^{4+}$ 1029.9

FT-HRMS: m/z for $C_{215}H_{264}N_{38}O_{46}^{+4}$ $[M+4H]^{+4}$ Exp: 1029.99539 Fnd: 1029.99596

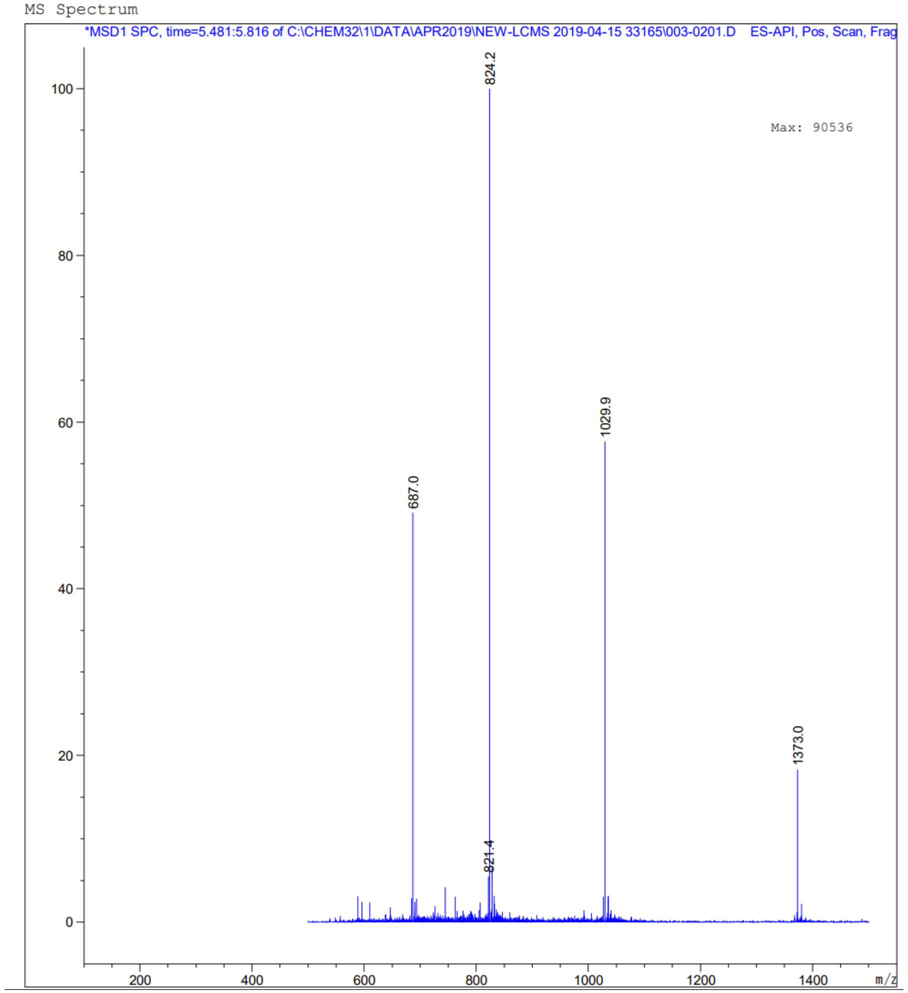

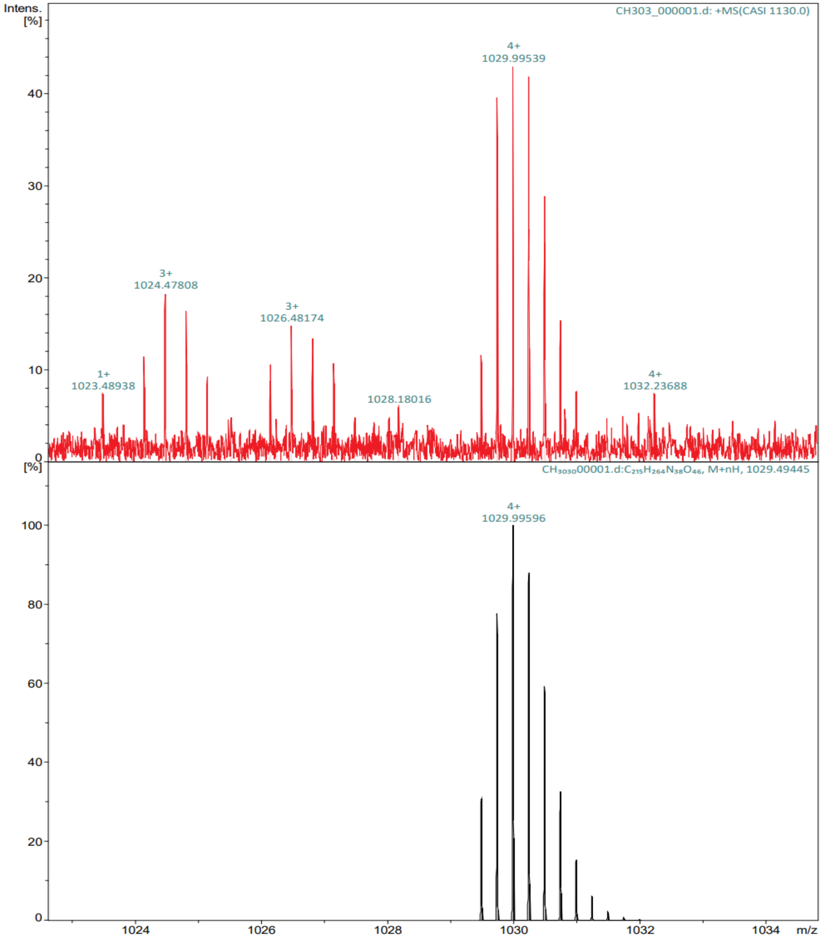

HNE-FQ^2

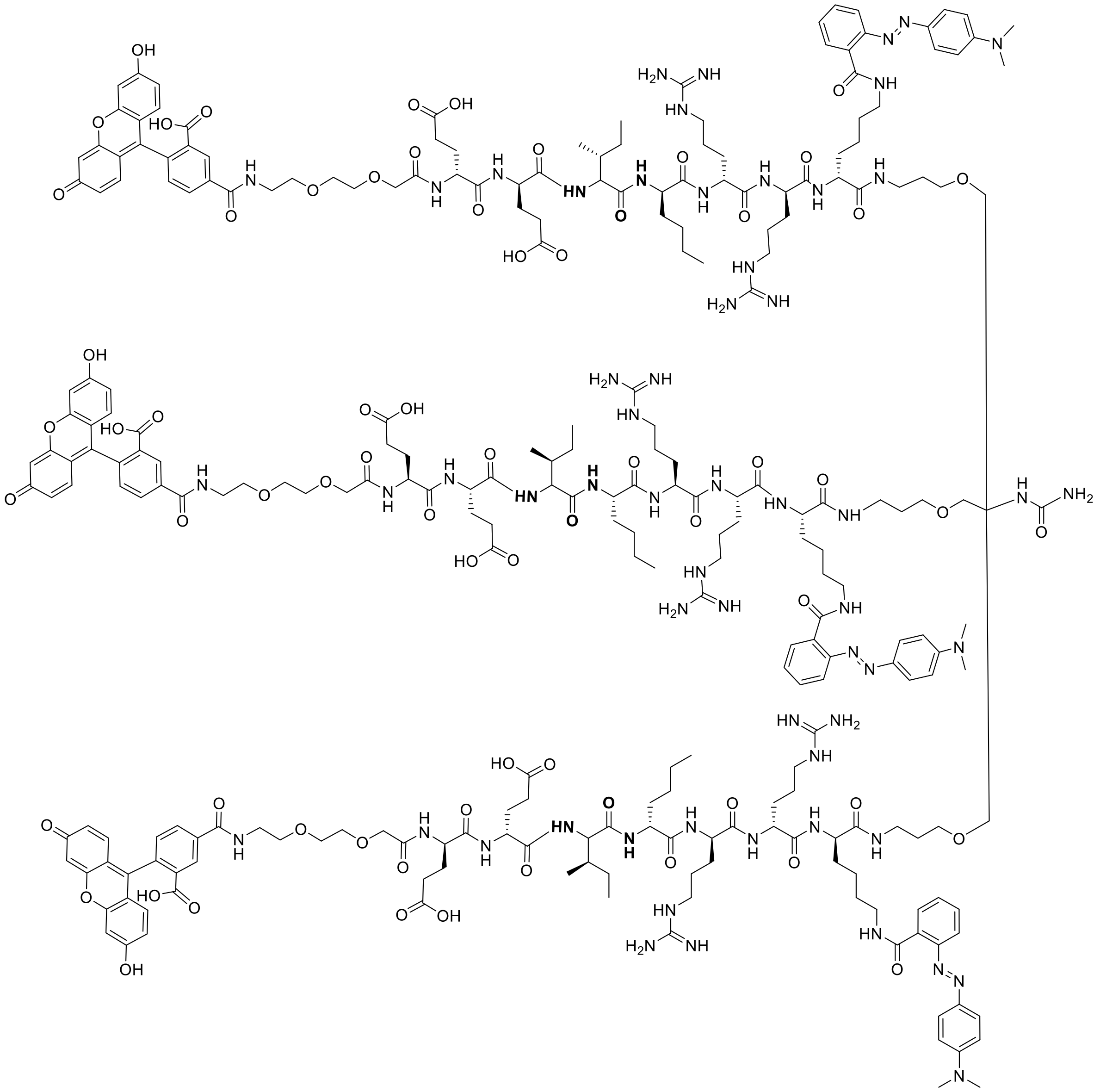

Chemical Formula: $C_{260}H_{351}N_{59}O_{67}$
Molecular Weight: 5375.01

FT-HRMS: Calculated m/z for $C_{260}H_{357}N_{59}O_{67}^{+6}$ [M+H]$^{+6}$ Expected: 896.77327 Found: 896.77101;

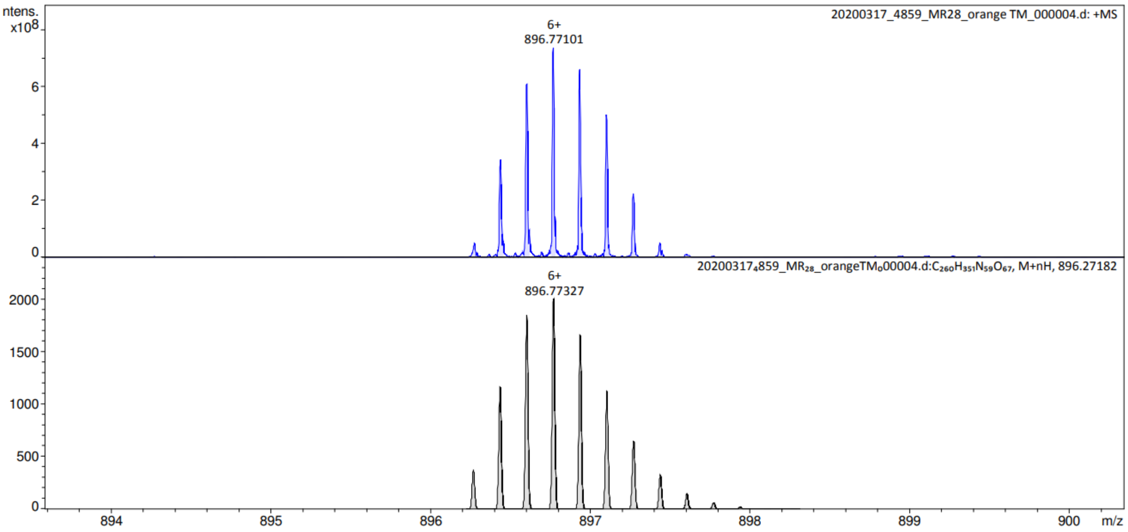

HPLC-UV (Method A, ELSD and 495 nm): r_t : 3.9 min

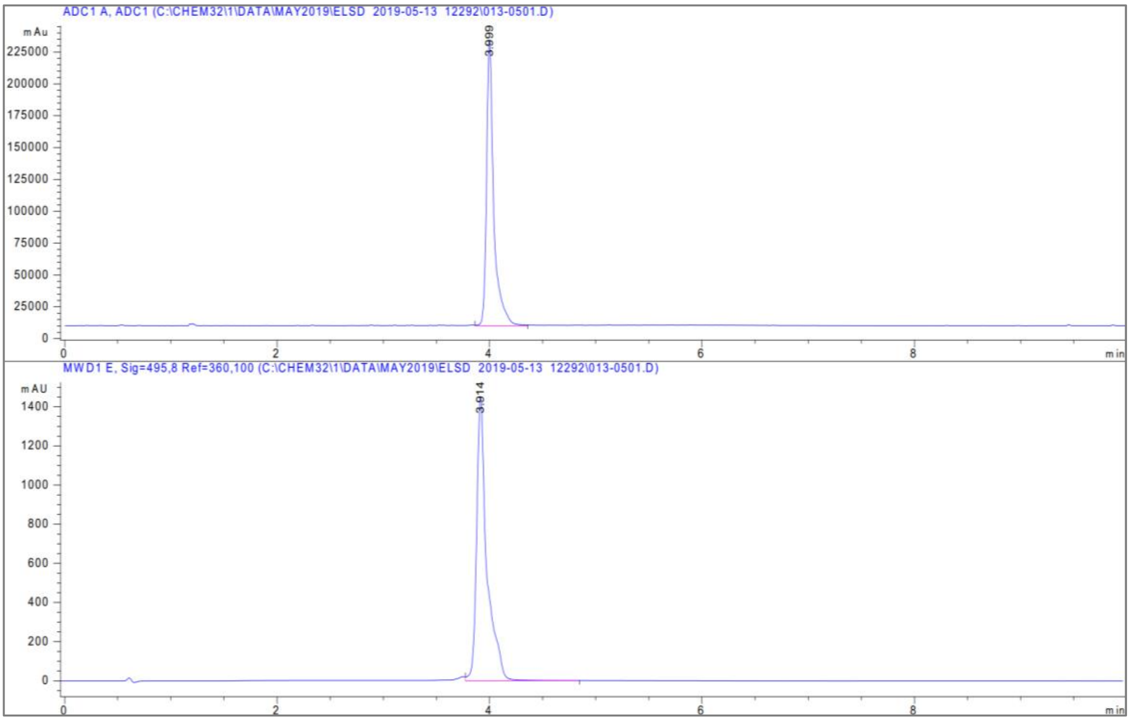

HNE-1F1Q

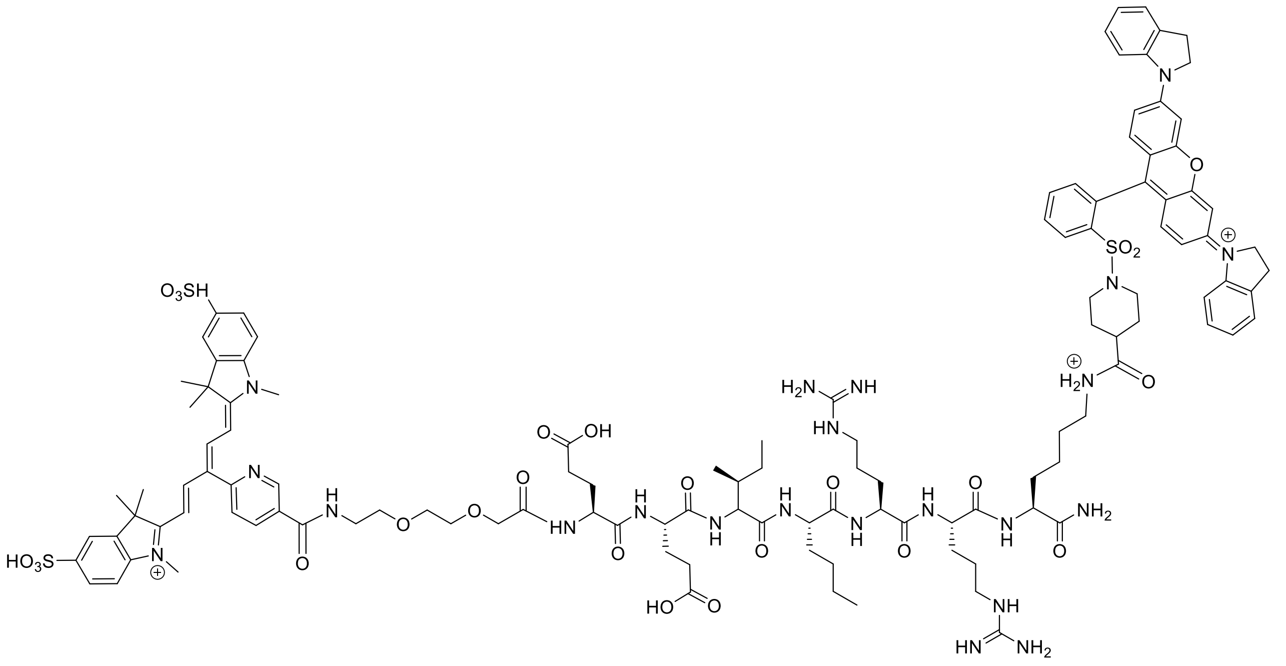

Chemical Formula: $C_{120}H_{153}N_{22}O_{25}S_3{}^{3+}$
Molecular Weight: 2399.85

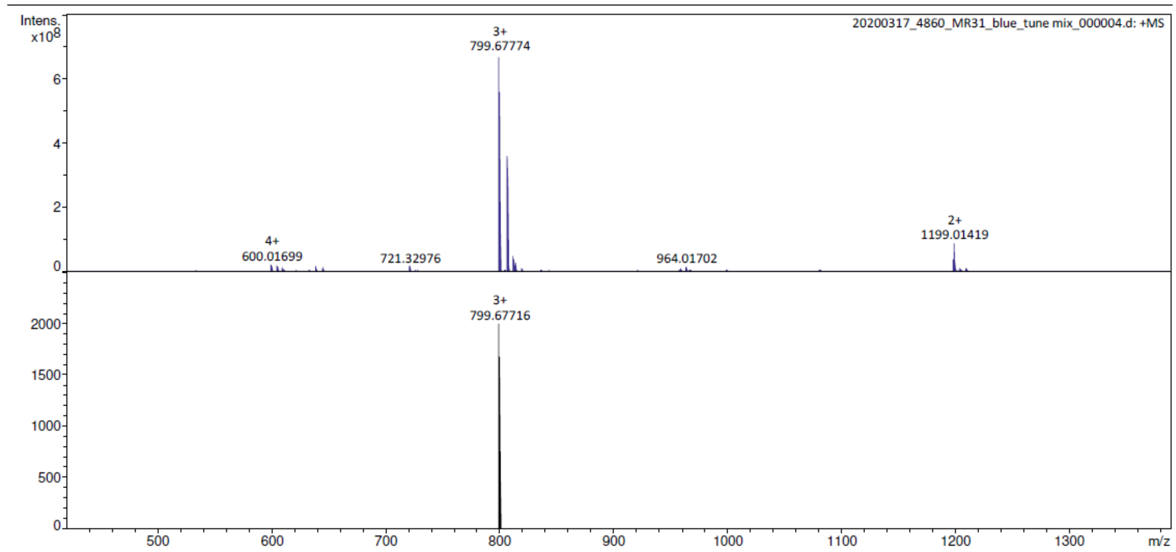

FT-HRMS: Calculated m/z for $C_{120}H_{153}N_{22}O_{26}S_3{}^{+3}$ $[M+H]^{+3}$ Expected: 799.67716 Found: 799.67774;

LC-MS : Found m/z $[M+H]^{3+}$ 800.0

HPLC-UV (Method A, 650 nm): r_t 3.6 min

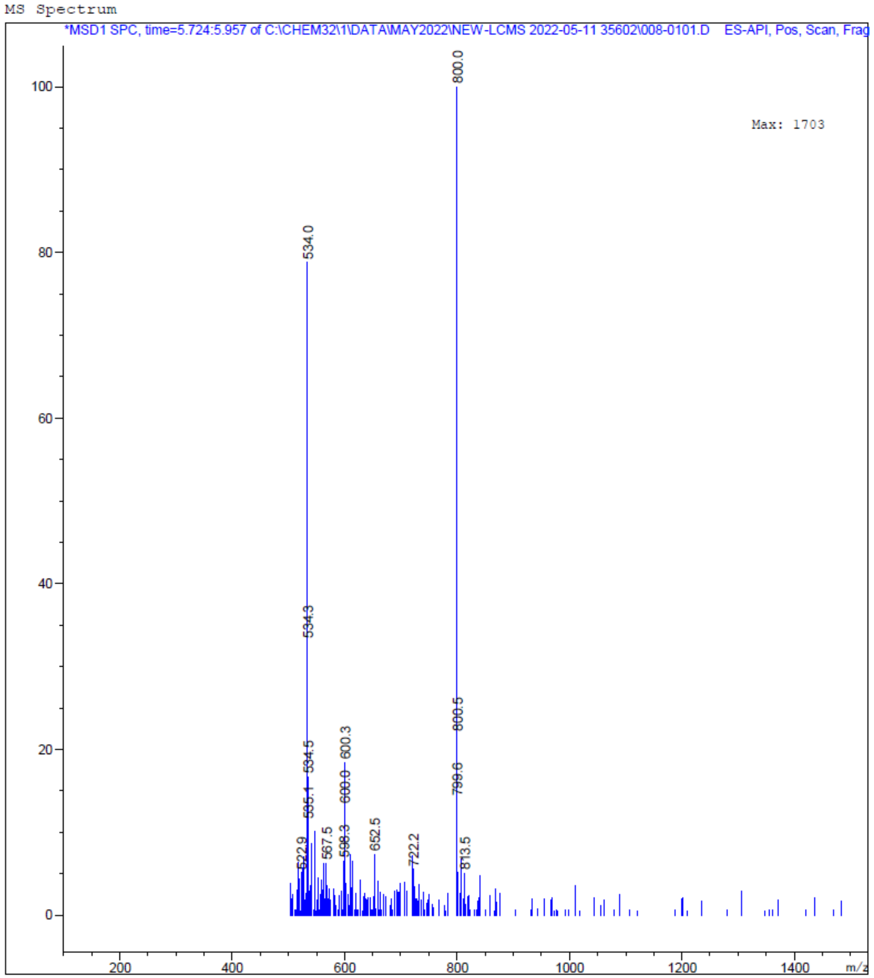

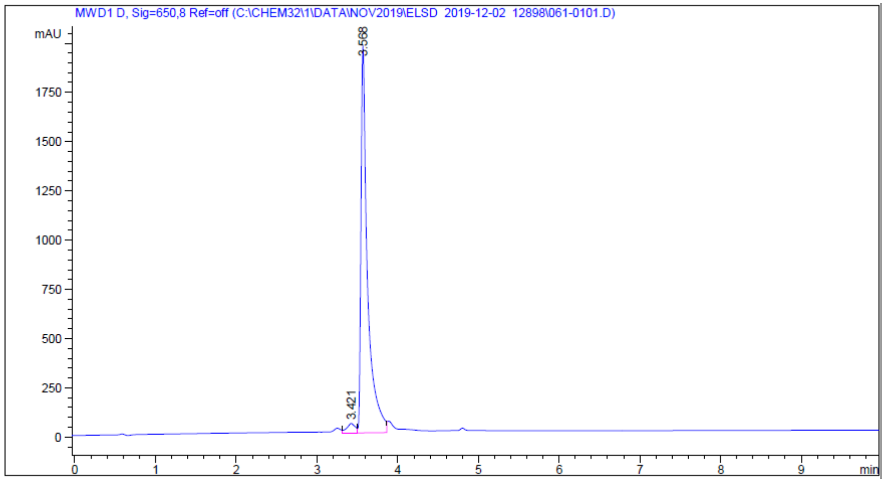

HNE-3F0Q

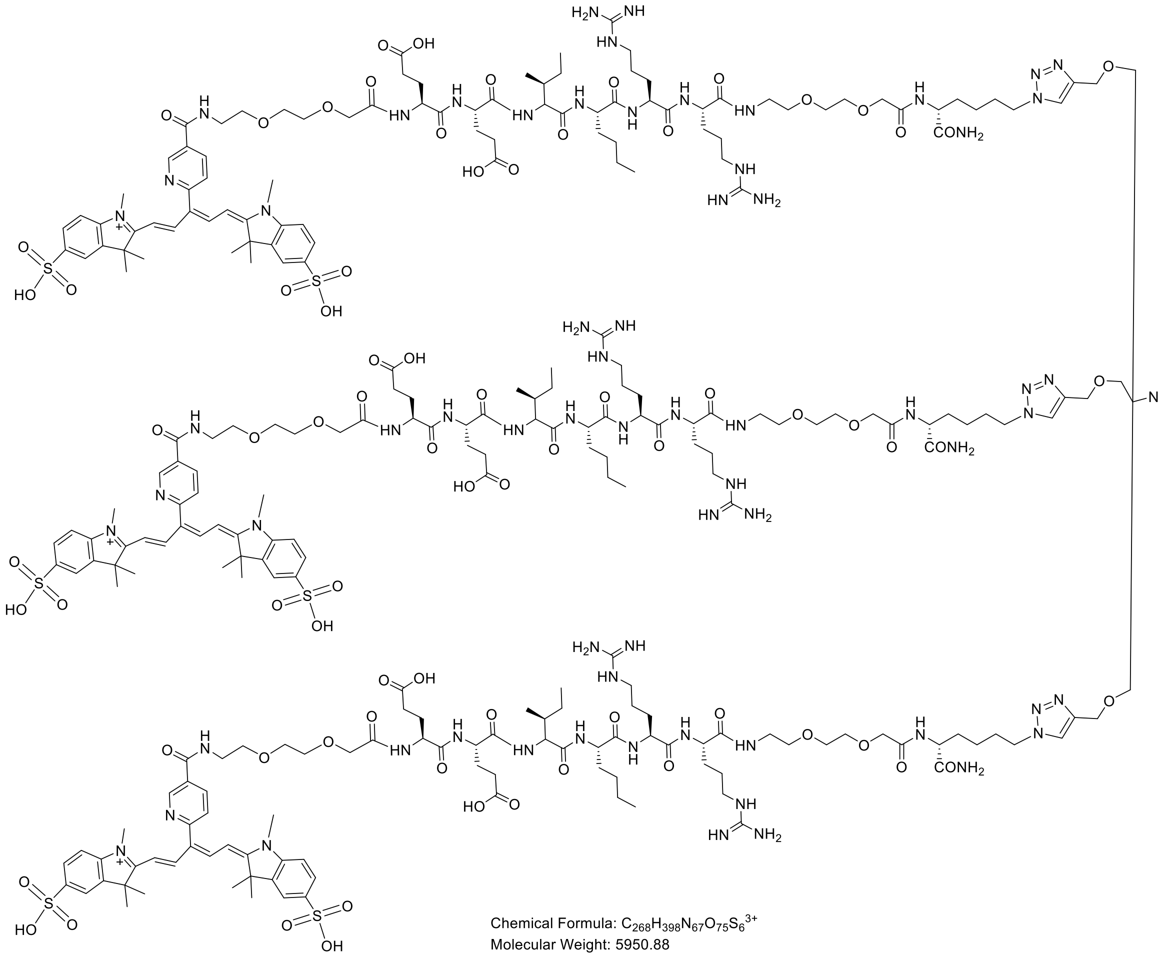

Chemical Formula: $C_{268}H_{398}N_{67}O_{75}S_6^{3+}$

Molecular Weight: 5950.88

FT-HRMS: Calculated m/z for $C_{268}H_{400}N_{67}O_{75}S_{65}$ $[M+2H]^{5+}$: 1190.358308 Found: 1190.356672

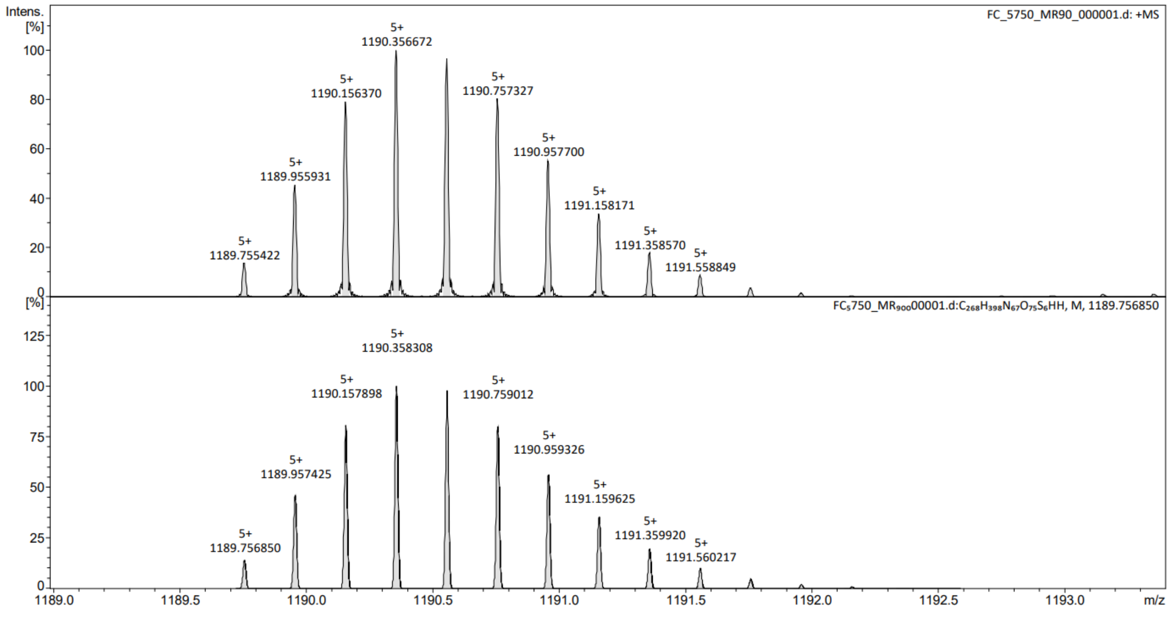

LC-MS : Found m/z $[M+H]^{4+}$: 992.2

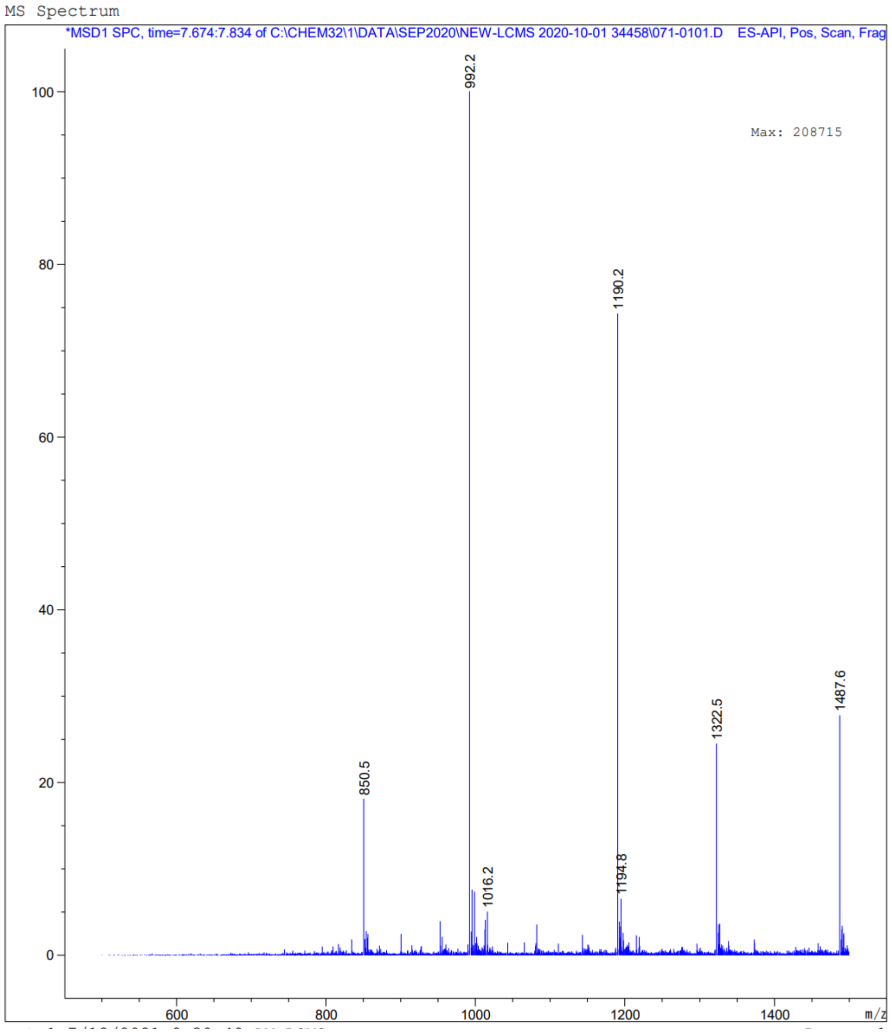

HPLC ELSD (Method C, 650 nm): r_t : 6.6 min

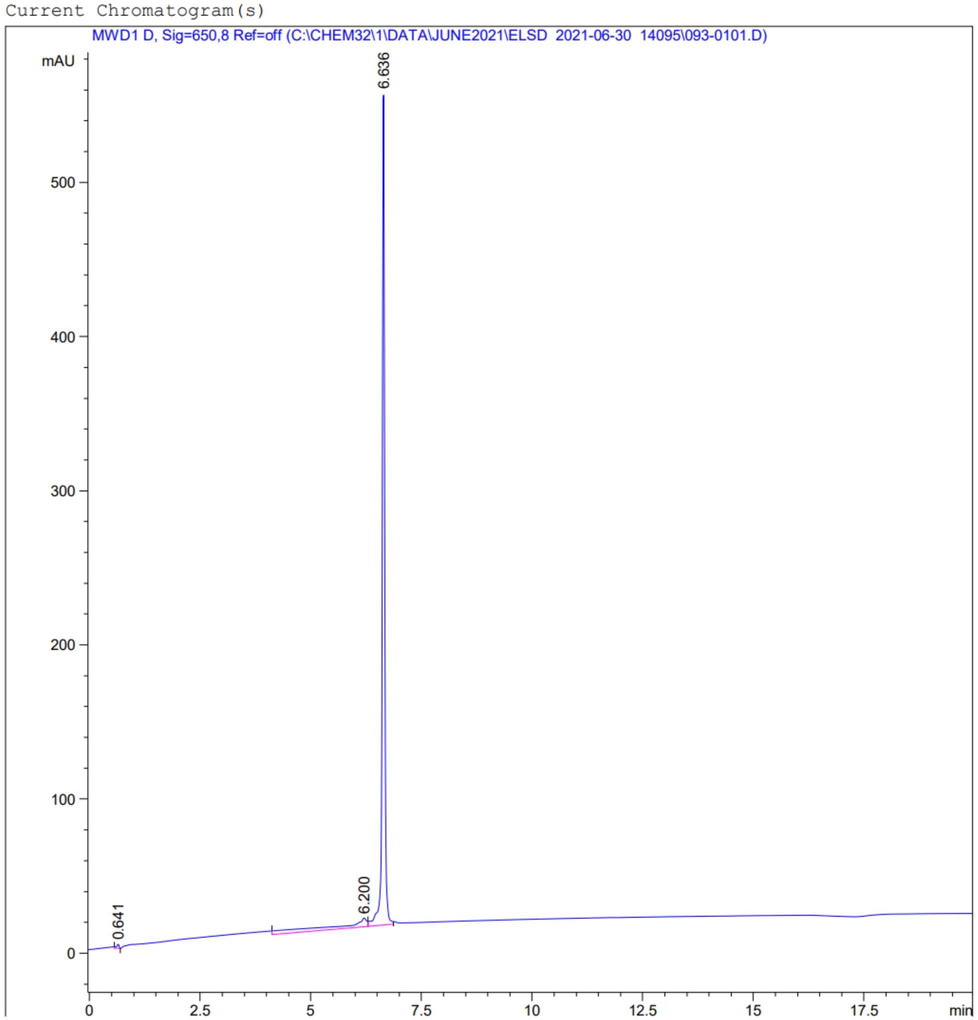

HNE-F31Q

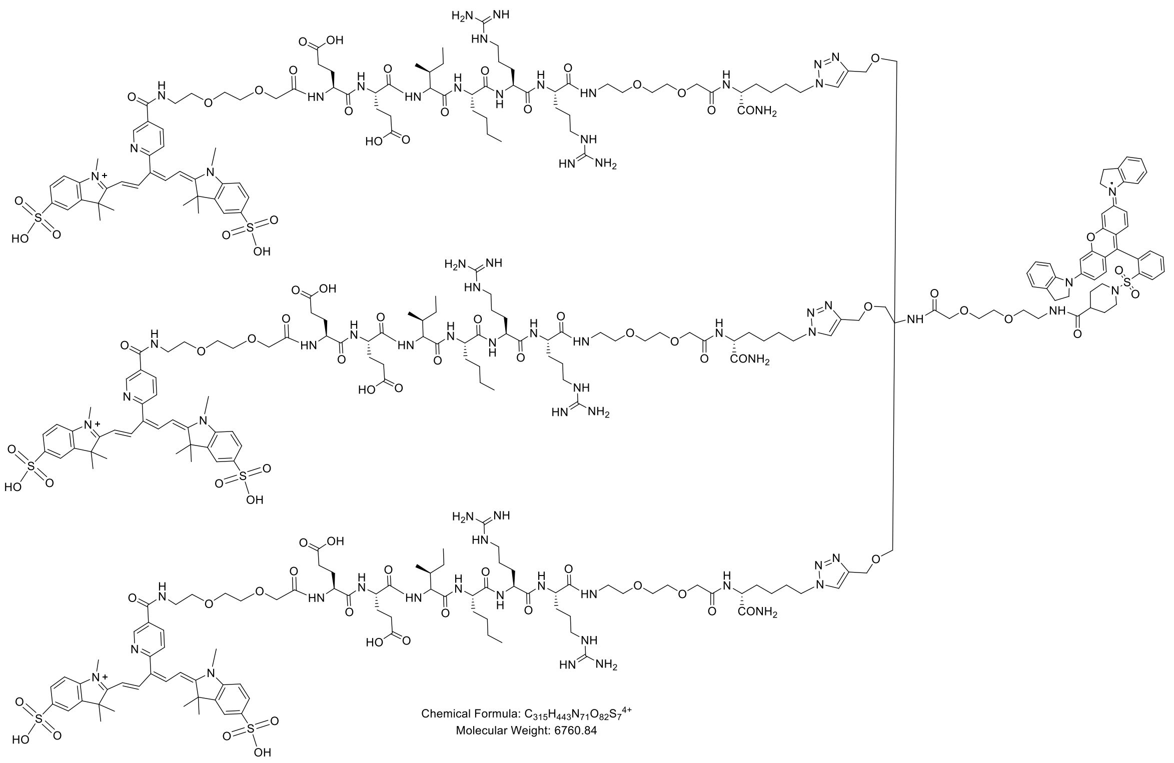

Chemical Formula: $C_{315}H_{443}N_{71}O_{82}S_7^{4+}$
Molecular Weight: 6760.84

FT-HRMS: Calculated m/z for $C_{315}H_{443}N_{71}O_{82}S_7$ $[M+H]^{5+}$ Expected: 1352.21737 Found: 1352.22055.

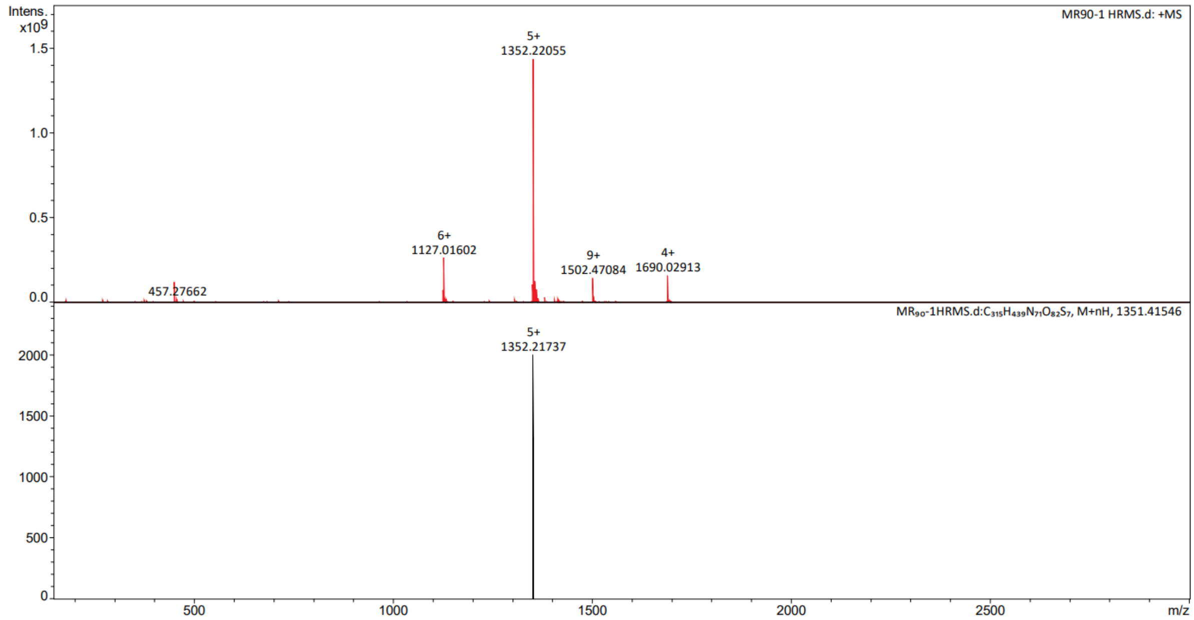

LC-MS : m/z $[M+H]^{5+}$ 1126.9

HPLC ELSD (Method C, 650 nm) : r_t 8.5 min

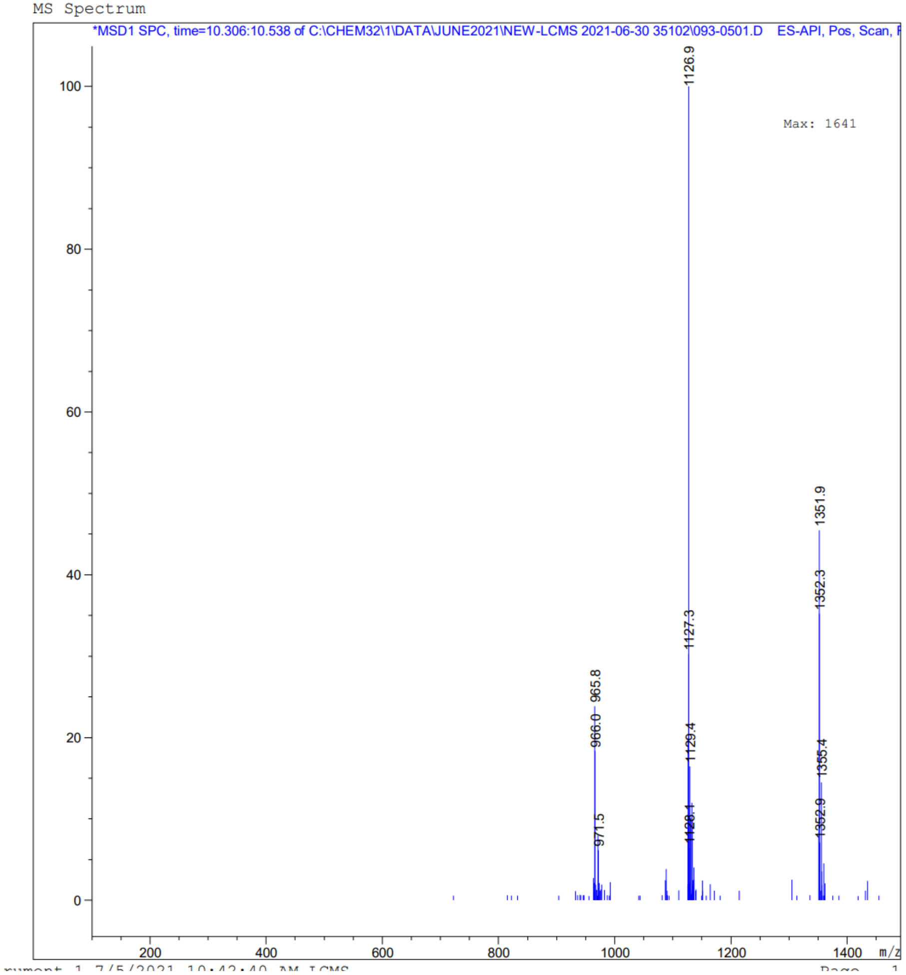

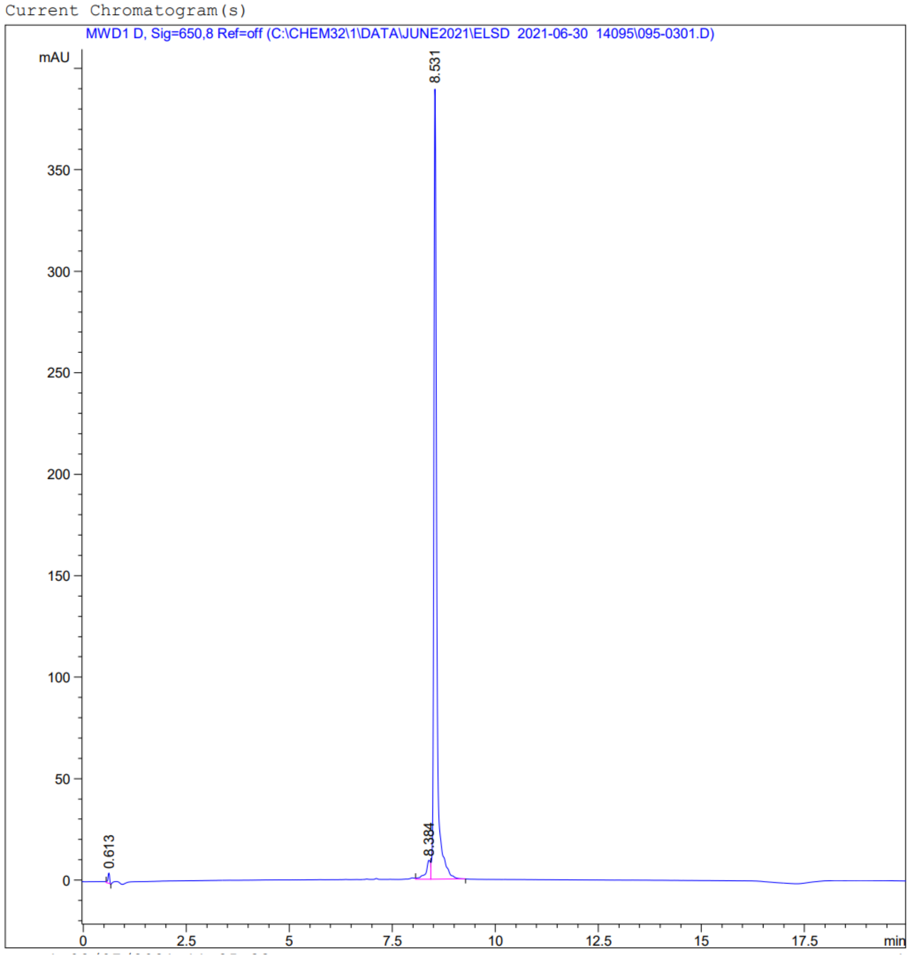

CatD-P1

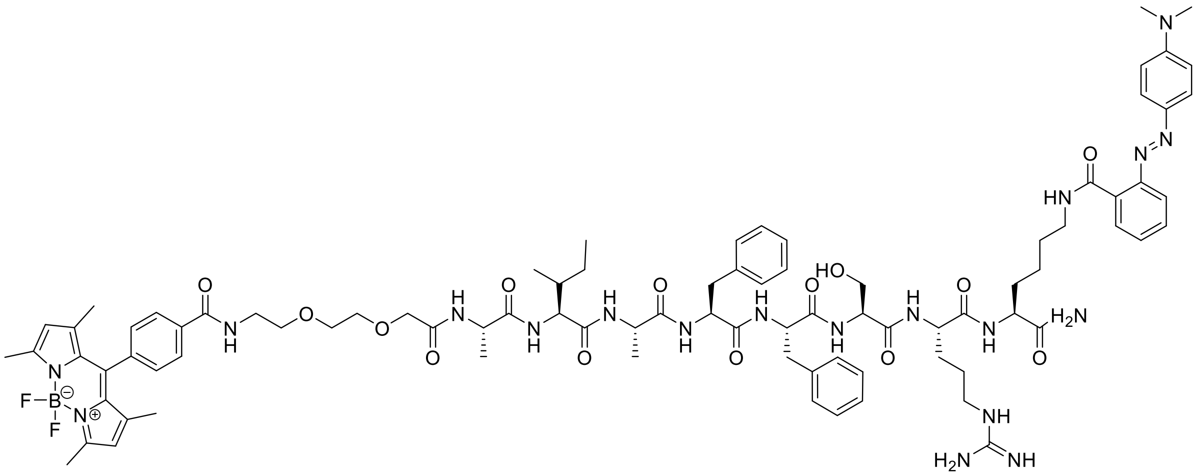

Chemical Formula: $C_{86}H_{112}BF_2N_{19}O_{14}$
Molecular Weight: 1684.77

FT-HRMS: Calculated m/z for $C_{86}H_{112}BF_2N_{19}O_{14}$ $[M+H]^+$ Expected: 1685.87628 Found: 1685.88073

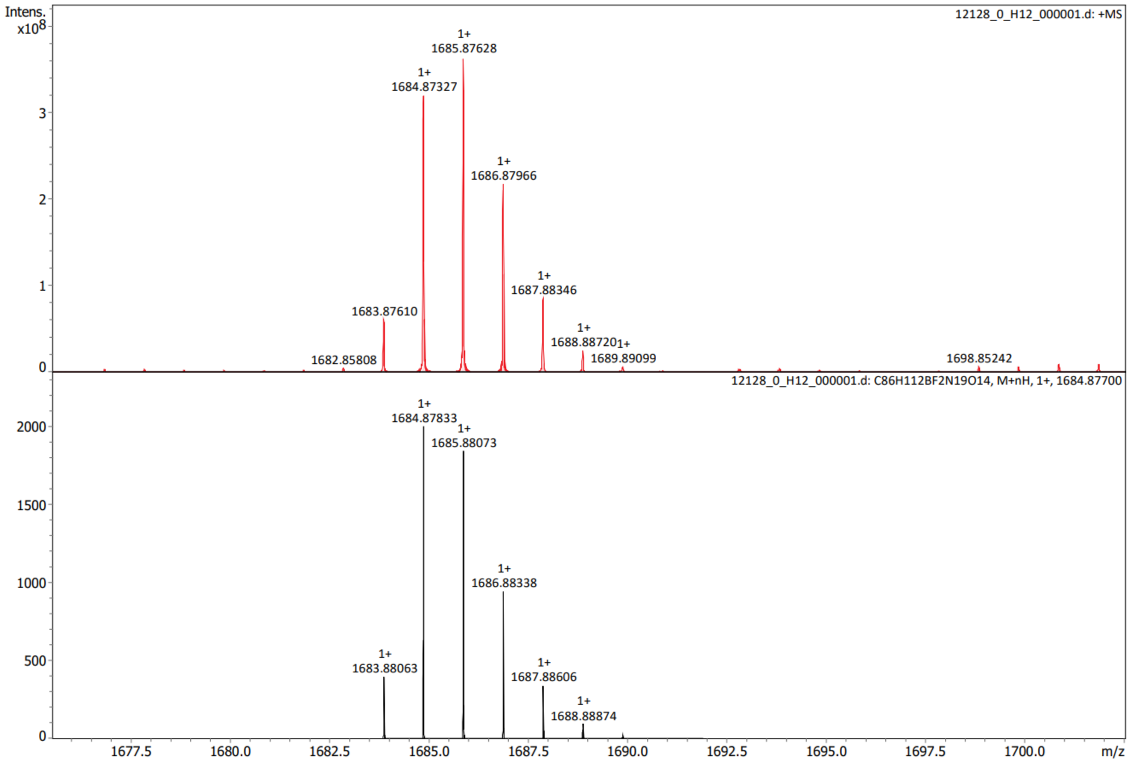

LC-MS : m/z $[M+H]^+$ 871.0

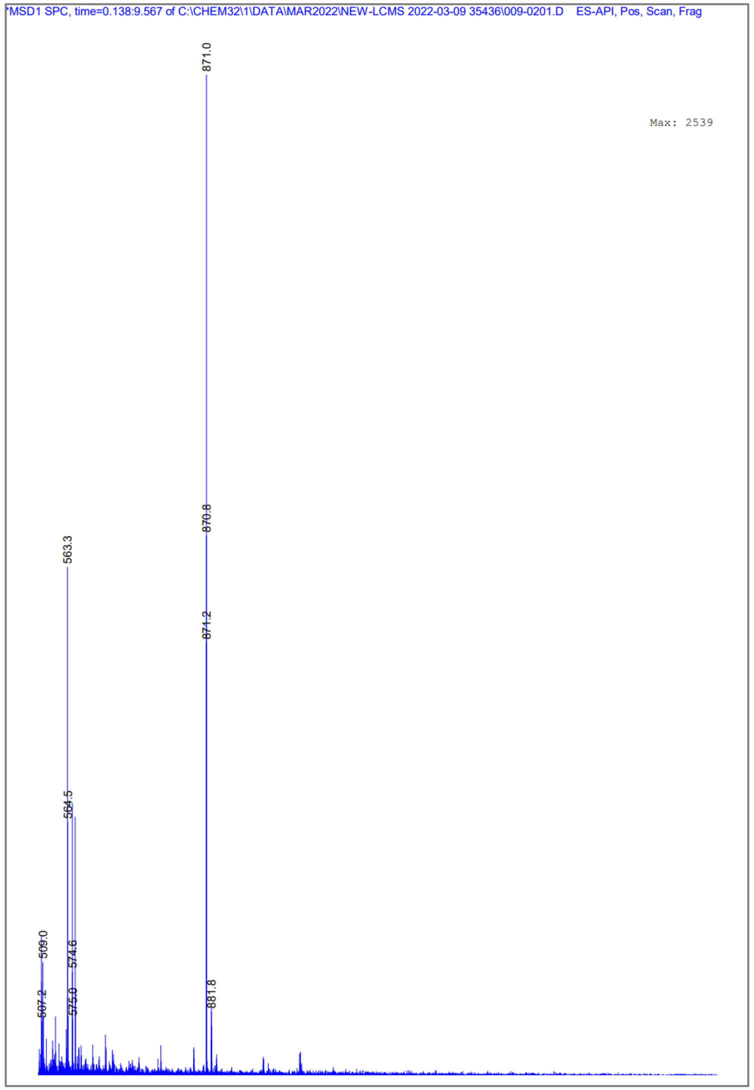

HPLC ELSD (Method A, 495 nm) : r_t 4.9 min

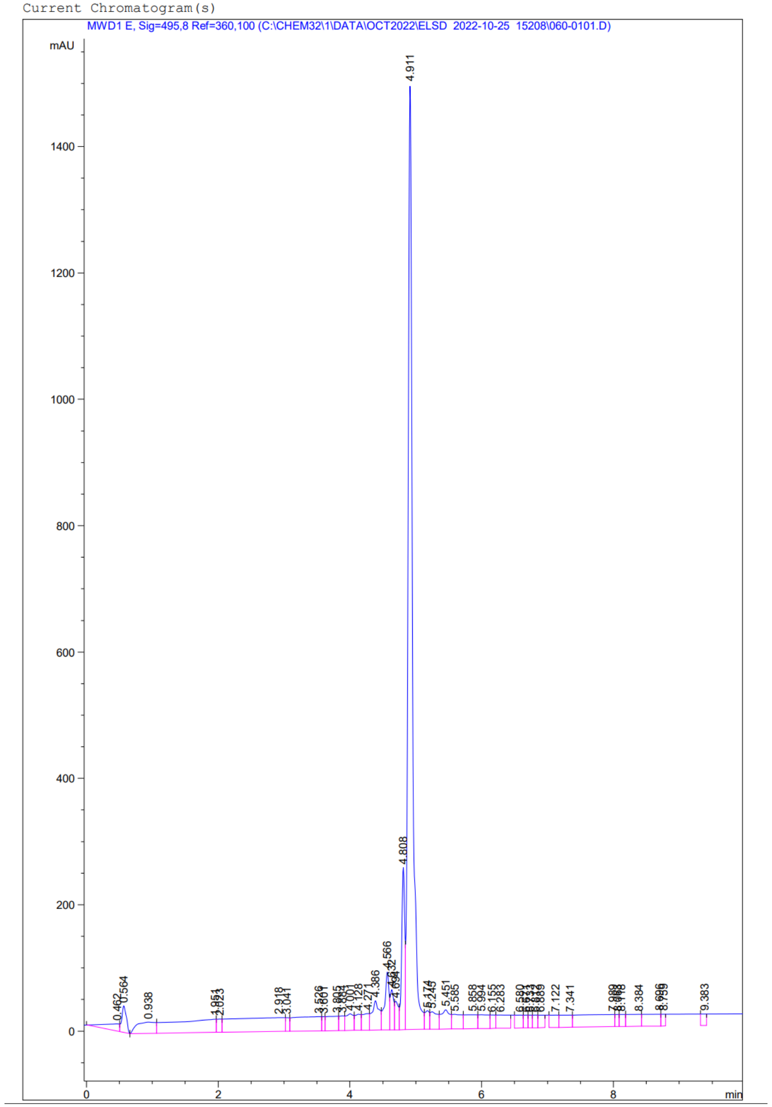

CatD-P2

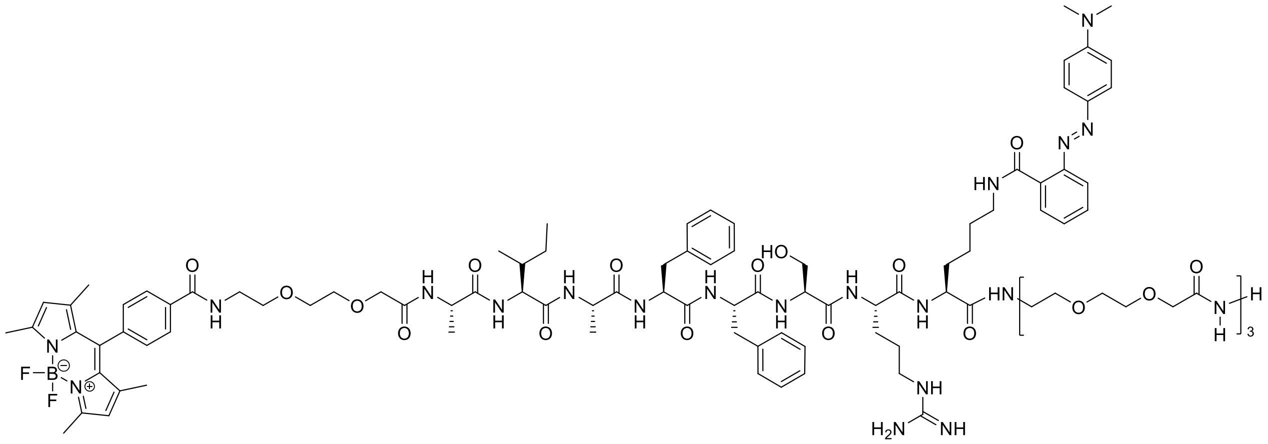

Chemical Formula: $C_{104}H_{145}BF_2N_{22}O_{23}$
Molecular Weight: 2120.24

MALDI-TOF MS: m/z expected: 2121.104; found: 2121.302

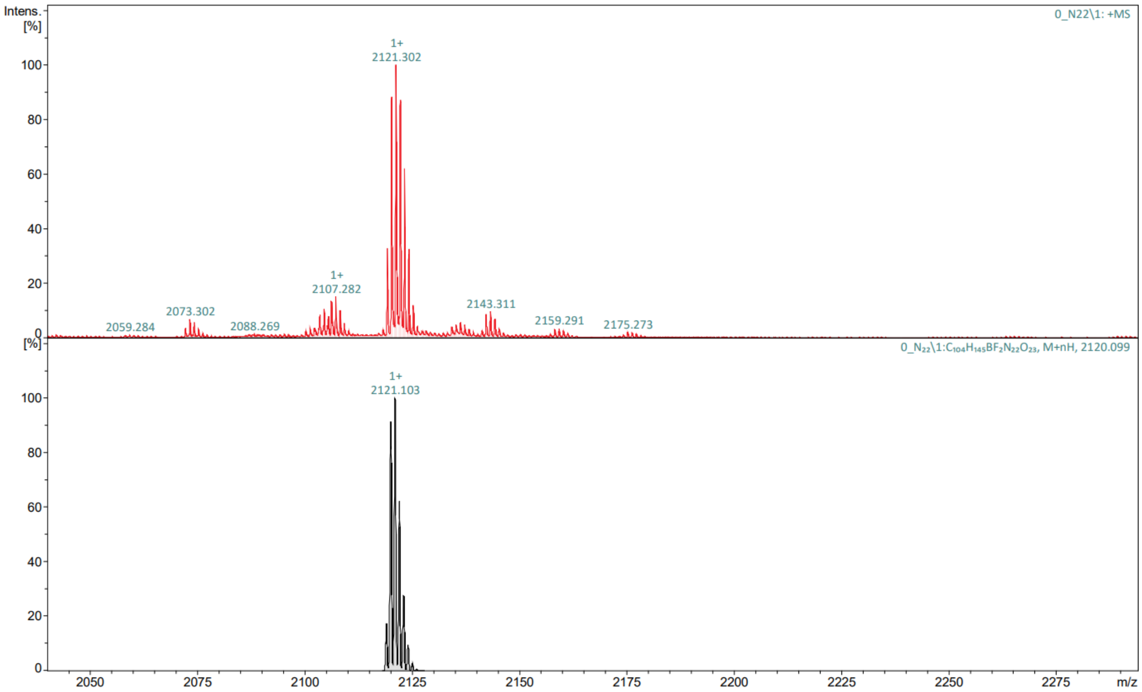

HPLC UV (Method B, 495 nm) : r$_t$ 6.8 min

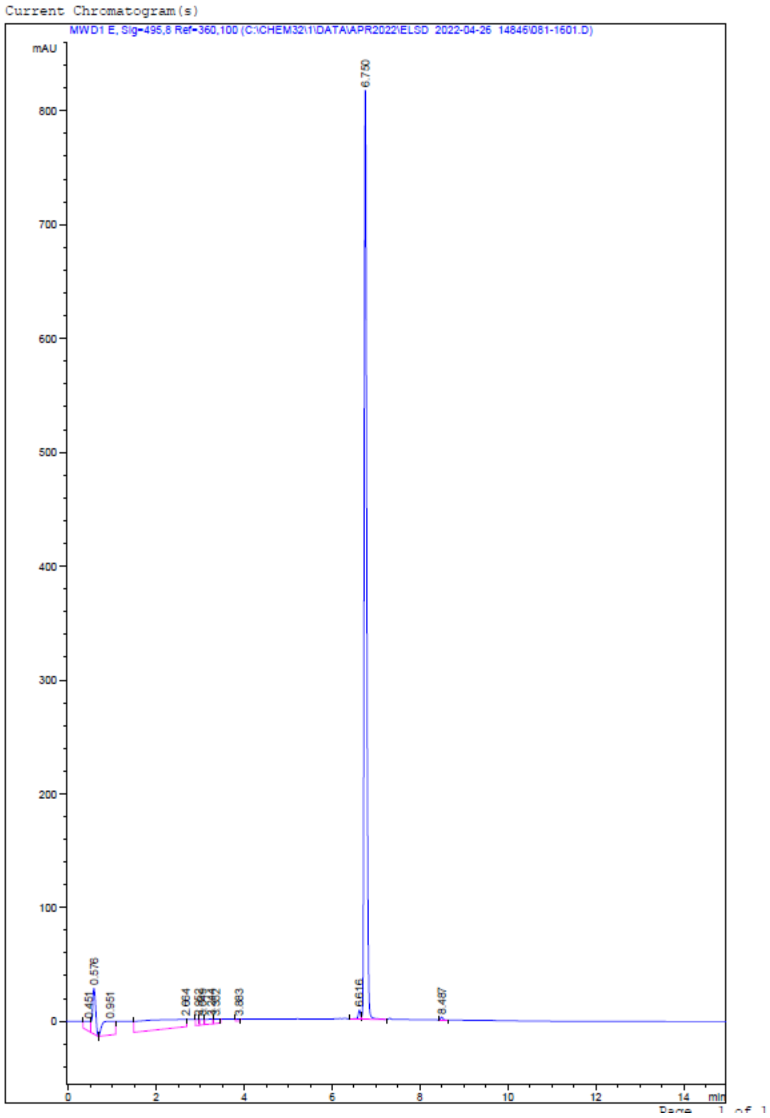

LC-MS : m/z [M+3H]$^{3+}$: 707.5

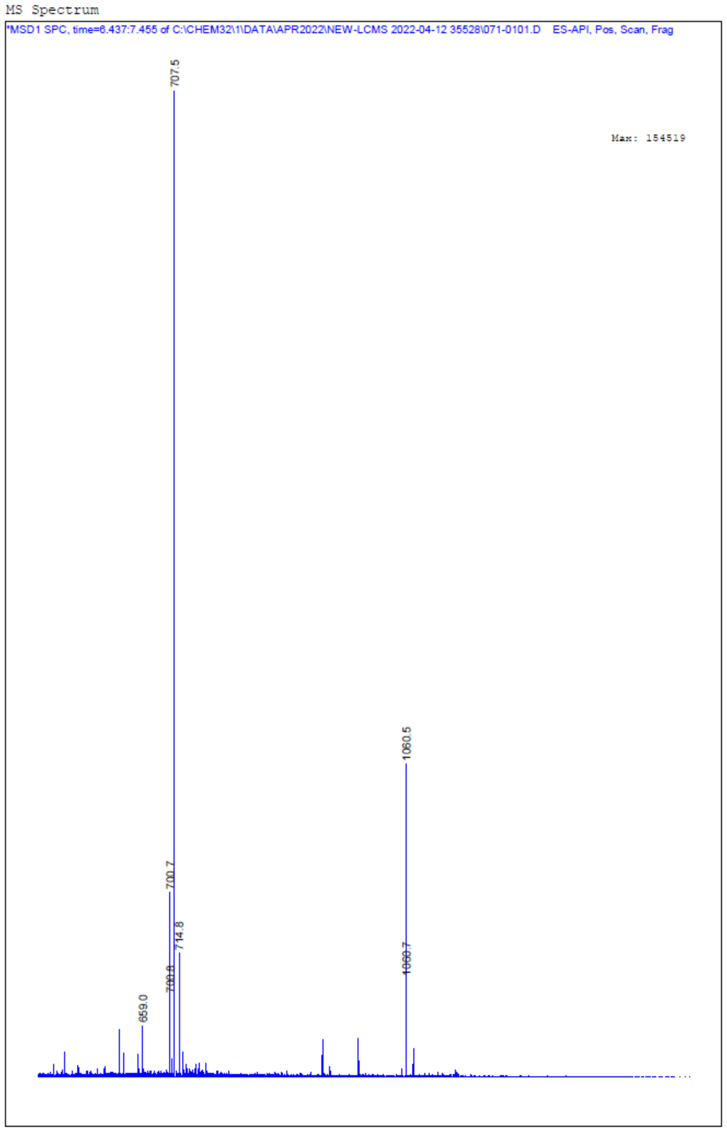

BODIPY-peptide

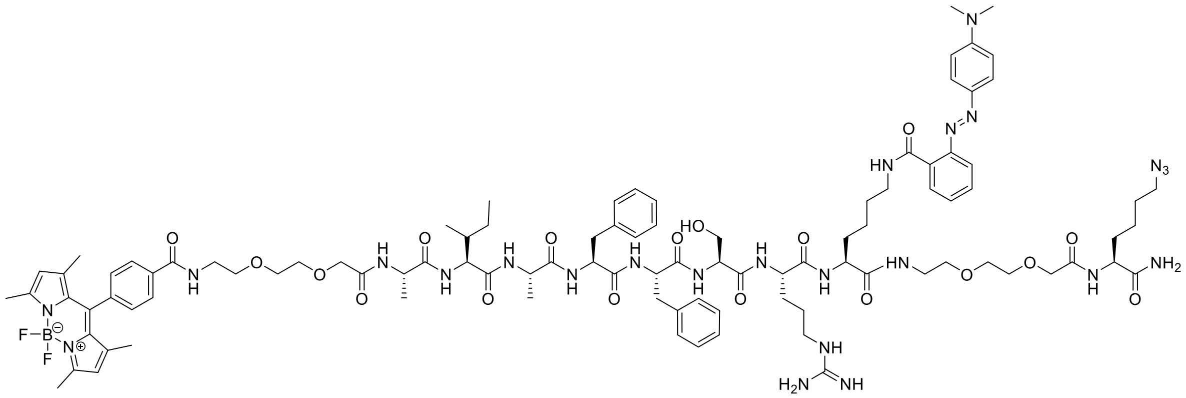

Chemical Formula: $C_{98}H_{133}BF_2N_{24}O_{18}$
Molecular Weight: 1984.10

FT-HRMS: Calculated m/z for $C_{98}H_{133}B_1N_{24}F_4O_{18}$ $[M+H]^+$ Expected: 1985.0401 Found: 1985.0386.

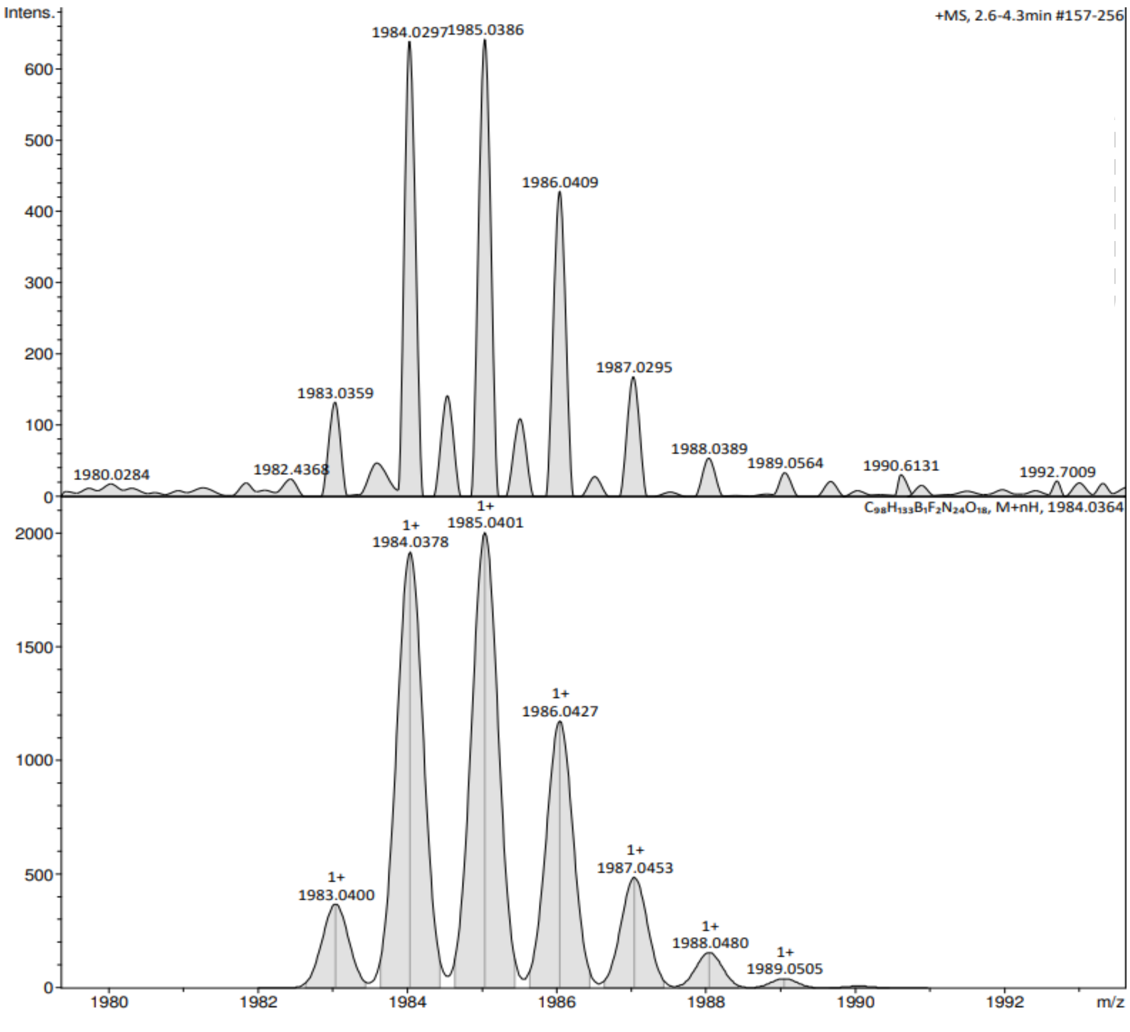

LC-MS : m/z $[M+2H]^{2+}$: 992.5

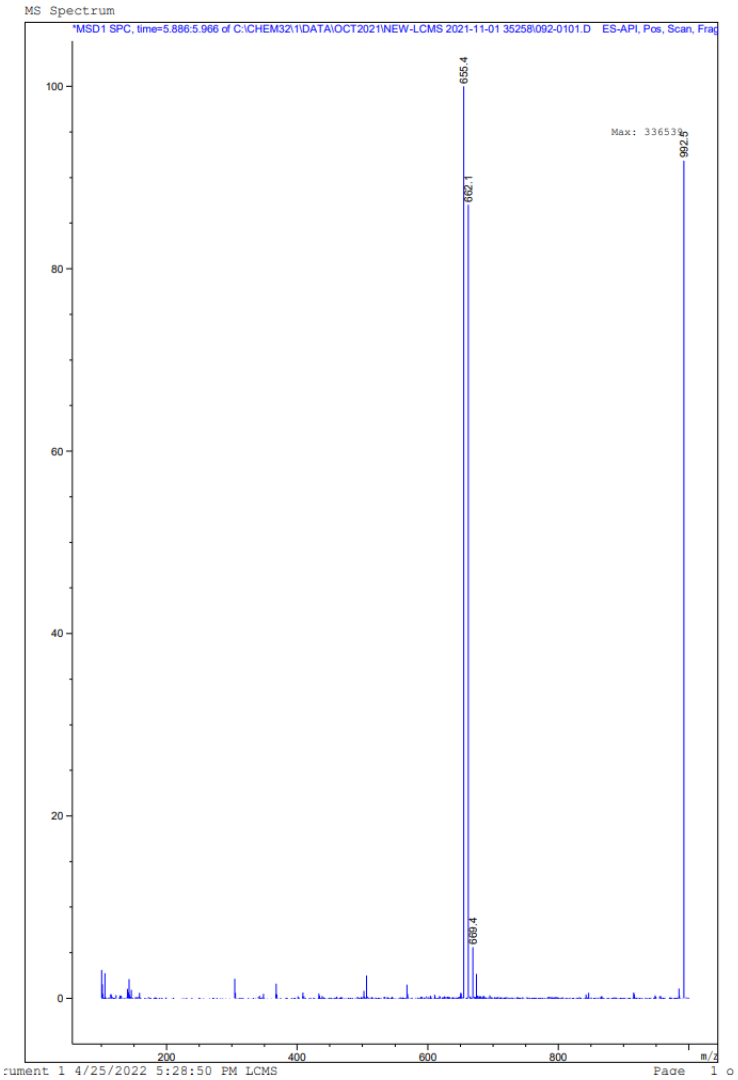

HPLC UV (Method A, 495 nm) : r_t 5.1 min

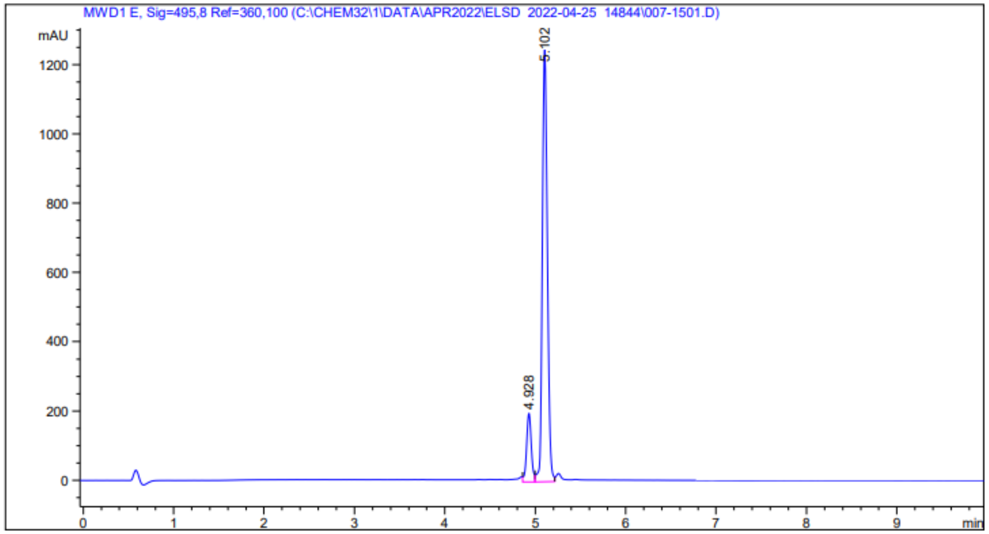

CatD-P3

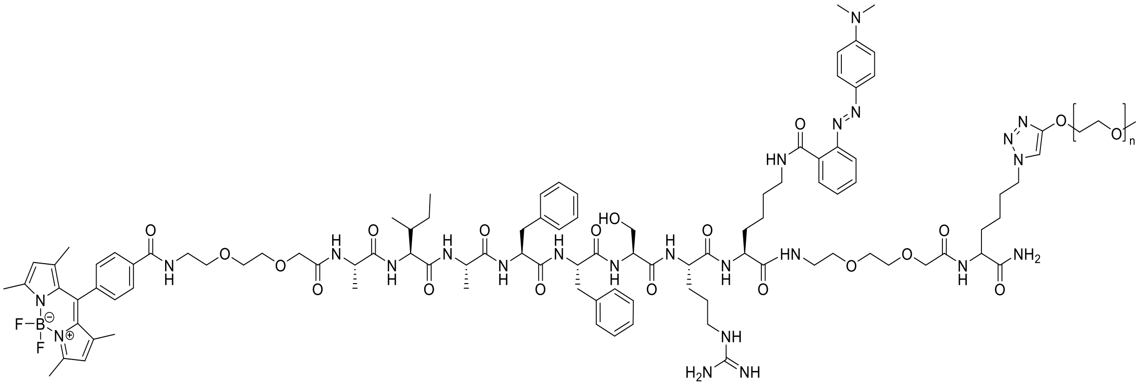

HPLC (Method A at 495 nm or ELSD) : r_t 4.6 min

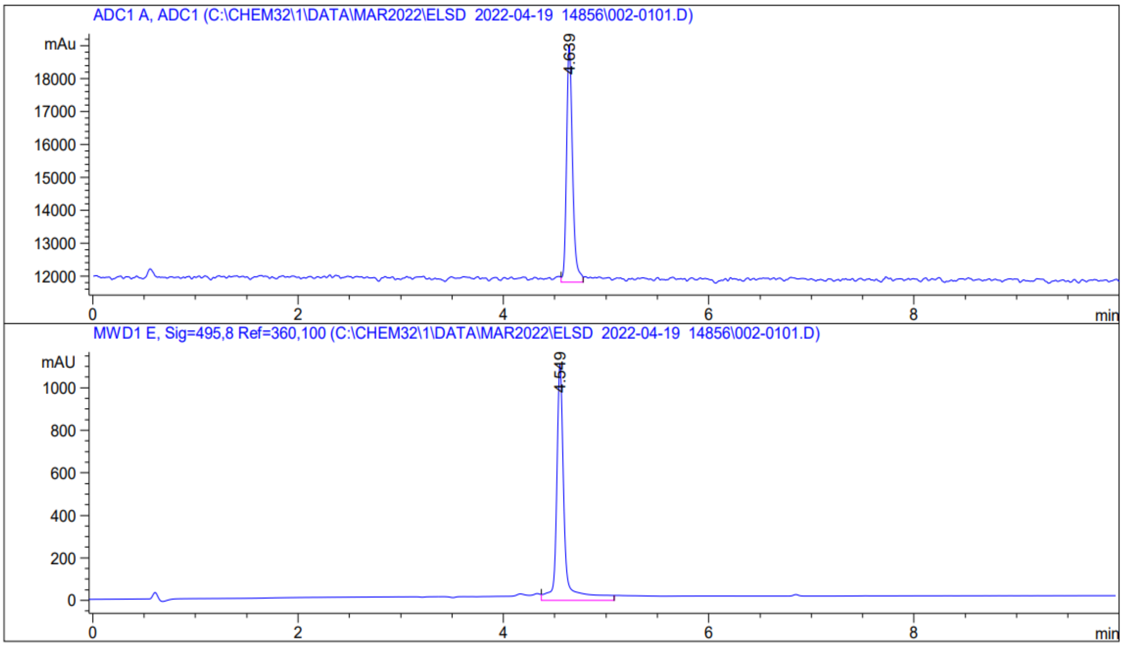

MALDI-TOF MS: m/z found 6000-8000